UNIVERSITY OF STRASBOURG

DOCTORAL THESIS

to obtain the degree of: **Docteur de l'Université de Strasbourg**

Specialty: *Photonics*

Defense: 6th April 2022

QUANTITATIVE MULTI-MODAL OPTICAL IMAGING FOR SURGERY

Doctoral Candidate:
Luca BARATELLI

Supervisor:
Prof. Sylvain GIOUX, HDR, Intuitive Surgical Sàrl
Co-Supervisor:
Ass. Prof. Manuel FLURY, HDR, INSA Strasbourg, ICube

Reviewers:
Prof. Brian W. POGUE, Dartmouth College
Prof. Daniel ELSON, Imperial College London

Examiners:
Prof. Antonio PIFFERI, Politecnico di Milano
Prof. Michele DIANA, IRCAD, University of Strasbourg

ED 269 - Mathématiques, Sciences de l'Information et de l'Ingénieur (MSII)

UMR 7357 - Laboratoire ICube, Équipe Instrumentation et Procédés Photoniques (IPP)

Academic Years 2019-2022

"Come è più difficile a 'ntendere l'opere di natura che un libro d'un poeta."

Leonardo Da Vinci

UNIVERSITY OF STRASBOURG

Abstract

QUANTITATIVE MULTI-MODAL OPTICAL IMAGING FOR SURGERY

by Luca BARATELLI

Surgery is still nowadays facing a major problem concerning the performances of the gesture, due to a lack in the specificity of the diagnosis. As a matter of fact, in most cases, the success of the surgical procedure relies on the experience of the surgeon and on their capacity to distinguish a pathological tissue from an healthy one. In this sense, it is of outstanding interest to develop real-time quantitative tools to assist the physicians during a surgical procedure, in order to minimize the impact of their experience on the success rate of the treatment. Wide field diffuse optical imaging methods, including fluorescence imaging, have shown a strong potential to provide surgeons with a non-invasive and real-time feedback during procedures. The aim of this doctoral thesis project is to develop innovative, real-time multi-modal optical imaging techniques for open and minimally invasive surgery, by providing information on fundamental physiological parameters of a certain tissue, such as the oxygen saturation. This work is built on Spatial Frequency Domain Imaging (SFDI) and more specifically on its real-time derivation "Single Snapshot imaging of Optical Properties" (SSOP). One of the goals is to bring SSOP to minimally invasive surgery by implementing a clinically compatible endoscopic imaging system based on the latest developments of SSOP powered by deep learning architectures and GPGPU computing. At first, a benchtop prototype was validated on tissue mimicking phantoms and then further developed into an handheld version adapted for pre-clinical trials. As a second objective, a multi-modal referencing platform was developed for the spectroscopic optical characterization of diffusive media. The instrument combines SFDI and Time-resolved Diffuse Optical Spectroscopy (TDOS) for the implementation of a cross-reference approach for the quantification of tissue optical properties. A first performance validation showed promising results for the combination of the two techniques. In perspective, we foresee for the platform a more robust characterization of absorption and reduced scattering by investigating the highlighted discrepancy between SFDI and TDOS, as well as an extension of the spectroscopic range to a larger wavelength window (400-1000 nm). For the endoscopic imaging system, pre-clinical trials and an optimization of the form factor are the main objectives for future work.

Keywords: Diffuse optical imaging, spatial frequency domain imaging, time domain spectroscopy, endoscopic imaging, image-guided surgery, deep learning.

UNIVERSITY OF STRASBOURG

Résumé

La chirurgie est encore aujourd'hui confrontée à un problème majeur concernant les performances du geste, à cause du manque d'outils de quantification pour le diagnostic. En effet, dans la plupart des cas, le succès de la procédure exploitée repose sur l'expérience du chirurgien et sur sa capacité à distinguer un tissu pathologique d'un tissu sain. Dans ce sens, il est d'un intérêt crucial de développer des outils quantitatifs pour assister en temps réel les médecins pendant une opération, afin de minimiser l'impact de leur expérience sur le taux de réussite du traitement. L'imagerie optique diffuse à champ large, ainsi que les techniques d'imagerie par fluorescence, offrent un fort potentiel, notamment en tant que des méthodes non invasives pour la chirurgie guidée par l'image. L'objectif du projet de thèse est de développer des techniques d'imagerie optique multimodale innovantes en temps réel pour la chirurgie ouverte et mini-invasive, en fournissant des informations sur les paramètres physiologiques fondamentaux d'un certain tissu, comme la saturation en oxygène qui seront directement utilisées dans l'environnement clinique. Ce travail s'appuie sur la Spatial Frequency Domain Imaging (SFDI) et plus particulièrement sur sa dérivation en temps réel "Single Snapshot imaging of Optical Properties" (SSOP). L'un des objectifs est d'introduire la SSOP dans la médecine mini-invasive en mettant en œuvre un système d'imagerie endoscopique cliniquement compatible basé sur les derniers développements de la SSOP, alimenté par des architectures Deep Learning et le calcul GPGPU. Un premier prototype a été validé sur des fantômes imitant des tissus, puis développé en une version portable adaptée aux essais précliniques. Comme deuxième objective, une plateforme de référencement multimodal a également été développée au cours du projet de thèse pour la caractérisation optique spectroscopique des milieux diffusifs. L'instrument combine la Spatial Frequency Domain Imaging (SFDI) et la Time-resolved Diffuse Optical Spectroscopy (TDOS) pour la mise en œuvre d'une approche de référence croisée dans la quantification des propriétés optiques des tissus. Une première validation des performances a montré des résultats prometteurs pour la combinaison des deux techniques. Nous prévoyons pour la plateforme une caractérisation plus robuste de l'absorption et de la diffusion réduite en étudiant la divergence encore presente entre SFDI et TDOS, ainsi qu'une extension de la gamme spectroscopique à une plus grande fenêtre de longueur d'onde (400-1000 nm). Pour le système d'imagerie endoscopique, des essais précliniques et une optimisation du facteur de forme sont les principaux objectifs des travaux futurs.

Mots-clés: Imagerie optique diffuse, spatial frequency domain imaging, time domain spectroscopy, endoscopie, chirurgie guidée par l'image, deep learning.

Acknowledgements

My doctoral journey comes to a conclusion in this manuscript, which formally and practically encloses the scientific results of a three years experience in academic research. Despite the many challenges encountered in the process, I am proud to look back at the work conducted in the laboratory as a great achievement that would have not been possible without a strong motivation towards giving a tiny (but relevant) scientific contribution to the development of photonics technologies for surgical guidance. I feel I managed to give all my effort to be an active member of a highly stimulating research group, that gathers some of the kindest, most skillful and intelligent people I had the luck to know and work with. In this sense, I would like to sincerely thank some of the people that have been part of this enriching experience (I apologize in advance for the list of "Thank you" that does not represent an amazing proof of creativity, but that it actually embeds the most genuine appreciation for all the people mentioned in the following...):

*Thank you to my thesis Director and Supervisor, **Prof. Syvlain Gioux**. You have been a strong guide for the entire duration of the work, and a great source of mentorship, creativity, experience and scientific rigor that supported me and allowed me to reach this great achievement.*

*Thank you to my thesis Co-Supervisor, **Prof. Manuel Flury**. Despite the fact that you joined my supervision after the first year of work, you provided a fantastic contribution with interesting ideas and with the support necessary to complete many tasks of the thesis.*

*Thank you to all the members of the jury, and in particular: **Prof. Brian W. Pogue** and **Prof. Daniel Elson** for accepting to be the reviewers of this manuscript; **Prof. Antonio Pifferi** for assuming the role of examiner, for which you agreed to follow my work right from the start (together with Prof. Pogue); **Prof. Michele Diana** for accepting to be part of the jury as an internal examiner, but also for coordinating and performing several pre-clinical experiments in the surgical room.*

*Thank you to the **ICube Laboratory**, and in particular to the team IPP for allowing me to conduct my work in such an amazing environment.*

*Thank you to my fellow colleagues **Silvère**, **Agathe**, **Fabrice** and **Emmanuel**, for welcoming me, an almost completely bald Italian doctoral student landing in France: thank you for your patience in talking to me in a language that was native to none of us, but also to giving me the possibility to practice my extremely Italian accented French; thank you for the countless beers and tartes flambées shared in pretty much all the bars in and around Strasbourg; thank you for sharing your culture, and of course thank you for sharing some sleepless nights in the lab, am I right Silvère?!*

*Grazie alla mia **Famiglia**, che mi ha sempre sostenuto in qualsiasi circostanza nelle scelte che ho fatto e nel percorso appena completato. Non vi nego che a volte è stato difficile non poter rientrare a casa, e senz'altro la presenza di una pandemia non ha di certo aiutato in questo senso, ma vi ho sempre avuto nel mio cuore e nei miei pensieri, come sono sicuro abbiate fatte anche voi (spero?!). E tu, Topoletto (a.k.a. Andrea Jr.), sei il sorriso di cui non possiamo più fare a meno, ma sappi che appena diventi grande lo zio ti insegnerà tutto quello che sa sulla materia più affasciante e stupenda che conosce, perchè sono sicuro che sarai più intelligente di tutti noi messi insieme!*

*Merci à toi, ma **Bretonne Préférée**, pour la patience que tu m'as montrée dans ces derniers mois de travail, de rédaction (et pas beaucoup d'autres choses) et pour le soutien incroyable que tu m'as donné pendant mon parcours. Je suis heureux de t'avoir dans ma vie !*

Grazie ai miei fidati ***amici italici****, con i quali ho condiviso anche questa avventura e che mi hanno sempre sostenuto a distanza (o via Zoom!!) in tutti questi mesi. Siete fantastici!*

And I think that should probably be it, and hopefully by the time this manuscript reaches all the people mentioned in these acknowledgments I might have achieved the title of:
Luca Baratelli, Ph.D..

Strasbourg, 6th April 2022
L.B.

Contents

List of Figures

List of Tables

List of Abbreviations

1D	**1**-**D**imensional
2D	**2**-**D**imensional
3D	**3**-**D**imensional
AC	**A**lternating **C**urrent
AL	**A**nastomotic **L**eak
ALU	**A**rithmetic **L**ogic **U**nit
AMD	**A**dvanced **M**icro **D**evices
API	**A**pplication **P**rogramming **I**nterface
AR	**A**ugmented **R**eality
BIP	**B**asic **I**nstrument **P**erformance
BITMAP	**B**rain **I**njury and **T**rauma **M**onitoring using **A**dvaced **P**hotonics
CFD	**C**onstand **F**raction **D**iscriminator
CNN	**C**onvolutional **N**eural **N**etworks
CPU	**C**entral **P**rocessing **U**nit
CT	**C**omputed **T**omography
CUDA	**C**ompute **U**nified **D**evice **A**rchitecture
CW	**C**ontinuous **W**ave
DC	**D**irect **C**urrent
DCR	**D**ark **C**ount **R**ate
DE	**D**iffusion **E**quation
DFT	**D**iscrete **F**ourier **T**ransform
DFU	**D**iabetic **F**ood **U**lcers
DL	**D**eep **L**earning
DMD	**D**igital **M**icromirror **D**evice

DNL	**D**ifferential **N**on **L**inearity
DNN	**D**eep **N**eural **N**etworks
DO	**D**iffuse **O**ptics
EBC	**E**xtrapolated **B**oundary **C**onditions
FD	**F**requency **D**omain
FDA	U.S. **F**ood and **D**rug **A**dministration
FFT	**F**ast **F**ourier **T**ransform
FIGS	**F**luorescence **I**mage-**G**uided **S**urgery
fMRI	**f**unctional **M**agnetic **R**esonance **I**maging
FOM	**F**igures **O**f **M**erit
FPA	**F**ocal **P**lane **A**rray
FPS	**F**rames **P**er **S**econd
FT	**F**ourier′s **T**ransform
FTIR	**F**ourier′s **T**ransform **I**nfra**R**ed
FWHM	**F**ull **W**idth at **H**alf-**M**aximum
GAN	**G**enerative **A**dversarial **N**etworks
GANPOP	**G**enerative **A**dversarial **N**etworks **P**rediction of **O**ptical **P**roperties
GC	**G**astric **C**onduit
GPGPU	**G**eneral **P**urpose computing on **G**raphics **P**rocessing **U**nits
GPU	**G**raphics **P**rocessing **U**nit
HSI	**H**yper**S**pectral **I**maging
ICG	**I**ndo**C**yanine **G**reen
IR	**I**nfra**R**ed
IRF	**I**nstrument **R**esponse **F**unction
LED	**L**ight-**E**mitting **D**iode
LUT	**L**ook-**U**p **T**able
MC	**M**onte **C**arlo
MCA	**M**ulti**C**hannel **A**nalyser
MIS	**M**inimally **I**nvasive **S**urgery
MLP	**M**ulti-**L**ayered **P**erceptron
MRA	**M**agnetic **R**esonance **A**ngiography
MRI	**M**agnetic **R**esonance **I**maging
MSI	**M**ulti**S**pectral **I**maging
NBI	**N**arrow **B**and **I**maging
NIR	**N**ear-**I**nfra**R**ed
NIRS	**N**ear-**I**nfra**R**ed **S**pectroscopy
OCT	**O**ptical **C**oherence **T**omography
OHI	**O**rgan **H**emoglobin **I**ndex
OP	**O**ptical **P**roperty
PAD	**P**eripheral **A**rterial **D**iseases
PAS	**P**erformance **A**ssessment and **S**tandardization
PDW	**P**hoton **D**ensity **W**ave
RAM	**R**andom **A**ccess **M**emory
ROI	**R**egion **O**f **I**nterest
RTE	**R**adiative **T**ransfer **E**quation
sCMOS	**s**cientific **C**omplementary **M**etal **O**xide **S**emiconductor
SFDI	**S**patial **F**requency **D**omain **I**maging
SiPM	**Si**licon **P**hoto**M**ultiplier
SMM	**S**treaming **M**ultiprocessor **M**axwell
s-MTF	**s**patial **M**odulation **T**ransfer **F**unction
SNR	**S**ignal to **N**oise **R**atio

SPAD	**S**ingle **P**hoton **A**valanche **D**iode
SRS	**S**patially **R**esolved **S**pectroscopy
SSOP	**S**ingle **S**napshot imaging of **O**ptical **P**roperties
TAC	**T**ime-to-**A**nalog **C**onverter
TCSPC	**T**ime-**C**orrelated **S**ingle **P**hoton **C**ounting
TD	**T**ime **D**omain
TDOS	**T**ime-resolved **D**iffuse **O**ptical **S**pectroscopy
THI	**T**issue **H**emoglobin **I**ndex
TWI	**T**issue **W**ater **I**ndex
US	**U**ltra**S**ound
UV	**U**ltra-**V**iolet
VIS	**VIS**ible

Dedicated to my Family

Chapter 1

INTRODUCTION

The technological evolution that we are witnessing in the first decades of the 21^{st} Century is without any doubt one of the greatest achievements in the human history. "Connectivity" is probably the term that best summarizes the driving force of the scientific, industrial and socio-economical effort of the recent years to improve the lifestyle of the world population[1]. Accessibility to internet resources has never been this simple thanks to miniaturized workstations that we can comfortably carry in our pockets every day. 4-5 Generation communication technologies (with 6G architectures that are just around the corner...) that allow for the remote connection of machines and individuals at the opposite sides of the planet (and even further). Social media, that in some cases[2] have started leaving behind their original skin of highly efficient and simple connection tools to bring people together, beginning a transition to the new era of "parallel" universes based on virtual reality and "meta-experiences"[3]. The *Green Revolution*, with the rise of renewable energy sources, electrical and hydrogen-fueled vehicles with the aim of tackling the climate change emergency. The (second) run to space that might enable a new chapter of the travel industry, to name only a few.

Undoubtedly, these great achievements have only been possible thanks to the unprecedented improvements in the technological understanding of our World, pushing the boundaries of our reach to limits that were definitely almost unthinkable a few years back. Nonetheless, even in this privileged context, a sanitary crisis happened: the *COVID-19* pandemic broke into our lives with striking force, threatening to shatter completely our day-to-day routines, destroy our social relationships and doubt the whole socio-economical system that we have been building. But most importantly, it took more than 5 Million people[4] and determined the renewed awareness on the role of healthcare in our society. In this sense, it also launched the sprint to the identification and production of a vaccine, resulting into an unprecedented technological accomplishment that reached its final stages with a rapidity that we had never seen before, thanks to the incredible effort provided by the entire scientific community.

Given this particular scenario, it is evident that we do not pretend to propose our work in biomedical optical physics has a comparable impact on healthcare as the one determined by the latest achievements in viral disease sciences and pharmaceutics, but we think that our contribution fits well in the context of providing novel technological assets and tools for improving the surgical guidance in a completely non-invasive way. Indeed, despite the outstanding technological advances just mentioned, together with the improvements in the medical practice that we are experiencing on a day-to-day basis, it is certainly surprising how the performance of medical procedures depend in large part on the human factor. As matter of fact, surgery is still facing a major problem concerning the performances of the gesture, due to a lack in the specificity of the diagnosis. In most cases, the success of the exploited procedure relies on the experience of the surgeon and on their capacity to distinguish a pathological tissue from a healthy one. As a consequence, the results of the procedure remain extremely user-dependent and it is therefore of outstanding interest to develop real-time quantitative tools to assist the physicians during surgical procedures, in order to minimize the impact of their experience on the success rate of the treatment. In this framework, wide field diffuse optical imaging methods, including fluorescence imaging, have shown a strong potential to provide surgeons with a non-invasive and real-time feedback during procedures.

---

[1] The author is aware that this represents quite a bold statement that requires evident caveats which lie way beyond the scopes of this work however.

[2] Of course one in particular, we let the reader figure it out...

[3] Again, the aim here is to give an objective perspective to the changes in our society, and not a personal opinion on them. Therefore, we will stay as far as possible from discussing scandals, privacy issues etc...

[4] At the time of writing this manuscript: January 2022.

For this purpose, the first diffuse optics technique exploited in our work is called Spatial Frequency Domain Imaging (SFDI) [1] and it enables the imaging of the optical properties of a tissue (i.e. absorption and reduced scattering) over a large field of view. In a nutshell, by projecting spatially modulated patterns of light on the sample, it is possible to directly measure the absorption and reduced scattering coefficients over the entire field of view, through the use of light propagation models such as Monte-Carlo or Diffusion Approximation in the spatial frequency domain. In addition, a wide amount of information about the tissue can be estimated through a spectroscopic analysis. Indeed, the use of multiple wavelengths to interrogate living tissues with SFDI allows us to quantify the concentration of its fundamental constituents, thanks to the Beer's law, as well as to gather information relative to the microscopic structures, by analyzing the scattering parameters. Moreover, due to the need of real-time capabilities during surgical procedures, an improved acquisition method called "Single Snapshot imaging of Optical Properties" (SSOP) [2] was also developed by our group. The method is based on the same physical principles as SFDI but it is applicable to a real-time routine thanks to the minimization to a single frame of the data necessary to extract the optical properties of the sample. Following this methodological development, the adaptation of SSOP to an endoscopic configuration was a major development proposed in this doctoral project. In parallel, we developed a novel platform to combine two diffuse optical spectroscopic imaging techniques in order to obtain a cross-referencing capability for the validation of the instrumentation developed by our team. The multi-modal platform is based on SFDI and Time-resolved Diffuse Optical Spectroscopy (TDOS) [3]: this is a technology that exploits a point-like illumination configuration, for the spectral characterization of tissues, and is generally considered the referencing standard for optical properties measurement. Finally, several pre-clinical trials on swine models were conducted to validate the real-time capabilities, the quantification accuracy and the image quality of a clinically compatible device based on SFDI, SSOP and fluorescence.

To conclude the introduction to our work, we propose a summary of the contents of each chapter present in the manuscript:

- **Chapter 2 - "Medical Imaging and Surgical Guidance"**

  The chapter is dedicated to provide an overview of the clinical context of our work, and more specifically we are going to present the conventional imaging techniques available as standard of care in the medical framework. This chapter is concluded with a comparison of advantages and drawbacks of each imaging modality, in order to highlight the potential of advanced optical systems for the real-time, quantitative assistance in surgical guidance.

- **Chapter 3 - "Advanced Optical Imaging"**

  The chapter covers the theoretical background of the physical phenomena governing advanced optical imaging. In particular, after an introduction to the main physical principles of light-matter interaction in diffusive media, we are going to describe the mathematical framework of diffusion-based approaches as well as Monte Carlo stochastic algorithms for the modeling of photon propagation in biological tissues, together with a short analysis of fluorescence processes. An overview of the different imaging domains will be proposed to provide a sufficient background on the main diffuse optics techniques used in the experimental work, time domain and spatial frequency domain approaches above all. The chapter closes on the description of the clinical applications of advanced optical imaging that resulted the most relevant to our analysis.

- **Chapter 4 - "Motivations and Objectives"**

  This chapter summarizes the main scientific questions that lead our experimental work and it gives a snippet of the solutions proposed to tackle them.

- **Chapter 5 - "Multi-modal Referencing Platform for DOS Instruments"**

  The chapter is dedicated to the description of the implementation and validation of a multi-modal referencing platform for diffuse optical spectroscopic instruments. The experimental set-up is based on the combination of Spatial Frequency Domain Imaging and Time-resolved Diffuse Optical Spectroscopy to provide a cross-referencing approach for the quantification of tissue optical properties (i.e. absorption and reduced scattering). Firstly, we present the instrumental configuration for both systems. Secondly, we propose the results of the validation process conducted on tissue mimicking phantoms, with a particular focus on the European action (BITMAP) conducted to address the standardization of the assessment of instruments performance.

- **Chapter 6 - "BITMAP Exercise"**

  The chapter reports our work on one of the biggest collaborations between several European research teams for the performance assessment of diffuse optical instruments under the Horizon 2020 project BITMAP (*Brain Injury and Trauma Monitoring using Advanced Photonics*).

- **Chapter 7 - "SSOP Endoscopic Imaging"**

  The chapter outlines the development of an SSOP-based endoscopic imaging system for oxygenation imaging in real-time. The instrument design is first presented as a result of the adaptation of an SSOP imaging configuration to the rigid two channels endoscope. It follows the description of the validation process conducted to characterize the image quality and the quantification accuracy of tissue optical properties on solid phantoms and on *in-vivo*. Finally, we address the adaptability of the instrument to its use with a surgical robot in a pre-clinical environment.

- **Chapter 8 - "SSOP for the Perfusion Assessment in the Gastric Conduit"**

  The chapter reports our work on the application of SSOP for the perfusion monitoring of the gastric conduit during the performance of esophagectomy on swine models.

- **Chapter 9 - "Bowel Perfusion Assessment via SSOP"**

  The chapter reports our work on the application of SSOP for the perfusion assessment of the small bowel while performing a complete ischemia model, as well as an ischemia/reperfusion protocol on swine models.

- **Chapter 10 - "Conclusions & Perspectives"**

  In this chapter we summarize the main challenges that characterized the experimental work, and the results obtained in the process. Finally we propose a few perspectives on further developments of our technologies and their future role in the context of image-guided surgery.

- **Chapter 11 - "Scientific Contributions"**

  The chapter is dedicated to reporting the main scientific contributions published on scientific journals and the presentations given during national and international conferences on biomedical optics.

- **Chapter 12 - "Extended Abstract (French)"**

  The chapter contains an extended abstract in French to summarize the subject of each chapter present in the manuscript.

Chapter 2

MEDICAL IMAGING AND SURGICAL GUIDANCE

Medical imaging covers a wide range of technologies developed as diagnostic, screening and monitoring tools for the imaging of the human body. X-rays, Magnetic Resonance Imaging, Ultra-Sounds are the most common techniques already available as standard of care for surgical guidance, together with fluorescence-based systems. The scope of this chapter is therefore to give a brief overview of the clinical context of our work with a particular interest on the advantages and limitations of the different imaging modalities hereby presented.

2.1 Medical Imaging: State of the Art

In order to understand the role of this thesis work in the framework of biomedical optics applied to surgical guidance, it is worth analyzing the context in which the techniques we are going to discuss about in the following chapters find their applications. In particular, medical imaging provides the starting point for the development of innovative imaging technologies aiming at fulfilling unmet needs between the research community (together with the industrial counterpart in some sense) and the clinical world. Furthermore, they contribute to the improvement the standard of care for patients with concrete benefits in terms of both higher performances and lower costs. For these reasons, the following sections are going to cover a brief description of the most common imaging modalities already available to physicians, in order to set the ground for the following discussion on a more advanced optical approach.

2.1.1 X-Rays & Computed Tomography

Among all the imaging technologies nowadays available for surgical guidance, X-rays can definitely be considered the starting point of the whole medical imaging discipline. As published in his first paper of 1895, W. Roentgen was the first to obtain a 2-D representation of a human tissue (Fig.2.1), by exploiting its interaction with light, and more in particular with a specific region of the electromagnetic spectrum determined by high frequency radiation that became to be known as "X-rays".

FIGURE 2.1: *Ms. Roentgen's hand obtained with the first x-rays image in the history.*

Though extremely premature in terms of image capabilities and understanding of the interaction phenomena involved, the first x-rays images opened the path to the development of the future technologies devoted to produce bi-dimensional or tri-dimensional images of a structure inside a human body. Today, we are well aware that the fundamental principles behind x-rays images are [4]:

1. **Photoelectric absorption**: the radiation is completely absorbed from an electron tightly bounded within an internal electronic shell of an atom of the tissue.

2. **Compton's scattering**: part of the absorbed energy is transferred to an electron in an outer electronic shell.

These two mechanisms allow us to register on a detector the variation of intensity of the signal arising from the travel of photons within the tissue, thus enabling the reconstruction of the imaged structure. Clearly, depending on the composition and conformation of the tissue, different responses can be probed and therefore several applications are possible. Briefly, we can provide a few examples of x-rays application for surgical guidance:

- **Radiography**: bi-dimensional x-rays images for general clinical purposes.
- **Fluoroscopy**: derivation of radiography with real-time capabilities to provide high frame rate images directly during operation. A common practice is to monitor the surgical gesture intraoperatively via a *C-arm* (similar to the one shown in Fig.2.2).
- **Angiography**: imaging technique exploiting the x-rays technology to display vasculatures and blood flow. It is typically deployed together with an exogenous contrast agent injected in the vascular system to improve the imaging capabilities. A further development is represented by the so called *"rotational angiography"*, where a series of images are acquired by means of a C-arm.
- **Computed Tomography (CT)**: 3-D enabled x-rays technology based on the acquisition of several stacks of bi-dimensional images to reconstruct the whole investigated volume. In this case, arrays of sources and detectors are rotated around the surgical field to provide a full tri-dimensional dataset that can be exploited to recover the full field of view with relatively high depth resolution. The main advantage of CT scans with respect to standard radiography is the localization power that rather quickly enables the physician to highlight and determine the position of a pathology.

Evidently, the invasive interaction of the radiation with tissues allows us to achieve high imaging capabilities for soft tissues, bones, as well as vasculatures, but simultaneously prevents a frequent use of such technology on the same patient. In addition, for intraoperative use, the risk of collateral effects associated to the radiation generates a safety issue for the entire surgical team involved in the procedure. Nevertheless, the range of medical applications for x-rays is extremely vast and still barely comparable with any other imaging modality, ranging from emergency medicine to detect internal bleeding associated to traumas, to diagnose skeletal fractures, to image intracranial aneurysms [6], to evaluate carotid artery stenosis [7] or to assist the performance of cerebrovascular stenting [8].

FIGURE 2.2: *Philips BV Pulsera Mobile C-Arm. [5]*

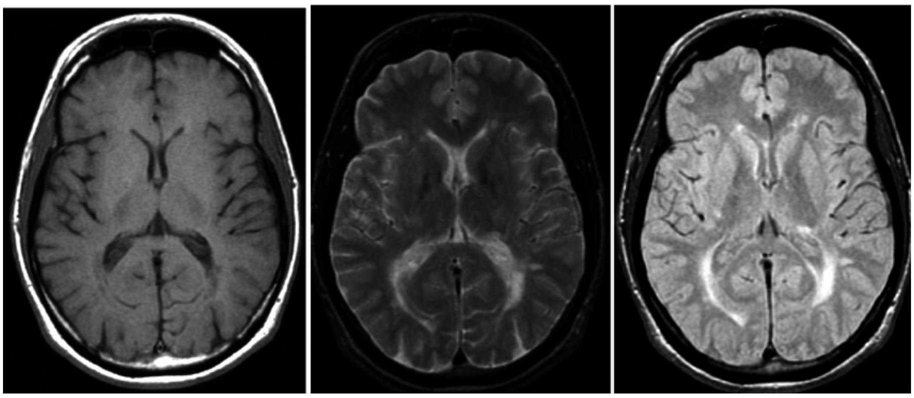

FIGURE 2.3: *T_1, T_2 and PD-weighted axial head scans of a multiple sclerosis patient.* [10]

2.1.2 Magnetic Resonance Imaging

Magnetic Resonance Imaging (MRI) is a medical imaging technique characterized by extremely high spatial resolution and tissue contrast, thus making it one of the most common technologies adopted for the localization and identification of soft biological structures embedded in tissues. Completely non-invasive for the patient, MRI is based on the immersion of the investigated medium in a strong magnetic field ($\geqslant 1.5\ T$) and the exploitation of the dependency of the natural resonance frequency of protons in water with respect to the field gradient. In a nutshell, by means of a radiofrequency excitation field generated with a superconductive material, protons belonging to water molecules can transition to excited states by absorbing the energy provided by the field at the specific resonant frequency [9]. This process is characterized by a relaxation time that corresponds to the average lifetime of the excited state: transversal and longitudinal relaxation processes occur after the transition to bring the system back to the ground state, with exponential decay times[1] of T_1 and T_2, respectively. This property determined by the interaction of the water molecules with the magnetic field permits to map the distribution of water-based fluids in the human body, thus allowing to probe the majority of tissues with high contrast, by tuning the frequency and intensity of the excitation field.

Typically, different kinds of images can be extracted from an MRI scan depending on the choice of the temporal distance between the excitation sequences and with respect to the measurement interval (in Fig.2.3 the three sequences are illustrated):

- ***PD-weighted***: distribution of proton density (PD) in the sample.
- T_1***-weighted***: distribution of T_1 transitioned protons, to enhance the signal coming from the tissue structures (high intensity) rather than from the fluids (low intensity).
- T_2***-weighted***: distribution of T_2 transitioned protons, to enhance the signal coming from the fluids (high intensity) rather than from the tissue structures (low intensity).

In addition, exogenous contrast agents can be injected intravenously to boost the image capability of specific structures, and spatially sectioned sequences can be acquired to obtain volumetric representations of the investigated medium, thus opening the way to 3-D reconstructions. Moreover, functional imaging is also achievable through a magnetic resonance approach (i.e. "f-MRI"): metabolic and physiological mechanism can be analyzed by monitoring over time the proton distribution inside specific targeted structures under stress, as shown in Fig.2.4.

---

[1] The decay time of the process is defined as the average time required to reach $1 - 1/e$ (i.e. 63%) from the peak.

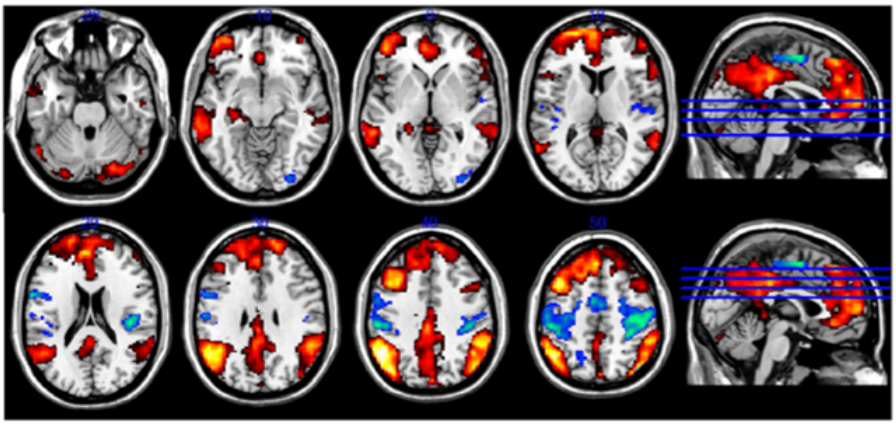

FIGURE 2.4: *Functional magnetic resonance imaging (f-MRI) contrast. [11]*

The great advantage of MRI-based imaging is undoubtedly the high contrast that provides significant spatial resolution as well. However, the main drawback is associated to the instrumentation cost which mainly derives from the superconductive technology. Furthermore, the bulkiness of an MRI machine and the presence of strong magnetic fields prevent this technology to be easily accessible from an on-the-field surgical perspective, even though some intra-operative devices are available for specific tasks (i.e. compensation for brain shift [12], biopsy guidance [13] etc.) that do require downsized excitation fields of $0.5 - 1\ T$.

2.1.3 Ultrasonography

UltraSonography (US) or *medical sonography* is a medical imaging technology that was initially developed in the 1940s by Dussik for tumor imaging in the brain, the main advantage being the capability to penetrate the different layers of the scalp [14]. Despite being one of the oldest forms of navigation and imaging of the human body, US is still nowadays one of the most widely used tool and a standard of care for several applications in medicine, thanks to its complete non-invasiveness and a relatively low cost compared to more sophisticated technologies such as x-rays or MRI. As an example, among many others, ultrasounds are typically adopted in:

- **Cardiology**: Echocardiography is the US assessment of the functionality status of heart ventricles and valves, together with many other features of the cardiovascular system.

- **E.R. Medicine**: one of the most important procedures that involves an US analysis is the Focused Assessment with Sonography for Trauma (FAST) which is a standard routine in E.R. medicine. FAST is a complete "fast" exam to identify the presence of hemoperitoneum or pericardial tamponade after trauma.

- **Gastroenterology**: ultrasonography is used to image solid organs in the abdomen such as pancreas, liver, kidneys and bladder. The main limitations of such application is associated to the reliability of the acquired image because of the presence of fat layers and gas bubbles in the assessed body parts.

- **Gynecology & Obstetrics**: the application of US in both these fields is surely one of the most common. Indeed one of the exploited procedures is to check on the development of the fetus during pregnancy.

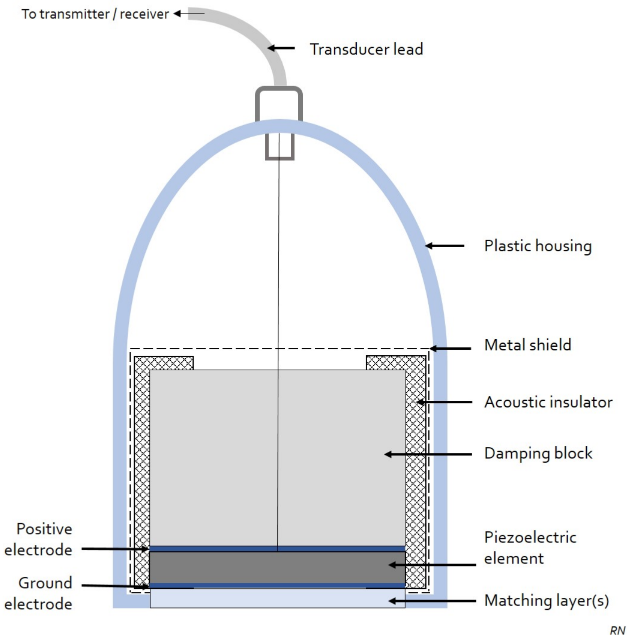

FIGURE 2.5: *Ultrasound probe design. Case courtesy of Dr Rachael Nightingale, Radiopaedia.org, rID: 54040*

- **Neonatology**: trans-cranial Doppler is largely used for basic assessment of intra-cerebral structural abnormalities, bleeds or hydrocephalus and anoxic insults.
- **Orthopedics**: here US is an alternative to x-rays for the detection of fractures in the wrist, elbow or shoulder for patients up to 12 years of age. Moreover it can be used to analyze the status of tendons, muscles, nerves and ligaments.
- **Anesthesiology**: in order to guide the injection of needles for local anesthetic solutions, the US machine can provide a reliable help to the physician, in particular when bearing with fragile nerves in proximity to the region of interest.

It is worth highlighting that, even today, one the main drawbacks of ultrasonography is associated to the subjectivity of the diagnosis stemming from the rather qualitative analysis of the sonogram. As a result, US are typically adopted in multi-modal configurations in order to reduce at the minimum the impact of the physician experience on the screening outcome.

The fundamental principle of US lies on the propagation in the tissues of sound waves in the *MHz* frequency regime. More precisely, ultrasounds are waves whose propagation direction is parallel to the oscillation direction of the field generated by the pressure fluctuation of the medium (i.e. *longitudinal* waves). In particular, the molecules feel the effect of a pressure force applied to them, which results into the formation of zones of compression where the particles are forced to collapse in a concentrated region, alternated to zones of rarefaction, in which the space between the molecules is wider. In this sense, the motion of the wave inside the medium is sustained by means of the migration of the high and low pressure regions throughout the entire volume. In general, different tissues have mechanical properties that depend on their morphology and structure, thus determining specific responses to an ultrasound perturbation [15],[16]. The intensity, attenuation and propagation velocity of ultrasound waves are the main parameters that are analyzed on the field to assess the status of the investigated medium.

The standard procedure to perform an US involves a specific probe for the generation and detection of the sound waves. A simplified sketch of the device can be found in

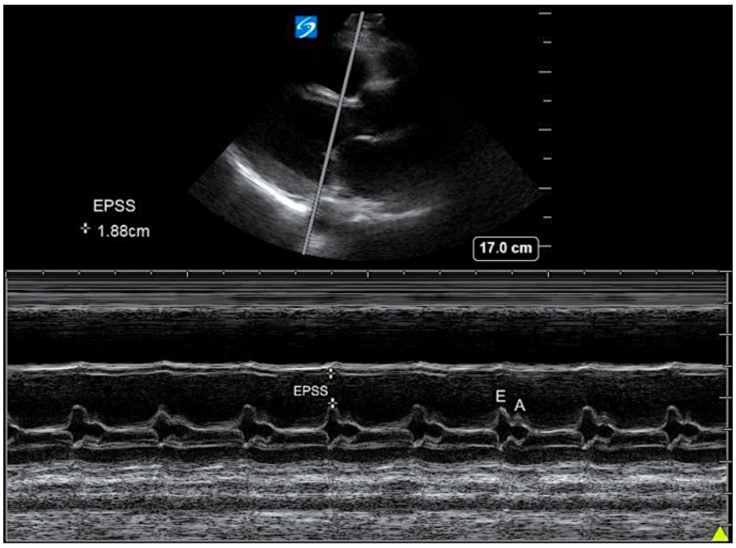

FIGURE 2.6: *Example of M-Mode ultrasonogram. [17]*

Fig.2.5: the fundamental element for an US probe is the piezolectric transducer for the conversion of pressure waves into electrical signals. It is also worth mentioning that miniaturized versions of such probes are also adopted in several application for internal screening of tissue pathologies (e.g. gynecology and gastrointestinal medicine). In any case, the transducer is placed by the physician on the surface of the body (or inside it, if necessary to improve the diagnostic capability) with an index-matching gel spread over the contact area. The tissue can then be imaged in real-time by adopting one of the following modalities, which are based on the encoding of time travel into distances from the probe, in order to provide a morphological view of the scanned area (i.e. *echoranging*):

- ***A-Mode***: the transducer captures echoes that are subsequently shown as a voltage signal on an oscilloscope: the x axis encodes time, whereas on the y axis the voltage amplitude (i.e. "A" for "Amplitude") is represented. Moreover, by assuming constant propagation speed in the medium, it is possible to encode the time axis into a distance information. Finally, we note that the A-Mode reveals the location of the sources of echo signals only in the direction of propagation of the ultrasound wave.

- ***B-Mode***: this methodology exploits a bi-dimensional representation of the echo-pulses structures on a screen, by means of tuning the brightness (i.e. "B" for "Brightness") of the (x, y) pixel coordinate proportionally to the amplitude of the signal. Depending on the application, the image can be "Black-on-white", i.e. the bright spot represents low amplitude regions, or conversely "White-on-Black" where a bright pixel is referred to a high amplitude signal. Moreover, in B-Mode there is the possibility to produce real-time or static images.

- ***M-Mode***: this operating mode exploits the position-time relationship of each echo source. Moreover, the depth of those structures is represented by a series of dots in the vertical direction on the screen. This strategy is suitable to characterize moving features (see Fig.2.6).

In terms of real-time capabilities, US are fundamentally limited by the propagation speed of the sound wave in the tissue and by the processing time required to convert the pressure signal into an electronic one, and the subsequent 2-D (or 3-D) rendering of the acquired image. Typically, it is possible to estimate the maximum frame rate (FR) of the device, as a function of the field of view (FOV) of the source and of the total number (N) of line scans exploited [15]:

$$FR = \frac{1}{13 \times 10^{-6} \times FOV \times N} \tag{2.1}$$

Where we used a time-to-distance conversion factor of 13 ms/cm by considering as a propagation velocity of the US in the medium $v = 1540\ m/s$.

2.1.4 Optical Imaging

Optical imaging refers to the wide area of imaging technologies that exploit light-tissue interactions in a completely non-invasive way (i.e. without the use of ionizing radiation for instance) in order to provide more quantitative and qualitative information to the physician for screening, diagnostic and monitoring purposes [18]. In general, the fundamental concept at the basis of such techniques is the analysis of the optical response of a tissue to a certain illumination provided with photon energy covering the ultraviolet $(200 - 400\ nm)$, visible $(400 - 700\ nm)$ or infrared $(700 - 10^4\ nm)$ region of the electromagnetic spectrum. More specifically, reflection, refraction and transmission of light inside the media can be exploited to separate biological structures, thanks to their different optical properties, and several macroscopic and microscopic approaches can be utilized to achieve specific imaging targets that can then be used as an additional diagnostic tool [19]. Indeed, in many applications the identification of a pathology might appear visible at naked eye due to a change in the morphological and biological structure of the unhealthy tissue, thus making the medical screening relatively easy. However, the adoption of specific optical imaging techniques can improve the analysis of the target by means of providing high resolution data visualization and more precise understanding of the medical scenario[20].

Before entering a brief description of three main categories of optical imaging techniques in use today (i.e. multi-spectral imaging, microscopic imaging and fluorescence imaging), it is worth mentioning that the simplest solution for providing a visual support during a surgical procedure or a diagnostic screening is via white light illumination of the field. This corresponds to the use of broadband light sources such as LED and lamps that cover a wide range of the electromagnetic spectrum (typically the whole visible range and a small section of the infrared) in order to facilitate the visualization of the tissue on the field. In this sense, it is evident that though being extremely easy to implement, this first approach does not bring any additional information but it could also lead to the identification of local color changes that might be associated to a pathology.

2.1.4.1 Multi-spectral imaging

Stemming from the white-light approach, multi-spectral imaging is characterized by the use of a larger spectral region of photon energies, and in particular by the selection of specific illumination bands to probe different structures in the tissues. As we mentioned before, the optical properties of tissues are responsible for peculiar responses of the investigated medium and the measurement of the reflected or transmitted light arising from the tissue at different wavelengths can be extremely useful.

Narrow Band Imaging (NBI) is considered the most widely available imaging technique that exploits a multi-spectral approach for endoscopic applications. In particular, blue (415 nm) and green (540 nm) wavelengths are used to illuminate the tissue by means of an electronic filter embedded in the endoscope, thus allowing to enhance the visualization of vessel structures thanks to the different response of hemoglobin to the two wavelength bands. As a result, applications such as the diagnosis of *Barrett's esophagus*, the identification of polyps and tumors or the presence of dysplastic cells can be performed with the use of flexible endoscopes. An example of a medical device using NBI for gastrointestinal surgery is shown in Fig.2.7. In addition, multi-spectral imaging techniques find their application in the clinics for intra-operative ischemia monitoring, skin bruises characterization, metabolic changes visualization during anasthomosis and transplants, among many others [21].

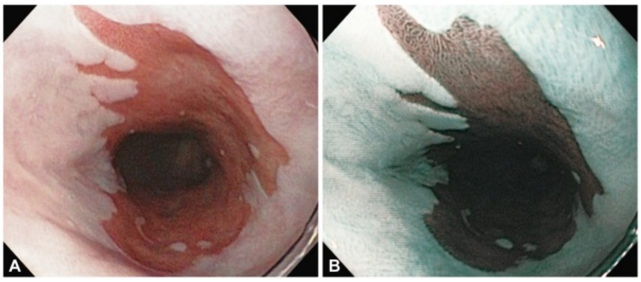

FIGURE 2.7: *White light imaging of Barrett's esophagus (A), and corresponding NBI image (B). [22]*

2.1.4.2 *Microscopic imaging tools*

Macroscopic techniques such as NBI are not the only available technologies to improve the visualization of tissue structures via optical imaging. Microscopic approaches are also extremely common in the medical framework, owing in particular to the unmatched spatial resolution that they can provide. Probably the first imaging technology employed in the surgical field, microscopy has the advantage of providing high contrast and high resolution images of small structures, which can be used as an helpful guidance for complex manipulations (i.e. tumor margin diagnosis in the mucosa and sub-mucosa). For this reason, it is widely adopted as a standard of care in ophthalmology, plastic and neurological surgery, but also for diagnostic screening prior to the intervention. Furthermore, exogenous contrast agents (i.e. methylene blue) can be utilized to boost the image capability in specific contexts.

Optical Coherency Tomography is considerably the most common microscopic clinical tool available. By exploiting an interferometric approach for the detection of changes

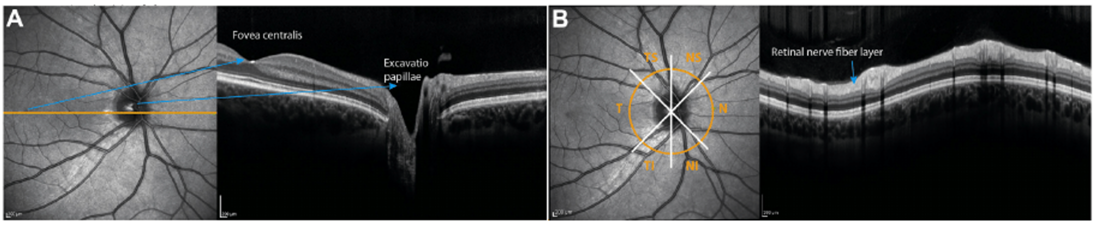

FIGURE 2.8: *OCT-derived cross-sectional images of the retina. Notes: (A) A line scan through the fovea centralis and the optic nerve head. The left image shows the fundus image, which is acquired simultaneously to the OCT image. The orange line indicates the location of the cross-section. The right image is the respective retinal OCT scan as a grayscale image. (B) The retinal nerve fiber layer thickness is usually acquired by a peripapillary ring scan. Image analysis provides the thickness values for the overall ring, but also for the sectors. Abbreviations: NS, nasal-superior; N, nasal; NI, nasal-inferior; TI, temporal- inferior; T, temporal; TS, temporal-superior; OCT, optical coherence tomography. [23]*

in the index of refraction in the different layers of a tissue [24], OCT is capable of providing micrometric resolution sections of the investigated medium that can be compared to hystopathological sequences for the analysis of pathological structures. Additionally, tri-dimensional volumes can be reconstructed by linear scanning of the field. As a consequence, it is largely utilized in ophthalmology for the screening of retina (see Fig.2.8) diseases but also in interventional cardiology for the monitoring of coronary artery degradation.

2.1.4.3 *Fluorescence imaging*

Fluorescence imaging is an extremely powerful optical imaging technique that exploits the light emission properties of specific fluorophores which can be optically activated by illumination with a characteristic wavelength band (see Section 3.1.4, 3.3.1 for more details) [25]. Endogenous biological structures can be imaged thanks to their natural fluorescence behavior (i.e. collagen and many protein-based structures), however it is also common practice to utilize exogenous molecules (i.e. "fluorescent dyes") injected in the vascular or lymphatic system in order to target specific biological systems [26]. An example of fluorescent image-guided surgery application to the digestive system is shown in Fig.2.9.

2.1.5 Surgical guidance in the computing era

Surgery is still nowadays a medical practice that thrives on the great skills of the practitioners and of the medical staff involved. Nevertheless, the introduction in the surgical room of advanced computing tools for image-assisted performance such as artificial intelligence and augmented reality has definitely raised the quality and efficiency of treatments thanks to the benefit provided by an enhanced vision of the surgical field.

Artificial Intelligence (AI) penetrates nowadays many aspects of our lives, finding applications in the most different areas from face-recognition for security purposes to customer preference feeds for improving the user experience in many on-line services. Not surprisingly, the development push towards such wide audiences enabled the rapid

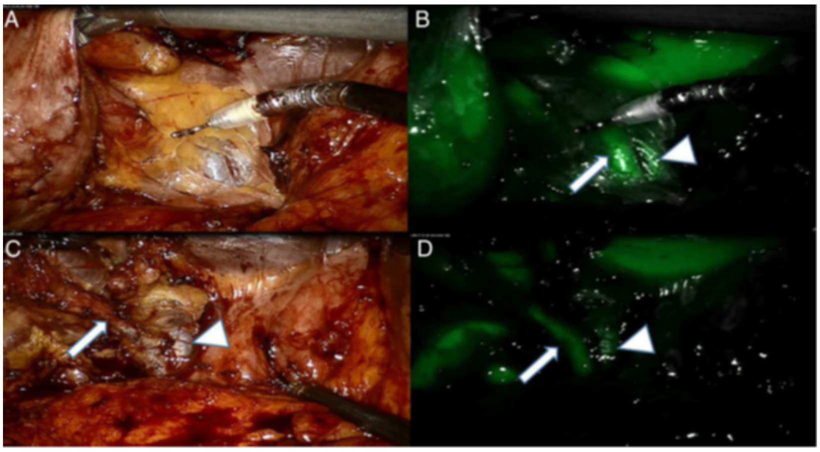

FIGURE 2.9: *(A) White light imaging of Calot's triangle area after an initial opening of the peri-gallbladder adipose tissue. A tubular structure can be identified. (B) At near-infrared (NIR), a second structure is identified adjacent to the previous one, allowing to identify them as the Cystic Duct (CD; arrow) and the Common Bile Duct (CBD) respectively; see arrow head. (C) White light view after some dissection allowing to dissect the CD. (D) NIR imaging confirms the accurate interpretation of the anatomy.* [27]

FIGURE 2.10: *FDA 510k-approved True 3D glasses. Echopixel*$^{©}$ *[32]*

development of the algorithms and hardware supports at the basis of these technologies, thus paving the way to an easy access also in the research and medical community [28].

Machine Learning and Deep Neural Networks have found their way into the medical imaging framework for several purposes, such as tissue navigation and recognition via segmentation utilities, or pathology identification thanks to classification algorithms [29]. In the same direction, these tools have allowed the achievement of high quality image rendering (in a similar way to the specific case of Single Snapshot imaging of Optical Properties (SSOP), as we are going to describe in Section 3.3.5.2). In all these cases, the amount of literature associate to application of ML and DNN for biomedical applications is growing every year at an incessant rate.

Similarly, Augmented Reality (AR) has become a relatively common feature in many surgical rooms, where, with the aim of providing 3-D vision to the practitioner during the procedure, several devices have been proposed and adopted in many operating scenarios. Indeed, despite the wide availability of different imaging technologies, x-rays, CT scans and MRI films are usually consulted before the procedure or shown on a screen in real time in the OR. In this sense, the advantage of adopting AR systems is determined by the possibility to add a volumetric and real-time view of the surgical field based on pre-registered scans of the body or of the tissue of interest, in order to improve the accuracy of the surgical act, especially in complex conditions where biological features might obstruct the field. It is worth mentioning though, that a perfect co-registration pipeline is required beforehand to ensure that the reconstructed view is representative of the actual surgical field, thus reducing at a minimum the risk of relying on incorrect landmarks during the performance of the surgical act. Nevertheless, the introduction of virtual reality tools in the operating room has received a vast acceptance, finding its way in several applications such as plastic, neurological, cardiovascular and thoracic surgery [30], with devices similar to the one presented in Fig.2.10. Understandably, the popularity of such technologies forces also a change in the training of the professionals who need to familiarize with the new generation of surgical tools. However, this process has been facilitated in the last years by the growth of several training platform and simulators specifically designed for the purpose [31].

2.2 Comparison of Imaging Techniques: Summary

In order to conclude this brief overview of some of the most common medical imaging modalities, it is worth summarizing the different characteristics of each of the described technologies, together with their advantages and limitations.

From a fundamental standpoint, x-rays and CT imaging provide the highest spatial resolution in comparison with the other imaging techniques described. However, as we mentioned in Section 2.1.4, some optical implementations such as microscopy can undoubtedly achieve comparable, if not higher performances for the *in-vivo* and *ex-vivo* imaging of living tissues. Clearly, in the case of diffuse optical techniques, the spatial information is harder to preserve due to the high scattering regime.

Depth sensitivity is also extremely challenging in diffusive media, for the same aforementioned reason. Indeed, due to absorption and scattering the penetration depth of optical imaging techniques are bounded to few centimeters in the best case scenario (i.e. for time-resolved Diffuse Optical Tomography (DOT)). Ultrasounds surely provide higher penetration depth, but x-rays, CT and MRI remain the gold standard for deep tissue investigation. As we mentioned in Section 2.1.1, the penetration depth of x-rays radiation is barely affected by the optical properties of tissue, and a similar reasoning can be made for MRI scans. In terms of soft tissue contrast, optical imaging techniques and MRI scans provide comparable high performances, whereas radiation-based approaches come with poor sensitivity and specificity. Nevertheless, x-rays, MRI and US allow for the investigation of a larger spectrum of tissue structures that are impossible to access with optical devices only.

Functional and structural parameters can be addressed by means of optical devices thanks to the investigation of tissue optical properties. More specifically for the case of a functional analysis, x-rays remains the only technology of the ones mentioned not capable of targeting this task. Conversely, structural parameters are accessible to each imaging technique.

Optical imaging also benefits from the completely non-invasiveness of the interaction between photons and tissue structures. This crucial feature is shared with MRI and US, which are techniques that do not determine a disruptive effect on the investigated system, as we mentioned in Section 2.1.2 and 2.1.3. On the contrary, x-rays and CT scans exploit high energy, ionizing radiations to probe tissues. A major point of concern is therefore determined by the fact that x-rays are proven to have a degrading effect on biological cells, facilitating the growth of cancerous structures as well, in the case of excessive dosage provided to the patient.

From an instrumental point of view, optical systems are proven to be real-time compatible, similarly to the case of ultrasounds technologies and a few x-rays implementations. Acquisition and visualization pipelines can be efficiently optimized to provide real-time feedback during surgical procedures. MRI in this sense remains the slowest technique where the acquisition of a full dataset can be consistently more time consuming with respect to the other imaging methods, resulting into a significant limiting factor for intra-operative use.

In addition, the cost-effectiveness of optical imaging technologies without any doubt surpasses the other standard of care devices such as MRI scanners and x-rays machines. In this sense, x-rays, CT scans and MRI are undoubtedly an extremely expensive solution due to the need for specific radiation generation (i.e. x-rays) and superconductive materials to achieve strong magnetic fields (i.e. MRI). However, such machines have the great advantage of providing high quality and high contrast (mostly for MRI) images. Portability determines another benefit of optical-based devices against bulkier solutions such as x-rays and MRI. The latter being characterized by a safety concern arising from its use in a surgical setting (as discussed in Section 2.1.2), where the effect of the field does not directly determine an issue for the human body, but still imposes some extra limitations on the use of the technology in an operating room environment.

Furthermore, multi-modal approaches deserve a particular mention[2]. Indeed, the combination of different imaging modalities can produce an extremely interesting winning strategy to tackle specific tasks that remain inaccessible by a single technology alone, whose weaknesses can be compensated by introducing a complementary technique. As an example, it is worth mentioning the case of a proposed solution for a diffuse optical tomography (DOT) imaging system dedicated to the screening and monitoring of breast cancer. The project *Solus*©[33] was born with the aim of implementing a smart optode for the tomographic reconstruction of tissue optical properties in the breast by combining a standard diffuse optical technology with ultrasonography. In this case indeed, the main weakness consisted on the poor spatial resolution of DOT that directly affects the reconstruction properties. Therefore, the aim was to improve the tomographic analysis by utilizing US scans as *a priori* morphological information of the investigated system.

To summarize, optical imaging represents one of the best candidate among the other medical techniques for cost-efficient, non-invasive, real-time and quantitative imaging of biological tissues. In addition, thanks to its adaptability to different configurations, it offers great potential for surgical guidance either in the form of open surgery or for minimally (and robot-assisted) invasive treatments. Nevertheless, it is fundamental to be aware that the introduction of novel imaging techniques and devices into the traditional medical imaging framework comes at a cost. The need for additional training of the practitioners and an efficient communication of the advantages with respect to the current standards are only a few elements that play a central role in facilitating the transition of the community involved.

2.3 Conclusions

This chapter was dedicated to the introduction of the medical context of the thesis work, by giving a concise overview of the most common medical imaging modalities available in the clinical settings as standard of care. In particular, we focused on x-rays technologies, magnetic resonance imaging, ultrasounds and fluorescence which undoubtedly represent the most widely used techniques adopted in healthcare and surgery for countless applications. The aim of the discussion was to state the role of optical imaging within this framework, as a powerful tool to provide quantitative information in a safe and non-invasive way for surgical guidance. In this sense, a comparative analysis of the benefits and drawbacks of the mentioned imaging modalities was also proposed.

---

[2] We would like to stress that in some sense augmented and virtual reality approaches can be considered as a multi-modal approach together with the standard clinically available imaging technologies. Clearly though, the advantages brought with the enhanced visualization capabilities have an impact on the surgical act on their own.

Chapter 3

ADVANCED OPTICAL IMAGING

Advanced optical imaging is a dynamic field that has experienced a rapid development due to the increasing interest towards non-invasive, real-time and cost-effective clinically compatible imaging technologies. In this chapter, we propose an overview of the main advanced optical techniques available, starting from the fundamental theories governing the physics of light-tissue interactions. It follows a short description of their principles and applications with a particular focus on Spatial Frequency Domain Imaging (SFDI), Time Domain (TD) approaches, fluorescence and hyperspectral imaging.

3.1 Physics of Light-Matter Interaction

Following the comparative discussion proposed in Section 2.2, we are now going to introduce the theoretical principles of advanced optical imaging in biological tissues, with a particular focus on the physical modeling of light-matter interaction and its consequences for medical imaging and surgical guidance. More specifically, we are going to cover a brief description of the main physical phenomena related to tissue optics (i.e. absorption and scattering), following with a concise introduction to two main modeling frameworks for the photon propagation inside turbid media (i.e. the diffusion approximation and the Monte Carlo approach). To conclude, we are going to define the parameters utilized in functional and structural imaging techniques (i.e. chromophore quantification and scattering properties), as well as provide a short section on the fundamentals of fluorescence imaging.

3.1.1 Fundamentals of biological tissue optics

Diffuse optics is the study of the photon random migration through highly scattering media (also referred to as "turbid"). The propagation of light through biological tissues, and more specifically in a range of wavelength spanning from 400 nm to 1100 nm [34], can usually be explained by two main phenomena occurring at a microscale level: absorption and scattering. Optical absorption is the process that determines the annihilation of a photon during propagation through the medium. It is possible to quantify the absorption properties of a medium in terms of the probability for a photon of being annihilated while freely traveling through it, hence defining an absorptive cross-section whose characteristics depend on the presence of specific chromophores inside the tissue. In this specific wavelength regime, the most common absorption centers for biological tissues are: hemoglobin (both oxygenated and deoxygenated), water, lipids, collagen and melanin, among others [35].

While optical absorption is a mechanism associated to specific compounds present in the medium, the physics of scattering is driven by its micro-structure. This is due to the fact that the phenomenon of diffusion consists on the deviation of a photon trajectory along preferential directions and with specific magnitudes that are determined by the change in refractive index of the microscopic structure of the turbid medium. Similarly to the previous case, it is possible to define a diffusion cross-section also for scattering, by quantifying the likelihood for a photon to undergo a change in the propagation trajectory due to the interaction with a scattering center (a simplified representation of these phenomena is shown in Fig.3.1).

In the most general framework, the mathematical description of light-matter interaction in highly diffusive media is extremely complex. On one hand, we need to take into

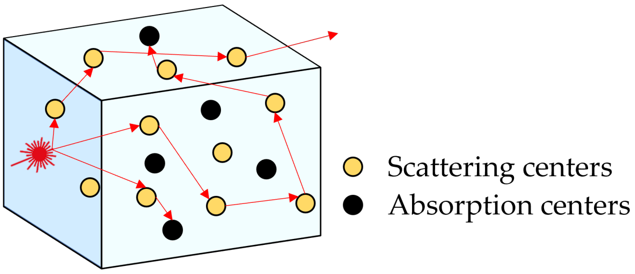

FIGURE 3.1: *Simplified sketch of absorption and scattering mechanisms in a diffusive medium. Scattering centers are responsible for an elastic deviation of the photon trajectory, whereas absorption sites define the location where the annihilation of photons occurs.*

account the simultaneous presence of both absorption and scattering in order to understand the fundamental optical properties of biological tissues. On the other hand, the physical domain in which this mechanisms take place is inherently not homogenous due to the presence of several heterogeneous structures with different physical properties, such as muscular and nervous fibers, vasculatures and bones, thus demanding a strong modeling effort to achieve a comprehensive description of the structure and geometry of the propagative medium.

Nevertheless, the starting point for the physical model for light propagation in turbid media are Maxwell's equations, an analytical approach that could substantially provide the most complete knowledge of the mechanisms linked to the interaction of photons with matter. However, the complexity of the investigated system prevents us to obtain these solutions in a complete form, and even a numerical approach seems unachievable unless trivial and fairly unpractical working conditions are considered. For this reason, the most common approaches to tackle this task are: 1) the Diffusion Approximation (DE) [36] of the Radiative Transfer Equation (RTE), which provides the closest neighbor to a fully analytical solution of the problem; 2) a random-walk-based Monte Carlo model for a stochastic approach to the description of the absorbing and scattering properties of biological tissues [37]. Evidently, choosing one approach or the other requires a trade-off which is essentially determined by the modeling accuracy and the computational effort.

Before entering a brief introduction on the diffusion and Monte Carlo model of photon propagation inside turbid media, it is worth stating that they both consider light on the basis of its corpuscular nature: as a matter of fact, the traveling of light through biological tissues can be described with the same tools utilized for the analysis of the physical phenomena occurring when a system of particles of any particular nature propagate through a diffusive medium. For this reason, it is convenient at this point to define a few fundamental quantities that are essential to describe the concept of optical properties of the biological tissues that we are going to deal with in the next chapters.

The starting point for a complete understanding of the radiative propagation theory is the concept of mean free path: this is the average distance traveled by a photon inside the medium, in between two absorption (or scattering) events. Consequently, we can also refer to the mean free path as the inverse of the probability per unit length for the same photon to be annihilated (or scattered). Therefore, we can generally define μ_a and $\mu_s^{'}$ as the absorption and scattering coefficients as:

$$\mu_a = \frac{1}{l_a} \tag{3.1}$$
$$\mu_s = \frac{1}{l_s}$$

Where we l_a and l_s are the absorption and scattering mean free path, respectively. These parameters directly refer to the optical properties of the medium, inherently quantifying the capability of the system to absorb and to diffuse light. As a result, if we consider a laser beam of intensity I_0 impinging on a turbid medium of thickness L , it is possible to determine the effect of the combined action of photon annihilation and scattering in terms of intensity loss, as follows:

$$I(z) = I_0 \exp\left(-(\mu_a + \mu_s)z\right) \tag{3.2}$$

This result can easily be interpreted as an exponential decrease of light intensity at the output of the medium caused by the interaction of photons with absorptive and scattering centers. In general though, we refer to the "optical properties" of a tissue in terms of the absorption coefficient (μ_a) and the reduced scattering coefficient ($\mu_s^{'}$), the latter being defined as:

$$\mu_s^{'} = \mu_s(1-g) \tag{3.3}$$

Where g is the anisotropy coefficient of the medium, which takes into account the directionality of the scattering event. The anisotropy coefficient is a measure of the probability of a scattering event to be isotropic or anisotropic. Indeed, it is defined as:

$$g = <\cos\theta> = 2\pi\int_{-\infty}^{+\infty} p(\theta)\cos\theta\sin\theta d\theta \tag{3.4}$$

Where $p(\theta)$ is the probability that a photon trajectory is deviated along the direction defined by the angle θ. For this reason, if $g \to 0$ the scattering event is totally isotropic. The value of the anisotropy coefficient in most biological tissues is between 0.5 and 0.9, depending on the microstructure of the tissue.

Another fundamental parameter for the description of the optical properties of a highly diffusive medium, is the optical *albedo*, which represents the effects of scattering and absorption on the attenuation of light. It is defined as:

$$a = \frac{\mu_s}{\mu_s + \mu_a} \tag{3.5}$$

Therefore, in case of low albedo, the light attenuation is determined only by absorption. Conversely, the high albedo regime determines the predominant effect of scattering over absorption. It is worth noticing that in the wavelength region corresponding to the optical window ($600-1100\ nm$) the albedo for biological tissues is ≈ 1.

As mentioned before, while the absorption of a tissue intrinsically depends on the specific chromophores that constitutes it, scattering (and consequently reduced scattering) is a consequence of the molecules' sizes and shapes of a specific tissue layer. In general, *Mie* theory describes the phenomenon of scattering for spherical and homogeneous particles. *Rayleigh* scattering represents the approximation to the Mie theory for scattering centers characterized by a size much smaller than the light wavelength. Hence, in practice, depending on the dimension of the scattering centers with respect the operating wavelength (λ), we can identify two regimes:

1) if $\lambda \leq d \Rightarrow$ *Mie scattering*

2) if $\lambda \gg d \Rightarrow$ *Rayleigh scattering*

Where we defined d as the diameter of a scattering center. Naturally, considering the heterogeneity of biological tissues, several different scattering structures can be found. For example, chromophores such as entire cells, whose average size is around 10-30 μm, fall into the Mie regime, whereas protein-like structures are better described within the framework of Rayleigh's scattering [38].

3.1.2 Light propagation models in biological tissues

The following section is dedicated to the description of two main mathematical models for the light transport in diffusive media: firstly an analytical diffusive approximation approach, and secondly a stochastic model based on Monte Carlo.

3.1.2.1 Diffusion model for the photon radiative transfer in a diffusive medium

The mathematical modeling of light-matter interaction for turbid media is based on the corpuscular nature of light: similarly to a propagation model for particles in a scattering environment, photons follow characteristic paths inside the medium, that are inherently determined by the presence of scattering and absorbing centers. In this sense, the analytic description of the system can be performed under the hypothesis of the photon migration theory, and more specifically by means of the most general Radiative Transfer Equation (RTE). As part of the underlying hypotheses of this theory, in the following we are going to consider the scattering centers to be solid spheres, thus providing a full elastic response to the perturbation of a photon trajectory inside the medium.

3.1.2.1.1 Radiative Transfer Equation

Let us consider an elementary volume dV inside the turbid medium, and let μ_a ,$\mu_s^{'}$ be the absorption and reduced scattering coefficients respectively: the aim is to evaluate the net energy flux of light through dV.
Defining $N(\vec{r},\vec{\Omega},t)$ as the photon density, i.e. the number of photons per unit volume, traveling along the direction defined by the unitary vector $\vec{\Omega}$ within the solid angle Ω, at time t in the position $\vec{r}$, the total number of photons within the elementary volume dV that are propagating along $\vec{\Omega}$ within the infinitesimal solid angle $d\Omega$ is given by:

$$\vec{j} = N\vec{v} = Nv\vec{\Omega} \tag{3.6}$$

where we defined $\vec{v} = v\vec{\Omega}$ the photon velocity in the medium. Moreover, taking advantage of the definition of the absorption and scattering coefficients mentioned before, as the inverse of the mean free path for absorption and scattering respectively, it is possible to characterize the probability of an event of annihilation and scattering as:

- $dl\mu_a =$ probability of absorption event
- $dl\mu_s =$ probability of scattering event

Being dl the elementary segment of the photon path inside the medium. Lastly, let us define:

$$p(\vec{\Omega},\vec{\Omega}') \tag{3.7}$$

as the photon diffusion probability, meaning the probability for a photon propagating along the direction $\vec{\Omega}$ of being scattered along the direction $\vec{\Omega}'$. The resulting balance equation for the time evolution of the photon density inside the elementary volume dV reads as follows:

$$\begin{aligned}\overbrace{\frac{\partial N(\vec{r},\vec{\Omega},t)}{\partial t}}^{1)} = & \overbrace{-v\vec{\Omega}\cdot\nabla N(\vec{r},\vec{\Omega},t)}^{2)}\overbrace{-vN(\vec{r},\vec{\Omega},t)\,[\mu_a(\vec{r})+\mu_s(\vec{r})]}^{3)}+\\ & \underbrace{+v\mu_s\int_{4\pi}p(\vec{\Omega},\vec{\Omega}')N(\vec{r},\vec{\Omega},t)d\vec{\Omega}'}_{4)}+\underbrace{s(\vec{r},\vec{\Omega},t)}_{5)}\end{aligned} \tag{3.8}$$

The building blocks of the radiative transfer equation (RTE), as depicted in Fig.3.2, are:

1. Time evolution of the photon density within the elementary volume dV.
2. Total flux exiting the infinitesimal volume dV. It is a negative contribution to the balance, provided the sign convention for which an exiting flux is considered negative, whereas an entering flux is positive.
3. Total photon losses due to absorption and scattering events, respectively.

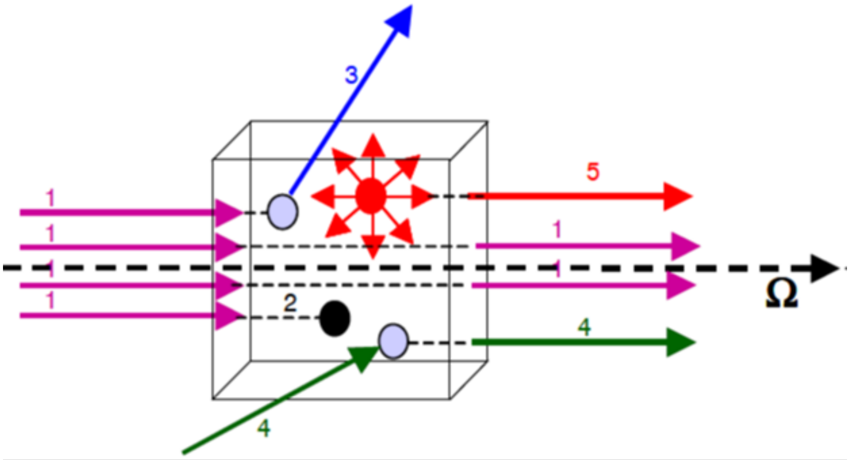

FIGURE 3.2: *Sketch of the contributions to the balance equation for a diffusive and absorbing mechanism in the medium.*

4. Positive contribution to the density of photons inside the volume dV, corresponding to the scattering of photons originally propagating along the direction $\vec{\Omega}'$ but now traveling along $\vec{\Omega}$.
5. Source term deriving from the potential presence of photons originated inside the volume dV.

Finally, in order to write the RTE, we need to define:

- $L(\vec{r},\vec{\Omega},t) = h\nu \cdot vN(\vec{r},\vec{\Omega},t)$ as the *radiance* $[u.m.\ Wm^{-2}sr^{-1}]$. L represents the average power flowing through the unit area along the direction $\vec{\Omega}$, per solid unit angle, at time t.
- $\phi(\vec{r},t) = \int_{4\pi} L(\vec{r},\vec{\Omega},t)d\vec{\Omega}$ as the *fluence* $[u.m.\ Wm^{-2}]$. ϕ represents the total power flowing through the unit area, at time t.
- $\vec{J}(\vec{r},t) = \int_{4\pi} \vec{\Omega}L(\vec{r},\vec{\Omega},t)d\vec{\Omega}$ as the *photon flux vector* $[u.m.\ Wm^{-2}]$.
- $q(\vec{r},\vec{\Omega},t) = h\nu \cdot s(\vec{r},\vec{\Omega},t)$ as the *energy source* term $[u.m.\ Wm^{-2}]$.

With these definitions, the Radiative Transfer Equation results in:

$$\begin{aligned}\frac{1}{v}\frac{\partial L(\vec{r},\vec{\Omega},t)}{\partial t} =& -\vec{\Omega}\cdot\nabla L(\vec{r},\vec{\Omega},t) - L(\vec{r},\vec{\Omega},t)\left[\mu_a(\vec{r})+\mu_s(\vec{r})\right]+\\ &+\mu_s\int_{4\pi} p(\vec{\Omega},\vec{\Omega}')L(\vec{r},\vec{\Omega}',t)d\vec{\Omega}' + q(\vec{r},\vec{\Omega},t)\end{aligned} \tag{3.9}$$

3.1.2.1.2 Diffusion approximation of the RTE

The complexity of the solution of the radiative transfer equation can be reduced by introducing some hypotheses on the light sources present in the medium. In particular, the turbid medium can be assumed to present a high concentration of perfect solid-sphere-like scattering centers responsible for multiple elastic diffusion events. Moreover, we can identify the following hypotheses:

1. The radiance of the field ($L(\vec{r},\vec{\Omega},t)$) can be considered to be almost isotropic, due to the larger contribution of scattering with respect to absorption, hence:

$$L(\vec{r},\vec{\Omega},t) = \frac{1}{4\pi}\phi(\vec{r},t) + \frac{3}{4\pi}\vec{J}(\vec{r},t)\cdot\vec{\Omega} \tag{3.10}$$

2. The source is isotropic, meaning:

$$q(\vec{r},\vec{\Omega},t) = \frac{q_0(\vec{r},t)}{4\pi} \tag{3.11}$$

3. The photon flux variation is negligible with respect to the flux itself, over the total mean free path (it follows $\mu_s \gg \mu_a$):

$$l_t = \frac{1}{\mu_a + \mu_s} \tag{3.12}$$

4. The system is radial symmetric, therefore $p(\vec{\Omega},\vec{\Omega}^{'})$ depends only on the scalar product $(\vec{\Omega}\cdot\vec{\Omega}^{'})$.

Under these assumptions we obtain the diffusion equation for a homogeneous medium in its time-dependent form, as:

$$\frac{1}{v}\frac{\partial\phi(\vec{r},t)}{\partial t} - D\nabla^2\phi(\vec{r},t) + \mu_a\phi(\vec{r},t) = q_0(\vec{r},t) \tag{3.13}$$

Where we have defined:

- $D = \frac{1}{3\mu_s^{'}}$ as the *diffusion coefficient*, with $\mu_s^{'}$ the reduced scattering coefficient.
- $\vec{J}(\vec{r},t) = -D\nabla\phi(\vec{r},t)$ from the *Fick's law* for diffusion.
- $q_0(\vec{r},t) = \int_{4\pi} s(\vec{r},\vec{\Omega},t)d\vec{\Omega}$ as the isotropic light source term.

The solution of the RTE can be obtained with the Green's method, taking advantage of the linearity of the equation. In a nutshell, by assuming a point-like source of the kind:

$$s(\vec{r},\vec{\Omega},t) = \delta(\vec{r}-\vec{r^{'}})\delta(\vec{\Omega}-\vec{\Omega}^{'})\delta(t-t^{'}) \tag{3.14}$$

It is possible to apply the superposition principle to represent the source term as a linear superposition of Dirac's delta functions, providing a solution for the radiance such as:

$$L(\vec{r},\vec{\Omega},t) = \int_V\int_{4\pi}\int_{-\infty}^{+\infty} L(\vec{r},\vec{r^{'}},\vec{\Omega},\vec{\Omega}^{'},t,t^{'})s(\vec{r},\vec{\Omega},t)dV^{'}d\vec{\Omega}^{'}dt^{'} \tag{3.15}$$

Furthermore, it is worth mentioning that within the diffusion approximation, the diffusion equation is not dependent on the absorption coefficient, as if we consider a totally non absorbing medium, for which $\mu_a = 0$, we can determine the fluence of an equivalent system characterized by a non null absorption coefficient μ_a by applying:

$$\phi(\vec{r},t,\mu_a) = \phi(\vec{r},t,\mu_a = 0)\exp(-\mu_a vt) \tag{3.16}$$

Provided that $\phi(\vec{r},t,\mu_a = 0)$ is a solution of Eq.(3.13) for the particular case of $\mu_a = 0$.

3.1.2.2 Introduction to a Monte Carlo model for light-matter interaction in a diffusive medium

The main advantage of a diffusion equation-based model relies on the possibility to have an analytical expression to rapidly interpret the experimental data. Conversely, one of the major drawbacks of this approach consists of the limiting hypotheses on the diffusion regime on which it is built. In fact, in many practical applications, to ensure the applicability of the diffusion approximation some specific working conditions needs to be accounted for. For instance, in the case of a time-resolved measurement configuration (see Section 3.2.1), a lower bound on the inter-fiber distance should be established in order to guarantee a minimum amount of scattering events before detection. This constraint usually comes at the cost of low signal, thus determining difficult measurement conditions for the extraction for the investigation of the optical properties of the system.

In some sense, the counterpart of the diffusion approximation approach lies in the Monte Carlo modelisation of the photon interactions inside a turbid medium. In fact, despite being a more probabilistic-based approach, rather than an analytical computation of the net energy flux, Monte Carlo simulations have the advantage of being completely independent on the albedo regime. Therefore, they allow us to investigate a wide spectrum of optical properties that results inaccessible by analytical diffusion equation approaches. Clearly, in this framework, the computational power is the real limiting factor that might prevent the most complete description of the problem, due to the need for simulating millions of photon paths inside the medium in order to achieve statistical significance (i.e. the statistical accuracy grows with a $\sqrt{N}$ law, where N is the number of photons generated).

The core idea of a Monte Carlo approach for the photon propagation in a diffusive medium is to consider the initial state of one elementary entity (i.e. a photon) to be defined by a weight. Due to the propagation inside the medium, and due to the presence of scattering and absorption events, by also taking into account the geometry of the system, the weight will then undergo a certain decrease depending on the probability of the photon of being either scattered or absorbed and of it exiting the medium by crossing a boundary. In general, the limit for a photon to survive withing the medium and (or) exiting it at some point, is usually set by a threshold value on the weight which inherently depends on the optical properties of the tissue and on its conformation.

In this sense, let us consider a photon at its initial state, and inside the medium let us also define a step Δs of a probabilistic length associated to the total mean free path. By making a step Δs within the medium, the photon has now a non null probability of being absorbed, hence it is possible to calculate the reduction rate of its initial weight due to the presence of an absorption event. After that, if the remaining weight is higher than the pre-selected threshold, a probability of a scattering event is computed, resulting into a change in traveling direction with respect to the initial trajectory. The surviving photon can proceed with the following step Δs inside the medium following the same routine until the remaining weight reaches a value lower than the threshold. It is worth noticing that at each step, a probability for the photon to cross an interface is also calculated in order to take into account the mechanism of total internal reflection (for which the photon is going to remain in the medium) or an event of transmission outside the medium. Moreover, a "survival roulette" process is also implemented in order to preserve the energy balance within the system: whenever the photon weight reaches a value close to the threshold, there is a $\frac{1}{N}$ probability that the next weight value w_{n+1} will be $w_{n+1} = N * w_n$, N being the number of photons within the medium. Finally, this entire routine (as summarized in Fig.3.3) is replicated for $N > 10^6$ photons to guarantee statistical significance of the stochastic process.

It is evident from this brief introduction how computationally challenging the modelization of a turbid medium under the Monte Carlo approach could be, due to the need for a large amount of photons trajectories to simulate for each combination of optical properties. For this reason, it is sometimes preferred to reduce the computational effort by applying the *White Monte Carlo* approach as a scaled derivation of the more general framework previously described. In a nutshell, a White Monte Carlo model allows us to simulate the photon paths within the medium for a single pair of absorption and reduced

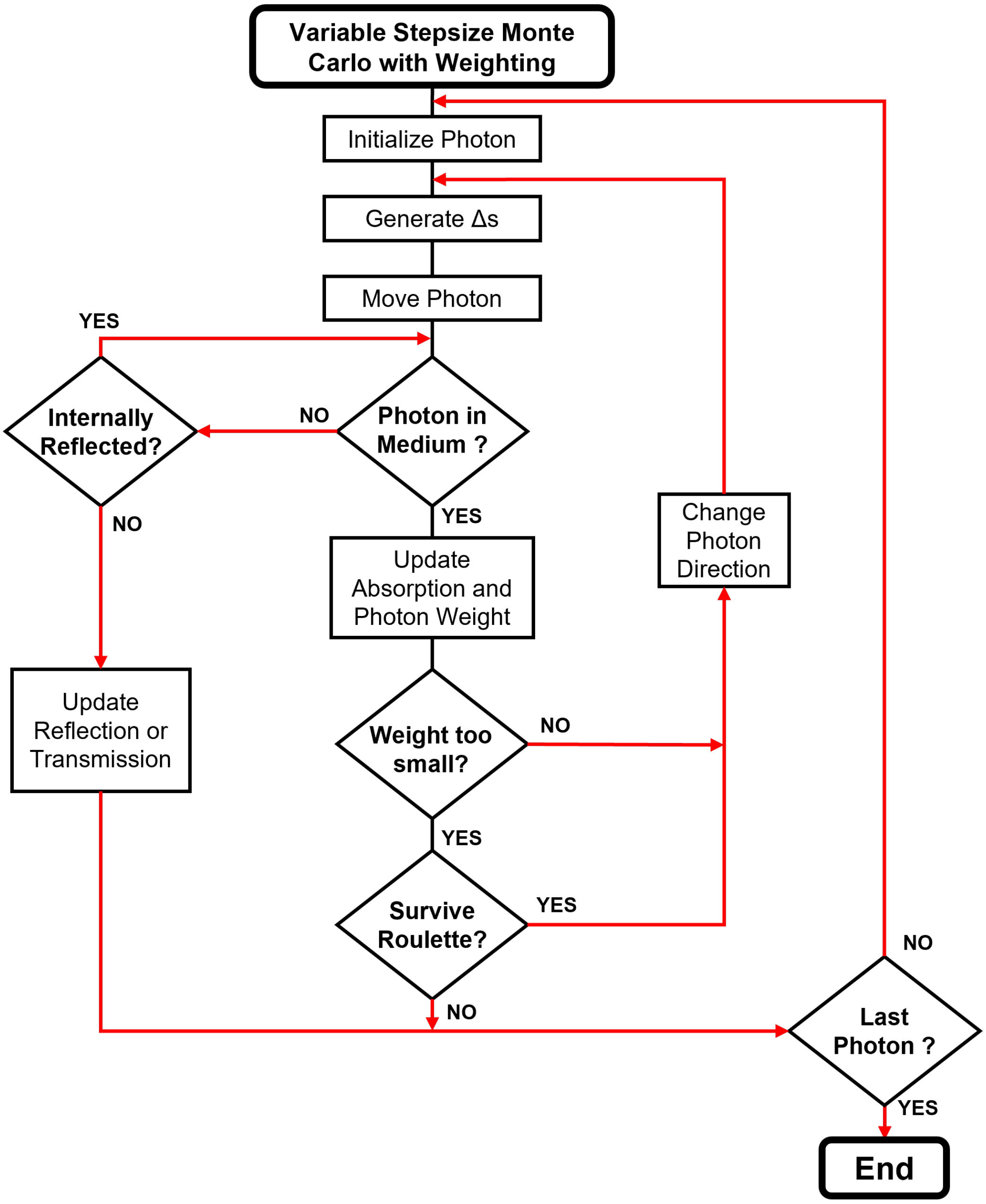

Figure 3.3: *Monte Carlo algorithm for photon transport in a diffusive medium.* [37]

scattering, in order to then scale the results to include all the interesting combinations of optical properties. Though being overall less accurate then a fully Monte Carlo simulation, a White Monte Carlo approach can dramatically reduce the computation time that might be the limiting factor for a real-time application of the algorithm.

A stochastic approach for the photon propagation in biological tissues based on a Monte Carlo routine was first proposed by Wilson and Adam [39] and it is now being considered the gold standard for the numerical simulation of light-matter interaction in diffusive media thanks to its flexibility and accuracy. In addition, the development of graphic processing units (GPUs) and their implementation into processing pipelines has opened the way to challenging simulation tasks that were previously considered inaccessible. Another reason for a community-wise preference of Monte Carlo approaches over a more diffusion equation-based framework for biomedical optics applications lies on the possibility to speed up even more the computation of optical properties by means of the use of pre-computed Look-Up Tables (LUTs). These are multi-dimensional datasets containing the values of diffuse reflectance for several combinations of optical properties, that can be easily accessed at runtime. The advantage of using LUTs is extremely relevant especially for real-time solutions of photon migration problems, since they allow us to exploit the accuracy of Monte Carlo simulations without the limiting pull arising from the computational time required for them.

3.1.3 Functional and structural imaging: chromophore quantification and scattering analysis

In the previous Section 3.1.1 we have introduced the notions of optical properties of biological tissues in the form of absorption and scattering. As mentioned above, it is possible to summarize the main optical mechanisms within the definition of the absorption and reduced scattering coefficients, as the two parameters that are directly related to the response of the tissue to the interaction with light. However, from a clinical point of view, these two quantities can be extremely hard to interpret by a professional not specifically trained on the subject. It is therefore our goal to translate the quantification of optical properties into a language that is easily accessible from a physician point of view, thus providing useful information that can be monitored during surgical procedures.

In this sense, we know that the optical properties of turbid media can be exploited to quantify physiological parameters that are of large interest for the surgical guidance. In particular, being optical absorption a consequence of the presence of different chromophores withing the tissues, it is possible to extract the concentration of such chromophores having determined the values of the absorption coefficient within a band of wavelengths or for a subset in the window of interest, i.e. $600 - 1000$ *nm* is also referred to as *therapeutic window* or *optical window*. Indeed, as shown in Fig.3.4 where the absorption spectra of different specimens present in biological tissues are presented, if we consider the previously mentioned *"therapeutic window"*, the most common absorbing structures are:

- Hemoglobin (both oxygenated and deoxygenated)
- Water
- Lipids
- Collagen
- Melanin

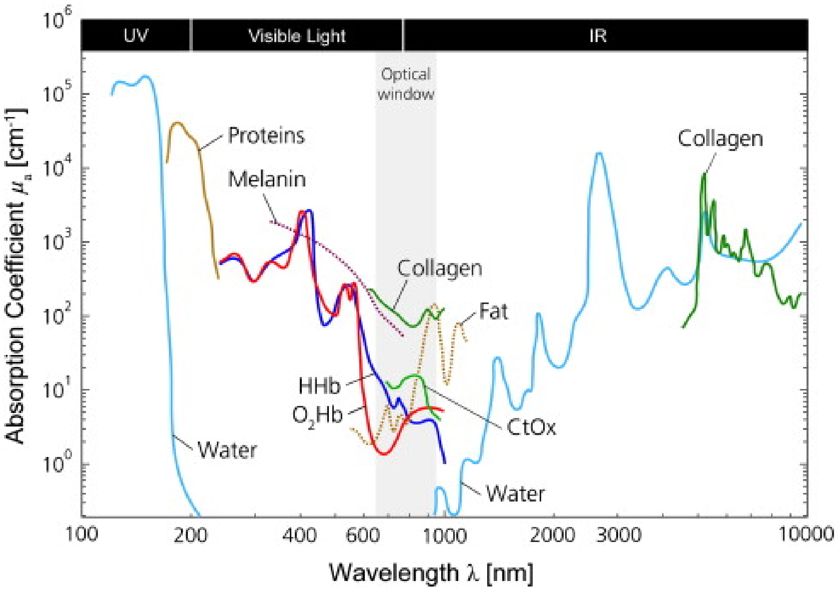

FIGURE 3.4: *Absorption spectra of tissue chromophores.* [35]

All these parameters can be quantified by investigating the tissue in different spectral bands through the exploitation of the *Beer's* law for absorption which reads as follows:

$$\mu_a(\lambda_i) = \sum_{n=1}^{N} c_n \epsilon_n(\lambda_i) \tag{3.17}$$

Where c_n is the concentration of the n_{th} chromophore and $\epsilon_n(\lambda_i)$ is the extinction coefficient of the n_{th} chromophore at the corresponding wavelength. A notable example of functional imaging that is of high interest for our purposes is the quantification of oxygen saturation in a tissue. This procedure is enabled by the measurement of the absorption coefficient at (at least) two wavelength, i.e. $\lambda_1 = 665\ nm$ and $\lambda_2 = 860\ nm$ in our case, that allows us to compute the concentration of oxygenated and non-oxygenated hemoglobin in the medium, thus resulting into the formula:

$$[HbO_2] = \log_{10} e \cdot \frac{\epsilon_{Hb}(\lambda_2)\mu_a(\lambda_1) - \epsilon_{Hb}(\lambda_1)\mu_a(\lambda_2)}{\epsilon_{HbO_2}(\lambda_1)\epsilon_{Hb}(\lambda_2) - \epsilon_{HbO_2}(\lambda_2)\epsilon_{Hb}(\lambda_1)} \tag{3.18}$$

$$[HbO] = \log_{10} e \cdot \frac{\epsilon_{HbO_2}(\lambda_1)\mu_a(\lambda_2) - \epsilon_{HbO_2}(\lambda_2)\mu_a(\lambda_1)}{\epsilon_{HbO_2}(\lambda_1)\epsilon_{Hb}(\lambda_2) - \epsilon_{HbO_2}(\lambda_2)\epsilon_{Hb}(\lambda_1)} \tag{3.19}$$

$$StO_2 = \frac{[HbO_2]}{[HbO_2 + Hb]} \cdot 100 \tag{3.20}$$

Where:

- ϵ_{Hb} is the extinction coefficient of the deoxy-hemoglobin.
- ϵ_{HbO_2} is the extinction coefficient of the oxy-hemoglobin.
- $\mu_a(\lambda_i)$ is the absorption coefficient of the tissue at the $\lambda_{i_{th}}$ wavelength.

Similarly, also a scattering analysis can be implemented to address the structural properties of the investigated tissue. In fact, the concentration and size of diffusion centers determine the scattering properties of the medium and as a consequence, by quantifying the reduced scattering coefficient of the tissue it is therefore possible to extrapolate the structural information [40] by exploiting the *Mie's* (or *Rayleigh's*) law in it's approximated form, which reads:

$$\mu_s^{'} = A\left(\frac{\lambda}{\lambda_0}\right)^{-b} \qquad A, b > 0 \tag{3.21}$$

where λ_0 is a reference wavelength (i.e. $\lambda_0 = 600\ nm$), A is defined as the scattering amplitude (i.e. $\mu_s^{'}(\lambda = \lambda_0)$) and b is the scattering power. The Rayleigh's approximation can be obtained when $b \simeq 4$.

Structural analysis are quite common for the diagnosis and screening of breast cancer, where the it has been shown that a morphological alteration of healthy tissues is a frequent sign of neoplastic growth [41]. As a result, the cancerous tissue presents a rather stiffer profile with respect to the surroundings[1], thus legitimizing the utility of a structural imaging analysis for the investigation.

3.1.4 Fluorescence

In biological tissues, the absorption of light within a certain spectral range can also result into the emission of photons of specific energy. Indeed, the absorption of a photon can produce an electronic transition to an excited state, which can consequently relax back to the ground state by means of an optical phenomenon that depending on the nature of the excited state can produce a fluorescence emission. Fluorescence stems from the optically allowed relaxation of an electron from a singlet electronic state to the ground state, with the consequent emission of a photon of energy equal to the energy gap between the excited and the ground state. Typically, such transitions are characterized by a decay rate of $10^8\ s^{-1}$, thus determining a fluorescence lifetime (τ), i.e. the average time span that corresponds to the electronic excitation before the relaxation, in the order of few nanoseconds. τ mainly depends on the characteristics of the chromophore, but also on its environment that can contribute to a reduction of the lifetime to hundreds of picoseconds due to the molecular interactions with the solvent.

A fluorophore is a molecule that is characterized by a particular fluorescence footprint that can be identified in its absorption and emission spectra. These are graphs that represent the light intensity as a function of wavelength in nm (or of the wavenumber in cm^{-1}). As mentioned before, the fluorescent molecule environment plays a role in the light emission, thus resulting into different emission (and absorption) spectra with respect to the condition in which the fluorophore is dissolved. Similarly, the molecular configuration of the chromophore can contribute to a modification of the fluorescence activity and therefore of the spectrum. As an example, in Fig.3.5 we report the absorption and emission spectra of *fluorescein*, an aromatic molecule typically used in ophthalmology for the screening of the ocular tone [42].

The *Jablonsky* diagram is a graphical tool to illustrate the energy levels of fluorescent compounds and the transitions taking place between each state. In Fig.3.6 an example of such diagram is shown: the arrows pointing upwards represent the absorptive transitions to excited singlet states. Conversely the arrows pointing downwards refer to the relaxation and the energy transfer to optically allowed transitions such as fluorescence, or towards other non-radiative phenomena such as intersystem crossing and internal conversion. In addition, the horizontal lines present for each singlet state represent the different vibrational levels of the molecule. It is worth mentioning that the absorption of light can produce the transition to an excited electronic state within which the molecule is also characterized by an excited vibrational state. However, the vibrational relaxation

---

[1] It is worth mentioning that an alteration of the structural conformation of the tissue is not the only sign of the presence of a cancerous body.

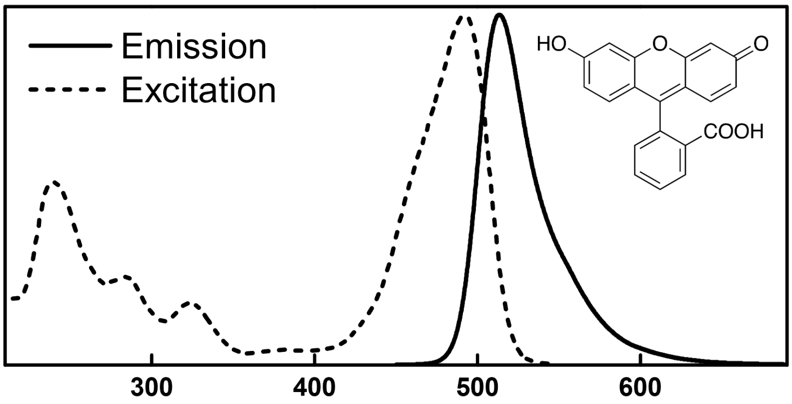

FIGURE 3.5: *Absorption and emission spectrum of a fluorescein molecule.*

(i.e. *internal conversion*) is typically order of magnitudes faster than the electronic one ($10^{-12}\ s$ against $10^{-9} - 10^{-8}\ s$) thus being completed before the electronic transition takes place. As a result, the absorption and emission spectrum of the molecule present a similar profile (i.e. *mirror symmetry*), however the emission line band is characterized by a *"Stokes shift"* towards red wavelengths due to the slightly lower energy gap associated with the radiative phenomenon, due to the thermal relaxation of the vibrational state. It is worth noticing that several fluorescent molecules have an emission spectrum that is deformed with respect to its mirrored absorption version, as a consequence of different mechanisms occurring in the excited states that modify the conformation of the nuclei thus mainly impacting the vibrational transitions (see Fig.3.6 for the vibrational structure of the molecule).

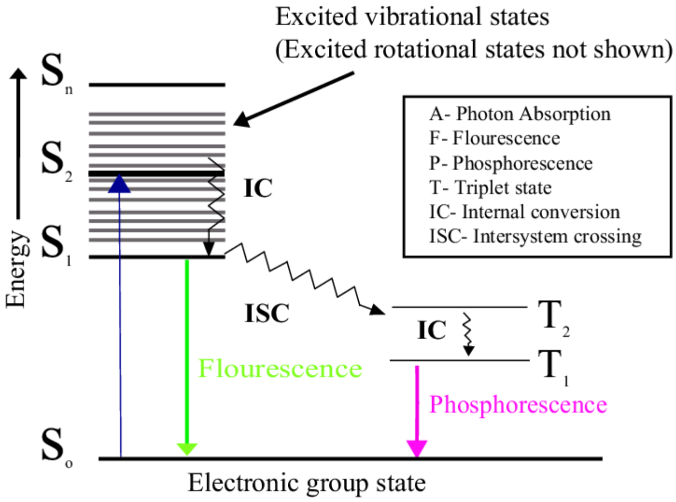

FIGURE 3.6: *Jablonsky diagram to illustrate the phenomena of photoluminescence, fluorescence, and phosphorescence. [25]*

The fluorescence activity of a molecule can be analyzed in terms of two main parameters: the fluorescence lifetime (τ) and the quantum yield (Φ). As we introduced before, the fluorescence lifetime is a measure of the time interval of the fluorophore in the excited state, whereas the quantum yield represents the ratio between the number of absorbed photons with respect to the amount of photons emitted during the radiative decay. More specifically, by defining [43]:

- k_f = fluorescence decay rate

- k_{nr} = non-radiative decay rate

We can determine the quantum yield Φ as:

$$\Phi = \frac{k_f}{k_f + k_{nr}} \tag{3.22}$$

Similarly, the fluorescent lifetime τ ought to be:

$$\tau = \frac{1}{k_r + k_{nr}} \tag{3.23}$$

The resulting temporal decay of the fluorescent intensity can be determined as follows:

$$I = I_0 \exp(-t/\tau) \tag{3.24}$$

Another important parameter to consider is the *natural fluorescence lifetime* (τ_n). This quantity represents the average lifetime of the excited state in absence of non-radiative energetic transitions (i.e. $k_{nr} = 0$), and it can be extrapolated from the absorption spectrum of the molecule, its extinction coefficient and the fluorescence emission spectrum with the following equation [43]:

$$\frac{1}{\tau_n} = k_f = 2.88 \times 10^{-9} n^2 \frac{\int F(\nu) d\nu}{\int \frac{F(\nu)}{\nu^3}} \int \frac{\epsilon(\nu)}{\nu} d\nu \tag{3.25}$$

Where ν represents the wavenumber (in cm^{-1}), n is the index of refraction, $\epsilon(\nu)$ is the extinction coefficient of the molecule, and $F(\nu)$ is the fluorescence emission spectrum. Clearly, following the given definitions, it is then possible to empirically calculate the natural lifetime τ_n starting from the quantum yield of fluorescence and the total lifetime, being:

$$\tau_n = \frac{\tau}{\Phi} \tag{3.26}$$

In order to understand the behavior of fluorescence dyes in solutions, it is necessary to discuss a mechaninsm called *"quenching"*, which is the phenomenon at the origin of the reduction of fluorescence intensity caused by interactions of the chromophore with its surroundings. One major form of quenching is the so called *"collisional quenching"*: in this case, the fluorescence molecule collides with the molecules present in the solution, thus reducing its lifetime in the excited state and therefore its radiative energy conversion efficiency.

Quantitatively, the quenching effect can be addressed by considering the emission intensity of the molecule in presence and in absence of the quencher, and by exploiting the property that the quencher introduces a new non-radiative energy transfer mechanism in the system. Under these assumptions, by defining F_0,F the unperturbed fluorescence intensity and the intensity in presence of the quencher, respectively, and by introducing k_q as the non-radiative decay rate associated to the presence of a quencher with concentration $[Q]$, we can write the *Stern-Volmer*'s equation [43]:

$$\frac{F_0}{F} = \frac{\frac{k_f}{k_f + k_{nr}}}{\frac{k_f}{k_f + k_{nr} + k_q[Q]}} =|_{k_f + f_{nr} = 1/\tau_0} 1 + \tau_0 k_q [Q] = 1 + K[Q] \tag{3.27}$$

Where, being τ_0 the unperturbed fluorescence lifetime, we defined the *quenching constant* K as:

$$K = \tau_0 k_q \tag{3.28}$$

From these results we can also notice that any sort of quenching affects not only the fluorescent intensity but also the lifetime, in fact:

$$\tau = \frac{1}{k_f + k_{nr} + k_q[Q]} \quad and \quad \frac{F_0}{F} = \frac{\tau_0}{\tau} \tag{3.29}$$

To conclude, the behavior of fluorescent molecules in solutions requires an analysis in depth for their application for *in-vivo* imaging. Nevertheless, as we are going to discuss in the following sections, the use of fluorescent dyes has become standard practice in medicine and in image-guided surgery, thanks to the capability of targeting specific compounds in the human body such as cancerous tissues [44].

3.2 Advanced Optical Imaging for Surgery: Principles

The quantitative assessment of tissue health is the main goal of diffuse optical imaging applied to surgical guidance owing to its potential of providing a quantitative imaging feedback in real-time, as previously discussed in Chapter 2. Over the last decades diffuse optics has witnessed major developments concerning the different techniques available to achieve this purpose. In general it is practical to represent the tissue response to a light stimulus in four main domains based on the physics of the interactions and signal processing approach [45]:

- **Time domain**: in this case the output of a measurement is the *temporal Point Spread Function* (t-PSF), which represents the temporal spreading of a light pulse due to the propagation in the tissue.
- **Time Frequency domain**: in this case the output of a measurement is the *temporal Modulation Transfer Function* (t-MTF), which represents the attenuation and phase delay of a periodically varying photon density wave.
- **Spatial domain**: in this case the output of a measurement is the *spatial Point Spread Function* (s-PSF), which represents the spatial spreading of a point-like illumination due to reflection or transmission from a turbid medium.
- **Spatial frequency domain**: in this case the output of a measurement is the *spatial Modulation Transfer Function* (s-MTF), which represents the attenuation and phase delay associated to a spatially modulated light signal interacting with the tissue.

A graphical representation of the four domains is given in Fig.3.7: it is worth noticing that each of the curves plotted in the graphs directly depend on the optical properties of the tissue analyzed, thus allowing us to recover the absorption and reduced scattering coefficient via an inverse problem solving algorithm. Continuous Waves (CW) approaches are also possible for the characterization of tissue responses, and they are usually achieved by plain illumination of the sample and by the acquisition of the reflected light arising from it. In addition, as we know, time and space are not the only parameters that represent the physical world: energy is the other fundamental entity that we need to consider as well. In this sense, after the description of the time-space domain (together with their reciprocals), we are going to briefly mention spectral approaches which correspond to the analysis of the purely energy components of the optical responses, which is generally encoded into the spectral characteristics.

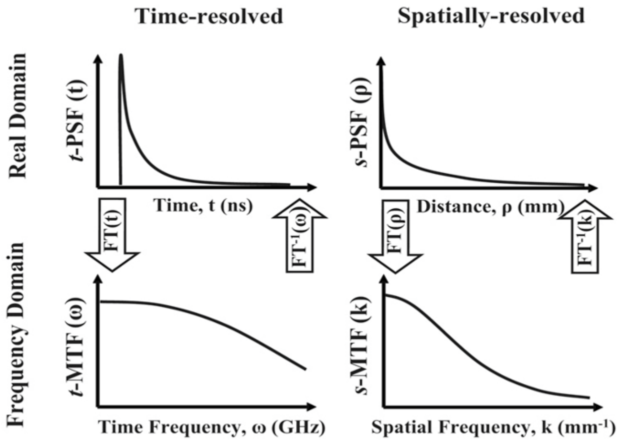

FIGURE 3.7: *Illustration of the four measurement domains for diffuse optics. [45]*

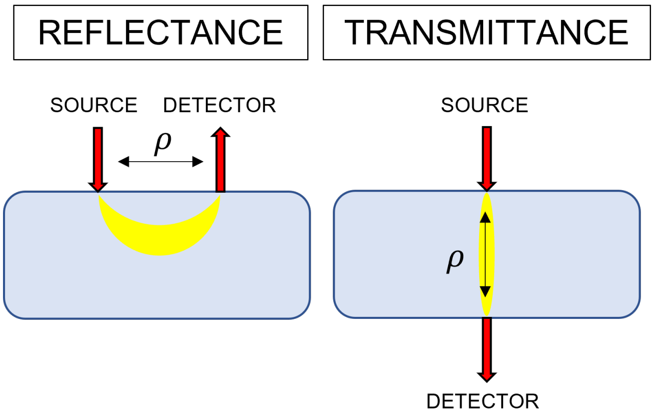

FIGURE 3.8: *Measurement configurations for time-resolved diffuse optics.*

3.2.1 Time Domain Diffuse Optics

In Section 3.1.2 we described a light propagation model based on the radiative transfer equation and its diffusion approximation. In our analysis, we considered the energy balance through an elementary volume at a time interval, thus obtaining the time-dependent diffusion approximation of the RTE in the form of Eq.(3.13). In the following section we are going to analyze the solution of such equation for an infinite and semi-infinite homogeneous medium in order to determine the effect of a short pulse injected in a biological tissue and its relationship with the optical properties of the investigated system [46].

Let us consider an infinite homogeneous medium with absorption and reduced scattering coefficients μ_a and $\mu_s^{'}$, respectively. In addition, let us suppose to inject a short light pulse ($FWHM \sim ps$) of a given wavelength λ from the surface of the medium. Our goal is to determine the t-PSF of the system after propagation in two configurations (as shown in Fig.3.8):

- **Reflection** geometry: consists of measuring the diffused light emitted from the same surface of the sample after propagation.
- **Transmission** geometry: consists of measuring the diffuse light from the opposite side of the injection surface, thus analyzing the photon paths that covered the entire thickness of the medium.

In both cases, the diffusion equation can be analytically solved without further approximations thanks to the spatial invariance of the system in all directions, and the resulting solutions can be adopted as building blocks for more complex geometries.

Under these hypotheses, if we consider Eq.(3.13) in the case of a point-like source of the form:

$$q_0(\vec{r},t) = \delta(\vec{r})^3\delta(t) \tag{3.30}$$

It is possible to compute the corresponding time-dependent Green's function [46] for the fluence rate $\phi(\vec{r},t)$ as:

$$\phi(\vec{r},t) = \frac{v}{(4\pi Dvt)^{3/2}} \exp\left(-\frac{r^2}{4Dvt} - \mu_a vt\right) \quad , \quad t > 0 \tag{3.31}$$

And similarly, by exploiting Fick's law for diffusion we can determine the Green's function for the diffuse flux $\vec{J}(\vec{r},t)$ and for the radiance $I(\vec{r},\vec{\Omega},t)$ as:

$$\begin{aligned} \vec{J}(\vec{r},t) &= \frac{r}{16(\pi D v)^{3/2} t^{5/2}} \exp\left(-\frac{r^2}{4Dvt} - \mu_a v t\right) \cdot \vec{r} \\ I(\vec{r},\vec{\Omega},t) &= \frac{1}{(4\pi)^{5/2}(Dvt)^{3/2}} \left[v + \frac{3r}{2t}(\vec{r}\cdot\vec{\Omega})\right] \exp\left(-\frac{r^2}{4Dvt} - \mu_a v t\right) \end{aligned} \tag{3.32}$$

It is worth noticing that the solution provided by Eq.(3.31) foresees energy also for times $t < t_b = r/v$, where t_b represents the ballistic time necessary to propagate from the source to the receiver throughout a straight path. This property of the solution derives from a simplifying assumption made to solve the Diffusion Equation, but it would provide an infinite speed for the propagation of energy over the sample. As a consequence, the causality principle would be violated in such a system thus determining a non-physical situation.

The general solution described by Eq.(3.31) can be further developed for a slab-like geometry, which in many cases better represents the physical system that constitutes a biological tissue. Indeed, a semi-infinite[2] geometry is typically preferred for practical applications to include the presence of physical boundaries between the tissue and the environment. In this case, it is also possible to reach a solution for the diffusion approximation of the RTE and to obtain it let us assume a Dirac's delta point-like source of the kind:

$$q(\vec{r},t) = \delta^3(\vec{r}-\vec{r_s})\delta(t), \tag{3.33}$$

where $\vec{r_s} = (0,0,z_s)$ with $0 \le z_s \le s$. In addition, let us assume *Extrapolated Boundary Conditions* (EBC) for the partial differential equation, by setting the radiance to be null at a distance from the surface of the sample equal to:

$$z_e = 2AD \tag{3.34}$$

Where we define[3]:

$$A = \frac{1 + 3\int_0^{\pi/2} R_F(cos\theta) cos^2\theta sin\theta d\theta}{1 - 2\int_0^{\pi/2} R_F(cos\theta) cos\theta sin\theta d\theta} \tag{3.36}$$

Hence, by exploiting the method of the source images [46], the Green's function for the time-resolved fluence oughts to be:

$$\begin{aligned} \phi(\vec{r},t) =& \frac{v}{(4\pi D v t)^{3/2}} \exp\left(-\frac{\rho^2}{4Dvt} - \mu_a v t\right) \times \\ &\times \sum_{m=-\infty}^{m=+\infty} \left\{ \exp\left[-\frac{(z-z_m^+)^2}{4Dvt}\right] - \exp\left[-\frac{(z-z_m^-)^2}{4Dvt}\right] \right\} \end{aligned} \tag{3.37}$$

---

[2] It is important to underline that the semi-infinite medium approximation holds as long as the slab is "sufficiently thick", which means that the probability for the radiation to escape from the surface opposite to the source can be considered as negligible.

[3] R_F represents the *Fresnel's reflection coefficient* for unpolarized light, and it can be calculated from [46]:

$$\begin{aligned} R_F(\hat{s'}\cdot\hat{q}) &= \begin{cases} \frac{1}{2}\left\{\left[\frac{n_d cos\theta - n_e cos\theta_r}{n_d cos\theta + n_e cos\theta_r}\right]^2 + \left[\frac{n_e cos\theta - n_d cos\theta_r}{n_e cos\theta + n_d cos\theta_r}\right]^2\right\} & \text{if} \quad 0 < \theta < \theta_c \\ 1 & \text{if} \quad \theta > \theta_c = arcsin\left(\frac{n_e}{n_d}\right) \end{cases} \\ \theta_r &= arcsin\left[\left(\frac{n_d}{n_e}\right) sin\theta\right] \end{aligned} \tag{3.35}$$

being θ the angle of incidence, θ_r the angle of refraction, n_d and n_e the index of refraction of the diffusive and external medium respectively.

With $\rho = \sqrt{x^2 + y^2}, 0 \leq z \leq s$ and:

$$\begin{cases} z_m^+ & = 2m(s + 2z_e) + z_s \\ z_m^- & = 2m(s + 2z_e) - 2z_e - z_s \\ m & = 0, \pm 1, \pm 2, ..., \pm\infty \end{cases}$$

Similarly to the infinite case, by applying Fick's law we obtain:

$$\begin{aligned} \vec{J}(\vec{r}, t) &= -D\nabla\phi(\vec{r}, t) \\ I(\vec{r}, \vec{\Omega}, t) &= \frac{1}{4\pi}\phi(\vec{r}, t) - \frac{3}{4\pi}D\nabla\phi(\vec{r}, t) \cdot \vec{\Omega} \end{aligned} \tag{3.38}$$

It is then possible to retrieve the diffuse reflectance $R(\rho, t)$ by computing the power crossing the surface at $z = 0$, per unit area, at a distance r from the z axis, with any exit angle. In this case we have:

$$R(\rho, t) = \vec{J}(\rho, z = 0, t) \cdot \vec{q} = D\frac{\partial}{\partial z}\phi(\rho, z = 0, t) \tag{3.39}$$

And similarly for the transmittance $T(\rho, t)$ (by defining s the thickness of the slab):

$$T(\rho, t) = \vec{J}(\rho, z = s, t) \cdot \vec{q} = -D\frac{\partial}{\partial z}\phi(\rho, z = s, t) \tag{3.40}$$

Finally, we can remove the dependency of the source-detector separation ρ by computing the following integrals:

$$\begin{aligned} R(t) &= \int_0^{+\infty} R(\rho, t) 2\pi\rho d\rho \\ T(t) &= \int_0^{+\infty} T(\rho, t) 2\pi\rho d\rho \end{aligned} \tag{3.41}$$

Which allows us to retrieve the time-resolved reflectance and transmittance equations for the semi-infinite medium as:

$$\begin{aligned} R(t) &= -\frac{\exp(-\mu_a vt)}{2(4\pi Dv)^{1/2}t^{3/2}} \times \sum_{m=-\infty}^{m=+\infty} \left\{ z_{3m} \exp\left(-\frac{z_{3m}^2}{4Dvt}\right) - z_{4m} \exp\left(-\frac{z_{4m}^2}{4Dvt}\right) \right\} \\ T(t) &= -\frac{\exp(-\mu_a vt)}{2(4\pi Dv)^{1/2}t^{3/2}} \times \sum_{m=-\infty}^{m=+\infty} \left\{ z_{1m} \exp\left(-\frac{z_{1m}^2}{4Dvt}\right) - z_{2m} \exp\left(-\frac{z_{2m}^2}{4Dvt}\right) \right\} \end{aligned} \tag{3.42}$$

With:

$$\begin{aligned} z_{1m} &= (1 - 2m)s - 4mz_e - z_s \\ z_{2m} &= (1 - 2m)s - (4m - 2)z_e + z_s \\ z_{3m} &= -2ms - 4mz_e - z_s \\ z_{4m} &= -2ms - (4m - 2)z_e + z_s \end{aligned} \tag{3.43}$$

Evidently, the summations with respect to the index m ought to be extended to infinite values of m, but for practical reasons they can be truncated to a finite number of elements. This procedure is allowed since the contributions of the sources associated to high values of m cannot be neglected only in the case of very high source-detector distance ρ, or alternatively, very long times t.

3.2.2 Time Frequency Domain

Diffuse optics in the time frequency domain is typically performed by introducing a phase and amplitude modulation on an optical signal generated by either a laser source or a broadband lamp, most commonly in the radio-frequency range ($100 - 500$ MHz)

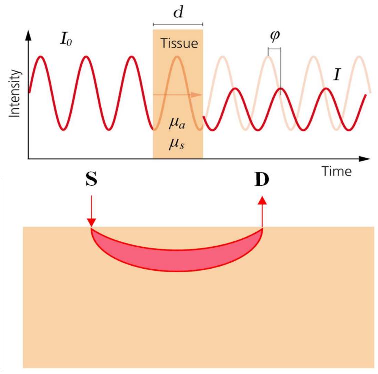

FIGURE 3.9: *Time frequency domain measurement approach.*

[47]. The detection chain is characterized by a photon counting system or by a gain-modulated area detector that is associated to a demodulation circuit for the extraction of the phase and amplitude of the measured signal (as a function of the propagation distance withing the tissue, see Fig.3.9) that permits the computation of the optical properties of the sample, i.e. the absorption and reduced scattering coefficients. Several configurations can be implemented to perform a FD measurement, however they can be summarized into three major categories:

- Single wavelength with a fixed inter-optode distance;
- Multiple wavelengths with a fixed inter-optode distance;
- Single wavelength with multiple inter-optode distances.

In all these approaches, the optical properties computation is enabled via the measurement of the DC and AC components of the emitted signal, as well as the phase shifts, the latter being also exploited for localization of the origin of the signal [48].

An interesting property of FD techniques lies on the fact that the mathematical framework used to describe the response of biological tissues to frequency modulated signals is the Fourier's domain of the widely utilized time-resolved approaches, thus providing a relatively easy access to the development of such technologies. However, the main drawbacks of such systems is the tendency to be limited by the noise produced by high frequency signals, the need for a calibration step to recover the MTF and the poor sensitivity to weak optical responses.

3.2.3 Spatial Domain

This measurement technique is based on the use of continuous illumination of the sample either with laser or white light sources, followed by the detection of the emitted signal by means of photodetectors, photomultipliers or specific custom-made optodes. In practice, it is generally performed in two different configurations, as illustrated in Fig.3.10. The former is exploited to obtain angle-dependent diffuse reflectance signals by directing the sources at different inclinatiosn with respect to the surface of the sample; the latter instead, is characterized by several measurements performed at different source-detector separations in order to characterize multiple photon paths within the tissue (Spatial Resolved Spectroscopy, SRS) [49]. Typically, the instrumentation required for these approaches is relatively less expensive with respect to the time-resolved counterpart, which could be an advantage for the direct application to a clinical environment. These techniques allow for the quantification of tissue optical properties by extracting

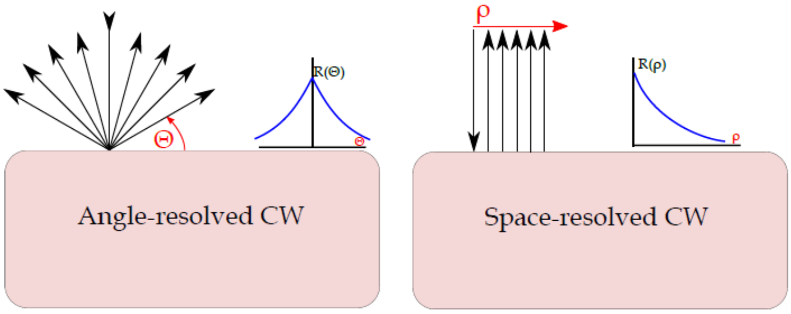

FIGURE 3.10: *CW measurement configurations: on the left side the Angle Resolved set-up; on the right side, the Space Resolved system.*

the contributions of absorption and scattering from the the reconstruction of the photon path inside the medium. The main drawback of such systems is the need for multiple measurements of the same sample at different source-detector separations, differently from the time-resolved approaches where theoretically a single measurement is enough to characterize μ_a and $\mu_s^{'}$ for the investigated sample.

3.2.4 Spatial Frequency Domain

The theoretical description of the interaction of a tissue with a spatially modulated photon density (PDW) wave can be found in [45]. Briefly, we are going to follow the same workflow proposed by *Cuccia et al.* by starting from a diffusion equation-based framework, to discuss the main properties of the system, leaving the Monte Carlo adaptation to the reference.

Let us assume a periodically varying plane wave q propagating with normal incidence with respect to the surface of a semi-infinite homogeneous diffusive medium characterized by absorption and reduced scattering coefficients μ_a and $\mu_s^{'}$, respectively. In addition, let us suppose that the PDW is determined by the spatial frequencies f_x and f_y and spatial phases α and β on the tangential plane. In this case, we can write the source term as:

$$q = q_0(z)\cos(k_x x + \alpha)\cos(k_y y + \beta) \tag{3.44}$$

Where we defined the wave vectors $k_x = 2\pi f_x$ and $k_y = 2\pi f_y$. If we now consider the time-indipendent diffusion equation[4]:

$$\nabla^2\phi - \mu_{eff}^2\phi = -3\mu_{tr}q \tag{3.45}$$

With:

- $\mu_{tr} = \mu_a + \mu_s'$ (*transport coefficient*)
- $\mu_{eff} = \sqrt{3\mu_a\mu_{tr}}$

Provided that the response of the medium is proportional to the input intensity, i.e. linear medium, the corresponding fluence rate profile ϕ within the medium will be characterized by the same spatial frequency and phase [50]:

$$\phi = \phi_0(z)\cos(k_x x + \alpha)\cos(k_y y + \beta) \tag{3.46}$$

---

[4] We are referring to Eq.(3.13) in case of $\frac{\partial\phi(\vec{r},t)}{\partial t} = 0$.

Therefore, if we replace Eq.(3.44) and Eq.(3.46) into Eq.(3.45) we have:

$$\frac{d^2}{dz^2}\phi_0(z) - \mu'^2_{eff}\phi_0(z) = -3\mu_{tr}q_0(z) \tag{3.47}$$

Where we can define the effective penetration depth δ'_{eff}, function of the optical properties and the spatial frequency, as:

$$\delta'_{eff} = \frac{1}{\mu'^2_{eff}} = \frac{1}{\sqrt{\mu^2_{eff} + k_x^2 + k_y^2}} \tag{3.48}$$

For simplicity, in the following we will consider the 1-D solution of Eq.(3.47), by considering a fully constant planar illumination along y (i.e. $k_y = 0$). In this case, by defining the *reduced albedo* a' as:

$$a' = \frac{\mu'_s}{\mu_{tr}} \tag{3.49}$$

And by assuming an extended isotropic source q_0 of the form [51]:

$$q_0(z) = P_0\mu'_s \exp(-\mu_{tr}z) \tag{3.50}$$

The solution for the fluence rate ϕ_0 results to be:

$$\phi_0(z) = \frac{3P_0a'}{\frac{\mu'^2_{eff}}{\mu^2_{tr}} - 1}\exp(-\mu_{tr}z) + C\exp(-\mu'_{eff}z) \tag{3.51}$$

Where C is a generic constant that depends on the boundary conditions assumed for the system. For instance, let us assume *partial current* boundary conditions [52], for which the photon flux j is proportional to the fluence at the interface $z = 0$, i.e.:

$$j|_{z\to 0^+} = \frac{-\nabla\phi|_{z\to 0^+}}{3\mu_{tr}} = -A\phi|_{z\to 0^+} \tag{3.52}$$

Where we defined:

$$A = \frac{1 - R_{eff}}{2(1 + R_{eff})}$$

$$R_{eff} = 0.0636n + 0.668 + \frac{0.710}{n} - \frac{1.440}{n^2}$$

Under these hypotheses, it is possible to calculate the arbitrary constant C as:

$$C = \frac{-P_0 3a'(1 + 3A)}{\left(\frac{\mu'^2_{eff}}{\mu^2_{tr}} - 1\right)\left(\frac{\mu'_{eff}}{\mu_{tr}} + 3A\right)} \tag{3.53}$$

Thus allowing us to compute the diffuse reflectance $R_d(k)$[5], function of the wave vector k, as:

$$R_d(k) = -\frac{j|_{z\to 0^+}}{P_0} = \frac{3Aa'}{\left(\frac{\mu'_{eff}}{\mu_{tr}} + 1\right)\left(\frac{\mu'_{eff}}{\mu_{tr}} + 3A\right)} \tag{3.54}$$

---

[5] Clearly, the superposition principle can be applied to generalize the 1-D solution for an illumination source of arbitrary geometry.

As a result, R_d represents the spatial MTF of the turbid medium for a given pair of optical properties μ_a and $\mu_s^{'}$. It is worth noticing that the frequency dependence of the diffuse reflectance follows an inverse polynomial function of the factor:

$$\frac{\mu'_{eff}}{\mu_{tr}} = \left(\frac{\mu_{eff}^2 + k^2}{\mu_{tr}^2}\right)^{\frac{1}{2}} = \left(3\frac{\mu_a}{\mu_{tr}} + \frac{k^2}{\mu_{tr}^2}\right)^{\frac{1}{2}} = \begin{cases} \sqrt{3(1-a')}, & k = 0 \\ \frac{k}{\mu_{tr}}, & k \gg \mu_{eff} \end{cases} \tag{3.55}$$

The relationship obtained in Eq.(3.55) highlights the natural low-pass filtering properties of a biological scattering medium. Moreover, from the same equation we can distinguish the different sensitivity of the modulation transfer function to absorption and reduced scattering, indeed:

- If $k \ll \mu_{eff}$ (i.e. low frequency regime), absorption has a primary impact on the diffuse reflectance .
- If $k \gg \mu_{eff}$ (i.e. high frequency regime), by considering the diffusion limit:

  $$\mu_{tr} \approx \mu'_s \, , \tag{3.56}$$

  scattering has the major impact on the diffuse reflectance.
- If $k = 0 \rightarrow R_d(k) = R_d(a')$.

This is an extremely powerful property that enables the disentanglement of the two contributions on the MTF of absorption and scattering, thus paving the way towards a quantitative measuring capability of the technology. In addition, another fundamental property of this solution is the direct relationship between the diffuse reflectance and the transport coefficient. Indeed, similarly to the definition of μ_a and $\mu_s^{'}$, if we define the *transport mean free path* l_{tr} as:

$$l_{tr} = \frac{1}{\mu_{eff}} \tag{3.57}$$

It is possible to quantify the natural boundaries of validity of the diffusion model in terms of the minimum distance ρ of the detection position with respect to the collimated light source:

$$\rho \gg l_{tr} \tag{3.58}$$

This limit corresponds to an upper bound for the spatial frequency of modulation that can be derived with the condition:

$$f_x \ll \mu_{tr} \equiv \frac{1}{l_{tr}} \tag{3.59}$$

In practice, a good rule of thumb for the choice of the spatial frequency is represented by setting the maximum limit for f_x to $3\mu_{tr}$. Finally, it is worth highlighting that the diffusion approximation also determines a condition on the albedo, i.e. $a' \ll 1$.

3.2.5 Spectral Domain

The spectral characterization of biological tissues deserves a brief mention as the energy counterpart of the time-space analysis of photon-tissue interactions. In particular, we refer to this domain every time we consider the investigation of a biological structure by means of a continuous illumination of the system followed by the acquisition of the spectral information buried in a reflectance (or transmittance) measurement. Fluorescence,

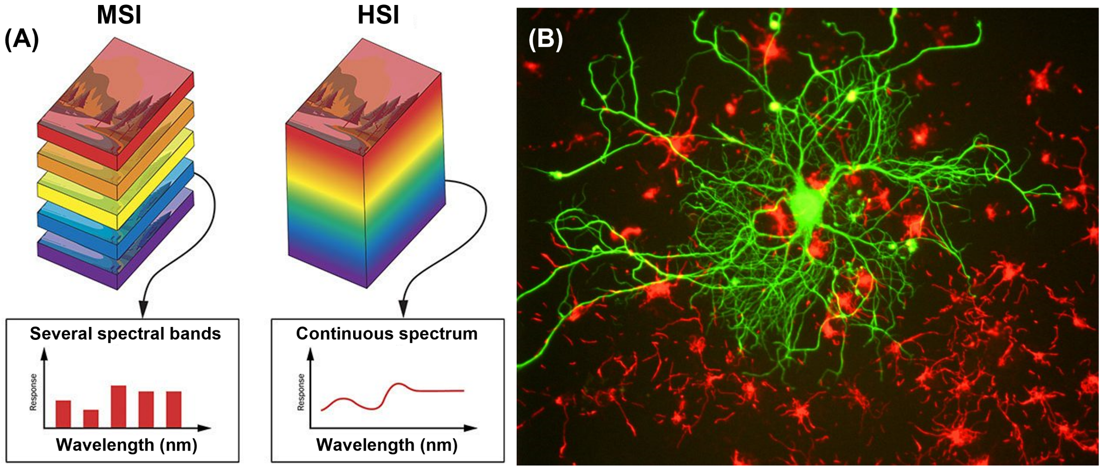

FIGURE 3.11: *Summary of spectral domain imaging of biological tissues. (A) Multi- and hyperspectral stacks of images. Comparison of the image stacks in MSI, in which several images are taken across various discrete wavelength regions, and HSI, in which images are taken over a larger continuous range of wavelengths. Courtesy of Edmund Optics. (B) Differentiating between different kinds of brain cells with fluorescence microscopy. A neuron is labeled for the neuron-only protein beta-tubulin III with green fluorescence, and surrounding astrocytes are labeled for the astrocyte-only protein GFAP with red fluorescence. This makes it easy to distinguish between different cells, as well as display cell morphology, size and spread. Courtesy of GerryShaw/Wikimedia Commons.*

together with multispectral and hyperspectral [21] imaging represent the major implementations of such approaches, but also spectral-domain OCT [53] can be considered an advanced optical imaging technology belonging to this framework.

As we mentioned in Section 3.1.4, fluorescence imaging is characterized by the probing of endogenous or exogenous fluorescent emission of tissue structures. A light source of a specific wavelength band is used to excite the fluorophore, and an imaging optics is adopted to register the signal corresponding to the emission wavelength.

Multispectral (MSI) and Hyperspectral (HSI) imaging devices are instead based on the acquisition of several wavelength bands into a 3-D stack where the spatial and spectral information is stored. The main difference between MSI and HSI lies on the spectral coverage provided by the camera sensors and by the imaging optics. In this sense, MSI is characterized by a sub-sampling of the light spectrum in the optical window, with preferential selection of certain bands that are representative of tissue chromophores such as oxy and deoxy-hemoglobin. Conversely, hyperspectral imaging devices are built on the acquisition of a finely sampled spectrum, that together with the spatial information constitutes an *hypercube* (see Section 3.3.2 for more details.).

The spectral analysis of tissues allows for functional imaging capabilities, thus enabling the quantification of tissue constituents in the form of blood perfusion indexes, water, lipids contents, to cite a few. A representative sketch of the spectral domain investigation of biological tissues is reported in Fig.3.11.

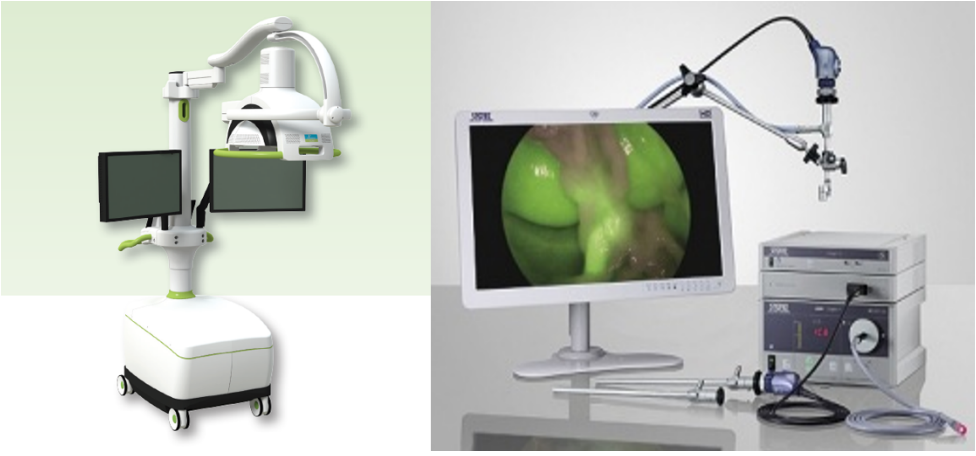

FIGURE 3.12: *Solaris^{TM} open-air fluorescence imaging system from PerkinElmer (PerkinElmer, Inc.) [54] and IMAGE1 S NIR/ICG fluorescence imaging system [55] from KARL STORZ (KARL STORZ Endoscopy-America, Inc.)*

3.3 Advanced Optical Imaging for Surgery: Implementations

In the following sections, we are going to discuss a few notable techniques that correspond to the previously described physical domains (CW, time and spatial domains) with a particular focus on time-resolved approaches and spatial frequency domain technologies. In addition, we are going to present for each of them a few state of the art examples of their application to surgical guidance and the respective medical fields in which they are employed.

3.3.1 Fluorescence Image-Guided Surgery

Fluorescence Image-Guided Surgery (FIGS) represents a vast portion of imaging technologies for the support of surgical guidance both as diagnostic and an intra-operative on-the-field monitoring tool. Overall, this field has seen a major development in the last decades thanks to the development of many imaging tools for not only open surgical guidance (Fig.3.12 (left)) but also laparoscopic minimally invasive surgery (Fig.3.12 (right)) opening to robotized-assisted treatments.

In general, these devices are characterized by common fundamental components, despite the availability of several implementations. The basic building-blocks for a FIGS device can be summarized into:

- Light source for the generation of the excitation field for the specific dye.
- Optical filters for the selection of the appropriate imaging band.
- Detection optics for high sensitivity imaging.

Evidently, many factors are responsible for the high quality imaging capabilities for FIGS systems. First of all, the light source should provide efficient illumination of the fluorescent dye to provide optimal excitation at the chromophore peak absorption wavelength and in order to fulfill this requirement, powerful and spectrally resolved sources are essential. Furthermore, the design of the filtration system needs to be optimized to allow the rejection of the excitation light on the imaging path, as well as reducing at a minimum the losses on the emission band. Finally, the specifications of the detection optics are essential to cope with background noise, low fluorescent signals and sensitivity: in

Contrast Agent	**Application**	**Excitation λ**	**Emission λ**	**FDA-Appr.**
Fluorescein	Angiography and opthalmology	464 nm	521 nm	✓
Methylene Blue (MB)	Generic	668 nm	688 nm	✓
Indocyanine Green (ICG)	Generic	780 nm	820 nm	✓
cGRD-ZW800-1	Pancreatic tumor tracking	770 nm	780 nm	
EpCAM-F800	Colorectal tumor tracking	773 nm	792 nm	

TABLE 3.1: *Contrast agents for fluorescence image-guided surgery [26],[56].*

this sense, high bit-depth monochrome cameras (> 12 bits) are typically preferred for the registration of fluorescent images.

In addition, it clearly goes without saying that a major role for the good outcome of fluorescence image-guided surgery is played by the fluorescent dye. More specifically, the spectral response of the fluorophore is not the only parameter that needs to be taken under consideration at the design stage: the targeting specificity of the fluorescent molecule is also extremely important in many applications, as well as the washout times, the delivery protocols and the quenching effects from other imaging modalities are worth investigating before the use on the field.

In this context, several natural and artificial markers are available nowadays for exogenous fluorescence image guided surgery. Clearly, the biotechnological development of the last decades has boosted consistently the production of fluorescent molecules capable of targeting specific markers and tissues for the detection or monitoring of the pathology of interest. In general, regulatory bodies are in charge of approving the use of such markers for clinical purposes, and the approval can be quite long depending on the technology involved. In our case, we just wish to give a quick overview of the most common exogenous fluorescent probes found in the clinical environment during either pre-clinical or clinical trials. Table 3.1 summarizes some FDA-approved fluorophores together with a few novel molecules that target specific structures in the human body.

Finally, we want to provide a few examples of state of the art FIGS devices already available in the operating rooms for clinical applications that range from angiography, flap surgery, lymph node mapping and biopsy, cardiac surgery etc. Specifically to open surgery: Solaris™ Open-Air Fluorescence Imaging System (PerkinElmer©, Inc.), Stryker© Spy-Elite™ (Stryker©), FLUOBEAM® (FLUOPTICS©) [57]. A few intra-operative examples are: IMAGE1 S NIR/ICG fluorescence imaging system (Karl Storz, Fig.3.12 (right)), PINPOINT™ Endoscopic Fluorescence Imaging System (Stryker©), Firefly™ (da Vinci©). Other devices such as the SPY Portable Handheld Imager (SPY-PHI) from Stryker© or the The QUEST SPECTRUM© from QUEST© can provide fluorescence imaging in both open and minimally invasive procedures.

3.3.2 Hyperspectral and Multispectral Imaging

Hyperspectral Imaging (HSI) and Multispectral Imaging (MSI) belong to the CW techniques together with CW fluorescence based systems, and it deserves a particular mention due to the increased interest that it is receiving from the medical imaging community [58]. HSI is an emerging imaging technique stemming from remote sensing, that finds numerous applications in different fields such as astronomy, industry, agriculture and most importantly for our discussion, medicine. The fundamental working principle is the combination of pure imaging and spectroscopy by additionally acquiring spectral information for each pixel of a 2-D sensor array, thus producing a 3-D dataset referred to as hypercube (see Fig.3.13 for a representation of the principle). In this sense, the spatial information is exploited to localize features on the imaged field, whereas the spectral

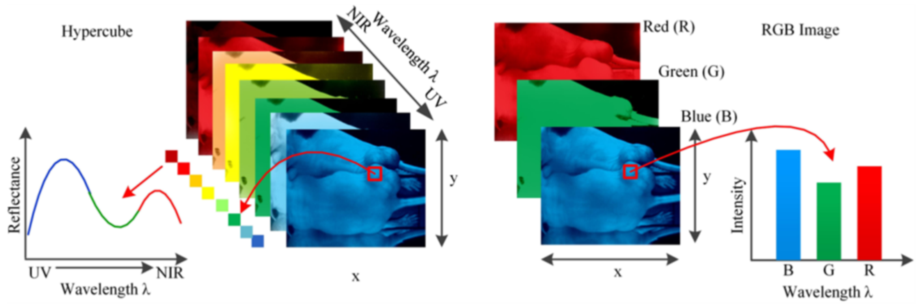

FIGURE 3.13: *Comparison of hypercube and standard RGB imaging acquisition.* [59]

component of each pixel is used to target the spectral response of the tissue for the quantification of specific biomarkers. Typically, the hypercube is constructed with hundreds of wavelengths bands in order to cover a large area of the spectrum within the therapeutic window. As a result, the main spectral parameters that define the imaging properties of a standard HSI device are:

- Spectral coverage: it represents the total wavelength range covered.
- Spectral resolution: it refers to the average FWHM of each wavelength band in the hypercube.

3.3.2.1 Instrumental set-up & acquisition workflow

Typically, a pushbroom HSI imaging system is characterized by three main stages: a broadband light source, some wavelength dispersion devices and an area detector. In a nutshell, the sample is illuminated by means of the light source and the resulting backreflected (or transmitted) light is let propagate through a front lens and a narrow line slit. Following a collimation stage, a dispersive device (i.e. grating, prism, filter wheel etc...) splits the light into several narrow bands for the spectral acquisition and an imaging lens is used to focus the light onto the detector (i.e. CCD and CMOS sensors or PMT are the most common). A schematics of the pushbroom acquisition design is shown in Fig.3.14. In general, depending of the acquisition mode, HSI systems can be distinguished into:

- **Spatial scanning**: hypercube acquisition by registering a full spectrum for each pixel of the image in the case of *whiskbroom* devices, or for a complete line of pixels in the case of *pushbroom* systems.
- **Spectral scanning**: hypercube acquisition by a single exposure of the full 2-D area detector followed by the acquisition of the spectral data for each wavelength band.
- **Fourier's Transform Infrared imaging** (FTIR): combination of Fourier's transform spectrometer with a Focal Plane Array (FPA) for the parallel acquisition of the spectra in each location of the detector. The system exploits the information contained in the interferometric optical path difference of each series of images to recover the hypercube by fast Fourier's transform.

Despite the different acquisition modalities, the data processing of a hypercube can be quite complex due to spectral correlation of adjacent bands and the variability of the hyperspectral signatures. For this reason, advanced classification algorithms are usually employed to extract the interesting spectral information from each dataset.

Normalization, image registration and filtering are the most common techniques in a processing HSI pipeline. The first one is required to convert the acquired raw signals into

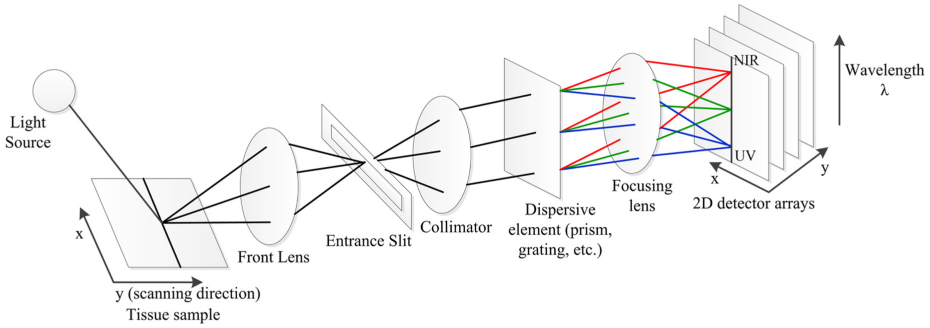

FIGURE 3.14: *Optical design of a pushbroom hyperspectral imaging system.* [59]

useful optical information such as reflectance or absorbance as follows:

$$I_{ref} = \frac{I_{raw} - I_{dark}}{I_{white} - I_{dark}} \tag{3.60}$$

$$I_{abs} = -\log \frac{I_{raw}}{I_{cal}} \tag{3.61}$$

Where we defined:

- I_{raw} as the raw radiance data;
- I_{dark} as the dark current data (more specifically to CCD detectors)
- I_{white} as the white reference intensity: this image is typically acquired using a standardized highly reflective surface such as a 99% *Spectralon*.
- I_{cal} as the calibration image, to account for the instrument response function.

In addition, image registration is fundamental to exploit the spectral information of the same imaged field at different spectral bands, to avoid spatial misalignment of the acquired stack. In this sense, it is worth mentioning that artificial intelligence has found in HSI an extremely fertile ground for several applications ranging from registration algorithms, image classification and features extraction [60].

3.3.2.2 *Applications to surgical guidance*

Hyperspectral imaging is nowadays employed in several medical applications either for diagnostics purposes or as a tool for image-guided surgery, thanks to the capability of delivering almost real-time imaging rates and quantitative information of useful parameters such as blood perfusion and methabolic consumption of tissues. A general overview of some applications and imaging devices is given in Table 3.2, where the main surgical fields are highlighted, together with the trial stage of each study reported in the references. Finally, we would like to present two examples of medically approved HSI imaging system that entered the medical imaging market with application to open surgical

Surgical Appl.	**Target**	**Subject (n)**	**Scanning**	**Acqu. Time**	**Spatial Res. (px)**	**Spectral Range**	**Ref.**
Cancer recognition	Brain tumor	Human (16)	Spatial	$\approx 1\ min$	1004×1787	$400 - 1000\ nm$	Fabelo et al.[61]
Colorectal surg.	Colonic perf.	Human (32)	Spatial	$-6\ s$	1004×1787	$400 - 1000\ nm$	Jansen-W et al.[62]
Reconstructive surg.	Flap perf.	Human (22)	Spatial	$-6\ s$	640×480	$500 - 1000\ nm$	Kohler et al.[63]
Urology	Renal perf.	Pig (7)	Spectral	$< 30\ s$	ND	$520 - 645\ nm$	Tracy et al.[64]
Neurosurgery	brain perf.	Human (4)	ND	$5 - 16\ s$	640×480	$400 - 800\ nm$	Mori et al.[65]

TABLE 3.2: *Summary of HSI applications for intra-operative guidance.* [66]

FIGURE 3.15: *Hyperspectral clinically compatible imaging devices TIVITA® Tissue (left) and TIVITA® Mini Endoscopy Edition (right), from Diaspective Vision©.*

guidance, and minimally invasive treatments (Fig.3.15): TIVITA® Tissue and TIVITA® Mini Endoscopy Edition, from *Diaspective Vision© [67]*.

The TIVITA® Tissue is the first medical approved HSI system that finds application in plastic surgery, dermatology, vascualar medicine and burn medicine among others, for the perfusion assessment of tissues. The main strength of the device is the capability to provide information on tissue saturation ($StO_2[\%]$), Tissue Hemoglobin Index (THI [index value]) or Organ Hemoglobin Index (OHI [index value]), NIR Perfusion Index (NIR [index value]) and Tissue Water Index (TWI [index value]) through a relatively fast acquisition ($\approx 6\ s$) of a $640 \times 480 \times 100$ ($px \times px \times \lambda$) hypercube.

Similarly, TIVITA® Mini Endoscopy Edition represents the intra-operative counterpart of the open air version previously described, and it targets the assessment of anastomoses and the precise determination of resection positions during minimally invasive treatments, with fields of application ranging from thoracic surgery, gynecology and surgical oncology, to cite a few. In addition to the physiological parameters provided by the TIVITA® Tissue, this system features also the quantification of Tissue Lipids Index (TLI [index value]). Finally, current research applications are analyzing the advantage of such device with respect the ICG imaging systems as proposed in [68].

3.3.3 Time-resolved Diffuse Optical Spectroscopy (TDOS)

3.3.3.1 Instrumental set-up & acquisition workflow

Time-resolved spectroscopic analysis of the optical properties of biological tissues in the NIR wavelength region can be performed with several implementations of three main components:

- Broadband picosecond-pulsed light source to cover the $600 - 1000\ nm$ spectral range.
- Optical elements to provide the illumination light to the sample and to harvest the diffused signal.

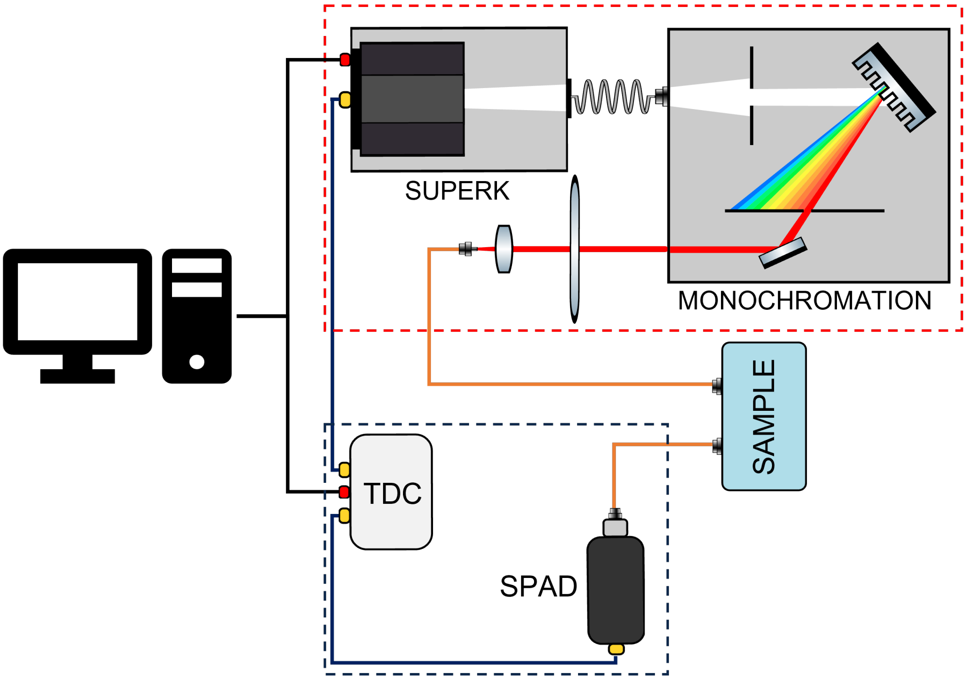

FIGURE 3.16: *Instrumental set-up for time-resolved diffuse optical spectroscopy of tissue.*

- Detection chain for *Time-Correlated Single Photon Counting* (TCSPC) to retrieve the waveform of extremely faint optical signals arising from the sample (either in reflectance or in transmittance geometry).

More specifically to our work (see Section 5.2.1 for more details), as shown in Fig.3.16, the instrumental set-up can be based on a pulsed (< 10 ps) supercontinuum laser source (SuperK Extreme, NKT Photonics© A/S, Denmark) fiber coupled into a tunable single line filter (SuperK VARIA, NKT Photonics© A/S, Denmark). At the output of this device, a cascade of neutral density filters is utilized to tune the power of the optical signal to be provided to the sample and finally the delivery of the optical pulses is obtained in the form of a point-like illumination through propagation in a multi-mode step-index optical fiber ($\varnothing_C = 1000\ \mu m$, $NA = 0.39$). The detection chain consists of a large core multimode step-index optical fiber ($\varnothing_C = 1000\ \mu m$, $NA = 0.39$) for maximizing the point-wise harvesting of the diffused light. The resulting signal is then delivered to a Single-Photon Avalanche Diode (ID100-MMF50, ID Quantique© SA, Switzerland). Subsequently, the detector is connected to a Time-to-Digital Converter (HRMTimeR, SensL© Technologies Ltd., USA) in order to acquire the time-resolved reflectance (or transmittance) curves by means of a standard TCSPC technique.

3.3.3.1.1 Detection chain and TCSPC general framework

The spectral measurements are performed by acquiring the waveform of weak and fast optical pulses. In order to achieve that, the detection chain is composed by essentially two devices: a single photon detector and a TCSPC board. In Fig.3.16 the detection path is underlined by blue wirings between the components involved, and we can appreciate that also the laser system is involved in the chain, as clarified in the following.

The *Time-Correlated Single Photon Counting* technique can be efficiently employed for the measurement of faint time-resolved optical signals by reconstructing of the light

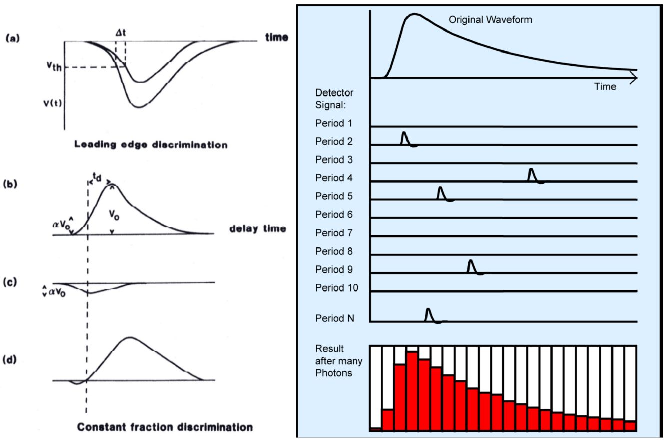

FIGURE 3.17: *Scheme representing the routine performed by the CFD and MCA to reconstruct the time shaped curve. [69]*

waveform that corresponds to the photon trajectories inside the medium as a distribution of the delays between the start and stop signals generated by the detection and illumination systems, respectively. As a consequence, the probability that more than one photon per pulse can reach the detector has to be consistently minimized, and multiple measurements have to be carried out in order to get the final t-PSF.

In its standard configuration[6] (and for sake of generalization), the essential devices that constitute a TCSPC acquisition system are:

- *Constant Fraction Discriminator* (CFD), together with the amplification and delay chain associated to it.
- *Time to Amplitude Converter* (TAC).
- *Multichannel Analyser* (MCA).

For a start, the laser source emits the train of pulses that is driven to the sample. At the same time, the firing signal for the pulses, which is usually referred to as *"Sync" signal*, is transmitted to the CFD, where it is attenuated by a factor α. Similarly, the optical pulse harvested from the sample is converted into a voltage signal (the *"CFD" signal*) in the photo-detector and passed to the CFD unit where it is amplified, inverted and finally delayed by a time value t_d[7].

Afterwards, the two obtained signals are summed up to achieve a curve with a *zero-crossing* point which is going to be used to quantify the delay between the acquired photons. Moreover, the CFD is characterized by a threshold regulator which can be adjusted to set the amplitude of the pulses that need to be disregarded during the acquisition. The second step is the conversion of the time of arrival of the light signal into a voltage amplitude by the TAC. To complete this task, the triggering signal from the laser is used as a stopwatch for the converter, whereas the detection of a single photon, that generates the "CFD" signal, is employed as a start trigger for the time conversion. Therefore, the delay between these two events is quantified as the actual arrival time of the photon on the photon multiplier, and then converted into a voltage signal whose amplitude is proportional to the value of the time delay.

---

[6] It is worth highlighting that in our set-up the functions of the CFD, TAC and MCA are performed by the time-to-digital converter (TDC). The most general description we proposed is to provide a more detailed analysis of the acquisition process.

[7] The optimal working point of the CFD system is achieved when operating with a signal with a steep rising edge (< 1 ns) and a falling edge relatively slow (~ 10 ns).

FIGURE 3.18: *NIRSbox from PIONIRS© s.r.l. [71]*

Finally, the output signal of the TAC is transferred to the MCA. This device is dedicated to the discretization of the voltage values originated from the TAC into a predefined number of channels. By acquiring a statistically relevant number of measurements, the photon counts are stored into different channels depending on the time of arrival, following a specific probability distribution. The final result of the MCA process is a histogram of the photon counts which can be converted into a time shaped waveform of the pulses. The routine followed by the CFD and MCA is represented in Fig.3.17.

Though extremely efficient, the TCSPC technique still suffers from two main sources of noise which can degrade the performances: the first source originates from the dark counts of the detector (DCR), which gives rise to a random background noise. Such noise can limit the sensitivity of the system but the mean value of the dark counts can be calculated and easily removed in post-processing. Instead, the second source of noise is associated to the statistical arrival time of photons, which follows a *Poisson's* distribution. Indeed, the histogram generation is a time consuming process and within this time interval, other photons can be detected but cannot be stored as relevant signal due to the latency of the chain. The associated loss of information on the pulse waveform is referred to as *"pile-up"* and it can determine a miss-shaped waveform at longer delays [70][8].

3.3.3.2 State of the art: PIONIRS©

A notable example of state of the art diffuse optical instrument based on time-resolved diffuse optical spectroscopy is produced by PIONIRS©, a spin-off company of Politecnico di Milano, based in Milan (Italy). The company focuses on delivering compact and user-friendly near-infreared spectroscopic devices for tissue optical characterization, by exploiting the high-level and long-term experience of the interdisciplinary team in diffuse optics, single photon counting and electronics. The core business revolves around the first product *"NIRSbox"* (Fig.3.18), that was launched in 2020 with the aim of providing a portable, "plug-and-play" solution for the investigation of tissue oxygenation with application ranging from real-time, non invasive brain measurements to effective muscle oxygenation monitoring [72].

More specifically, the device encloses two pulsed diode laser sources for the illumination of the sample at 670 nm and 830 nm, which are coupled into a multimode graded-index glass optical fiber bundle with a single output. The light harvesting is performed at 30 mm from the injection point with a $\varnothing_C = 0.9\ mm$ graded-index glass fiber to maximize the light detection. Both injection and detection fibers are placed on the tissue via a 3-D printed probe and a 90° prism at each side to deliver light perpendicularly to the surface by maintaining the fibers parallel to it. The detection chain is based on a SiPM detector and a custom made timing electronic for the TCSPC stage. Finally, the system

---

[8] A good rule of thumb to minimize this effect, is to keep the ratio between the number of detected photons and the total number of cycles below 5%.

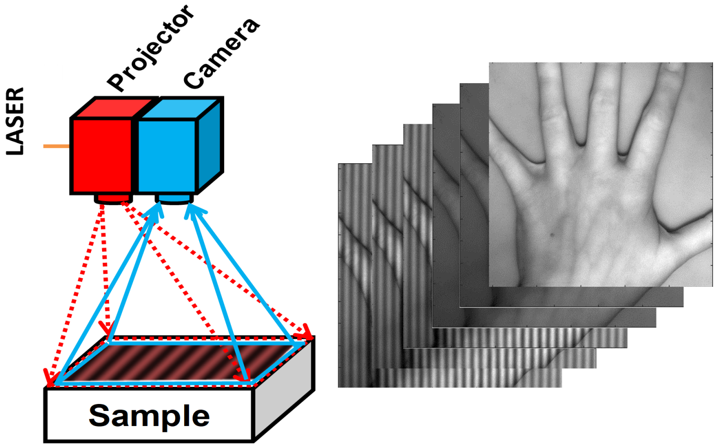

FIGURE 3.19: *Simplified sketch of a typical SFDI set-up, and corresponding two frequencies, three phases acquisition dataset.*

is operated via a Li-ion battery to allow for portability of the box and an embedded PC is used to interface and control the unit (even remotely via WiFi or Bluetooth) [72]. It is worth mentioning that the system has real-time capability for the tissue characterization and oxygenation.

3.3.4 Spatial Frequency Domain Imaging (SFDI)

3.3.4.1 Instrumental set-up & acquisition workflow

A typical instrumental set-up for a modulated imaging application is characterized by three main components (as shown in Fig.3.19)[73]:

1. Light source.
2. Spatial modulation system.
3. Detection optics.

Specifically to our case (see Section 5.2.1 for more details), the light source of choice is a multiple wavelength custom-made laser module based on high power ($3 - 6\ W$) laser diodes, fiber coupled to large core ($300 - 1000\ \mu m$) multimode glass optical fibers. In addition, the spatial modulation system is determined by a Digital-Micromirror-Device (DMD) high-speed projector (High-Speed V-7000, Vialux® GmbH, Germany) that allows us to generate sinusoidal patterns of light over a large field of view ($> 15 \times 15\ cm^2$) at a working distance of 45 cm. Furthermore, the detection optics is implemented with a 16-bit, high frame-rate, 5.5 MPixels sCMOS camera (PCO.edge 5.5, Excelitas® PCO GmbH, Germany), for the acquisition of the spatially modulated images of the sample. Finally, a pair of linear polarizers (PPL05C, Moxtek Inc., USA) in cross configuration on the illumination and imaging sides complete the imaging system: these are required to reject the specular component of the backreflected light.

Concerning the acquisition workflow, let us assume to project on the sample a 2-D sinusoidally modulated pattern of light characterized by a spatial frequency f_x. This source term can be written as [45]:

$$Q = \frac{Q}{2}\left[1 + \cos(2\pi f_x x + \varphi)\right] \tag{3.62}$$

Therefore, the acquired reflected intensity can be decomposed into a DC and an AC contribution, such as:

$$I = I_{DC} + I_{AC} \tag{3.63}$$

Where the AC component is of the form:

$$I_{AC} = M_{AC}(f_x, x)\cos(2\pi f_x x + \varphi) \tag{3.64}$$

The modulation amplitude $M_{AC}(f_x, x)$ represents the envelope of the photon density wave, and it can usually be extrapolated by means of a phase-shift demodulation algorithm that requires the projection of multiple phase-shifted patterns of light with the same spatial frequency f_x. In its simplest form, the workflow is characterized by the acquisition of three[9] 2-D sinusoids with $\varphi = 0, (2/3)\pi, (4/3)\pi$ followed by the extraction of the modulation amplitude with the following formula:

$$M_{AC}(f_x, x) = \frac{\sqrt{2}}{3}\left[(I_1 - I_2)^2 + (I_1 - I_3)^2 + (I_2 - I_3)^2\right]^{\frac{1}{2}} \tag{3.65}$$

Where we noted $I_i = I_i(f_x, x) = M_{AC}(f_x, x)\cos(2\pi f_x x + \varphi_i)$, $\varphi_i = 0, (2/3)\pi, (4/3)\pi$. Similarly, the DC component of the acquired intensity can be determined by:

$$M_{DC}(f_x = 0, x) = \frac{1}{3}\left[I_1(x) + I_2(x) + I_3(x)\right] \tag{3.66}$$

The next step in the processing pipeline is the computation of the diffuse reflectance of the sample, and the relationship between R_d and the modulation amplitude M can be described by introducing the modulation transfer function of the imaging system MTF_{sys} (which takes into account the effect of the response of the instrumentation) and the average intensity of the source I_0, thus resulting:

$$M_{AC}(f_x, x) = I_0 MTF_{sys}(f_x, x) R_d(f_x, x) \tag{3.67}$$

As it is evident for Eq.(3.67), a calibration step can be introduced to separate the contribution of the sample to the acquired modulation amplitude, from that of the imaging system. In this sense, by projecting the same patterns on a calibration sample of known optical properties, it is possible to obtain R_{DC} and R_{AC} for the investigated sample by simply applying the following:

$$R_d(f_x, x) = \frac{M(f_x, x)}{M^{cal}(f_x, x)} R_d^{cal}(f_x, x) \tag{3.68}$$

Clearly, given the simple referencing-based approach for the calculation of the diffuse reflectance, it is fundamental to ensure that potential sources of error such as height calibration differences and angle projection effects are numerically compensated for with surface profile correction algorithms. This is particularly important for in-vivo imaging, where the calibration plane can be different depending on the position of the surgical field with respect to the imaging system. Nevertheless, many correction algorithms can be applied as described in [75]. In a nutshell, two main sources of error related to the surface profile of the sample can be addressed: height mismatch with respect to the calibration plane, and light reflection from high angles on the surface of the sample due to its non flatness. The former, is typically corrected by calibrating the system for several

---

[9] To be exhaustive, a more accurate phase-shifting demodulation algorithm can be implemented with the projection of 7 phases instead of 3 (i.e. $\varphi = 0, \frac{\pi}{2}, \pi, \frac{3}{2}\pi, 2\pi, \frac{5}{2}\pi, 3\pi$) [74]. This method is usually preferred in order to avoid phase uncertainty on the projected patterns.

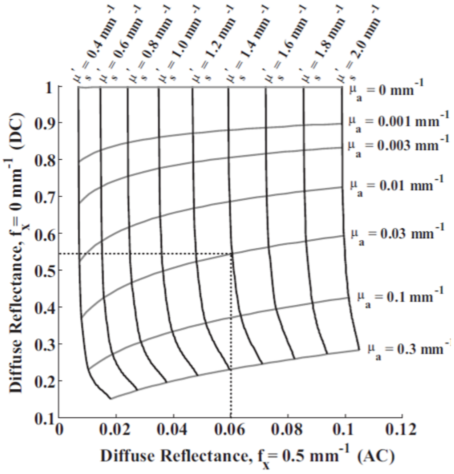

FIGURE 3.20: *2-D Look Up Table for fast extraction of absorption and reduced scattering coefficients with spatial frequency domain imaging. [45]*

height planes in a range that covers the standard operating working distances. In this way, a direct height-phase and height-intensity relationship can be extrapolated for each pixel of the image. The latter instead, is targeted by Lambertian-based projection models in order to reconstruct the angle maps of the reflected light arising from the sample. In both cases, a corrected value of the calibration modulation amplitude is computed and replaced in Eq.(3.68).

Finally, the acquisition workflow is completed by recovering the absorption and reduced scattering coefficient maps. Typically, for speed purposes, a 2-D LUT approach is implemented to solve the inverse problem, by pre-computing the diffuse reflectance values associated to each pair of μ_a and $\mu_s^{'}$ at two spatial frequencies: one low spatial frequency, i.e. $f_x = 0\ mm^{-1}$, and one high spatial frequency, i.e. $f_x = 0.2\ mm^{-1}$. In this way, provided that the chosen frequencies are well separated, so that to exploit the different sensitivity of the diffuse reflectance to absorption and scattering, it is possible to quickly extract from the LUT by triangulating and interpolating the values of μ_a and $\mu_s^{'}$ corresponding to the measured $R_d(f_{x_1}), R_d(f_{x_2})$ for each pixel in the image. An example of a 2-D Look Up Table for fast extraction of the optical properties is shown in Fig.3.20.

3.3.4.2 *State of the art: MODULIM®*

MODULIM© is the world leader for spatial frequency domain imaging systems that find applications in healthcare, agriculture and industry. The company found its position in the market in the 2010s when a first diffuse reflectance-based imager (*Reflect RS®*) was launched as a result of a clinical translation research project, with the aim of providing quantitative imaging capabilities of optical properties of diffusive media, as well as physiological parameters *in-vivo*. As of today, the company portfolio is focused around one main imaging system (in Fig.3.21): *Clarifi®* is a clinically compatible device that provides a non-contact, non-invasive assessment of tissue microvasculature by means of SFDI. More specifically, by quantifying specific hemoglobin biomarkers over a large field of view, the system enables the fast mapping of oxygenation and tissue perfusion for the identification of focal pre-ulcer and systemic circulatory issues, support care pathway decisions and follow-up frequency monitoring, and assess the responsiveness to therapeutic interventions with real-time guidance.

FIGURE 3.21: *Clarifi® by MODULIM© Inc. (left) and identification of systemic circulatory issues (right). [76]*

Overall, the main clinical applications of MODULIM technologies can be summarized into:

- **Diabetic Food Ulcers (DFU)** and **Peripheral Arterial Diseases (PAD)** in diabetes patients. In this context, studies show how SFDI can provide a unique signature of compromised peripheral circulation [77], the ability of the technology to differentiate the etiology (neuropathic vs. neuro-ischemic) of DFUs [78] and assessment capability of SFDI for stratifying the severity of microvascular disease in a completely non-invasive way [79].
- **Pressure ulcers monitoring**: SFDI is used to screen the circulation changes that are considered a precursor of ulcers or to track the changes of an already existing pathology and the effects of an on-going therapy [80].
- **Perfusion monitoring in reconstructive flaps surgery**: as a contrast-free technique, SFDI provides blood perfusion maps of the resected and reconstructed tissue during surgical intervention following mastectomies or tissue transfer flaps routines [81].
- **Burn wounds assessment**: the quantitative measurement of tissue optical properties allows clinicians to improve the evaluation of burn depth [82] without relying solely on visual inspection of either wound coloring, tissue necrosis or the burn surface area.

3.3.5 Single Snapshot imaging of Optical Properties (SSOP)

The main drawbacks of SFDI as a quantitative optical properties imaging technique can be summarized into:

1. Multiple frames are required to perform the extraction of the modulation amplitude of the optical signal arising from the sample. In one of the most standard configurations, $N = 6$ frames are registered (three frames per spatial frequency), thus setting a minimum acquisition time limit that can prevent the real-time performance of the imaging system.

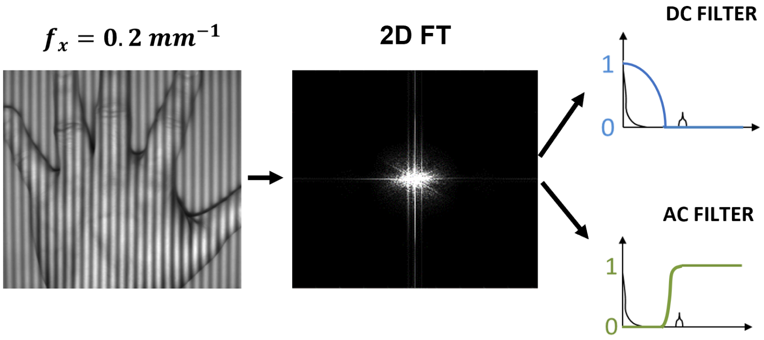

FIGURE 3.22: *Standard approach for the extraction of the modulated amplitude from an SSOP frame by means of a 2-D Fourier's transform filtering algorithm.*

2. The optical properties extraction can be time consuming even in the optimized case of a two frequency-based acquisition workflow. In fact, despite pre-computing the LUTs, the interpolation algorithms for the computation of μ_a and $\mu_s^{'}$ could be relatively slow.

To overcome the latter limitations associated to the inverse problem solution, linearly diffuse reflectance LUTs have been proposed as described in [83]. In this case, the main difference with respect to a standard optical properties LUT lies in the implementation of a linear sampling of R_d for each spatial frequency axis, rather than generating a linear space of μ_a and $\mu_s^{'}$ pairs. The main advantage being that the measured R_d can easily be found in the LUT by simple rounding in the 2-D space instead of interpolating, thus speeding up the extraction process by up to 100 folds [83].

Concerning the former limitation associated to the multiple frames constraint, another method has been proposed to reduce at a minimum the number of images required for the extraction of the s-MTF. This imaging technique is referred to as "*Single Snapshot imaging of Optical Properties*" (SSOP) and it is based on a Fourier's transform filtering approach that allows us to compute the modulation amplitude in the DC and AC components for the acquired signal from a single frame.

3.3.5.1 Principles of SSOP

SSOP is a spatial frequency domain imaging technique that has been developed to target the real-time quantitation of the optical properties of biological tissues over a large field of view. Implemented as a derivation of standard SFDI, this technique overcomes the time-consuming limitations associated to the need for multiple phase-shifted patterns for the extraction of the sample spatial modulation transfer function by requiring a single high frequency (i.e. $f_x = 0.2\ mm^{-1}$) pattern of light projected on the field. After the acquisition of the frame, a filtering algorithm is used on the Fourier's transform of the signal to extract M_{DC} and M_{AC}, as shown in Fig.3.22. It is worth noticing that for high quality computation of the modulation amplitudes, optimized filtering windows have been designed [84], thus reducing image artifacts and improving the overall rendering quality of the computed s-MTFs. Following the filtration step, the processing workflow for the computation of the sample optical properties is equivalent to the one of SFDI (see Section 3.3.4.1).

As previously mentioned, for correct quantification of tissue optical properties it is typically necessary to perform profile correction algorithms. In this sense, SSOP carries a powerful advantage with respect to SFDI thanks to the possibility to access not only the magnitude component of the Fourier's spectrum of the signal, but also the phase information. Indeed, by selecting a specific filtering window it is possible to extract the real and imaginary component of the phase that can further be utilized to determine the height-dependent correction factors for the calibration.

Therefore, from a single acquired frame with SSOP we are able to determine the full set of parameters required for a real-time profile corrected optical properties imaging of tissues. A great effort has been dedicated to developing optimal filtering windows at first [84], and subsequently to the introduction of Convolutional Neural Networks (CNNs) for the improvement of the demodulation step [85].

3.3.5.2 Deep Learning for SSOP

The first real-time deep learning optimized SSOP implementation based on a GPU enhanced processing workflow has been presented in 2020 by Aguénounon et al.[85]. Differently from the previously proposed approaches, in this work, the main goal is to develop an alternative to the Fourier's based processing typical of standard SSOP in the form of a Deep Neural Network approach and more specifically in the framework of Convolutional Neural Networks. Indeed as of 2020, in the literature it was possible to find applications of machine learning algorithms for SFDI in three main branches:

- Random Forest approaches for the mapping of tissue optical properties (i.e. absorption and reduced scattering coefficient) in the spatial frequency domain, stemming from the training on Monte Carlo simulations [86]. This first architecture was proven to sensibly speed-up the computation time for the optical properties reconstruction with respect to the standard inversion methods based on dense LUT (e.g. 450 *ms* for a 1 Mpixel image).
- DNN based on a Multi-Layered Perceptron (MLP) for the prediction of OP following a multiple spatial frequency fitting approach with the capability of boosting the inverse problem solving time up to 200 *ms* for 696 × 520 pixels image [87]. In this case, the main advantage determined by the DNN architecture was not only in terms of computational time but also in regards to the improved accuracy coming from the exploitation of a 5 spatial frequencies algorithm instead of the most commonly reduced framework based on solely 2 spatial frequencies.
- Generative Adversarial Networks (GAN) were proposed by [88] with the goal of taking advantage of the latest developments on CNN architectures and their implementation on GPU powered working stations. A "*Generative Adversarial Network Prediction of Optical Properties*" (GANPOP) [89] design was proven to outperform the state of the art in terms of speed (i.e. 40 *ms* for a 256 × 256 pixels image with a NVIDIA Tesla a P100 GPU Accelerator) and accuracy by directly predicting tissue optical properties starting from a single SSOP input image.

Proposed as a further development of the "GANPOP" approach, the work from Aguénounon et al.[85] focuses on implementing the CNN architecture for the extraction of the modulation amplitudes (i.e. M_{DC} and M_{AC}) from a single high frequency projected pattern, rather then addressing directly μ_a and $\mu_s^{'}$. More specifically, providing 3-D profile corrected SSOP processing, two identical newtworks are designed: the former is dedicated to the computation of M_{DC} and M_{AC}; the latter is devoted instead to the extraction of the real and imaginary part of the the signal for profilometry purposes. In both cases, the architecture of the newtork is shown in Fig.3.23. It is worth mentioning that the power of this implementation lies on the choice of reducing at a minimum the learning parameters ($< 2 \times 10^4$) together with a custom implementation of a GPGPU computing suite: these features allows us to obtain a computation time for the demodulation step

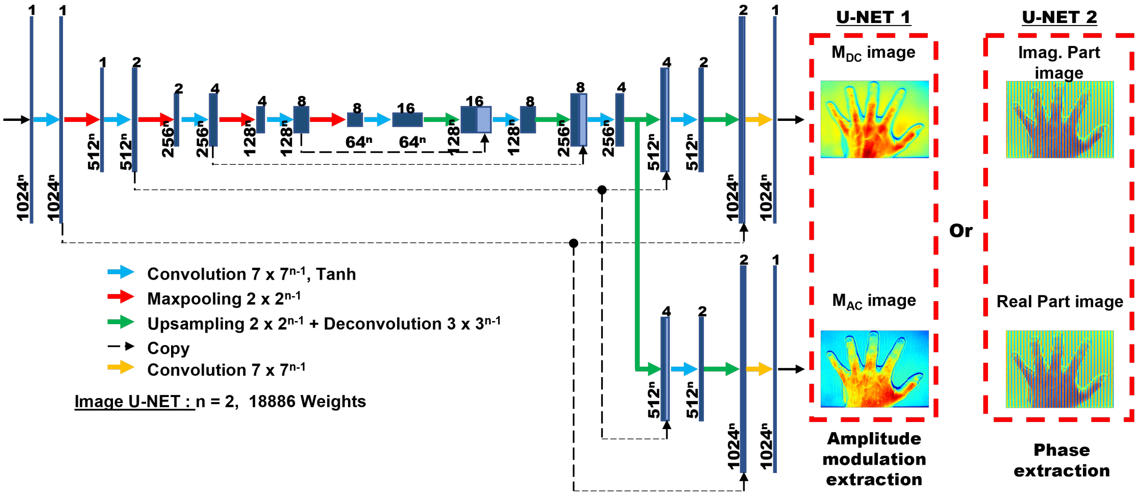

FIGURE 3.23: *U-Net architecture for deep-learning-optimized SSOP. [85]*

of < 10 ms for each network, thus enabling real-time optical properties imaging. As described in [85] in Table 7.3, the total computation time for a 1024×1024 pixels SSOP image for the optical properties extraction results to be ~ 20 ms (i.e. ~ 19 ns per pixel) for the given workstation.

3.4 Conclusions

In this chapter we described the fundamental principles of advanced optical imaging, by firstly giving a brief insight on the physical modeling of light-tissue interactions with a specific focus on diffusion approaches and Monte Carlo stochastic models. In addition, we analyzed the framework of structural and functional imaging, based on the spectroscopic characterization of the optical properties of biological tissues in the therapeutic window. Furthermore, we proposed an overview of different diffuse optical methods, as well as fluorescence and hyperspectral imaging techniques. We concluded the discussion with a few applications of the cited technologies towards the surgical guidance, with particular interest on Spatial Frequency Domain Imaging and Single Snapshot Imaging of Optical Properties as the strongest candidates for providing a quantitative tool for image guided surgery. Time Domain approaches were also introduced as a powerful technique to accurately quantify tissue absorption and reduced scattering.

Chapter 4

MOTIVATIONS AND OBJECTIVES

The chapter is dedicated to the introduction of the scientific challenges addressed in the manuscript and the proposed approaches.

4.1 Motivations

Advanced optical imaging techniques have reached an impressive interest for surgical guidance applications and as a result the literature shows an extensive amount of progress in the development of such technologies [90]. In particular, spatial frequency domain imaging systems have found their way to the operating rooms in several derivations, as we explained in the previous Chapter 3 (see Section 3.3.4.1) thanks to their capability to provide in real-time (more specifically for SSOP) accurate and useful information to the physicians either for pre and post-operatorial screening or intra-operatively. A slightly different perspective can be proposed for time domain diffuse optics techniques: in this case, the real-time capability is certainly not the main advantage, considering that the typical acquisition times are bounded by limitations on the time-correlated single photon counting statistics. In addition, there is a wide majority of systems that exploit processing algorithms for the recovering of the optical properties that are based on curve fitting of the analytical solutions of the diffusion equation (see Section 3.1.2.1). Therefore, the computation times required remains a limiting factor. Nevertheless, even in this field we are seeing a transition to Monte Carlo simulations and pre-computed LUTs that enables the fast computation of the inverse problem for the quantification of absorption and reduced scattering, as proposed in [72].

Though extremely important for the surgical application, real-time capabilities of time-resolved techniques are not strictly the main scientific challenge that we decided to face in our work. In fact, there is a more fundamental problem that we focused targeting which is related to both SFDI and TDOS: the accuracy in the quantification of tissue optical properties needs validation on many levels and one of the most important is the cross-validation between techniques based on different domains. The agreement between technologies with alternative operating principles has always represented a great challenge for the community, and a major effort is required in this direction for achieving some sort of instrument standardization to ensure the accuracy (and not only) of the measurements performed.

A second main challenge that we tackled concerns the adaptation of spatial frequency domain imaging approaches to minimally invasive surgical tools. Indeed, despite the growth of SFDI and SSOP in the recent years, and their application to medical imaging (mostly for SFDI) and the specific improvements in imaging capabilities especially for the case of SSOP, there is still a need to perform the clinical translation of an SSOP-based imaging device for minimally invasive care with the additional compatibility with robotized-assisted surgery.

4.2 Objectives of the Work

4.2.1 Cross-referencing approaches for diffuse optical spectroscopy of tissues

As we briefly discussed in the previous Section 4.1, the quantification of tissue optical properties is a powerful tool that still suffers from a general lack of cross-platform validation. In this sense, the first objective of our work is the development a multi-modal referencing platform for diffuse optical spectroscopy in the VIS-NIR regime, for the characterization of tissue optical properties.

More specifically, we combined a time-domain diffuse optical spectroscopy system and a spatial frequency domain imaging apparatus into a single measurement platform (as shown in Fig.4.1), in order to evaluate and validate the agreement in the quantification of absorption and reduced scattering coefficients in turbid media. The first version of the

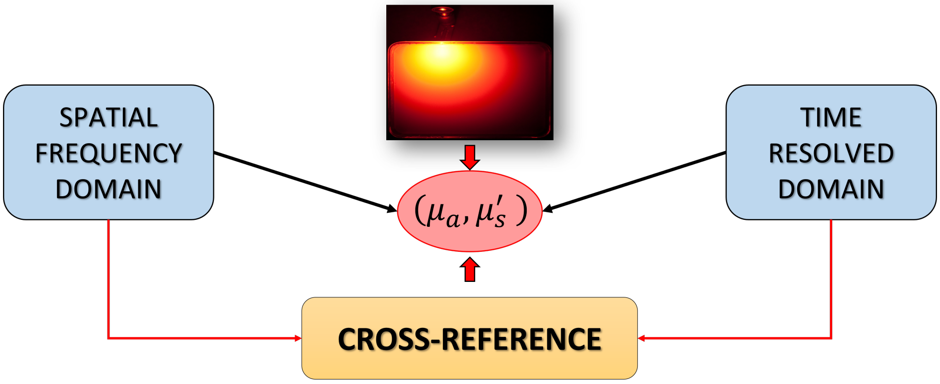

FIGURE 4.1: *Simplified representation of the fundamental idea behind the multi-modal referencing platform, combining SFDI and TDOS.*

platform was validated on tissue-mimicking phantoms by performing two largely recognized protocols (MEDPHOT [91] and BIP [92]) for the performance assessment of diffuse optics instruments, owing to a collaboration with several European research teams united under the Horizon 2020 project BITMAP ("*Brain Injury and Trauma Monitoring using Advanced Photonics*"). The results of this work is presented in Chapter 5, where we describe the design and validation of the multi-modal platform, and in Chapter 6 where a the outcomes of the BITMAP exercise are reported.

4.2.2 SSOP-based endsoscopic imaging system

A first example of endoscopic optical properties imaging based on SSOP was proposed by Angelo et al.[93]. In this case, a dual channel rigid endoscope was used to perform SSOP with real-time capabilities. However, as it is evident from Fig.4.2 one of the main remaining challenges of the device was represented by the poor image quality of the reconstructed absorption and reduced scattering maps. In this context, we designed a SSOP-based endoscopic imaging system that exploits the latest improvements in SSOP thanks to the use of Convolutional Neural Network architectures [85] for the extraction of the modulation amplitudes and the phase information of the acquired SSOP image. The system was validated on tissue-mimicking phantoms, as well as on *in-vivo* biological samples for a qualitative image capability characterization together with a quantitative assessment of tissue optical properties mapping. Being real-time compatible, we started the adaptation of the system to a pre-clinical implementation by designing a hand-held version of the device that is also compatible with a surgical robot. The content of this part of the project is analyzed in Chapter 7, which is dedicated to the presentation of the instrument design and its different validation steps.

4.2.3 Preclinical validation of SSOP

A validation of real-time, 3-D profile-corrected SSOP was also carried out through preclinical trials on swine models. The objective of this work was to address the performance of the Deep-Learning-enhanced technique in terms of both image quality and quantification accuracy within a surgical environment. For this purpose, pre-clinical trials were conducted to assess the capability of the system to monitor tissue perfusion in real-time, by performing ischemic protocols on different organs. In Chapter 8 we report the results of a first protocol on tissue oxygenation measurements during esophageal surgery, where we analyzed the correlation between blood saturation and capillary lactates for

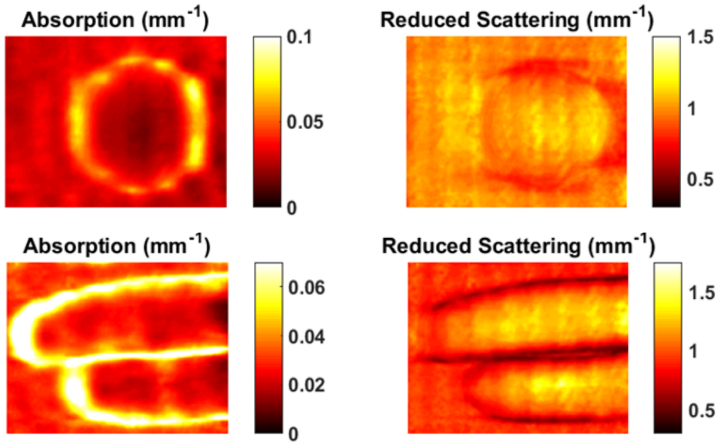

FIGURE 4.2: *Absorption and reduced scattering maps of a tissue mimicking phantom (top) and of a human hand (bottom) by means of SSOP-based endoscopic imaging.* [93]

the characterization of SSOP accuracy. Similarly, as described in Chapter 9, we performed on a small bowel section a total ischemia model for the same goal, as well as an ischemia/reperfusion protocol for the real-time monitoring of tissue perfusion. These studies, were conducted by exploiting a novel, clinically compatible imaging system developed by our team.

4.3 Conclusions

In this Chapter we introduced the main scientific issues that we addressed during in the work, starting from the more fundamental limit of cross-validation approaches for the accuracy assessment of diffuse optical spectroscopic instruments, and concluding with a more engineering-based challenge for the development of a surgical-robot-compatible endoscopic imaging device based on SSOP. In the next chapters we are presenting the work conducted for each of the objectives here presented together with the resulting scientific contributions.

Chapter 5

MULTI-MODAL REFERENCING PLATFORM FOR DOS INSTRUMENTS

The quantification accuracy of tissue optical properties is an open challenge despite the evident growth of diffuse optics-based techniques. In our work, we address this scientific issue by proposing a multi-modal referencing platform for diffuse optical instruments based on the combination of a Spatial Frequency Domain Imaging (SFDI) system and a Time-resolved Diffuse Optical Spectroscopic (TDOS) set-up. In this sense, we aim at providing a cross-referencing approach for the accuracy assessment of the optical characterization of biological tissues.

5.1 Introduction

The performance assessment of diffuse optical imaging systems often requires a benchtop analysis of the instrumentation capabilities. While many diffuse optical techniques are available to characterize the optical properties of biological tissues, a gold standard has not been proposed yet for referencing the results of these different technologies. In this sense, a crucial step for the validation of the developed instrumentation can be represented by the combination of multiple diffuse optical techniques in order to cross-reference the results obtained with the different configurations. In this context, we implemented and validated a multi-modal referencing platform for diffuse optical spectroscopic instruments, consisting of a benchtop Time-resolved Diffuse Optical Spectroscopic (TDOS) system, together with a second set-up based on Spatial Frequency Domain Imaging (SFDI).

In order to understand the context of this work, it is worth mentioning that several collaborations were carried out in the recent years between research institutions with the aim of achieving consolidated protocols to assess the main performance characteristics of diffuse optics systems for biomedical applications. In particular, a great effort was dedicated to derive standardized tests to determine measurable figures of merit capable of summarizing the most essential parameters of each developed technology, regardless from their implemented configuration and with the scope of being relatively flexible to different measuring domains as well. This was the case of the development of the MEDPHOT protocol [91], designed with the goal of assessing the accuracy, stability and reproducibility of near-infrared spectroscopic diffuse optical systems: the strength of this protocol is determined by the use of a single tissue mimicking phantom kit that can be circulated among different users to guarantee a consistent measuring set-up, by providing guidelines on specific tests to perform on the same phantoms. This protocol resulted into a valid measurement routine extendable to different instrumental set-ups and domains, even though it was originally designed for time-resolved imaging systems. In this direction, and more specifically to time domain optical systems once again, a second protocol was validated to address the instrumental characteristics converging into the Basic Instrumental Performance (BIP) protocol [94].

Nevertheless, the accuracy in recovering tissue optical properties remains a relevant challenge and despite the mentioned standardization efforts, the validation of diffuse optical spectroscopic systems is still a difficult process that requires a deep understanding of the possibility to compare the results from different systems. In fact, even in the case of SFDI, one main source of error [1] in the quantification of optical properties derives from the need for a calibration step for the computation of the instrument response as described in Section 3.3.4.1. Therefore, the accuracy of the retrieved μ_a and $\mu_s^{'}$ of the investigated tissues relies on the accuracy of the characterization of the optical properties of the calibration phantom itself. Typically, such parameters are referenced with a calibration-free technique, such as time domain diffuse optical spectroscopy or frequency domain based systems. As a result, it is fundamental to ensure the correspondence between different techniques in the quantification of μ_a and $\mu_s^{'}$.

In addition, it is worth mentioning that other sources of errors can be identified for the different techniques adopted for tissue detection [95],[96]: a major contribution arises from the modeling framework of light propagation in turbid media, which can either be based on a diffusion approximation approach or on a Monte Carlo statistics [1], as well as the use of homogeneous models or heterogeneous and multi-layer simulations; the accuracy can also be affected by the instrument implementation and the imaging configuration (i.e. height calibration effects and angle-dependent illumination issue); finally the depth sensitivity of the different technologies can determine a mismatch in the retrieved optical properties if not taken into consideration in the propagation models.

In this context, the aim of our multi-modal platform is to exploit a cross-referencing approach for the characterization of the optical properties of biological tissues, with the ultimate objective of establishing a ground truth compatible with both technologies. For this reason, we adopted tissue mimicking phantoms for the validation of the instrument and we also performed some of the protocols mentioned above, owing to a collaboration with the physics department of the Politecnico di Milano (Italy) as main contributor, together with the involvement in an European initiative (*"Brain Injury and Trauma Monitoring using Advanced Photonics"*, BITMAP) devoted to establishing protocols and assessing instrument comparison.

5.2 Materials and Methods

In the following section we are going to describe the platform instrumentation design that combines TDOS and SFDI together with the corresponding acquisition workflows and data analysis frameworks. It follows a brief description of the tissue mimicking phantoms used for the validation of the set-up at a laboratory level.

5.2.1 Instrumentation

The source side design is shared between the time-resolved system and the spatial frequency domain imaging set-up by employing a pulsed ($< 100\ ps$) supercontinuum laser source (SuperK Extreme, NKT Photonics® A/S, Denmark) fiber coupled into a tunable single line filter (SuperK VARIA, NKT Photonics® A/S, Denmark) necessary for the broadband investigation of the samples over a wavelength range spanning from $550 - 840\ nm$. At the output of this monochromation device, a cascade of neutral density filters is utilized to tune the power of the optical signal to be provided to the sample and finally the delivery of the optical pulses is obtained through propagation in a multimode step-index fiber ($NA = 0.39$, $\varnothing_{core} = 1000\ \mu m$). At this point, the optical path for the time-resolved system is terminated by point-like illumination of the sample (in contact with the surface). Conversely, the SFDI system requires the projection of the spatially modulated patterns of light: in this sense, a projecting system based on a Digital Micro-mirror Device (High-Speed V-7000, Vialux GmbH, Germany) is employed for the generation of wide-field ($> 15 \times 15\ cm^2$) bi-dimensional sinusoidal patterns at several spatial frequencies and phases at $45 \pm 5\ cm$ working distance.

The detection chain of the time-resolved system consists of a large core multimode step-index glass fiber ($NA = 0.39$, $\varnothing_{core} = 1000\ \mu m$) for maximizing the point-wise harvesting of the diffused light. The resulting signal is then delivered to a Single-Photon Avalanche Diode (ID100-MMF50, ID Quantique SA, Switzerland). Subsequently, the detector is connected to a Time-to-Digital Converter (HRMTimeR, SensL© Technologies Ltd., USA) in order to acquire the time-resolved reflectance (or transmittance) curves by means of a standard Time-Correlated Single Photon Counting (TCSPC) technique. In the second case instead, the SFDI images are collected with a high dynamic range (16 bits) and high frame rate ($> 100\ fps$) sCMOS camera (PCO.edge 5.5, Excelitas® PCO GmbH, Germany). It is worth mentioning that a pair of linear polarizers (PPL05C, Moxtek Inc., USA) arranged in a crossed configuration is also used on the projection and acquisition sides of the spatial frequency domain system to reject the specular component of the backscattered reflectance signal arising from the sample. A scheme of the multi-modal platform design is illustrated in Fig.5.1.

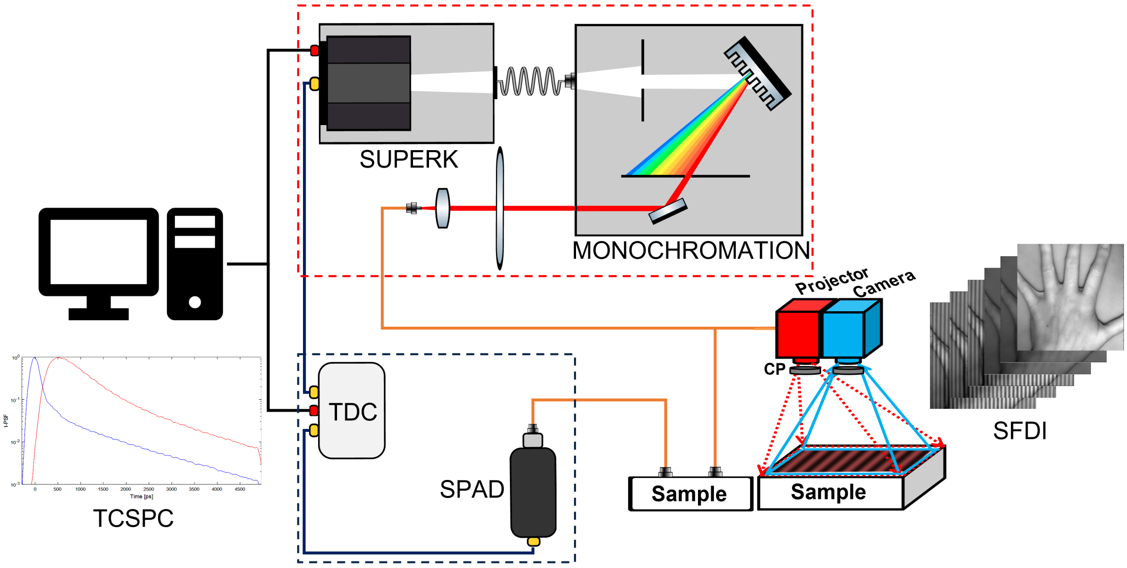

FIGURE 5.1: *Multi-modal referencing platform design. In the red box, the source side based on the supercontinuum laser generation and shared by both the TDOS and SFDI systems. In the blue box, the detection chain of the TDOS system: the blue wired connection represents the start-stop signals for the TCSPC acquisition routine. To mention, CP refers to the cross polarization of the projection and imaging side of the SFDI system.*

5.2.2 Acquisition workflow and data analysis

5.2.2.1 TDOS

Time-resolved diffuse optical spectroscopy is based on the injection of a short light pulse ($FWHM \sim ps$) on the sample, typically by means of an optical fiber in contact with the surface. After the propagation in the tissue, a second fiber is used to collect the optical signal arising from the sample, either in reflectance geometry (i.e. injection and collection fibers lying on the same surface and separated by a distance ρ) or in transmittance (i.e. collection fiber on the opposite surface of the injection point), as shown in Fig.3.8. The detection path is then characterized by the presence of a single photon detector connected to a timing electronics for the performance of a TCSPC acquisition algorithm. In particular, the TCSPC board receives a start signal from the detector for every single photon event, followed by a stop signal originated by the pulse triggering of the laser. In this way, the instrument is capable of reconstructing the waveform of the diffused signal by building a photon statistics based on the single photon events, as described in Section 3.3.3.

The recovered Distribution of Time Of Flight (DTOF) values represents the optical response in the temporal domain of the tissue to the injected pulse, however the response of the instrumentation alone is also required to take into consideration the effect of the propagation path from the laser to the sample, as well as the detection chain. For this purpose, an Instrument Response Function (IRF) measurement is performed by acquiring the DTOF obtained by placing the collection and detection fiber facing each other at a short distance. Furthermore, a thin layer of highly diffusive material, typically Teflon, is adopted to ensure the proper illumination and filling of the detection fiber.

Finally, the computation of the optical properties of the investigated sample, i.e. the absorption (μ_a) and reduced scattering ($\mu_s^{'}$) coefficients, is achieved by first convolving the IRF with a theoretical DTOF simulated with a diffusion equation approach [46], and secondly by feeding the resulting curve together with the measured DTOF of the sample to a least square fitting routine based on a Levenberg-Marquardt algorithm [97].

FIGURE 5.2: *Silicone-based tissue mimicking phantoms manufactured and used for the validation of the multi-modal referencing platform.*

5.2.2.2 *SFDI imaging*

SFDI is characterized by the projection on the sample of sinusoidally modulated pattern of lights and by the acquisition of the backscattered signal arising from the surface of the sample itself. Generally, a projection device such as a DMD is used to generate the spatially modulated signal, and an area scanning camera is utilized for the collection of the images. In its standard configuration [45], SFDI requires a total of six patterns to be projected on the sample: two spatial frequencies (i.e. $f_x = 0\ mm^{-1}$, $f_x = 0.2\ mm^{-1}$) and three phase shifts for each of them (i.e. $\varphi = 0, 2/3\pi, 3/4\pi$). In our case, the chosen sequence is characterized by seven phase shifts (i.e. $\varphi = 0, \pi/2, \pi, 3/2\pi, 2\pi, 5/2\pi, 3\pi$)[74] instead, in order to improve the image quality and reduce the effect of phase uncertainty. In this way, it is possible to extract the modulation amplitudes of the images by a simple phase-shifting demodulation step, thus determining the values of M_{DC} and M_{AC} for each pixel of the image. It follows a calibration step in order to characterize the effect of the instrumentation on the acquired signal, as described in Section 3.3.4.1. This is achieved by measuring with the same sequence a calibration phantom with known optical properties. In our case the calibration phantom ($210\ mm \times 210\ mm \times 20\ mm$) optical properties were: $\mu_a = 0.01\ mm^{-1}$, $\mu_s' = 1.1\ mm^{-1}$ at $665\ nm$; $\mu_a = 0.02\ mm^{-1}$, $\mu_s' = 0.7\ mm^{-1}$ at $860\ nm$[1]. As a result of the calibration step, the diffuse reflectance maps can be computed, i.e. $R_{DC}(f_x = 0\ mm^{-1})$, $R_{AC}(f_x = 0.2\ mm^{-1})$, and an inverse problem solver based on Monte Carlo pre-computed 2-D LUTs is implemented to extract the absorption and reduced scattering coefficients of the sample.

5.2.3 Tissue mimicking phantoms

A first validation of the platform was performed on tissue mimicking phantoms. In this sense, we elaborated a protocol for the manufacturing of silicone-based solid phantoms that can be used for both wide-field imaging and time-resolved measurements.

The protocol is based on a polydimethylsiloxane (PDMS) matrix (with SYLGARD™ 184 Silicone Elastomer for the curing process) in which TiO_2 powder is dissolved as scattering agent, whereas alcohol-soluble nigrosin is used as absorber. As a result, by finely

---

[1] The reported optical properties were referenced using a time domain photon counting system.

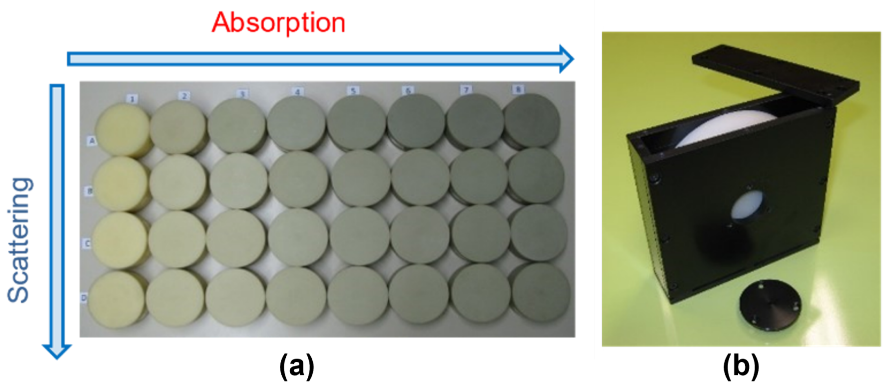

FIGURE 5.3: *(a) MEDPHOT phantom kit [91]; (b) BIP Responsivity phantom [94].*

tuning the concentrations of both agents it is possible to achieve a wide range of optical properties (i.e. μ_a and $\mu_s^{'}$), with the advantage of guarantying an almost flat spectroscopic response from nigrosin over the investigated wavelength range, as well as a smooth decrease in reduced scattering. An example of silicone-based tissue phantoms of different sizes and shapes is provided in Fig.5.2.

In addition to the aforementioned samples, the platform underwent a validation step by performing the *MEDPHOT* protocol [91] for the performance assessment of the DOS instrument. In particular, the matrix of 32 homogeneous epoxy resin-based solid phantoms (Fig.5.3 (a)) was measured with both systems, thus investigating a range of optical properties[2] ranging in absorption from $\mu_a = 0 - 0.35\ cm^{-1}$ in step of $0.05\ cm^{-1}$, and in reduced scattering from $\mu_s' = 5 - 20\ cm^{-1}$ in steps of $5\ cm^{-1}$.

Furthermore, the TDOS system was also tested in a second protocol for the characterization of the basic instrumental performance (BIP) [94]. In this case, a solid homogeneous highly diffusive slab of 2 cm thickness and 10.5 cm diameter (Fig.5.3 (b)) was used for the assessment of the instrument responsivity: the phantom provides an accurate transmission factor that is used to create a well defined diffuse light source, thus enabling the evaluation of the responsivity of the instrument detection chain[3].

5.3 Results

In this section we are going to provide an overview of the main results obtained from the validation process of the platform by first focusing on the time domain system and following by the description of the SFDI set-up. To conclude, we are going to outline a comparison of the two instruments. It is worth mentioning that the description of the results obtained in the framework of the BITMAP exercise [98] are reported in more details in the dedicated Chapter 6.

5.3.1 TDOS system: BIP protocol

The first figure of merit addressed by the BIP protocol is the Dark Count Rate (DCR) of the detection chain. In Fig.5.4(A) we report the test for the TDOS system for the 690 nm wavelength: the result shows a considerably low DCR value ($< 10^3\ counts/s$) that well

---

[2] We report the nominal values at 800 nm as reported in [91].

[3] This feature of the BIP protocol explains the reason for which we excluded the SFDI system from the validation protocol: the technique is in fact based on reflectance geometry, which prevents the use of the responsivity phantom as it is based on a transmission configuration.

fits with the specifications of the SPAD detector. In addition, a similar behavior was characterized for the rest of the wavelength bands acquired.

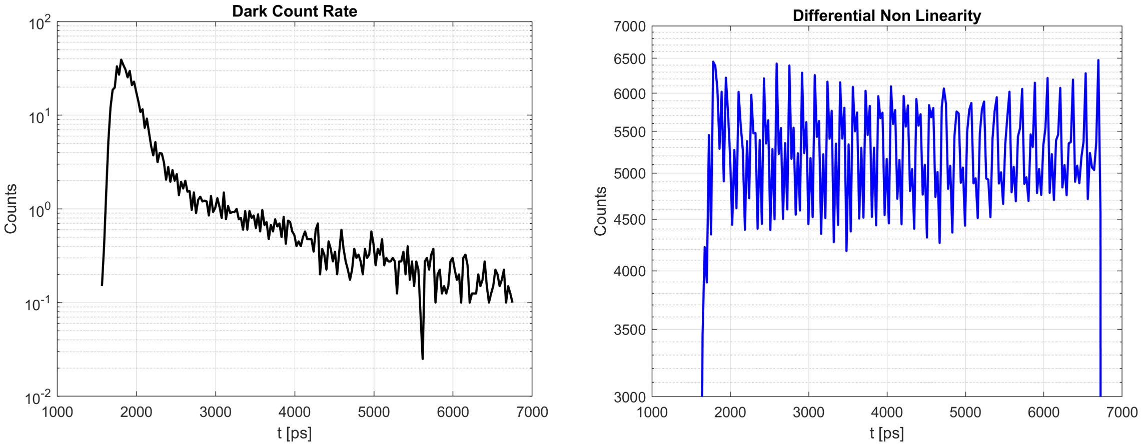

(A)

(B)

FIGURE 5.4: *(A) Dark count rate of TDOS system at* 690 *nm; (B) Differential non linearity measurements performed by illuminating the collection fiber with a white lamp.*

Following with the Differential Non Linearity (DNL) test (Fig.5.4(B)), the instrument showed a DNL average value of $< 13\%$. As explained in [94], the DNL stems from the choice of the timing electronics present in the TCSPC chain, but it could easily be compensated. Overall, the effect for our instrument is in the range of the standards obtained with different imaging configurations as reported in [94], [98].

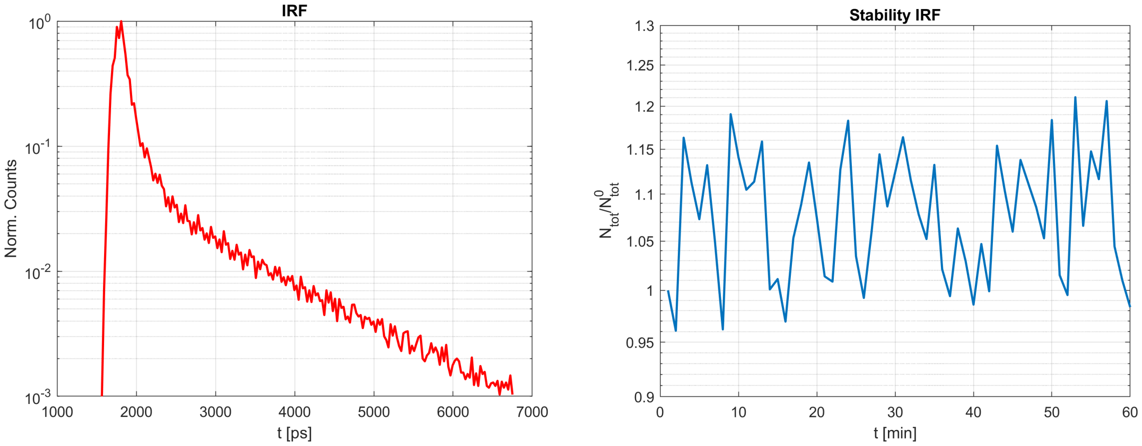

(A)

(B)

FIGURE 5.5: *(A) Instrument response function of TDOS system at* 690 *nm; (B) Total counts for repeated IRF measurements over 1 hour at* 690 *nm. The results are normalized to the starting time point of acquisition.*

Furthermore, we performed a characterization of the instrument response function of the system by acquiring IRF curves for each wavelength for a duration of 1 hour, in order to additionally assess the measurement stability. In Fig.5.5(A) and Fig.5.5(B) we report the results of the mentioned tests, for $\lambda = 690\ nm$. The temporal profile of the IRF shows a narrow response ($FWHM < 200\ ps$) with significant stability in the peak counts (Fig.5.5(B)) and in the temporal moments as well. In this sense, no evident trends could be highlighted.

Parameter	**Guideline**
Wavelength range	as many as possible
S-D distance	$> 2\ cm$, otherwise standard conditions
Acquisition time	$1\ s$
Target count rate	$500\ kcounts/s$
Repetitions	20

TABLE 5.1: *Summary of the guidelines followed for the MEDPHOT protocol.*

Finally, the responsivity of the instrument was characterized by a transmittance measurement of the responsivity phantom provided (Fig.5.3 (b)). The input power of the laser source was tuned to limit the total count rate to $\sim 500\ kcount/s$ and 20 repeated acquisitions were performed for each wavelength. By applying Eq.(4) from [94], we obtained a resulting value at $750\ nm$ of $s^L_{det} \simeq 10^{-12}\ m^2 sr$.

To conclude the discussion on the results of the BIP protocol, it is worth mentioning that a comparative analysis of the state of the art technologies analyzed under the BITMAP action is reported in Chapter 6. Therefore, in order to gather a better understanding of the performance of our TDOS system we are going to refer to the above mentioned chapter and more specifically to Section 6.3.1.

5.3.2 TDOS system: MEDPHOT protocol

As outlined in the protocol description reported in [91], the main goal of the exercise is to address specific figures of merit, and in particular: *linearity* (i.e. the ability of the instrument to quantify the optical properties by preserving the spectral shape and accounting for the cross-talk between absorption and reduced scattering), *accuracy* (i.e. the ability of the instrument to retrieve an absolute estimate of μ_a and $\mu_s^{'}$ for a referenced phantom), *stability* (i.e. the consistency of the quantification on a short time basis), *reproducibility* (i.e. the comparability of the retrieved optical properties on a longer time scale), *uncertainty* (i.e. the minimum working conditions necessary to confidently obtain the extraction of absorption and reduced scattering).

In this sense, the first parameters we addressed are the linearity and accuracy of the system in recovering the optical properties of the 32 homogeneous phantoms from the MEDPHOT kit. In particular, we followed the guidelines reported in Table 5.1 by still ensuring the standard working condition of the system: in this sense the following results are referred to a source-detector distance of $2\ cm$, an acquisition time for each curve of $1\ s$ and a total number of photon counts per curve of $500\ kcounts/s$. The following results are referred to $\lambda = 690\ nm$.

In Fig.5.6 the results of the linearity assessment are shown for the TDOS system. It is worth mentioning that the reference values (i.e. "REF" series in red) reported are the nominal values of the phantoms as reported in [91]. The system is characterized by consistent linearity in the retrieval of both μ_a and $\mu_s^{'}$ with clear exception for the high absorption and high scattering regimes ($\mu_a > 0.25\ cm^{-1}$, $\mu_s' > 15\ cm^{-1}$). A predominant overestimation of absorption can be highlighted as well (Fig.5.6 (a)), whereas for the reduced scattering the overall trend is consistent with the nominal values, with the same caveats just mentioned for the high scattering phantoms (Fig.5.6 (b,d)). A more quantitative assessment of the accuracy of the system can be appreciated in Table 5.2: overall, the TDOS instrument performs quite accurately for reduced scattering in the central region of the

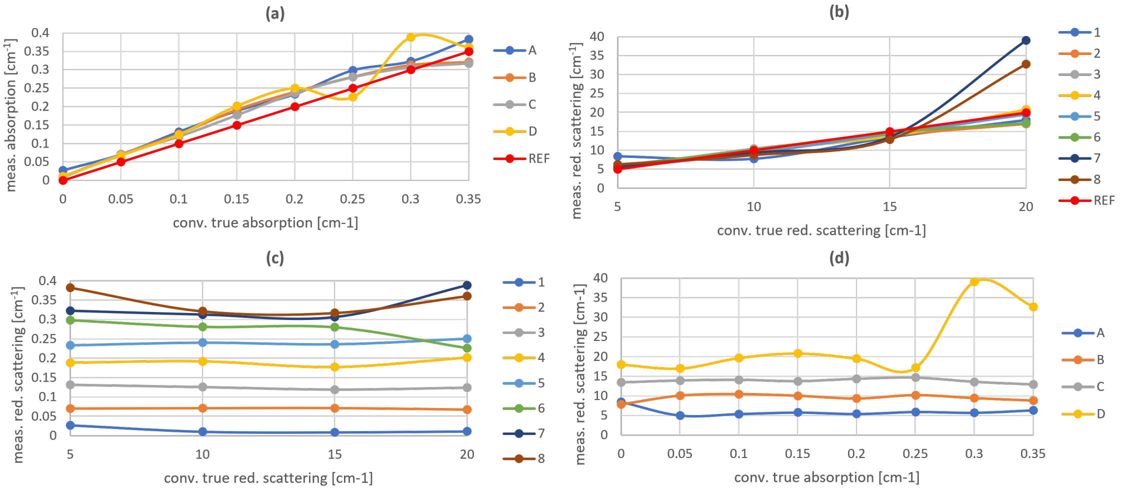

FIGURE 5.6: *Linearity plots for the TDOS system. (a) Linearity in recovering μ_a ; (b) Linearity in recovering $\mu_s^{'}$; (c) Linearity in recovering μ_a while linearly increasing $\mu_s^{'}$; (d) Linearity in recovering $\mu_s^{'}$ while linearly increasing μ_a .*

$\epsilon_r^{\mu_a}$	1	2	3	4	5	6	7	8
A	3%	42%	32%	26%	17%	20%	9%	7%
B	1%	35%	27%	25%	19%	11%	6%	-12%
C	1%	38%	25%	17%	15%	9%	-4%	-13%
D	1%	37%	26%	24%	16%	-6%	33%	2%
$\epsilon_r^{\mu_s^{'}}$	**1**	**2**	**3**	**4**	**5**	**6**	**7**	**8**
A	69%	-1%	8%	14%	7%	19%	15%	25%
B	-22%	-4%	5%	-3%	-7%	1%	-6%	-17%
C	-11%	-10%	-3%	-10%	-6%	-5%	-18%	-19%
D	-10%	-15%	-1%	-6%	-11%	-14%	105%	63%

TABLE 5.2: *Results of accuracy test for the TDOS system.*

optical properties range, with a relative error[4] below 10% for most of the phantoms, together with a systematic decrease in accuracy for the boundaries of the matrix. In terms of absorption, the accuracy is consistently lower with relative errors $> 10 - 15\%$ and positive, as representing an overestimation of the absorption coefficient.

The stability of the system was addressed by performing a repeated measurement over 1 hour of the same phantom in the same working conditions. Similarly, for the reproducibility test, the control phantom was measured over different sessions to assess the consistency of the measurement on a day-to-day basis. The results of the mentioned tests are illustrated in Fig.5.7 and Fig.5.8. For the latter, it is worth highlighting that we are showing the results of a follow-up measurement performed on a phantom different from the dedicated B2 phantom from the MEDPHOT kit. In addition, we replicated the measurement over a longer period of time (5 days instead of 3) to specifically target the comparison in performance between the TDOS system and the SFDI side of the platform, as it will be remarked in the following Section 5.3.4. The reason behind the choice of a

---

[4] The relative error is computed as follows: $\epsilon_r = \frac{\mu_m - \mu_n}{\mu_n}$, where μ_m, μ_n represent the measured optical property coefficient (i.e. μ_a and $\mu_s^{'}$) and the nominal value of the same, respectively.

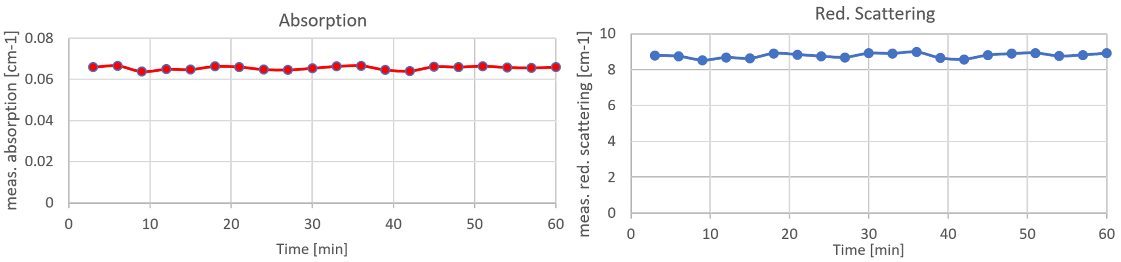

FIGURE 5.7: *Results of the stability test for the TDOS system. Repeated measurements were performed on the same phantom for a total duration of 1 hour.*

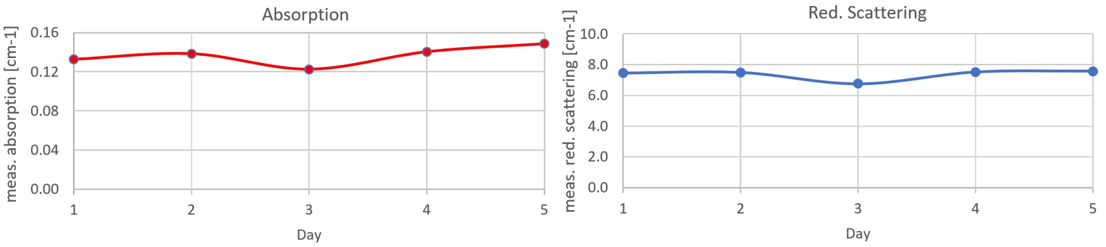

FIGURE 5.8: *Results of the reproducibility test for the TDOS system. In this case the same phantom was measured over 5 different days.*

different phantom is due to the short availability of the MEDPHOT kit. In any case, the TDOS system did not show any particular drifts or trends either in terms of stability or reproducibility.

To conclude the MEDPHOT protocol, an uncertainty test was also carried out to address the lower bound for the TCSPC photon statistics [91]. In this case, our system is demonstrated to provide $CV \simeq 1\%$ (Eq.(3) in [91]) in case of a total number of photon counts per acquisition of at least 500 $kcounts/s$ for both absorption and reduce scattering, as shown in Fig.5.9.

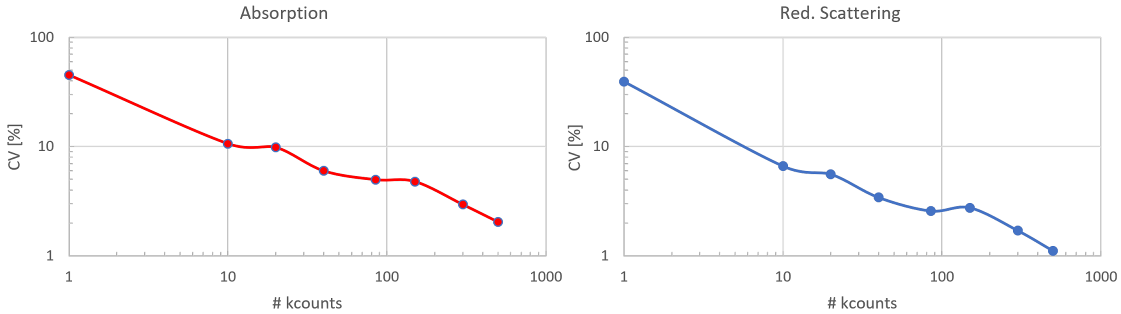

FIGURE 5.9: *Results of the uncertainty test for the TDOS system.*

5.3.3 SFDI system: MEDPHOT protocol

The guidelines proposed in Table 5.1 clearly do not fully apply to the SFDI system, due to the different technology involved. However, the parameters addressed by the MEDPHOT protocol can still be used to characterize the performances of the imaging side of the platform.

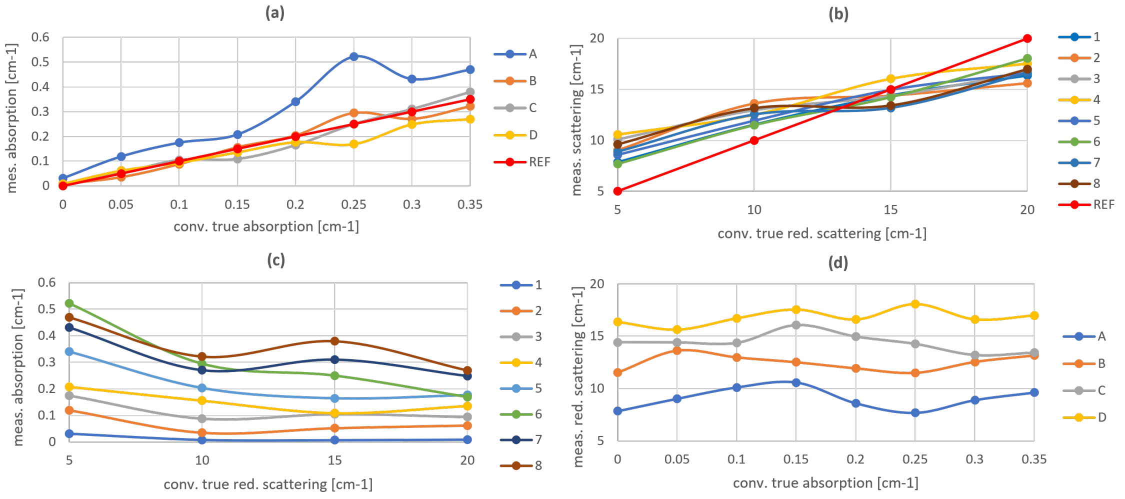

FIGURE 5.10: *Linearity plots for the SFDI system. (a) Linearity in recovering* μ_a *; (b) Linearity in recovering* $\mu_s^{'}$ *; (c) Linearity in recovering* μ_a *while linearly increasing* $\mu_s^{'}$ *; (d) Linearity in revovering* $\mu_s^{'}$ *while linearly increasing* μ_a *.*

$\epsilon_r^{\mu_a}$	1	2	3	4	5	6	7	8
A	3%	138%	75%	39%	71%	109%	44%	34%
B	1%	-30%	-12%	4%	2%	18%	-10%	-8%
C	1%	4%	5%	-27%	-18%	1%	4%	9%
D	1%	24%	-6%	-9%	-12%	-32%	-17%	-23%
$\epsilon_r^{\mu_s'}$	**1**	**2**	**3**	**4**	**5**	**6**	**7**	**8**
A	57%	81%	102%	112%	72%	54%	78%	92%
B	15%	36%	30%	25%	19%	15%	26%	32%
C	-4%	-4%	-4%	7%	-1%	-5%	-12%	-10%
D	-18%	-22%	-16%	-12%	-17%	-10%	-17%	-15%

TABLE 5.3: *Results of accuracy test for the SFDI system.*

In Fig.5.10 we report the results for linearity assessment of absorption and reduced scattering. Two main effects can be highlighted: first of all the linearity in μ_a retrieval is achieved for all the scattering series B,C,D except for the low scattering phantoms from the A series ($\mu_s' = 5\ cm^{-1}$), for which the system tends to overestimate the coefficient (Fig.5.10 (a,c)); secondly, the linearity test on the reduced scattering coefficient (Fig.5.10 (b,d)) shows a relevant trend in overestimating $\mu_s^{'}$ for the low scattering phantoms (series A,B) and an underestimation for the highly scattering series (C,D).

This effect is confirmed by means of the accuracy analysis, as reported in Table 5.3. From the table it is evident how the A series results to be the most difficult to optically characterize, as it represents the low μ_a and low $\mu_s^{'}$ regime. Instead, for the remaining phantoms the accuracy is relatively high with an error with respect to the nominal values below $< 15 - 20\%$ in absorption with a few exception, i.e. B2, C4, D2, D6, D8. Concerning the reduced scattering, the quantification accuracy results consistently lower, with only a few phantoms that are characterized by a relative error lower than 20%, especially in the C series. Nevertheless, the stability and reproducibility assessment provided satisfactory results also for the SFDI system, as summarized in Fig.5.11, 5.12. Similarly to the TDOS

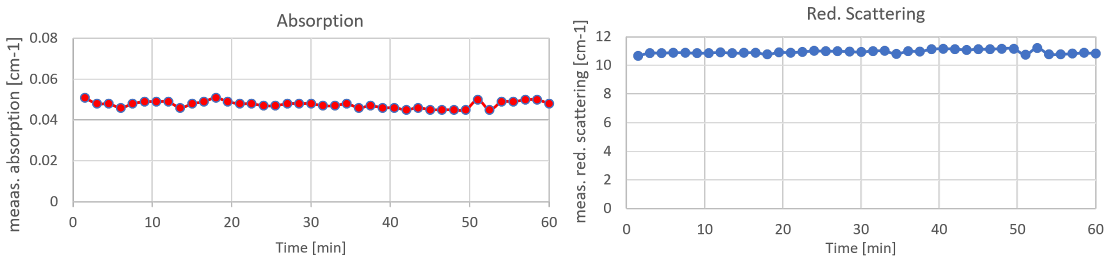

FIGURE 5.11: *Results of the stability test for the SFDI system. Repeated measurements were performed on the same phantom for a total duration of 1 hour.*

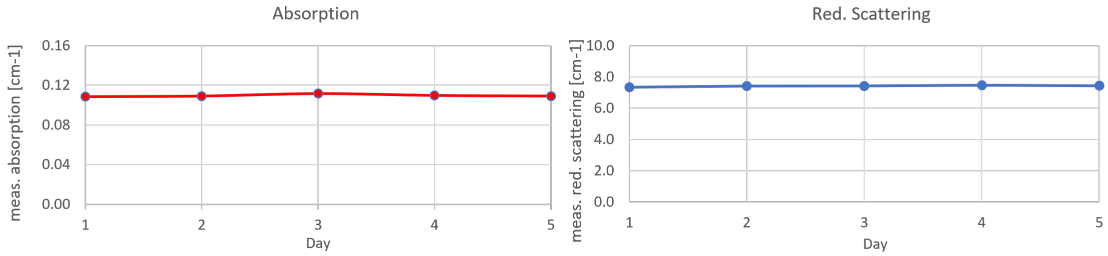

FIGURE 5.12: *Results of the reproducibility test for the SFDI system. In this case the same phantom was measured over 5 different days.*

system, the imaging platform shows consistent results for repeated measurements over a long session (Fig.5.11) with no evident trends, as well as for quantification reproducibility over multiple days (Fig.5.12).

To conclude, it is worth noticing that for the SFDI system we did not perform an uncertainty assessment.

5.3.4 Comparison of TDOS and SFDI

In order to summarize the main findings of the validation of the platform, we propose a comparative analysis of the time domain system and of the spatial frequency domain imaging set-up, by focusing in particular on the linearity and accuracy in the quantification of absorption and reduced scattering, as illustrated in Fig.5.13 and Fig.5.14.

As mentioned in the previous sections, the characterization of the absorption coefficient shows a consistent linearity trend for TDOS over almost the entire absorption spectrum, with exceptions for the highly scattering phantoms (Fig.5.13). However, it is worth mentioning the general overestimation in the optical absorption with respect to the nominal values of the phantom matrix proposed. A similar reasoning can be outlined for the SFDI platform, which performs with high accuracy in recovering absorption for the lower-middle range of μ_a , despite the evident issues represented by the A phantom series.

Concerning the quantification of μ_s' , the general variability among the different phantoms is much more evident, as illustrated in Fig.5.14. Clearly, the low scattering regime (series A) represents a challenge for SFDI with a definite overestimation ($> 50\%$ in some cases), whereas TDOS shows a more consistent behavior over the series with the only exception of the A1 phantom which lies at the very boundary of the matrix. In addition, it is worth highlighting that SFDI outperforms TDOS in the upper regime of scattering (D series), providing a more stable response for the phantoms with highest absorption.

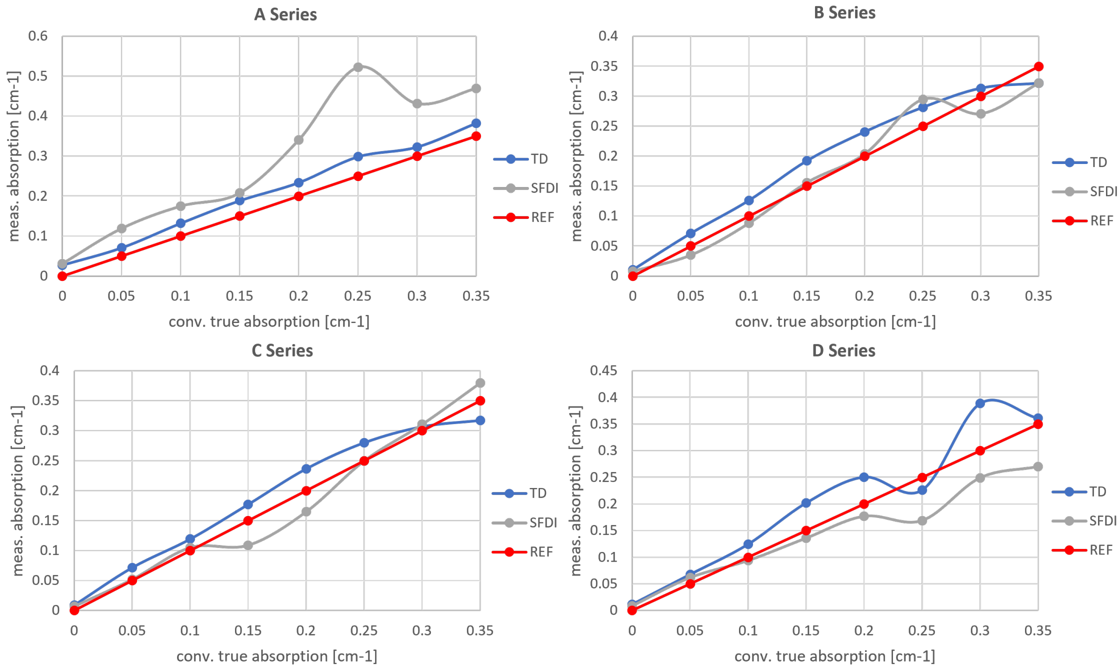

FIGURE 5.13: *Comparative analysis of the linearity assessment of the TDOS and SFDI systems for the recovering of* μ_a .

Following these results, we tried to address the discrepancy in the quantification of optical properties with the two methods, by performing a series of measurements on silicone-based tissue mimicking phantoms (see Section 5.2.3 for more details). A total of 23 phantoms with different optical properties were measured in several conditions with both systems and the results of the characterization are reported in Fig.5.15, for the 665 nm wavelength. In total we performed two sets of measurements in two days for each subsystem, however with SFDI we tested also the effect of different light sources, by also adding a single wavelength diode laser source. Once again, the reproducibility of the quantification is maintained despite the different operating conditions and implementations, for both SFDI and TDOS, though it is evident a mismatch in the retrieval of the optical properties for most of the phantoms. In this sense, it is worth mentioning that the first two samples measured (INOB0625F0628, INOB0643F0637) are tissue mimicking phantoms purchased off the shelf from *Biomimic*^{TM} *Optical Phantoms* (INO, Canada) with nominal values (at 800 nm) of absorption coefficient of $\mu_a = 0.07\ cm^{-1}$, $\mu_a = 0.26\ cm^{-1}$ and reduced scattering coefficient of $\mu_s' = 9.2\ cm^{-1}$, $\mu_s' = 7.6\ cm^{-1}$ respectively. These phantoms are expoxy resin-based, and they showed a considerable matching of optical property retrieval with respect to their nominal values, especially in the case of TDOS.

5.4 Discussion

The quantification of tissue optical properties is the main advantage of optical techniques based on near-infrared diffuse optical spectroscopy. Nevertheless, the accuracy in retrieving absorption and reduced scattering is affected by different sources of errors that can be specific to the imaging technology adopted. For spatial frequency domain imaging one major challenge is associated to the calibration step involved for the computation of the

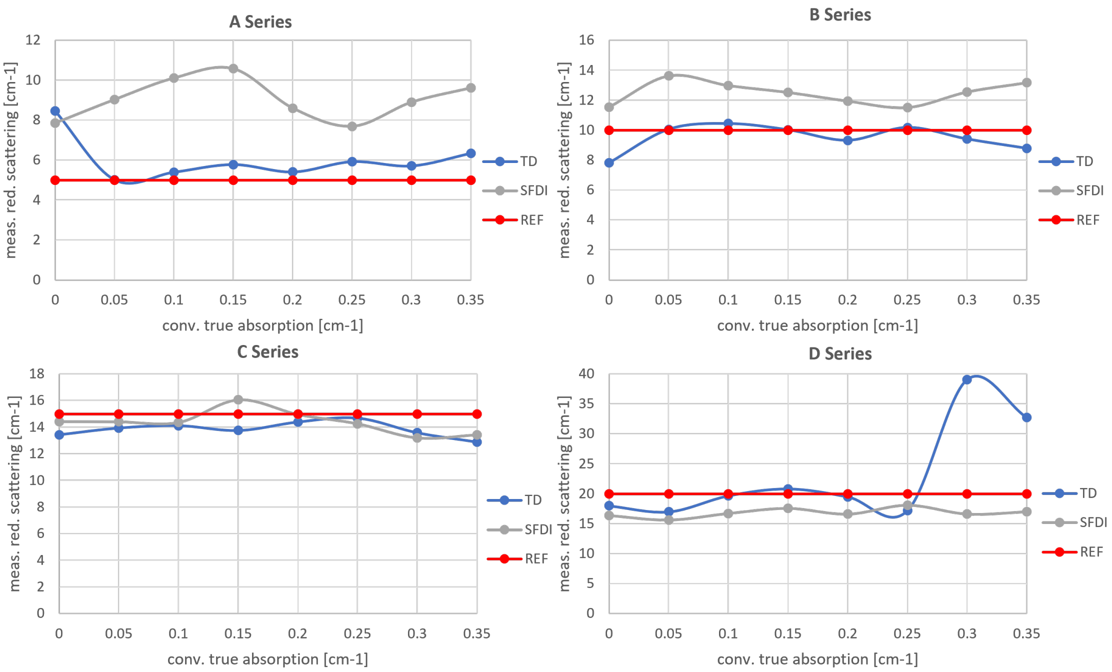

FIGURE 5.14: *Comparative analysis of the linearity assessment of the TDOS and SFDI systems for the recovering of* μ_s' .

diffuse reflectance of the sample: the need of a calibration phantom with referenced optical properties rises the question of the reliability of the characterization of such parameters, which usually is derived from a different measurement technique (i.e. frequency domain or time-resolved approaches)[1]. In this sense, it is well known that time-resolved techniques have usually been considered as referencing systems for the optical quantification of the properties of tissues, thanks to their calibration-free implementations.

In this sense, we proposed a multi-modal solution combining a time domain system with a spatial frequency domain imaging set-up, aiming at providing a cross-reference approach for the optical characterization of biological tissues in the therapeutic window.

As mentioned in [1], [95], one major source of error for diffuse optical imaging techniques lies in the modeling of the photon propagation in the medium. In our case, the TDOS system analysis is based on the solution of the diffusion approximation for the fully homogeneous case, whereas SFDI relies on multi-dimensional (2-D) look up tables computed with a White Monte Carlo approach. As a result, the discrepancy in optical properties reconstruction could be affected by the different modeling frameworks and in this sense we started to consider transitioning to a fully Monte Carlo-based approach for both sides of the platform to obtain a more uniform representation of the problem solving algorithm. However, a robust time-domain Monte Carlo analysis requires several millions of photons to be simulated for each t-PSF.

Secondly, the depth sensitivity of the two techniques is different by definition: due to the light modulation, SFDI patterns can hardly propagate more than a few millimeters under the surface of the samples, whereas time-resolved approaches can provide information from deeper layers in the samples. Evidently, this should not be a concern for homogeneous structures but we noticed that there is a clear discrepancy in the agreement between the two technologies once the surface structure of the phantoms are considered, such as in the case of silicone-based samples and epoxy resin-based structures (see Section 5.3.4).

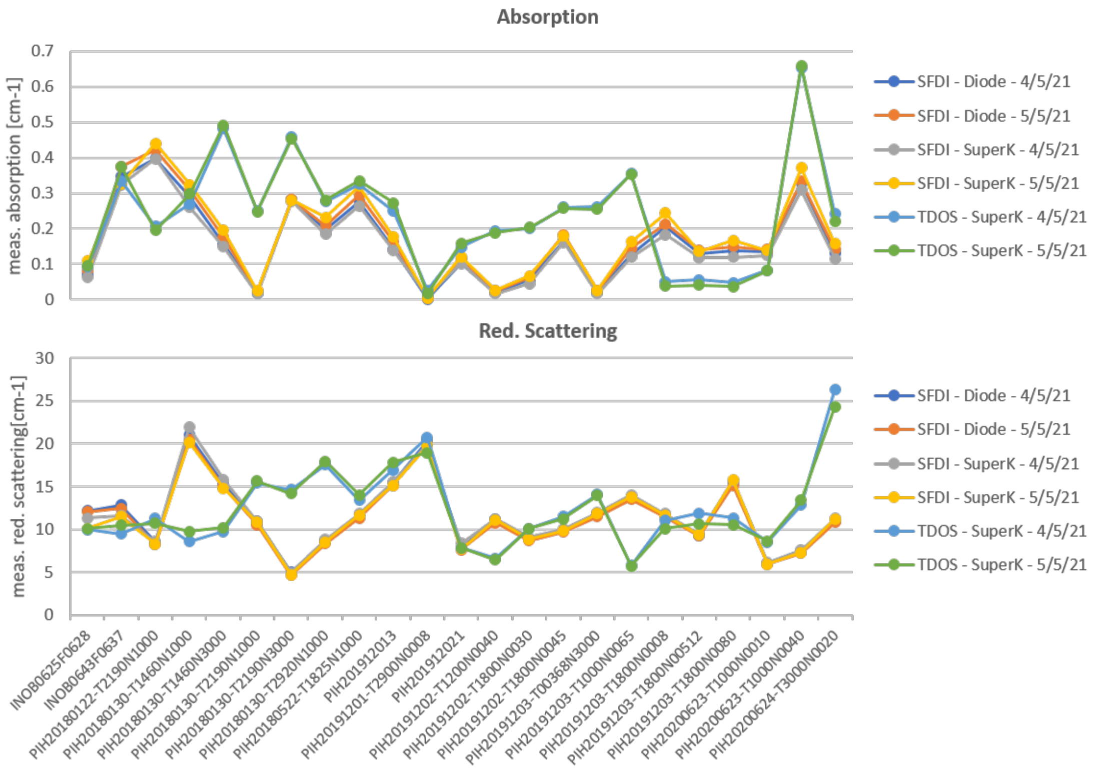

FIGURE 5.15: *Optical properties characterization of tissue mimicking phantoms for the validation of the platform.*

In addition, the sensitivity of the TDOS system to high absorption and scattering regimes resulted as a strong limitation of the instrument. As mentioned in the previous section, the quantification of the optical properties of highly absorbing phantoms ($> 0.25\ cm^{-1}$) was determined by low accuracy in both absorption and reduced scattering, with a more evident effect in highly scattering regimes as well. In this cases, the signal acquired with the TCSPC chain was most of the time too low to obtain a sufficient photon statistics to perform the fitting, thus pushing us to envision a new instrumental configuration based on a detector with larger active area but similar timing resolution. As a consequence we also tested a Silicon PhotoMultiplier (SiPM) detector with a $3\ mm^2$ active area ($>$ 100 times larger then the SPAD) with promising results, thus enabling us to foresee an extension of the measurement regime to a larger optical properties spectrum with respect to the previous configuration. Also, it allowed us to extend the source-detector separations available for the system thanks to the higher SNR.

Finally, the use of the single line filter for the monochromation stage, together with the small area detector limited the extent of the spectroscopic investigation to 800 nm. In this sense, we have been working on implementing a second version of the platform based on the use of acusto-optical tunable filters for the investigation of the entire therapeutic window (up to 1000 nm), in combination with the SiPM detector aforementioned.

5.5 Conclusions

In this chapter we described the design and implementation of a multi-modal referencing platform for diffuse optical spectroscopic instruments. The validation of the platform was carried out by conducting recognized protocols for the performance assessment of

NIRS instruments, namely the MEDPHOT and BIP (only for the time domain system). The two technologies, TDOS and SFDI, combined in a single measurement platform produced promising results for linearity, stability and reproducibility of the quantification of the optical properties of tissue mimicking phantoms, though arising some fundamental issues in the accuracy of the retrieval of the absorption and reduce scattering coefficients. In addition, a significant discrepancy between the two techniques in the quantification power was highlighted by performing sets of measurements on phantoms with different optical properties and materials. Finally, the platform was involved in an European action (BITMAP) aiming at a collaborative effort towards comparison and standardization of protocols for the performance assessment of DOS instruments. The results of this collaboration is reported in Chapter 6.

Chapter 6

BITMAP Exercise

Article Title : *"Multi-laboratory Performance Assessment of Diffuse Optics Instruments: the BITMAP Exercise"*

Authors : *P. Lanka, L. Yang, D. Orive-Miguel, J. Deepak Veesa, S. Tagliabue, A. Sudakou, S. Samaei, M. Forcione, Z. Kovacsova, A. Behera, T. Gladytz, D. Grosenick, L. Hervé, T. Durduran, K. Bejm, M. Morawiec, M. Kacprzak, P. Sawosz, A. Gerega, A. Liebert, A. Belli, I. Tachtsidis, F. Lange, G. Bale, L. Baratelli, S. Gioux, K. Alexander, M. Wolf, S. Konugolu Venkata Sekar, M. Zanoletti, I. Pirovano, M. Lacerenza, L. Qiu, E. Ferocino, G. Maffeis, C. Amendola, L. Colombo, M. Buttafava, M. Renna, L.Di Sieno, R. Re, A. Farina, L. Spinelli, A. Dalla Mora, D. Contini, P. Taroni, A. Tosi, A. Torricelli, H. Dehghani, H. Wabnitz, and A. Pifferi*

Journal : *Jounal Of Biomedical Optics (submitted 22/11/21)*

Diffuse Optics (DO) encompasses a range of photonics tools based on the study of photon random migration in highly scattering media – biological tissues in particular. Due to its unique features, Diffuse Optics is emerging as a powerful means for clinical or homecare diagnostics [99]. The basic physics of DO is related on the detection of temporal or spatial alteration in photon distribution re-emitted on the tissue surface [100]. Due to the low power (typically few mW) of injected near-infrared light (600-1100 nm range), DO is inherently non-invasive. The photon temporal (or spatial) distribution carries information on the absorption – ultimately related to tissue chemical composition, such as water, lipid, collagen content, oxy- and deoxy-hemoglobin concentration, cytochrome c-oxidase [101] – and scattering properties – linked to tissue microstructure. Further, DO is one of the few non-invasive modalities capable of providing functional information on e.g. brain or muscle activation [102]. It can be operated non-contact through remote light illumination and collection [103]. It explores the tissue well below the skin at depths of up to 2-4 cm. It can provide quantitative operator independent assessment of the tissue status, such as oxygenation level in brain. Finally, it is highly scalable, sharing the same technology from large clinical tomographic systems down to wearable devices or homecare appliances [3]. For all these aspects, DO is attracting more and more interest in many fields such as monitoring vital signs like brain oxygenation in critical care or during interventions [104], tumor diagnostics as for breast cancer [105], investigating the impact of lifestyle and nutrition on our body [106], or other fields like neuroscience and psychology [107], sport and leisure [108]. Even further, the operator-independency, the depth sensitivity, the scalability in addition to non-invasiveness makes this option attractive for telemedicine and homecare of patients remotely.

Performance Assessment and Standardization (PAS) are needed to secure solid growth in the field of DO and in general of biophotonics tools for clinical diagnostics. By PAS we mean all steps providing an objective quantitative assessment of some key figures-of-merit (FOMs) of a given device related to its clinical use. A first reason for adoption of PAS procedures is the need to anticipate as possible technical problems from the clinical ward back to the laboratory bench. Indeed, many issues or poor performances hampering clinical studies could be identified much earlier with great savings in efforts and public spending and less ethical concerns. PAS is useful to benchmark development and upgrade so to drive new design or improvements. PAS improves reliability and comparability of clinical studies by setting a common ground for comparison of instruments. Also, it facilitates machine learning algorithms by providing a testing dataset related to some universal features. Open Data and Open Science can benefit from a common ground of PAS since this improves interoperability of data and comparison of different datasets. Industrial deployment is advantaged since PAS figures-of-merits can be translated more easily in technical specification and can be also the basis for Industrial Standards, which is the ultimate step of PAS. Finally, also patients and the healthcare system benefit from PAS by improving the technical quality of instrument and reduce health-related costs by increasing reliability. Industrial standards and procedures for clinical validation are already well rooted in the DO community. Our goal is to anticipate many issues to the early stages and support the culture of PAS in the whole process.

Recently, much awareness on the need of PAS for Biophotonics and related tools has been raised by the scientific community [109],[110],[111], scientific publishers [112],[113], funding and regulatory bodies [114].

Our work within the BITMAP Exercise capitalizes over two decades of joint efforts within the DO field. In reviewing previous works, we will focus only on multi-laboratory actions, for the sake of brevity on one side but also for a methodological reason since PAS necessarily requires consensus from many players to be effective. The three pillars of the BITMAP exercise are three Protocols for Performance Assessment of DO instruments which were elaborated in the framework of large European projects or network consortia, namely the BIP [94], MEDPHOT [91] and NEUROPT [92] Protocols, involving 7-10 different institutions each. These codify the key FOMs, procedures and phantoms for testing a DO instrument from the side of i) the basic instrument performances (BIP); ii) the capability to retrieve the optical properties – absorption (μ_a) and reduced scattering coefficient ($\mu_s^{'}$) – of a homogeneous turbid medium (MEDPHOT); iii) the detection, localization and quantification of optical inhomogeneities buried into a diffusive medium (NEUROPT). While these protocols were proposed for specific classes of DO instruments – e.g. BIP for time-domain single-photon counting systems, MEDPHOT for assessment of tissue properties as in breast spectroscopy, NEUROPT for functional brain imagers – yet their scope can be quite general, as stated by the large variety of techniques and applications covered by the tested BITMAP instruments as reported in Section 6.2.3.

Another key multilaboratory undertaking is the accurate characterization of tissue equivalent phantoms to be used to test the systems in realistic scenarios. A multilaboratory exercise [115], involving 8 institutions led to an uncertainty within 2% on the accurate characterization of intrinsic absorption coefficient of India ink and the intrinsic reduced scattering coefficient of Intralipid−20%, which can now be used as easily reproducible reference materials for liquid phantoms. At a different stage, our work was inspired also from multilaboratory comparison on instruments enrolled in multicentric clinical studies. The ACRIN 6991 initiative [116] involving 6 centers provided an extensive test on equivalent phantoms of instruments engaged in monitoring and predicting neoadjuvant chemotherapy treatment for breast cancer. The aim of the SafeBoosC international randomized phase III [117] clinical trial [118] is to determine the benefit of cerebral oximeters in preventing brain lesions in preterm infants. Since currently cerebral oximeters provide systematically different values of tissue oxygen saturation [119], the different oximeters were compared in phantoms [120] before being eligible for the trial to achieve comparability of the alarm limits.

The BITMAP Exercise presented in this paper is the largest multilaboratory comparison of DO instruments, encompassing 12 institutions and 28 systems. It is an integrated initiative with three separate actions – as detailed in Section 6.1 – that are "Collection of experimental data" (Action 1), "Consolidation of open data" (Action 2), and "Common analysis of open data" (Action 3). The key aim is to enforce the culture of PAS in the DO community and beyond and propose a common methodology which could be adopted in other environments. Further, we compare the performance of the instruments based on various data acquisition techniques and analysis methods. Finally, the work is aimed to set a reference picture of DO instrument performances to grade instrument upgrades and new developments and to provide figures in design and simulation studies.

The scope is restricted to DO instruments based on μ_a and $\mu_s^{'}$ or directly related parameters (e.g., light attenuation) as key measurables. It includes different approaches (e.g., time-resolved, frequency-domain, continuous wave multidistance, spatial frequency domain as well as different application fields (e.g., optical mammography, brain imaging, tissue spectroscopy). We exclude sources of optical contrast other than μ_a $/\mu_s^{'}$, such as fluorescence or speckle.

The paper is structured as follows: first we present the BITMAP Exercise in the context of PAS (Section 6.1), then we describe the protocols, phantoms, instruments and analysis tools adopted in the exercise (Section 6.2, next we show case exemplary results explaining the meaning of each individual test and propose a set of 20 synthetic indicators (Section 6.3), further we sum-up all performance indicators in a summary table and discuss needs and perspectives highlighted by this study (Section 6.4), finally we draw the conclusions and the key messages of this study (Section 6.5).

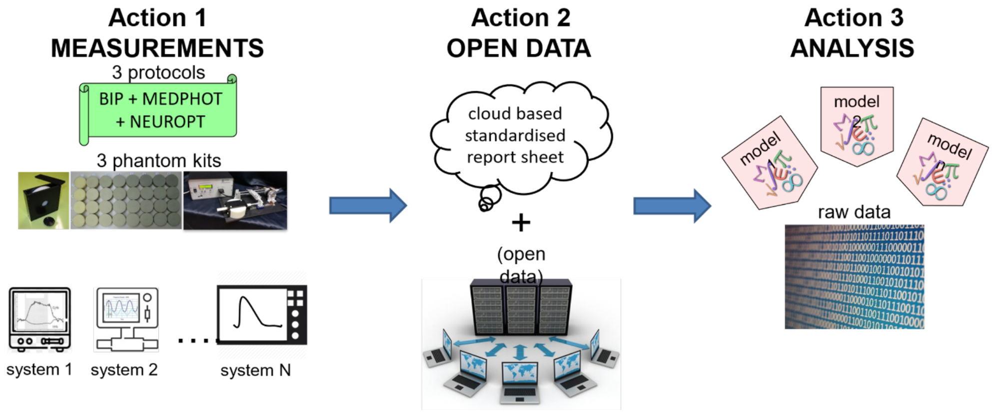

FIGURE 6.1: *The three actions involved in the BITMAP exercise.*

6.1 Methodology of the Bitmap Exercise

The BITMAP exercise originated from the Marie Skłodowska-Curie Innovative Training Network "Brain injury and trauma monitoring using advanced photonics" (BITMAP) funded by the European Commission within the Horizon 2020 program, and then evolved to include other researchers all over Europe. The whole initiative is divided in 3 actions, as depicted in Fig.6.1. The BITMAP exercise originated from the Marie Skłodowska-Curie Innovative Training Network "Brain injury and trauma monitoring using advanced photonics" (BITMAP) funded by the European Commission within the Horizon 2020 program, and then evolved to include other researchers all over Europe. The whole initiative is divided in 3 actions, as depicted in Fig.6.1.

Action 1 deals with gathering of experimental data. The instruments were challenged on 3 internationally agreed Protocols (BIP, MEDPHOT, NEUROPT, see Section 6.3) implemented with 3 phantom kits (Responsivity phantom, MEDPHOT Kit, Switchable Phantom, see Section 6.2.2). The 3 phantom kits and sets of instructions were circulated among laboratories over a period of about 2 years and an experienced researcher joined the local teams in most cases to grant uniform execution and quality control. At this stage, the data were processed by the local researchers adopting their own tools so to capture performances under the routine operation of the devices. The idea behind this is not to identify the best instrument performances achievable with the device, but rather to capture the real performances expected in a clinical scenario.

All data will be made available as Open Data in *Action 2* adopting the new SNIRF [121] format proposed by the Society for Functional Near Infrared Spectroscopy. This will permit re-use and further exploitation of the data. In this first paper, due to the vastity of results, we opted to provide only a descriptive picture of the outcome, just with few examples for clarifications. A more insightful analysis of correlation of specific hardware features with results could be pursued in focused works, also by other groups.

In particular, in *Action 3* all data will be processed using shared analysis tools so to disentangle variability due to the operator or the analysis method. Also, it will be ground to test differences among various analysis tools.

An excerpt of the results of Action 1 is presented in this paper, while the Open Data set is annotated in a companion paper in progress. The outcome of Action 3 is still ongoing and will be presented later.

Protocol	Tests	Phantoms	Measurable	Purpose
BIP	• IRF • DNL • Responsivity	Responsivity solid phantoms	• IRF (profile, background, stability) • DNL • Responsivity	Characterize the basic instrumental performances
MEDPHOT	• Accuracy • Linearity • Uncertainty • Stability • Reproducibility	Matrix of 32 homogeneous phantoms	• Absoprtion(μ_a) • Reduced scattering ($\mu_s^{'}$)	Characterize the ability of the instrument to accurately recover homogeneous optical properties
NEUROPT	• Detection • Localization • Quantification	Solid switchable phantom	• Contrast • Contrast-to-Noise Ratio	Characterize the ability of the instrument to detect an inhomogeneity

TABLE 6.1: *Summary of the Protocols, Phantoms and selected tests used for the BITMAP exercise.*

6.2 Materials and Methods

In this section, we briefly discuss the protocols and phantoms used in the BITMAP exercise and all the instruments involved.

6.2.1 Protocols

Table 6.1 summarizes the content of the three Protocols for PAS of diffuse optics-based instrumentation mentioned above, namely the BIP, MEDPHOT and NEUROPT. Each of these protocols is further divided into individual tests. A more detailed description of these tests will be presented in the results section. The measurands considered for the assessment of the instruments were limited to those relying on the estimate of homogeneous optical properties (μ_a , $\mu_s^{'}$) and the contrast of the measured on the inhomogeneous sample.

6.2.2 Phantoms

Three sets of phantoms linked to each of the above-mentioned protocols and thoroughly characterized in previous multi-laboratory studies were chosen for this exercise. In particular, we opted for solid phantoms to facilitate reproducibility of results and easy application of the tests. The phantoms were circulated sequentially to all laboratories following a round-robin scheme. In detail, for the specific test of the BIP protocol we chose a Responsivity phantom [94] (Fig.6.2a) which is a solid homogeneous turbid slab of 2 cm thickness and 10.5 cm diameter with accurately characterized diffuse transmittance factor, used to create a defined diffuse light source to evaluate the overall responsivity of the detection part of the instrument. For the MEDPHOT protocol (Fig.6.2b) we adopted the MEDPHOT kit which is a set of 32 homogeneous solid phantoms spanning a wide range of absorption and reduced scattering properties[91]. At the time of fabrication, more than 20 years ago, the nominal properties at 800 nm calculated from the concentrations of black toner and TiO_2 powder were assumed to be: μ_a from 0 to 0.35 cm^{-1} at steps of 0.05 cm^{-1}, and $\mu_s^{'}$ from 5 to 20 cm^{-1} at steps of 5 cm^{-1}. Finally, for the NEUROPt Protocol (Fig.6.2c) we used a solid switchable phantom [122] that is a solid epoxy resin matrix (120 × 80 × 45 mm^3) with standard optical properties ($\mu_a = 0.1\ cm^{-1}$ and $\nu_s' = 10\ cm^{-1}$

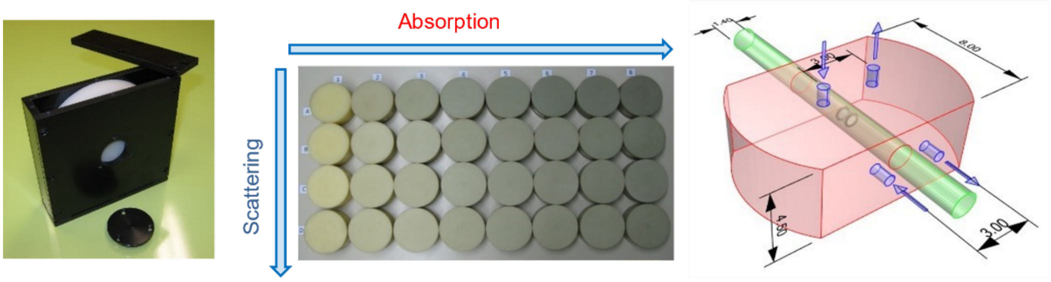

(a) (b) (c)

FIGURE 6.2: *All the phantoms used for this exercise. (a) Responsivity phantom (b) MEDPHOT kit and (c) the solid switchable phantom (dimensions in cm).*

at 700 nm) holding a rod which can slide along a direction parallel to the upper surface and set at a depth of 1.5 cm. The rod embeds a cylinder (length 0.5 cm, diameter 0.5 cm) which provides an optical perturbation equivalent to an absorption change of 0.17 cm^{-1} assuming $\mu_s' = 10\ cm^{-1}$ for the background [123].

6.2.3 Instruments and Institutions

A total of 28 instruments were enrolled for this performance assessment exercise. These instruments are listed in Table 6.2 along with some basic information on the modality and application. To give the reader an unbiased picture of the study a unique enrollment ID for each instrument will be used to represent the instrument from this point on. Not all the tests mentioned above are applicable to all the instrumentation presented in this table. For instance, the CW-only instruments (ID # 4, # 9 and # 20) were not assessed using the BIP protocols which is meant for TD Instrumentation, and neither with MEDPHOT which requires the estimate of the optical properties, which was not feasible for the above-mentioned systems. In other cases, the mechanical design or other similar obstacles restrict the application of certain tests or protocols to certain instruments, as in the case of ID # 21 and # 27 which are designed to work in transmittance alone whereas the NEUROPT protocol requires a reflectance geometry. Similarly, the design of instrument # 7 precludes the power measurement of the source (at a particular wavelength) thus making the instrument invalid for the Responsivity measurement of the BIP protocol. Table 6.3 provides a short overview of the different tests performed for each individual instrument. Irrespective of these limitations the cohort of instruments challenged under every test is still large enough to provide a valuable dataset for the other two actions. Another dimension in which the instruments enrolled show good variability is the Technology Readiness Level (TRL) [124]. A numeric scale from TRL1 to TRL9 stages the maturity of the technology, where TRL1 stands for *basic principles observed* and TRL9 to *final deployment in an operational environment*. System # 2, for example is based on an emerging technology involving a large area Silicon Photomultiplier (SiPM) detector and hence is low on the TRL scale. On the other hand, other instruments enrolled in clinical studies rank relatively higher. Finally, the ISS, NIRO and Artinis instruments (# 4, # 5 and # 20) are commercially manufactured instruments and are routinely used in a bed-side clinical environment thus exhibiting the highest possible TRL.

Instrument name	Institute	ID	Modality	Application	Analysis	TRL	Date	Ref
Clinical broadband TD-DOS	POLIMI[a]	1	TD	Spectroscopy	DE	5	02-2019	[125]
TD Large Area SiPM system	POLIMI[a]	2	TD	Oximetry	DE	3	02-2019	[126]
TD Lab system with HPM	PTB[b]	3	TD	Spectroscopy	MC	4	02-2019	[127]
NIRO 200NX	UHB/UoB[c]	4	CW	Oximetry	SRS	8	02-2019	[128]
ISS OXIPLEX-TS	UHB/UoB[c]	5	FD	Oximetry	FDMD	8	02-2019	[129]
TD Multiwavelength system	IBIB[d]	7	TD	Spectroscopy	MM	5	02-2019	[130],[131]
TD-DCS laboratory system	IBIB[d]	8	TD	Blood Flow	MM	4	02-2019	[132]
(CYRIL) SRS-CW system	UCL[e]	9	CW	Spectroscopy	SRS	6	02-2019	[49]
TRS-DCS FLOWer	ICFO[f]	10	TD	Oximetry	DE	7	02-2019	
TD lab system with MCP	PTB[b]	11	TD	Spectroscopy	MC	4	02-2019	[133]
Clinical TD oximeter	IBIB[d]	13	TD	Oximetry	MM	6	02-2019	[134],[135]
TD optical brain imager	IBIB[d]	14	TD	Oximetry	MM	6	02-2019	[136],[137]
TD MAESTROS	UCL[e]	15	TD	Spectroscopy	DE	4	12-2018	[138]
LUCA device	POLIMI[a]	16	TD	Spectroscopy	DE	6	02-2019	[139]
Oximin	IFN-CNR[i]	17	TD	Oximetry	DE	6	03-2019	[140]
Clinical Multichannel Oximeter	IFN-CNR[i]	18	TD	Oximetry	DE	6	02-2019	[141]
Wearable fNIRS (NIRSBOX)	POLIMI[a]	19	TD	Oximetry	DE	6	07-2019	[142]
OctaMon, Artinis	POLIMI[a]	20	CW	Oximetry	DE	8	01-2019	[143]
Mammot	POLIMI[a]	21	TD	Mammography	DE	6	02-2019	[144],[145]
"Fruit" spectrometer	IFN-CNR[i]	22	TD	Spectroscopy	DE	4	05-2019	[146]
OCTOPUS	POLIMI[a]	23	TD	Imaging	DE	4	05-2019	[147],[148]
Clinical DCS - BabyLux	POLIMI[a]/ICFO[f]	24	TD	Oximetry	DE	6	02-2019	[149]
Laboratory Broadband TD-DOS	POLIMI[a]	25	TD	Spectroscopy	DE	6	04-2019	[150]
Laboratory TD-DCS	POLIMI[a]	26	TD	Blood Flow	DE	4	01-2019	[151]
Mammot v2	POLIMI[a]	27	TD	Mammography	DE	6	11-2019	[152]
Benchtop DOS	UoS[g]	28	TD	Spectroscopy	DE	4	11-2019	
Multispectral SFDI	UoS[g]	29	SFDI	Imaging	MC	4	07-2020	[1],[85]
NIROT 'Pioneer' Imager	UoZ[h]	30	FD	Imaging	MC	8	02-2019	[153]

TABLE 6.2: *List of instruments involved in the BITMAP exercise:*
a - Politecnico di Milano, b - Physikalisch-Technische Bundesanstalt, Berlin, c - University Hospitals Birmingham, Birmingham/ University of Birmingham, Birmingham, d - Nalecz Institute of Biocybernetics and Biomedical Engineering, Warsaw, e - University College London, London, f - The Institute of Photonic Sciences, Barcelona, g - ICube Laboratory, University of Strasbourg, Strasbourg, h - Biomedical Optics Research Laboratory, University Hospital Zurich, Zurich, i – Istituto di Fotonica e Nanotecnologie, Milan

HPM - Hybrid photomultiplier, MCP-PMT-Micro Channel Plate photomultiplier, TD - Time Domain, CW - Continuous Wave, FD - Frequency Domain, SFDI - Spatial Frequency Domain Imaging, SRS - Spatial Resolved Spectroscopy, DCS - Diffuse Correlation Spectroscopy, DE-Diffusion Equation, MC- Monte Carlo, MM – Method of Moments, DOS - Diffuse Optical Spectroscopy, SiPM – Silicon PhotoMultiplier, SRS - Spatially Resolved Spectroscopy, FDMD - Frequency-Domain Multiple-Distance

ID # 6 and 12 correspond to instruments omitted from the exercise.

			BIP					MEDPHOT			NEUROPT
ID	**Modality**	**IRF**	**Resp**	**DNL**	**Dark**	**Lin**	**Acc**	**Stab**	**Noise**	**Rep**	**Detection**
1	TD	Y	Y	Y	Y	Y	Y	Y	Y	Y	Y
2	TD	Y	Y	Y	Y	Y	Y	Y	Y	Y	Y
3	TD	Y	Y	Y	Y	Y	Y	Y	Y	Y	Y
4	CW	N	N	N	N	N	N	N	N	N	Y
5	FD	N	N	N	N	Y	Y	Y	Y	Y	Y
7	TD	Y	N	Y	Y	Y	Y	Y	Y	Y	Y
8	TD	Y	Y	Y	Y	Y	Y	Y	Y	Y	Y
9	CW	N	N	N	N	N	N	N	N	N	Y
10	TD	Y	N	N	N	Y	Y	Y	Y	N	N
11	TD	Y	N	Y	Y	Y	Y	Y	Y	Y	Y
13	TD	Y	Y	Y	Y	Y	Y	Y	Y	Y	Y
14	TD	Y	Y	Y	Y	Y	Y	Y	Y	Y	Y
15	TD	Y	Y	Y	Y	Y	Y	Y	Y	Y	Y
16	TD	Y	Y	Y	Y	Y	Y	Y	Y	Y	Y
17	TD	Y	Y	Y	Y	Y	Y	Y	Y	Y	Y
18	TD	Y	Y	Y	Y	Y	Y	Y	Y	Y	Y
19	TD	Y	Y	Y	Y	Y	Y	Y	Y	Y	Y
20	CW	N	N	N	N	N	N	N	N	N	Y
21	TD	Y	Y	Y	Y	Y	Y	Y	Y	Y	N
22	TD	Y	Y	Y	Y	Y	Y	Y	Y	Y	Y
23	TD	Y	Y	Y	Y	Y	Y	Y	Y	Y	Y
24	TD	Y	Y	Y	Y	Y	Y	Y	Y	Y	N
25	TD	Y	Y	Y	Y	Y	Y	Y	Y	Y	Y
26	TD	Y	Y	Y	Y	Y	Y	Y	Y	Y	N
27	TD	Y	Y	Y	Y	Y	Y	Y	Y	Y	N
28	TD	Y	Y	Y	Y	Y	Y	Y	Y	Y	N
29	SFDI	N	N	N	N	Y	Y	Y	N	Y	N
30	FD	N	N	N	N	Y	Y	Y	Y	Y	N

TABLE 6.3: *An overview of the different tests applied to each of the instruments enrolled (Y-Yes/N-No).*

6.2.4 Data Analysis

For the Action 1 of the exercise, the analysis of the data obtained by each of the instruments was performed individually by the respective institutions using analysis procedures generally used when the corresponding instrument is employed e.g. in a clinical study. Particularly, for the TD instrumentation most instruments employed analysis models based on the Diffusion Equation (diffusion approximation of the Radiative Transport Equation), while some others used the stochastic MC (Monte Carlo) based models. Further information regarding data analysis for the individual instruments can be found in the instrument references in Table 6.2.

6.3 Results

The size of the dataset limits the display of the results of individual tests for all the instruments enrolled in the exercise. Rather, results are condensed to a single (or at most two) numeric values for each test, the aforementioned *figures of merit* (FOM). Exemplary plots with results from a few instruments are also plotted for specific tests in order to facilitate the readers' understanding.

6.3.1 Basic Instrument Performance (BIP)

As mentioned, this protocol concerns primarily the TD instrumentation and more specifically deals with recording the basic characteristics which influence the quality and accuracy of measurements in clinical applications. The BIP protocol collects basic information on the hardware, such as the average output power of the pulsed laser source, the repetition rate, the central wavelength and the width. But, more relevant, BIP prescribes tests on the whole system, that are: i) the temporal Instrument Response Function (IRF) - its shape, its background, and its stability in time; ii) the responsivity of the detection system; iii) the differential non linearity (DNL) of the timing electronics.

6.3.1.1 Intrument Response Function (IRF)

Measuring the IRF is crucial to understand the time resolution of a TD instrument and plays an important role in the model-based reconstruction of the optical properties. The IRF is usually measured by inserting a reference sample in between the source and detector (fibers). The reference sample should be chosen such that it duplicates the measurement conditions (such as filling the acceptance angle of the detectors/detection fibers) without modifying the temporal dispersion. A thin layer of highly scattering materials such as Teflon is used for this purpose. A detailed discussion of the IRF and the various factors that influence it can be found in Ref.[94]. However, as a first approximation, we consider the full width at half maximum (FWHM) measured in picoseconds to be the relevant metric or representative of the IRF. In other words, the *FWHM of the IRF* (at a specific wavelength) will be used as one of the synthetic descriptors.

6.3.1.2 Responsivity

The responsivity of the detection system in diffuse optics is a measure of the efficiency of detecting low light levels emerging from the tissue. In general, the responsivity of a detector is the ratio between the measured signal and the magnitude of the input illumination. In the present context, it is defined as the ratio of the photons counted by the TD instrument to the photon radiance exiting the diffusive sample. This measurement is performed with a specific "responsivity phantom" (Fig.6.2a) with known diffuse transmittance factor that acts as an approximately uniform light source with Lambertian angular characteristics [94]. A transmittance measurement is performed on this phantom and the number of photons collected at the detector over a specified time is recorded. The power input to the phantom at this specific configuration is also measured. Then substituting these values in the following formula gives the responsivity of the detector.

$$s_{det}^{L}(\lambda) = \frac{N_{tot}}{t_{meas}\kappa_p(\lambda)P_{in}(\lambda)} \tag{6.1}$$

Where $\kappa_p(\lambda)$ is the phantom-specific photon transmittance factor (expressed in units of $W^{-1}s^{-1}m^{-2}sr^{-1}$), $P_{in}(\lambda)$ is the input power at the specific wavelength (in W), N_{tot} is the total counts measured (after background subtraction) over a measurement time t_{meas}. The unit of $s_{det}^{L}(\lambda)$ is m^2sr. The *responsivity* of the instrument will be considered as the synthetic descriptor for this test. Fig.6.3 shows the responsivity of the eligible TD instruments against their corresponding FWHM (all values considered at/close to 830 nm). The instrument ID is annotated next to the data point while the application is distinguished by the marker shape in the legend, as for all subsequent population-wide plots. The spread suggests no direct coupling between these two parameters, though some general increase of FWHM upon increasing the responsivity is observed. The relatively large

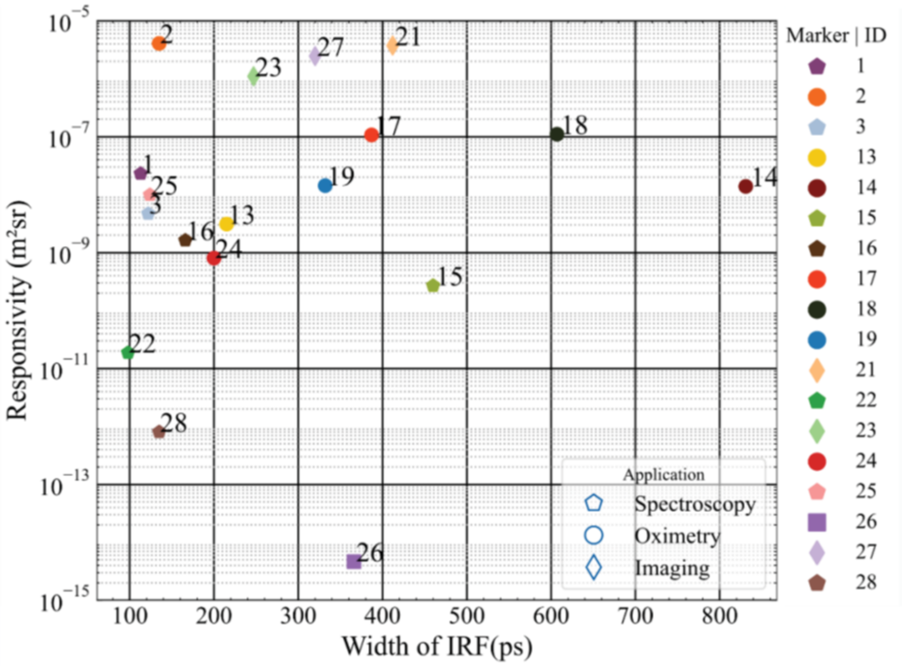

FIGURE 6.3: *Plot of the Responsivity and FWHM of the IRF of TD instruments ($\lambda \sim 830$ nm).*

responsivity of instruments # 2, # 21, # 23 and # 27 correspond to the large area SiPM detector and the two different embodiments of an optical mammograph (Mammot). All these devices work with the detector directly in contact with the sample (in this case the responsivity phantom). This explains the larger responsivity overcoming the limitation in numerical aperture and collecting area posed when using optical fibers and bundles. Most of the spectroscopy systems (hexagons) occupy the left-most part of the chart corresponding to shorter FWHMs. This substantiates the fact that the choice of the detector is much dependent on the target application of the instrument.

6.3.1.3 *Differential Non Linearity (DNL)*

DNL measures the nonuniformity of the time channel width in a TCSPC (Time-correlated single-photon counting) system. It appears as a more or less random modulation of the recorded constant photon distribution and can be corrected by a numerical equalization of the width of the time channels in case of static DNL.

The DNL is recorded as a response to a continuous signal. A battery-powered light source is preferable to avoid any electrical interference. To obtain the DNL with a good signal-to-noise ratio, each time channel should contain $\geq 10^5$ counts. Ideally, the photon counts in all time channels are expected to be equal. The deviation from this situation is characterized by the peak-to-peak difference normalized to the mean value.

$$\epsilon_{DNL} = \frac{N_{DNL,max} - N_{DNL,min}}{< N_{DNL} >} \tag{6.2}$$

6.3.1.4 *Dark Count Rate*

The dark count rate is another important feature that influences the dynamic range of the instruments' response in time domain diffuse optics. The signal-independent component of the background due to dark counts and residual ambient light can be obtained from a "dark" measurement with the laser source removed.

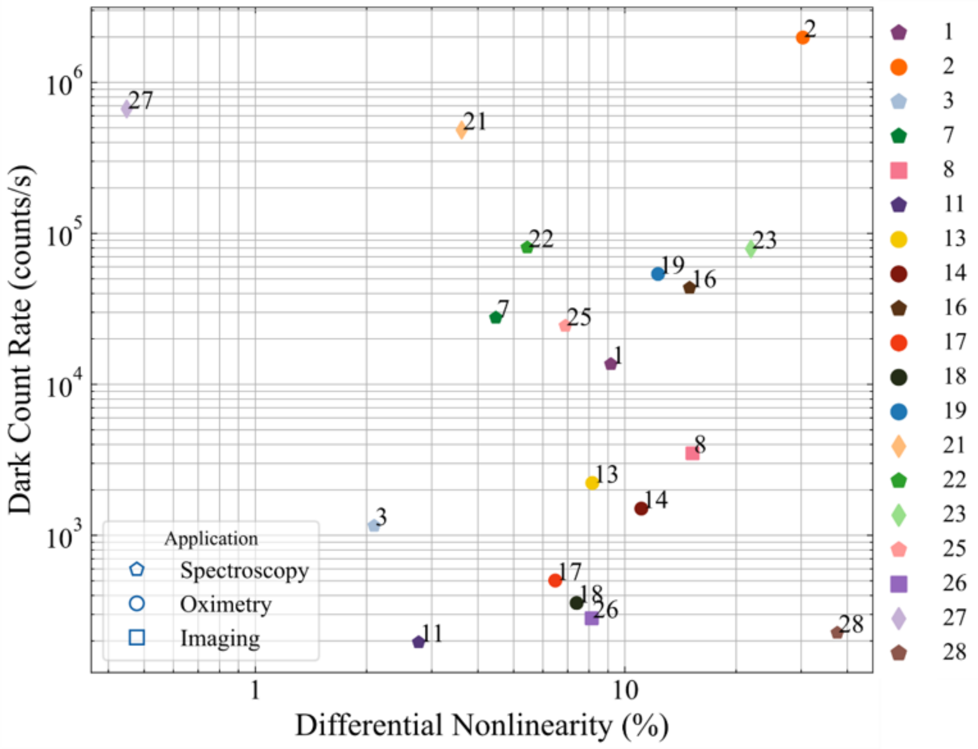

FIGURE 6.4: *Plot comparing the DCR and DNL of TD instruments.*

The *Dark Count Rate* and the *DNL* as defined in Eq.6.2 are plotted in Fig.6.4. The instruments which exhibited large responsivity in Fig.6.3 (# 2, # 21 and # 27) also demonstrate the highest values of dark count rate. While high dark count rates could reduce the dynamic range of the measurement this loss can be partially recovered by subtracting a common background value of counts.

The DNL does not seem to correlate with any particular category of instruments, being ultimately related to the compromise in cost/complexity of the TCSPC electronics. The range is quite large, but the actual impact on clinical measurements is not necessarily important, otherwise it can be corrected. For instance, when photons are summed over large ($\sim$ 500 *ps*) temporal gates for contrast measurements, the DNL has usually minor effects.

6.3.2 The MEDPHOT Protocol

Formulated in the early 2000s, MEDPHOT is a performance assessment protocol designed under the European Thematic Network with the same name. The different tests outlined in this protocol characterize the instruments' capabilities to accurately retrieve the absorption and reduced scattering coefficients. For this reason, only instruments capable of recovering absolute optical properties are eligible for this protocol. A detailed explanation of the protocol along with the tests involved can be found here [91]. Some of the tests in this reference article use "conventionally true" values of the optical properties and compare the results from the experiments to these values. However, in the interest of an unbiased understanding of the results, the same tests when applied here are slightly modified to eliminate the need for such "conventionally true" values.

Some general considerations for all the measurements performed as a part of the MEDPHOT protocol are.

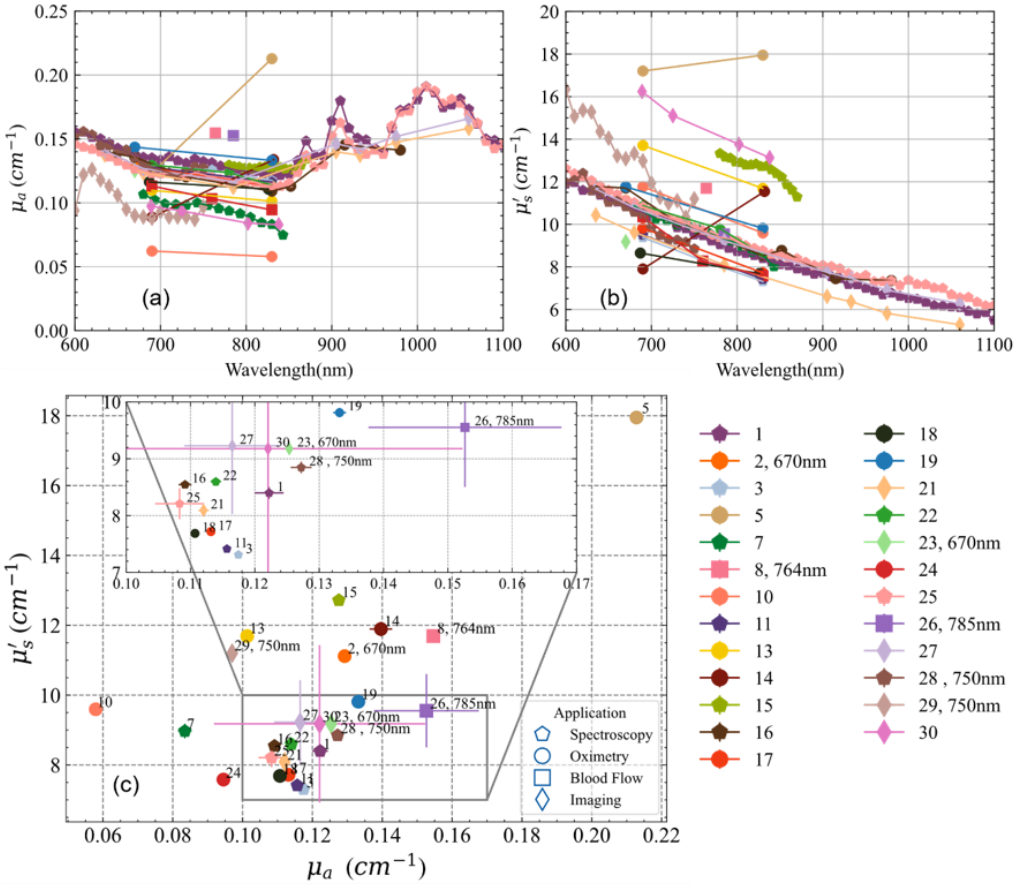

FIGURE 6.5: *The absorption (a) and reduced scattering (b) spectra of all the TD instruments measured on the Phantom B3 of the MEDPHOT kit. The panel (c) shows these optical properties plotted against each other at* 830 *nm (wavelength mentioned in cases where it is not* 830 *nm). Results represent the average over the 20 repetitions with the standard deviation plotted as error bars. The inset box is a zoom on the overlapped instruments. The instrument ID is annotated next to the datapoint and presented as a legend to the right.*

- The standard acquisition time of measurements was 1 s.
- Every measurement was repeated 20 times, the results presented are the average of the 20 measurements and the standard deviation over the 20 measurements is plotted as error bars (wherever applicable).
- Apart from the Accuracy and Linearity measurements (which were performed over the entire MEDPHOT kit) all the other tests were performed on the B2 Phantom of the MEDPHOT kit (nominal values at 800 nm: $\mu_a = 0.05\ cm^{-1}$, $\mu_s' = 10\ cm^{-1}$).
- The target count rate from the TD instrumentation was $5 \times 10^5\ s^{-1}$. But this particular condition was more suggestive than restrictive (in case the standard operating conditions of the instruments demanded a different count rate, as for large area SiPM detectors with high dark count rate).

6.3.2.1 Accuracy

The accuracy test addresses the capability of the system to retrieve the absolute estimate of the absorption and reduced scattering coefficients of a reference medium or phantom. As an example, Fig.6.5(a,b) displays the absorption and reduced scattering coefficients

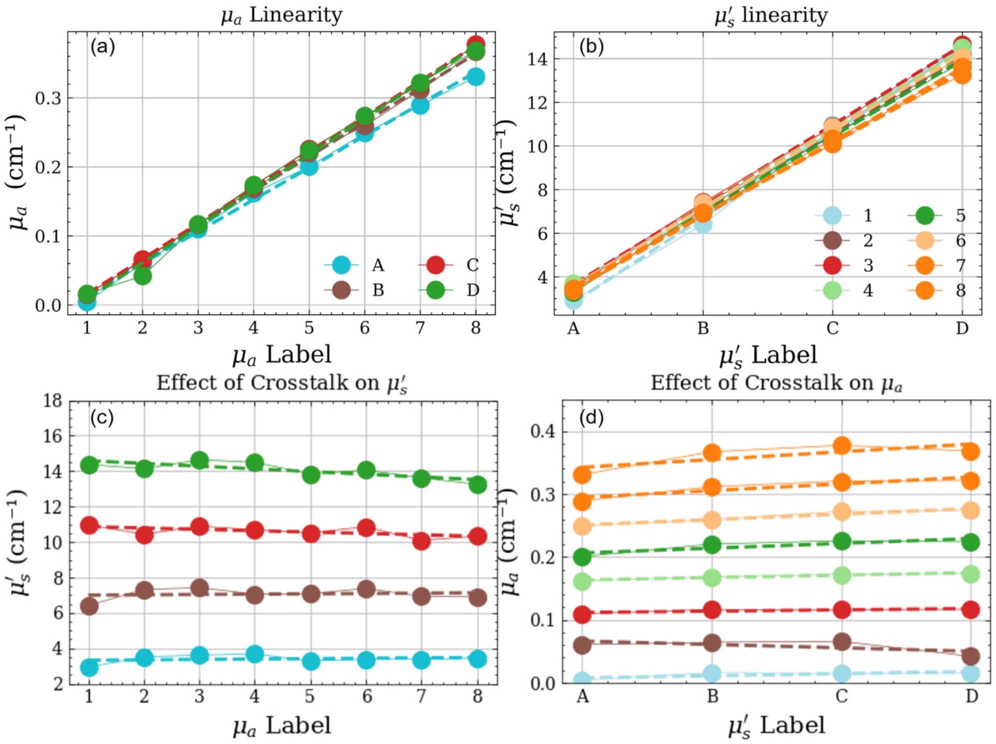

FIGURE 6.6: *An exemplary plot of the linearity and coupling between the optical properties. (a) and (b) show the linear increase in the absorption and reduced scattering coefficients for each series corresponding to their labels (x-axis). (c) and (d) show the influence of one optical property on the other.*

vs. wavelength obtained from all the instruments when measuring one of the phantoms (B3, nominal values at 800 nm: $\mu_a = 0.1\ cm^{-1}$, $\mu_s' = 10\ cm^{-1}$) of the MEDPHOT kit. Figure 6.5(c) shows the optical properties provided by different instruments at 830 nm (data for instruments not operational at this wavelength are provided at the wavelength closest to 830 nm). Overall, the mean deviation of instruments operating at 830 nm is 16% and 19% of the average value for absorption and reduced scattering, respectively. The data point with the maximum deviation from the rest (# 5) corresponds to one of the frequency domain instrument in the cohort, still this discrepancy could be due to the calibration procedure of this device rather than to the technique itself.

6.3.2.2 Linearity and Crosstalk

The aim of this test is to ascertain the linearity in retrieval of the optical properties which grants – for instance – the preservation of the spectral shape, and also to characterize the unwanted crosstalk between the two optical parameters leading to artefacts in the estimate of optical properties. Figure 6.6 shows an exemplary plot for a specific instrument (# 11). The upper row displays the linearity in μ_a (Fig.6.6a) and $\mu_s^{'}$ (Fig.6.6b), respectively. The lower row represents the absorption-to-scattering (Fig.6.6c) and scattering-to-absorption (Fig.6.6d) crosstalk, respectively. Ideally, points should be lying on the regression line in the top row and on horizontal lines in the bottom row, irrespective of the absolute values.

The synthetic indicators are obtained in the following way. For the linearity plots i.e. Fig.6.6(a,b) the median value of the relative deviation of the data-points and the linear fit (dashed line) over the different series is considered to represent the median deviation from linearity for the specific optical property.

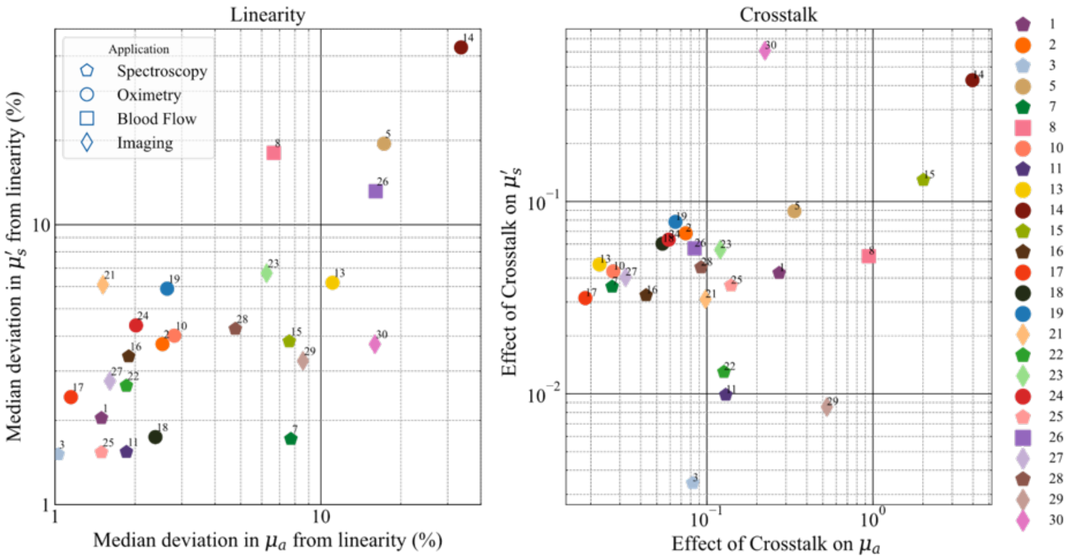

FIGURE 6.7: *FOM plots for the Linearity and Crosstalk tests of the MEDPHOT protocol.*

For the crosstalk plots in Fig.6.6(c,d), the median value of the absolute slopes of the linear fit (dashed line) over the different series is considered as a factor representative of the coupling between the two optical properties. Yet, to provide a more directly intelligible indicator, we prefer to refer the coupling to relative, rather than absolute changes in optical properties. In detail, let S_{μ_s'/μ_a} be the median of the absolute slopes of the linear regression of the different series in scattering (Fig.6.6c), and $\Delta\mu_a^{cause}$ be a variation introduced in the absorption coefficient. Then, $\Delta\mu_s^{\prime,effect}$ is the corresponding variation introduced in the reduced scattering coefficient due to the inherent coupling between the two parameters, that is:

$$\Delta\mu_s^{\prime,effect} = S_{\mu_s'/\mu_a} * \Delta\mu_a^{cause} \tag{6.3}$$

Now, expressing the same effect in relative terms with respect to reference optical properties ($\mu_a^0 = 0.1\ cm^{-1}$, $\mu_s^{\prime,0} = 10\ cm^{-1}$) we obtain:

$$\frac{\Delta\mu_s^{\prime,effect}}{\mu_s^{\prime,0}} = F_{\mu_s'\rightarrow\mu_a}\frac{\Delta\mu_a^{cause}}{\mu_a^0} \tag{6.4}$$

Where we define $F_{\mu_s'\rightarrow\mu_a} = S_{\mu_s'/\mu_a}\frac{\mu_a^0}{\mu_s^{\prime,0}}$ as the relative absorption-to-scattering coupling coefficient, which will be used as the FOM for crosstalk. A similar definition is provided for the relative scattering-to-absorption relative coupling, that is $F_{\mu_a\rightarrow\mu_s'} = S_{\mu_a\mu_s'/\mu_a\mu_s'}\frac{\mu_s^{\prime,0}}{\mu_a^0}$. For example, referring to Fig.6.6d, a relative scattering-to-absorption crosstalk $F_{\mu_s'\rightarrow\mu_a} = 0.13$ means that any factor resulting in an increment of 10% in the reduced scattering coefficient (cause) is expected to alter the measured absorption coefficient by $0.13 * 10\% = 1.3\%$ (effect). Surely, this definition is dependent on the choice of the reference optical properties and must be rescaled for different actual properties, but it is more effective than the absolute discrepancy from linearity to easily interpret the system performances.

Figure 6.7 presents the resultant plots for the linearity and crosstalk tests for the whole instrument population. The left pane shows the *linearity* of the two optical properties against each other (absorption on the x-axis and reduced scattering on the y-axis) while the right pane shows the crosstalk for the same properties. In the plot for *linearity*, 20 out of the 24 instruments enrolled exhibit a median deviation from linearity in both optical properties under or close to 10%. The instruments designed for DCS (blood flow, # 8, # 26) and the frequency domain instrument (# 5) show a little larger deviation in linearity. Again, most of the spectrometers (hexagons) are seen to have a deviation better than 3% in the linearity of reduced scattering ($\mu_s^{'}$) and better than 2% in the linearity of absorption. In general, there is a trend of correlation between the deviations in linearity in absorption and in scattering, which is reasonable since systems more optimized for e.g. spectroscopy are designed to accommodate large variations in signal intensity – by means for instance of low background noise – and variations in shape of the Distribution of Time of Flight (DTOF) – by adopting a detector with a narrow IRF and high dynamic range.

The plot for *crosstalk*, shows – for most of the instruments – a relative scattering-to-absorption ($F_{\mu_s' \rightarrow \mu_a}$) and absorption-to-scattering ($F_{\mu_a \rightarrow \mu_s'}$) crosstalk $< 20\%$ and $< 10\%$, respectively.

6.3.2.3 Stability

Fig.6.8 (a,b) displays some exemplary plots of the temporal stability in the retrieved optical properties based on a measurement over a period of more than 1 hour for two instruments. Both the absorption and reduced scattering coefficients are stable within a range of ±10% for # 2 while under 4% for # 19. In this case, the *range of variation* over the entire measurement period and the drift given by the *slope of the temporal evolution* plots were considered as the synthetic indicators.

Fig.6.8(c,d) plots the above-mentioned synthetic indicators for both optical properties for all instruments. Most of the instruments lie in the region with a range under 10% for both optical properties. Also, in most cases, the drift (slope) in estimated properties is $< 0.03\%$ per minute. This means that using any of these instruments for a continuous monitoring of the optical properties in a clinical environment, one can expect a maximum deviation of 0.03% in μ_a in one minute (or 3% in 100 minutes).

6.3.2.4 Noise-Uncertainty

A test of the influence of the collected energy (or total counts) on the uncertainty of the measured optical properties is performed by measuring the time-of-flight signals at different count rates. Twenty acquisitions, with 1 second acquisition time, were taken at different count rates. The coefficient of variation CV (defined as the ratio of the standard deviation of repetitive measurements over the mean value) for the retrieved optical properties at each count rate are plotted against the total counts as shown in Fig.6.9. As a general practice, a $CV = 1\%$ can be considered as a reasonable target for uncertainty of diffuse optics measurements.

The Noise/Uncertainty plot identifies the minimum number of counts or input energy required to reach such a goal (the dashed horizontal lines in Fig.6.9). This is further dependent on the maximum count rate of the system or the maximum input power and correspondingly affects the acquisition time.

The synthetic indicators chosen for the Noise test are the number of counts necessary to reach a CV of 1% in both the optical properties. Fig.6.10 plots the counts necessary to achieve 1% CV in $\mu_s^{'}$ against counts necessary to achieve 1% CV in μ_a . The requirement for a good CV in most cases is in between 10^5 and 10^6 counts and, in most cases, it is closer to the former. Also, all the results are not far from the line of identity in the plot suggesting the count rate necessary to achieve 1% CV is nearly the same in both optical properties. An interesting observation in this regard is that instrument # 7 that relies on the method of moments for fitting requires a substantially lower number of counts to achieve a minimal variation in the results as compared to the rest of the instruments. Thus, it would be interesting to understand how the usage of this method of analysis

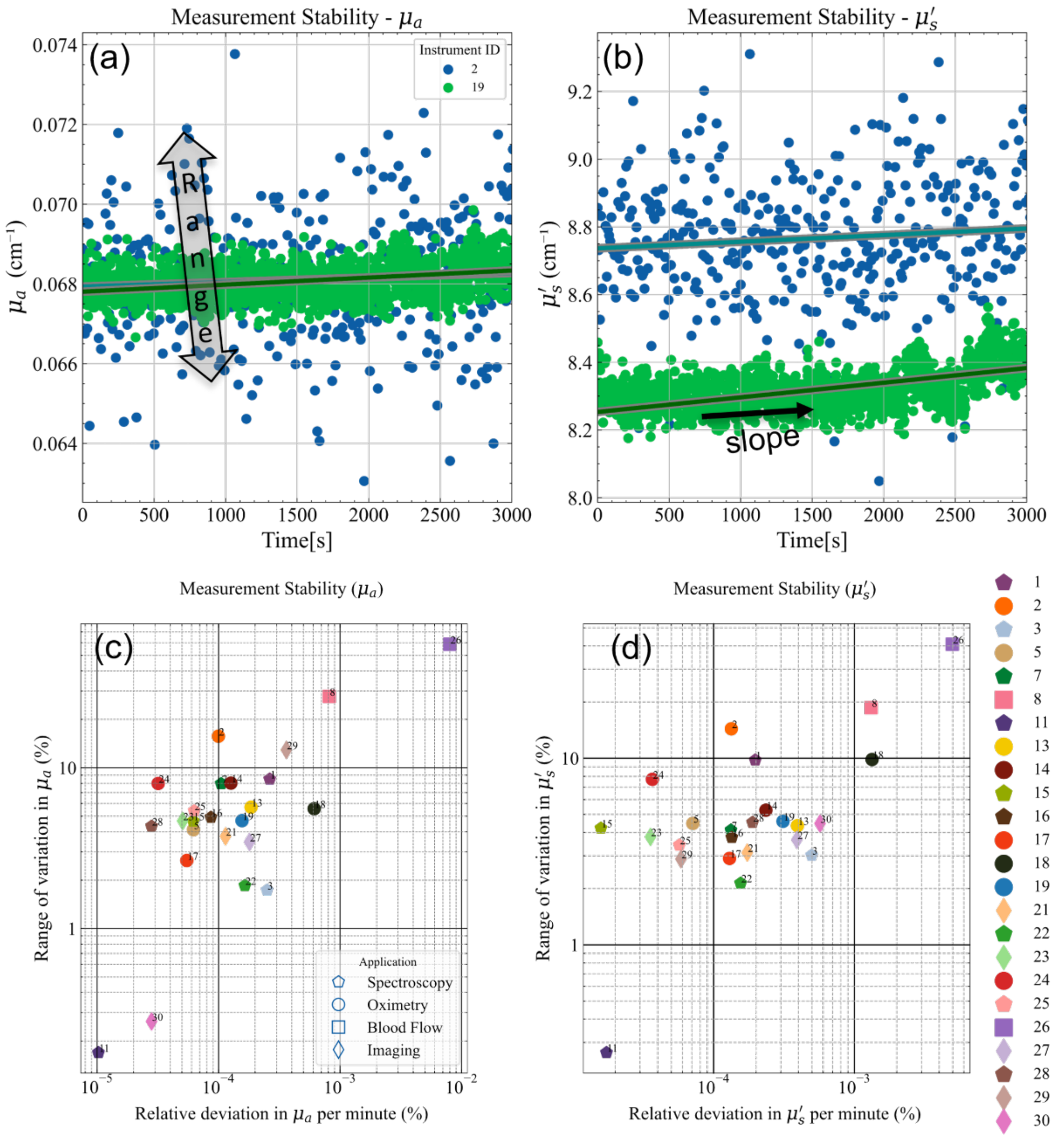

FIGURE 6.8: *Example (a and b) of the measurement stability plots for instruments 2 and 19 (on the B2 Phantom). The synthetic indicators (range and slope). The slope in this case describes the variation in the recovered optical property with time. The corresponding FOMs are presented below (c and d).*

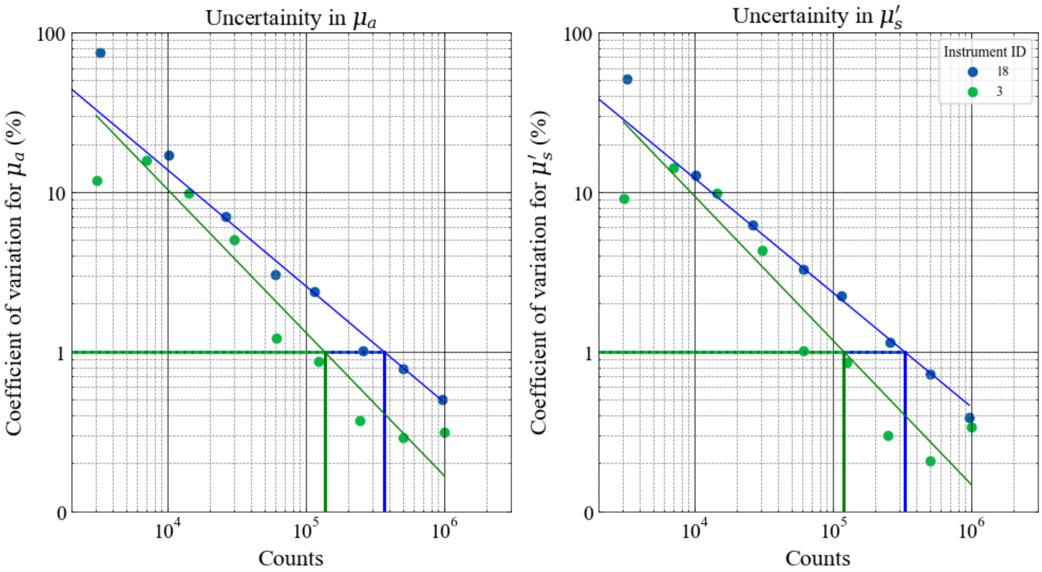

FIGURE 6.9: *Coefficient of Variation (%) in the optical properties plotted against the number of counts for instruments # 3 and # 18 (test performed on the B2 Phantom). A linear fit is performed to determine the number of counts necessary to achieve a CV of 1%. These values are used as the FOMs in Fig.6.10.*

(which is different from the traditional analytical solution based on the DE employed for a majority of the other instruments enlisted) fares with the other instruments. These kinds of studies will be undertaken in the Action 3 mentioned above.

6.3.2.5 Reproducibility

The reproducibility test, as the name suggests, is a general test of how reproduciblility of the instrument's performance on a day-by-day basis. Fig.6.11 displays the reproducibility for 3 instruments. Data were taken over 3 different measurement sessions (usually spanning 3 different days). As a synthetic indicator for this case, we adopted the CV over the 3 measurement sessions, which is plotted for the whole population in Fig.6.12 for both optical properties.

Generally ($>$ 70% of instruments), the reproducibility is better than 5% in both optical properties with some of them better than even 1%. Such a testing is critical in a clinical scenario and in general represents a good scientific conduct. Instruments with relatively large values of CV can still be utilized as long as sufficient measures are taken to address this concern. A good example for this would be the commercial frequency domain instrument enrolled in this study (# 5). A phantom (provided by the manufacturer) with known optical properties is generally used to calibrate the instrument before clinical use, which improves the reproducibility in the results.

6.3.3 The NEUROPT Protocol

While it was originally developed and first applied in the context of time-domain optical brain imaging, this protocol can be applied to other modalities as well, such as continuous wave and frequency domain. Two of the tests from this protocol were chosen for the BITMAP exercise, namely the Contrast and Lateral Resolution tests. Out of these, we present here the results from the contrast measurements.

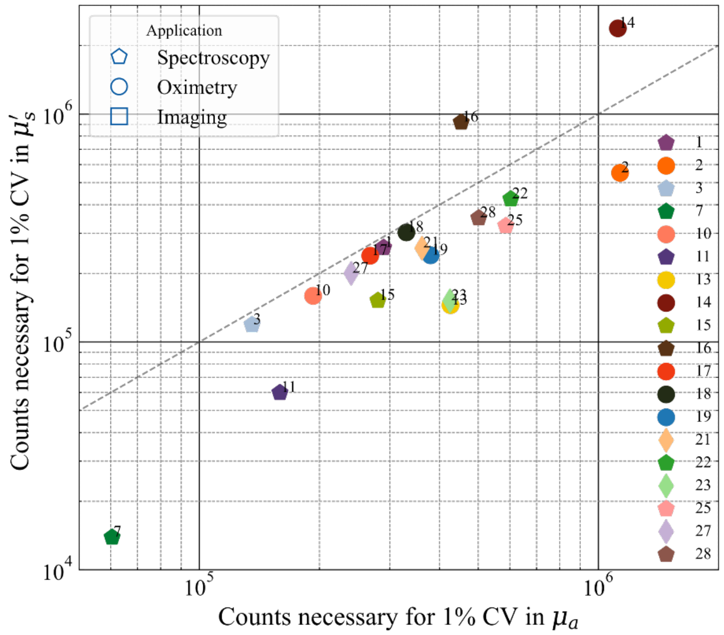

FIGURE 6.10: *Comparison of the different instruments in terms of the Noise/Uncertainty measurement.*

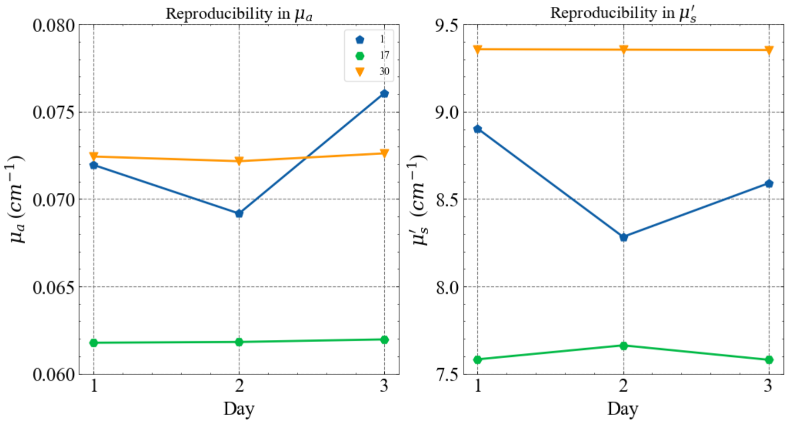

FIGURE 6.11: *Day-to-day reproducibility in both the optical properties for some of the instruments at* 830 *nm (all measured on phantom B2 of the MEDPHOT series).*

6.3.3.1 Detection of an inhomogeneity: Contrast and contrast-to-noise ratio

To ascertain the depth sensitivity of instruments to localized optical perturbations – for e.g. functional imaging of brain activity – the systems were tested on an inhomogeneous phantom made of a bulk homogeneous material holding a rod with an embedded inclusion (Fig.6.2c). A detailed description of the test can be found in Ref.[92]. Briefly, the test involved measuring the DTOF signals (for TD) or photocurrent (for CW) on the phantom seen in Fig.6.2c in reflectance with the inhomogeneity moving deeper into the phantom. This depth scan is realized by placing the optodes on the side surface of the phantom (at the positions marked in Fig.6.2c).

Then, the contrast is defined as the relative difference in total photon counts given by:

$$C_i = \frac{M_i - M_0}{M_0} \tag{6.5}$$

Here, C_i is the contrast at position i, M_i corresponds to the number of counts in a certain

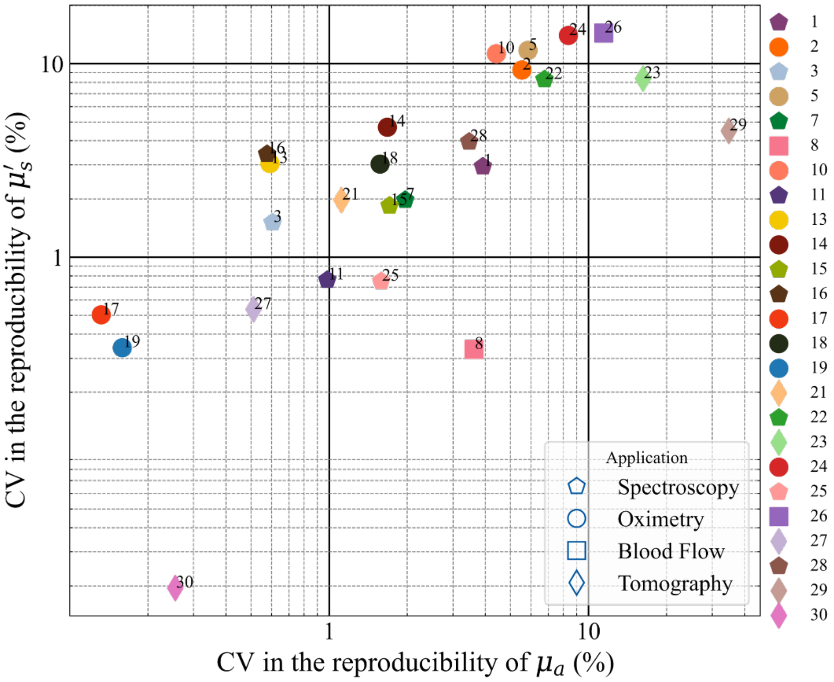

FIGURE 6.12: *Comparison between instruments for the day-to-day reproducibility.*

time window with the inclusion at position i and M_0 is the corresponding number of counts on the DTOF measured on a homogeneous region (far from the inclusion) of the phantom. Since each measurement was repeated for 20 times, this also allowed for a calculation of the Contrast-to-noise ratio (CNR) given by:

$$CNR_i = \frac{M_i - M_0}{\sigma(M_0)} \tag{6.6}$$

Here, $\sigma(M_0)$ refers to the standard deviation of the 20 acquisitions performed at each position at the baseline/homogeneous state. The black inclusion used for this exercise has a diameter of 0.5 cm and a length of 0.5 cm. The equivalent perturbation/inhomogeneity in absorption ($\Delta\mu_a$) achieved by this inclusion is 0.17 cm^{-1} supposing an effective volume of 1 cm^3 and for a background μ_s' of 10 cm^{-1} [123].

The two parameters described above, namely the *contrast* and the *CNR* ratio will be used as the synthetic indicators for this test. For time domain instrumentation, the resultant DTOFs can be sliced in time and the counts from the resultant "time-windows" can be inserted in the Eq.6.5 and Eq.6.6 to get the contrast and CNR at specific time windows. The DTOFs measured in the BITMAP exercise were divided into time windows of 400 ps width starting from the IRF which were then used to plot the contrast at early and late windows.

Exemplary plots of contrast and CNR for the depth scan at an "early" (corresponding to the time interval $400-800$ ps) and "late" time window (corresponding to the time interval $2000-2400$ ps) for instrument # 16 can be found in Fig.6.13. The contrast plots at early and late windows suggest that for early time windows the peak contrast is observed at shallower depths (at around 7 mm in this case) while the late windows see maximum contrast at deeper regions (around 11 mm). The CNR values as a function of depth have profiles similar to the contrast profiles. The maximum value of CNR at the early window is, however, much higher than the maximum value at a late window (logarithmic axis). The *contrast* and *CNR* values at the late window at a depth of 20 mm were chosen

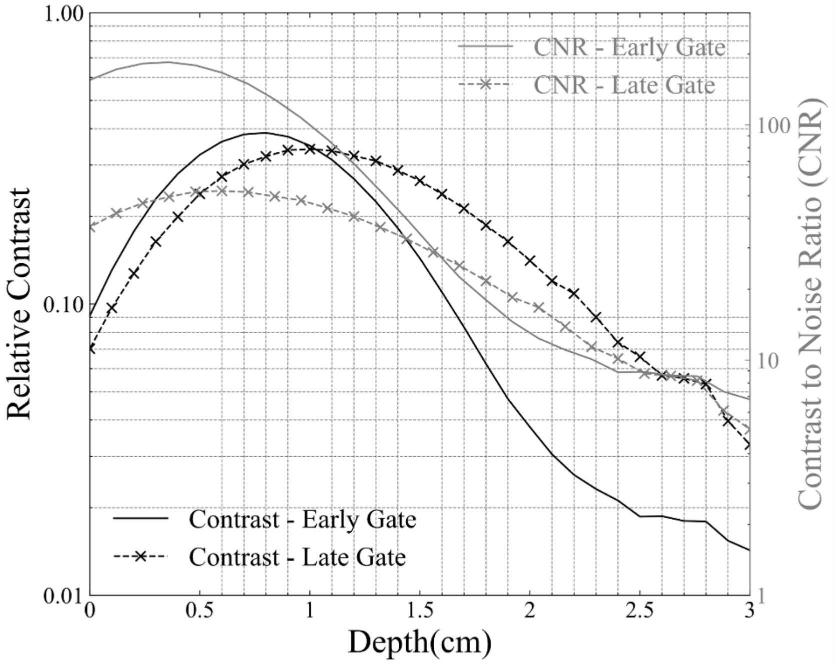

FIGURE 6.13: *Depth dependent Contrast and CNR values plotted against the inclusion depth for the Z-scan for an early and late time window. (Instrument # 16).*

as the two synthetic indicators for this particular test. Since the concept of windowing is applicable only to the TD instruments the contrast and CNR values of the CW instruments were calculated based on the total measured counts. The resultant plot is shown in Fig.6.14.

A good spread is evident both in contrast and CNR values over all the instruments enrolled. Literature suggests that the depth dependent contrast when analyzing time windows is influenced by the instrument response (IRF) [92]. This is confirmed from the results since all the instruments which have hybrid PMT or MCP based detection system (i.e. # 11, 3, 13, 14 and 15) are clustered at the top right corner of the plot suggestive of better contrast and CNR values. This could be attributed the IRF profiles of these instruments which have a fast-decaying tail with almost negligible influence at later photon arrival times. On the contrary, silicon-based detectors have an exponentially decaying tail which could affect the performance of the instruments employing these detectors (# 1, 2, 22, 23, 25, 19) thus leading to relatively lower values of contrast. Similarly, higher values of CNR were observed for instruments with higher responsivity since this implies lower photon noise for the same acquisition time and inter-fiber distance. CW instruments (empty markers) show very low values of contrast suggesting poor sensitivity at large depths (20 *mm*). The improved depth sensitivity for TD systems is due to the increasing mean photon depth upon increasing photon travelling time resulting in higher depth sensitivity for late time-windows [154].

6.4 Discussion

Table 6.4 summarizes the key statistical descriptors of the synthetic FOMs presented above in the summary figures. The table reports the number of instruments tested for each FOM (counts), the minimum, maximum, mean and standard deviation of the distribution, and the inferred values corresponding to the 25%, 50% (median) and 75% percentiles. Starting from the BIP Protocol, and specifically from the *FWHM* of the IRF,

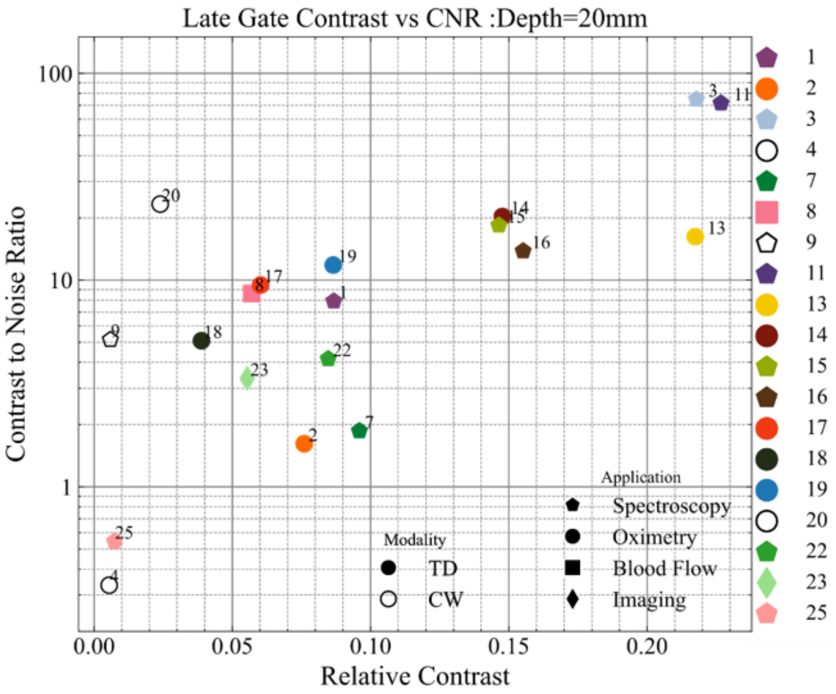

FIGURE 6.14: *Figure of Merit plot for the contrast test of the NEUROPT protocol (Contrast vs CNR at an inclusion depth of* 20 *mm).*

applicable only to TD system, sub-ns performances are always retrieved with typical values in the $150 - 400$ ps range ($25\% - 75\%$ percentile). The *responsivity* spans almost 9 decades, encompassing systems equipped with single-mode fiber (DCS) or very large area detectors, with a median value of 10^{-2} mm^2sr. Large differences in *dark count rate* and *DNL* are observed, spanning a range of 4 and 2 orders of magnitude (200-2,000,000 counts/s and $0.4\% - 40\%$) with median values of 10,000 counts/s and 8%, respectively. These huge differences reflect the wide heterogeneity of instruments, encompassing various photonics devices. These FOMs can be further studied to investigate the impact of hardware performances on clinically related results.

Moving to the MEDPHOT Protocol and starting from the accuracy test, to avoid bias due to erroneous knowledge of true optical properties, we describe the *accuracy* in terms of deviation around the median value. This figure has no meaning for the single instrument because the median is not a substitute for the true value, but it is relevant to describe the disagreement within the whole population. We obtained a median relative discrepancy $< 9\%$, with still 75% of instruments within a 20% displacement. In terms of linearity, most instruments perform well (median$< 4\%$, 75% percentile $< 8\%$). Median *crosstalk* is around 9% for $F_{\mu_s' \to \mu_a}$ and 5% for $F_{\mu_a \to \mu_s'}$. This means that, for instance, a change of 10% in μ_s' yields an artificial increase by 1% in the measured μ_a . In terms of *noise*, for half of the systems $< 3.6 \times 10^5$ and $< 2.4 \times 10^5$ counts are needed to obtain an uncertainty of 1% on μ_a and μ_s' , respectively. The *stability* of systems is rather good with a median range of variation $< 5\%$ and a median drift $< 0.01\%$ per minute. Day-by-day *reproducibility* on μ_a and μ_s' is on the order of $< 2\%$ and $< 3\%$, respectively, for half of the systems and still with an acceptable $< 6\%$ and $< 8\%$ for the 75% percentile.

Finally, the NEUROPT Protocol addresses the detection of a reference optical inhomogeneity at 2 cm depth within an otherwise homogeneous medium. For time-domain systems this test depends on the selected time-window, and we opted to compare all systems for a $2000 - 2400$ ps window. This leads to a median *contrast* of 9% and a median

Protocol	Test	Unit	FOM	Opt	count	mean	std	min	25%	50%	75%	max
BIP	IRF	ps	FWHM	All	18	293	197	98	135	231	382	831
BIP	Responsivity	mm^2sr	Responsivity	All	18	6.50E-01	1.30E+00	4.70E-09	1.00E-03	1.20E-02	1.10E-01	4.10E+00
BIP	DarkCounts	counts/s	Dark Counts	All	19	1.82E+05	4.71E+05	1.96E+02	8.30E+02	1.36E+04	6.64E+04	1.98E+06
BIP	DNL	-	DNL	All	19	11.00%	9.70%	0.40%	5.00%	8.10%	13.60%	37.60%
MEDPHOT	Accuracy	-	Deviation	Mua	25	15.30%	18.60%	0.00%	4.80%	9.20%	18.90%	82.70%
MEDPHOT	Accuracy	-	Deviation	Mus	25	16.70%	19.50%	0.00%	4.50%	11.80%	21.10%	95.50%
MEDPHOT	Linearity	-	Linearity	Mua	25	6.50%	7.60%	1.00%	1.90%	2.60%	7.70%	33.70%
MEDPHOT	Linearity	-	Linearity	Mus	25	6.70%	8.90%	1.50%	2.40%	3.70%	6.10%	43.00%
MEDPHOT	Linearity	-	Crosstalk	Mua	25	38.30%	85.80%	1.90%	5.40%	9.20%	22.40%	397.00%
MEDPHOT	Linearity	-	Crosstalk	Mus	25	8.40%	13.60%	0.30%	3.30%	4.50%	6.30%	60.80%
MEDPHOT	Noise	counts	Counts1%	Mua	19	4.18E+05	2.89E+05	6.05E+04	2.54E+05	3.61E+05	4.77E+05	1.13E+06
MEDPHOT	Noise	counts	Counts1%	Mus	19	3.81E+05	5.24E+05	1.39E+04	1.52E+05	2.40E+05	3.37E+05	2.38E+06
MEDPHOT	Stability	min^{-1}	Drift	Mua	24	0.05%	0.16%	0.00%	0.01%	0.01%	0.02%	0.80%
MEDPHOT	Stability	min^{-1}	Drift	Mus	24	0.05%	0.10%	0.00%	0.01%	0.02%	0.04%	0.50%
MEDPHOT	Stability	-	Range	Mua	24	8.60%	12.10%	0.20%	3.70%	4.80%	8.00%	58.60%
MEDPHOT	Stability	-	Range	Mus	24	6.90%	8.30%	0.30%	3.30%	4.30%	5.90%	40.80%
MEDPHOT	Reproducibility	-	Reproducibility	Mua	25	4.70%	7.40%	0.10%	0.60%	1.70%	5.50%	34.80%
MEDPHOT	Reproducibility	-	Reproducibility	Mus	25	4.50%	4.50%	0.00%	0.80%	3.00%	8.30%	14.40%
NEUROPT	Detection	-	CNR	All	19	20.8	30.7	0.3	3.7	12.5	20.9	104.9
NEUROPT	Detection	-	Contrast	All	19	8.60%	6.50%	0.50%	3.10%	8.40%	14.30%	20.00%

TABLE 6.4: *Summary statistics of the synthetic FOMs.*

CNR of 13. We stress again here that these synthetic indicators are obtained for reference conditions (in most of the cases for a background medium with $\mu_a = 0.1\ cm^{-1}$ and $\mu_s' = 10\ cm^{-1}$) and therefore should be interpreted properly for the real clinical situation.

This large-scale BITMAP campaign allowed us to identify some critical issues related to performance assessments in DO, that we will discuss in the following.

1. *Accurate multilaboratory characterization of solid phantoms*. While for liquid phantoms a good level of reliability in optical characterization was reached through multilaboratory studies [115], conversely solid phantoms – which are definitely more suitable for practical use – are still prone to a larger uncertainty in the determination of optical properties. The present BITMAP exercise cannot help in this direction since the goal was to compare instruments and not to accurately characterize phantoms. Therefore, data in Fig.6.5 cannot provide an estimate of the "conventionally true" phantom optical properties. What is needed instead – similarly to the process that led to the characterization of aqueous solutions of Intralipid and ink [115] – is a first set of individual works identifying the most suitable characterization approaches, followed by multilaboratory undertakings to converge to common values. This activity could surpass the specific realm of diffuse optics, since it is a common need for many other optical techniques (e.g. photoacoustics, fluorescence, optical coherence tomography, diffuse correlation spectroscopy, diffuse Raman spectroscopy).

2. *Easily available common phantom kits*. The whole BITMAP exercise was run using a unique collection of three phantom kits. In the ideal case, the availability of identical or highly reproducible phantom kits easily accessible for any laboratory would permit to repeat the test over time and benchmark system upgrade or development of novel instruments in an absolute way. These tools are already available in other more mature clinical techniques such as MRI and ultrasounds. Surely, the above-mentioned issue # 1 is a prerequisite.

3. *Link FOMs to specific clinical features*. The three protocols and related FOMs were designed starting from paradigmatic clinical problems. To derive clinical implications from the lab system performances we need to quantify the impact of a given FOM on specific clinical applications. For instance, using a set of equivalence classes, optical perturbations caused by brain activation or breast lesion were quantified in terms of an Equivalent Black Volume (EBV) [123] which is then directly mapped

to the *contrast* or *CNR*. For instance, in an exemplary case, a malignant breast lesion was graded at $EBV \approx 100\ mm^3$, while a subtle motor task brain activation at $EBV \approx 10\ mm^3$. Data in Table 6.4 were obtained for $EBV \approx 170\ mm^3$. Existing clinical datasets could be re-analyzed to link existing FOMs to clinical features and study the impact of system performances on *in vivo* measurements. Surely, the increasing availability of open data sets could unleash meta-analysis of different datasets, although informative metadata are often needed and not standardized yet to interpret DO data.

4. *Analysis*. Despite other direct imaging modalities (e.g. X-ray), DO results strongly depend on the model and data analysis in use. Often, it is not easy to disentangle inaccuracies related to the hardware from misfit in the model. The fairly large variability observed in Fig.6.6 could be reduced adopting the very same analysis tool. In this first *Action 1* we opted to present the results following the analysis approach chosen by each group in daily applications. This should roughly correspond to the expected behavior under clinical applications. In *Action 3*, we will pursue the common analysis of the whole dataset using the very same tools, hoping to reduce variability and identify the most effective and robust analysis methods. We observe a plethora of proposed approaches and implementations in retrieving optical properties of homogeneous media, ranging from the Diffusion Equation to different orders of approximation of the Radiative Transport Equation, from the Random Walk to Monte Carlo tools. Still, proprietary analysis tools, or complex-to-implement analytical solutions hinder reaching consensus or common daily use. Emerging of open software suites is definitely a plus in this direction, and again we need more and more interlaboratory studies or common analysis of multiple datasets.

5. *Interoperable data format*. Given the enormous effort involved in clinical studies, the possibility to reanalyze existing datasets is of great interest and efficiency. Even consolidated phantom measurements can be used to test new approaches. The adoption of open-source analysis platforms (e.g. HOMER [155], NIRFAST [156]) can speed the analysis process and consistency of results. Also, the deployment of Open Data sets, required by many funding agencies, will offer a wealth of *in vivo* and phantom data. Some attempts in setting data formats for DO were proposed following e.g. the HOMER [155] or SNIRF [121] standards. For the deployment of BITMAP open data, we will pursue the latter, proposed by the Society for Functional Near Infrared Spectroscopy [157]. Although tailored to a specific application, and lacking a bit of generality, yet the SNIRF format can reduce the Babel of individual data specifications to a single data format which then can be easily uploaded to analysis tools or converted to specific formats. Other fields reached impressive results in this respect – for example the DICOM format for clinical images – but also emerging areas such as Photoacoustics are setting a sound ground through the International Photoacoustic Standardisation Consortium (IPASC)[158], [159].

6.5 Conclusions

We have presented the largest interlaboratory comparison of performance assessment of DO instruments, enrolling 28 systems and involving >50 researchers out of 12 Institutions. The exercise capitalized on two decades of research in the EU leading to 3 Protocols (BIP, MEDPHOT, NEUROPT) and a set of solid phantoms implementing them. Instruments were based on different techniques, mostly ascribed to time-domain approaches, but encompassing also CW and frequency-domain, finalized for different applications, ranging from oximetry to tissue spectroscopy, from optical mammography to diffuse correlation spectroscopy. The tests assessed different features, mostly ascribed to specific clinical oriented needs, such as accuracy and linearity in the assessment of optical properties in homogeneous media, the stability of measured values over continuous measurements, their reproducibility on different days, the sensitivity in detecting optical inhomogeneities buried in depth in the medium. A large amount of heterogeneous data was generated by the exercise, and we tried to present them in a similar format. Further, we proposed a comprehensive synthetic-summary analysis of the multiple tests based on a set of 20 FOMs, mostly consolidated from previous papers and partially introduced here anew. In Table 6.4 we provided descriptive statistics of the FOMs for the whole instrument population which could be used as a reference table to benchmark a new instrument or simulate new applications.

In this study, we identified 5 needs/criticalities which are: i) the lack of reliable multicenter results on the characterization of solid phantoms; ii) the need for identical/reproducible phantom kits easily available for research centers; iii) the benefit of linking physical FOMs to specific features in the clinical measurements; iv) the role of data analysis and common analysis tools; v) the demand for standardized formats for open data and data sharing.

Our immediate future actions foresee deployment of the whole dataset in an open data repository with addition of relevant metadata to be able to further analyze specific aspects, such as influence of the basic instrument performances on the characterization of homogeneous or inhomogeneous media, the role of specific detectors or lasers, the impact of analysis methods. In particular, as a third action of the BITMAP initiative, we foresee to re-analyze the whole dataset using the very same tools to understand to which extent the observed inter-instrument variability can be attributed to different analysis methods.

Great advances in physics derived from precise measurements of specific physical quantities (e.g. planet orbits, speed of light, particle masses). Photon migration through the human body is complicated by the biological variability, but not the basic physics underlying it all. We can disentangle the uncertainties and artifacts produced by the instruments and analysis tools from the biological variability, with great impact on clinical use.

Chapter 7

SSOP ENDOSCOPIC IMAGING

Non-invasive real-time quantification of tissue optical properties is proven to have a significant potential for surgical guidance. The capability to provide quantitative information on the physiology of biological tissues intraoperatively and during minimally invasive treatments carries numerous advantages with respect to the standard of care imaging techniques. For this reason, we propose the implementation of an SSOP-based endoscopic imaging system for oxygenation imaging in real-time. The system has also been developed to be compatible with a surgical robot.

7.1 Introduction

A major goal for biomedical optical imaging techniques is to provide quantitative information in real-time as guidance for the surgical gesture during minimally invasive treatments, where the experience and expertise of the practitioner still play a central role for the successful outcome of the procedure. In fact, the development of imaging aids present nowadays in the operating rooms for endoscopic guidance has seen a progressive increase in the recent years thanks to the technological push provided by fundamental research in part, and mostly by industrial partners well rooted in the medical market (i.e. Intuitive Surgical©, Storz©, Olympus© etc...). The overall objective of these developments is to achieve highly efficient imaging capabilities in laparoscopic and endoscopic surgery, by lowering the healthcare financial footprint [160] and provide the highest patient care possible.

To address the lack of quantitative imaging tools for the endoscopic surgical guidance, advanced optical imaging techniques such as Spatial Frequency Domain Imaging (SFDI) [45] hold a great potential thanks to their suitability for real-time and wide-field applications, as well as their non-invasiveness and relatively low cost. In particular, SFDI has recently been pushed to real-time capabilities owing to the implementation of ultra-fast tissue optical properties extraction over a large field of view through single frame acquisition implementations in the form of Single Snapshot imaging of Optical Properties [2]. SSOP has also seen a progressive improvement in terms of both image quality and speed, thanks to the recent optimization of the demodulation technique [84] and the implementation of Deep Learning architectures [85] combined with GPGPU acquisition and processing pipelines [161]. Being contactless, non-invasive and wide-field, SSOP offers great potentials for a clinical application in endoscopic imaging due to its relatively simple instrumentation requirements. Furthermore, the main benefit is the capability to provide real-time, 3D-profile corrected maps of endogenous tissue constituents concentrations [162],[73], that enable the quantification of physiological parameters such as tissue perfusion [163] and tissue microscopic structure.

It is worth noticing however, that an endoscopic implementation of SSOP must require a different perspective with respect to standard spatial frequency domain applications, due to the specific optical characteristics of the instrument. Indeed, by construction, rigid and flexible endoscopes are typically designed with a constant angular field, thus enabling a zoomed view of the surgical field once the surgical tool is placed close to the tissue, together with a wide angle view of the scene when the instrument is positioned at a distance from the surface. However, this property is not compatible with the standard implementation of SFDI devices, which relies on quasi-telecentric spatial frequency projection over the field of view [45]. Therefore, to allow for SSOP endoscopic imaging, a projection of the spatially modulated pattern of light is required through the endoscope itself in order to follow the same angular field generated by the instrument. As a consequence, the projection of the 2-D sinusoids is characterized by a distance-dependent frequency variation, with a multi-plane calibration step necessary for the correct identification of the projected spatially modulated pattern [93].

In this framework, we present an endoscopic implementation of SSOP that provides high quality imaging capabilities over a large field of view (70 mm x 70 mm). The instrument is based on a rigid two channels endoscope that can be further adapted for robotized manipulation with systems such as "Da Vinci" for minimally invasive procedures. From the processing stand point, a deep-learning approach has been adopted for the extraction of the DC and AC modulation amplitude of the signal measured from the sample. The CNN is based on an efficient and relatively small ($< 2 \times 10^4$ parameters) U-Net architecture where the training dataset is based on standard phase-shift SFDI to

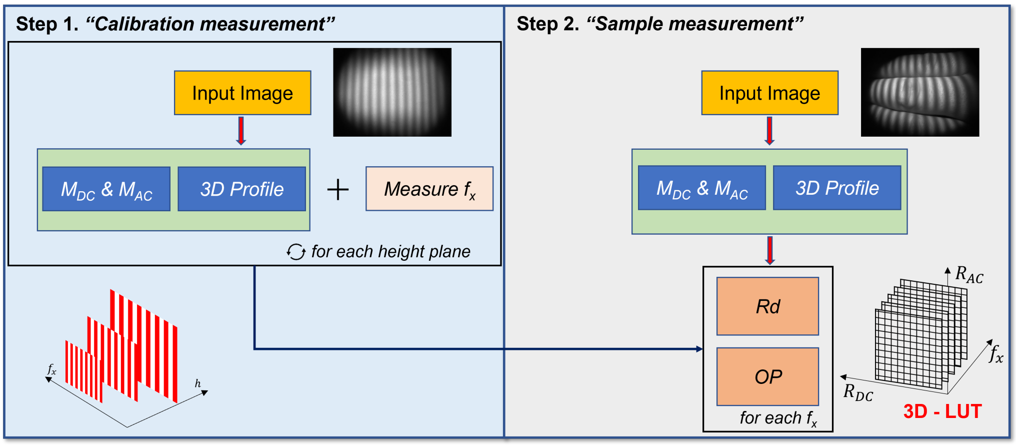

FIGURE 7.1: *Acquisition workflow for endoscopic SSOP imaging of tissue optical properties.*

boost SSOP image quality. Furthermore, the same network is used for the computation of the 3D profile of the investigated sample in order to provide profile-corrected tissue optical properties. The addition of these two processing stages provides better image quality with respect to standard SSOP, whereas the real time capability of the system is maintained thanks to a custom low-level GPGPU implementation for the processing and visualization which allows us to optimize the total computational time to enable high frame rate acquisitions (>10 fps).

7.2 Materials and Methods

7.2.1 Acquisition workflow and data analysis

SFDI is based on the projection of spatially modulated patterns of light on the sample (typically using a Digital Micromirror Device (DMD) system) and on the acquisition with a camera of the diffused backscattered light [45]. In its standard configuration, SFDI requires at least six frames to be acquired: two different spatial frequency patterns (e.g., $f_x = 0\ mm^{-1}$, $f_x = 0.2\ mm^{-1}$) and three-phase shifts for each of them (e.g. $\phi = 0, \pi/3, 4/3\pi$). The phase-shifted sequence is then used to demodulate the signal, hence obtaining the modulation amplitude (i.e. M_{DC} and M_{AC}) maps of the given sample at each spatial frequency [45]. A calibration step involving the measurement of a tissue mimicking phantom with known optical properties, is then utilized to compute the diffuse reflectance maps, i.e. R_{DC} ($f_x = 0\ mm^{-1}$) and R_{AC} ($f_x = 0.2\ mm^{-1}$). Finally, the solution of the inverse problem through ultra-fast 2-D LUTs [83] using a light propagation model based on Monte Carlo, allows the retrieval of the optical properties of the investigated sample (i.e., absorption (μ_a) and reduced scattering ($\mu_s^{'}$) coefficients) for each pixel of the image. Due to the need for at least six frames, SFDI is not real-time applicable. Instead, SSOP allows to sensibly reduce the acquisition time and to reach video rate performances, thanks to a single high spatial frequency frame required to extract the sample's M_{DC} and M_{AC}. The main difference in the workflow with respect to SFDI is determined by the use of a Fourier's transform-based filtering technique for the demodulation step [2]. After the extraction of the modulation amplitude maps, the processing workflow is the same as for SFDI. It is worth noticing that degradation in image quality and the presence of edge artifacts are the main consequences of the use of a single frame acquisition implementation. However, significant improvements have been achieved in recent years by first optimizing the filtering technique [84] and by adopting

Deep Neural Network approaches for the demodulation [86],[85]. Additionally, the latest developments on SSOP also account for a 3-D profile correction of the sample in order to reduce the quantification error of SFDI associated with a variation of light intensity across non-flat sample surfaces [75].

It is worth highlighting the need for a multiple distance calibration step for the characterization of the dependency on the distance from the endoscope of the projected spatial frequency. As mentioned in Section 7.1, due to the viewing angle of the instrument, the projection of the illumination patterns through one of the channels of the endoscope is necessary to follow the same angle field of the imaging side. This determines a non-telecentric divergent illumination of the surgical field with a non-constant projected spatial frequency. For this reason, it is fundamental to calibrate the system by acquiring a series of SSOP frames from different height planes from the endoscope, and by measuring for each of them the spatial frequency on the field. This information allows us to employ n-dimensional LUTs for the fast and correct extraction of the optical properties of the sample. Furthermore, the phase information embedded in the data is necessary to perform the profilometry analysis for the correction of the optical properties with the height profile of the tissue. In Fig.7.1 we summarize the acquisition workflow for the SSOP endoscopic imaging system with the aforementioned calibration step.

7.2.2 Deep Learning for endoscopic imaging

The processing pipeline is implemented with the latest Deep Learning optimized SSOP workflow, as described by Aguénounon et al.[85]. More specifically, the standard SSOP Fourier's domain filtering demodulation is replaced by two dedicated CNNs based on a U-Net architecture, as shown in Fig.7.2. The first network is dedicated to the extraction of the modulation amplitudes M_{DC},M_{AC} of the signal for each spatial frequency. The second architecture, identical to the first one by construction, is instead used for the profilometry analysis (i.e. the extraction of the real and imaginary part of the signal necessary to retrieve the phase information). Both networks are trained using high quality images obtained with SFDI acquisition sequences with 7 phase shifts (i.e. $\phi = 0, \pi/2, \pi, 3/2\pi, 2\pi, 5/2\pi, 3\pi$) instead of 3 to enhance quantification accuracy and image quality. In addition, they are optimized for efficient and low-cost computation performances, by reducing the number of parameters($< 2 \times 10^4$) and layers involved at a minimum, and subsequently allowing for a real-time high visual quality optical property

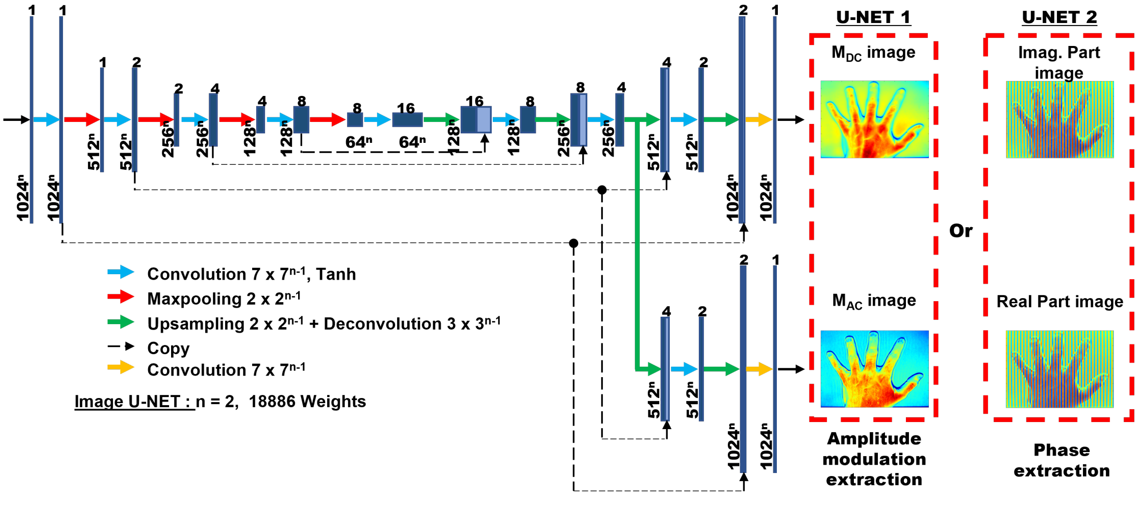

FIGURE 7.2: *U-Net architecture for deep-learning-optimized SSOP. [85]*

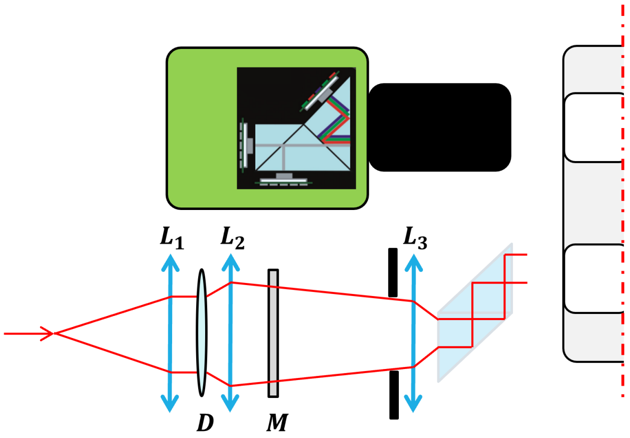

FIGURE 7.3: *Schematics of the design of the endoscopic imaging system. Light is delivered through fiber propagation and collimated by a first lens (L1) onto a top-hat diffuser (D). A condenser lens (L2) is used to illuminate the sinusoidal mask (M). A third lens (L3) in combination to a right-angle prism is employed to propagate the pattern through the illumination channel of the endoscope. The imaging channel of the scope is used to acquire the SSOP frames with a tri-sensor sCMOS camera to provide RGB view of the surgical field, and two NIR bands dedicated to oxygenation imaging.*

quantification for up to 1 MP images. The training dataset consisted of a total of 140 high quality images divided into $n = 40$ images of tissue-mimicking silicone phantoms with different optical properties ranging from $\mu_a = 0.005$ to 0.05 mm^{-1} for absorption and from $\mu_s' = 0.5$ to 3 mm^{-1} for reduced scattering; $n = 100$ images of hands from different Caucasian men in various configurations.

7.2.3 Instrumental set-up

The design of the imaging system is shown in Fig.7.3. The instrument is based on a rigid two channels endoscope where the openings normally dedicated to the white light illumination of the surgical field have been momentarily disabled. Conversely, the two channels used for the stereoscopic view of the field have been converted to the injection channel for the modulated laser illumination for the first one, and to the acquisition of the SSOP images for the second one. From the optical design point of view, the structured illumination through the first channel of the endoscope is achieved with a custom high power multiple wavelength laser source coupled to an optical path where high definition (>50000 dpi) 2-D sinusoidal patterns printed on a glass substrate are used for the generation of high spatial frequency images ($f_x = 0.1 - 0.5$ mm^{-1}). In the optical path, a first lens (L1) collimates the output of the optical fiber onto a 20° top-hat diffuser (D) for the homogenization of the illumination beam. It follows a condenser lens (L2) for the illumination of the glass substrate sinusoidal mask (M), and a third lens (L3) in combination with a right-angle prism is adopted to deliver the image of the pattern through the endoscope shaft. In addition a diaphragm is used before L3 to reduce the NA of the system and avoid stray light propagation through the endoscope. The second channel of the endoscope is instead employed for the acquisition of the SSOP frames and a high frame rate tri-sensor sCMOS camera (FS-3200T-10GE-NNC, JAI, Japan) is used in order to cover three main channels: an RGB channel, for the anatomical view of the surgical field, and two NIR channels selected for optimal oxygenation wavelength coverage (i.e. 730 nm and 860 nm). In addition, to avoid optical cross-talk between the two non-isolated channels of the endoscope, 3-D printed custom parts are adopted to occlude any open surface in the head of the instrument, as shown in Fig.7.4. These parts allows us to reduce the effect

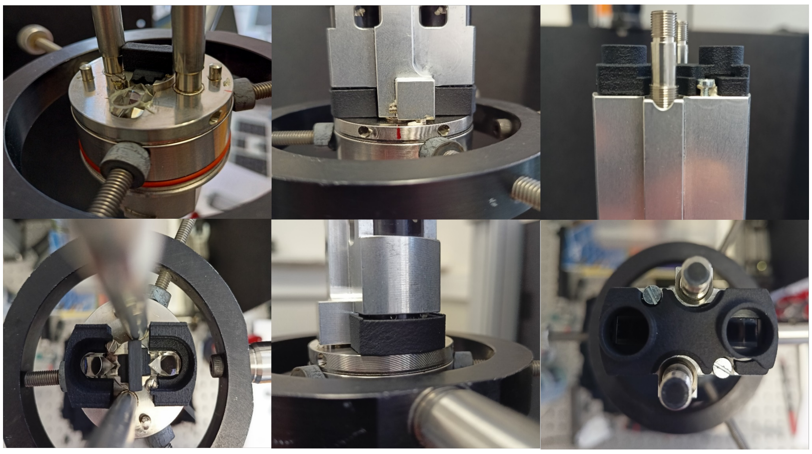

FIGURE 7.4: *3-D printed custom parts to optically isolate the two channels of the endoscope in the head of the instrument.*

of light escaping from the illumination channel, and propagating towards the imaging channel.

7.3 Results

A first benchtop validation was performed on tissue mimicking phantoms. A set of homogeneous silicon-based phantoms with TiO_2 as scattering particles and nigrosin as absorbing agent were characterized in terms of their optical properties (i.e. the absorption and reduced scattering coefficients) via SSOP imaging. Additionally, in order to address the accuracy of the instrument, a comparative set of measurements on the same phantoms have been performed with standard SFDI and TDOS, by employing the multi-modal referencing platform presented in Chapter 5. Summary charts of the characterization are presented in Fig.7.5. An ROI of 350 × 350 pixels was selected to analyze the quantification accuracy of SFDI and SSOP, while for TDOS a point-like reflectance measurement at $\rho = 20\ mm$ source-detector distance was performed to retrieve μ_a and $\mu_s^{'}$.

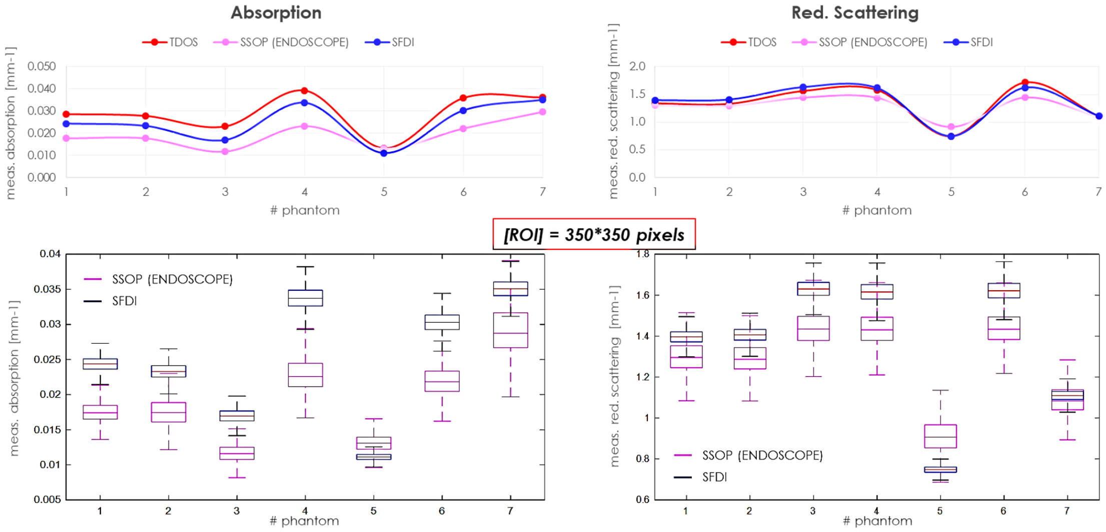

FIGURE 7.5: *Absorption and reduced scattering characterization of tissue mimicking phantoms using endoscopic SSOP, SFDI and TDOS.*

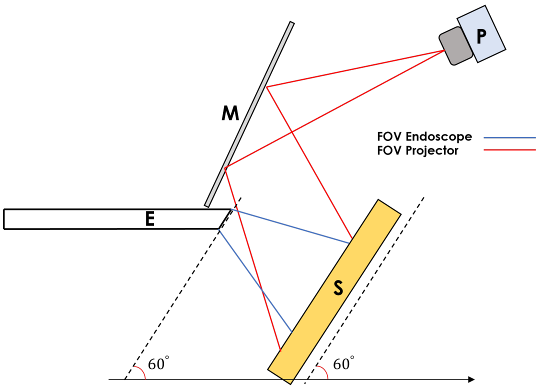

FIGURE 7.6: *Schematics of the external projection system employed for SFDI imaging through the endoscopic imaging system. A DMD projector at equivalent working distance of* 45 *cm was adopted to generate SFDI multi-phase patterns to illuminate the sample placed on the field of view of the endoscope.*

The results on the reduced scattering coefficient showed robust agreement among the three techniques with $< 10\%$ deviation between SFDI and TDOS for all phantoms with a slightly higher variation for SSOP ($< 20\%$). The absorption coefficient quantification presented a more significant discrepancy, as shown in the left charts of Fig.7.5: the reason for this poor agreement can be traced back to heterogenous illumination from the endoscopic system, where the pixel-by-pixel variability on the acquired image determines a noticeable error in the quantification, as highlighted by the boxplots.

A first image quality assessment was also conducted by measuring an *in-vivo* subject hand with both SFDI and SSOP with the endoscopic system. In this sense, an external projection system was implemented to generate multi-phase SFDI patterns on the field of view of the instrument. For this purpose, a DMD-based projector was used to generate sinusoidally modulated patterns of light at different spatial frequencies and phases and a mirroring system was employed to provide the SFDI illumination on the investigated sample, as shown in Fig.7.6. The results of this characterization are shown in Fig.7.7. It is worth mentioning that these results refer to an SSOP processing pipeline based on standard Fourier's domain filtering. Evidently, the SFDI images carry higher quality with artifacts-free rendering, thanks to the multi-phase demodulation algorithm. Conversely, for the SSOP imaging, it is possible to identify poorer quality and edge artifacts on both the absorption and reduced scattering maps due to the use of the filtering approach.

In order to address the improvement of image quality by the application of the Deep Learning architecture, a second validation step was carried out. In Fig.7.8 we report the results of the training of the Deep Learning architecture. As mentioned in Section 7.2.2, the dataset was acquired with 7-phases SFDI frames projected with the scheme shown in Fig.7.6, and it consisted of a total of 140 images subdivided into 100 *in-vivo* hands of white Caucasian men in different configurations, and 40 homogeneous tissue mimicking phantoms with different optical properties. Residual stripes in the UNET outputs are still noticeable in Fig.7.8 for the demodulated M_{DC} and M_{AC}. Furthermore, a validation dataset of tissue mimicking phantoms and *in-vivo* hands was also acquired to assess the performance of DL-SSOP with respect to SFDI and standard Fourier's filtering SSOP. A comparative analysis of the results is proposed in Fig.7.9,7.10. In this case, we performed measurements by illuminating the samples with the external projection system (that corresponds to the training configuration) and by exploiting the propagation and acquisition through the endoscope. Despite the promising results obtained after the training, the imaging through the surgical instrument is characterized by low SNR due to the poor coupling efficiency ($< 30\%$). As a consequence, both SSOP and DL-SSOP suffer

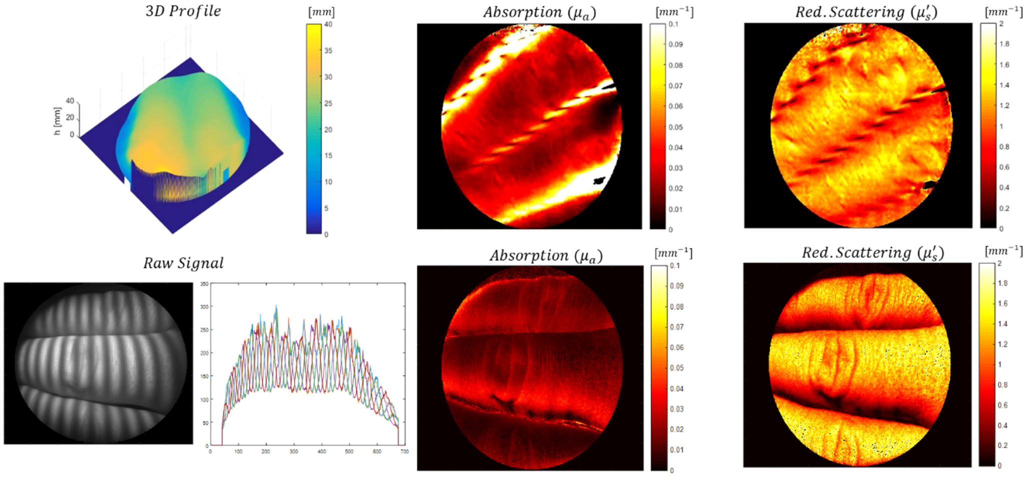

FIGURE 7.7: *Image quality assessment of the endoscopic imaging system. On the top row, SSOP results of profile correction, absorption and reduced scattering coefficients for in-vivo hand at 14 fps. On the bottom row, the same subject was imaged by 7 phase SFDI acquisitions through the endoscope, adopting the external projection system.*

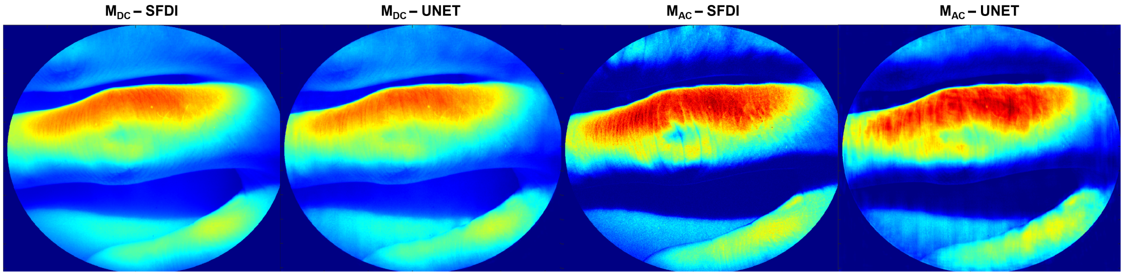

FIGURE 7.8: *Comparative analysis of the Deep Learning training. 7-phases SFDI shows better image quality than UNET for the demodulation of the* M_{DC} *and* M_{AC}*, with some residual stripes present in the latter.*

from low image quality in the extraction of the modulation amplitudes with a similar presence of edge artifacts and residual stripes. In this sense, further optimizations of the illumination path needs to be addressed to improve the throughput of the instrument.

7.4 Discussion

Single Snapshot imaging of Optical Properties represents a powerful candidate for image guided surgery. The capability to provide quantitative information on tissue optical properties in real-time, and over a large field of view enables its application to several scenarios for both open surgery [1],[163] and minimally invasive treatments. SFDI and SSOP were already validated on the field for reconstructive breast surgery [81] and tissue perfusion in the gastric conduit [163], but a minimally invasive adaptation of these techniques has still not found its way to the surgical room.

Studies have shown the compatibility of SSOP to endoscopic imaging for real time quantification of tissues optical properties [93], but at the time the technology still suffered from low image quality and rendering artifacts due to the filtering technique employed for the demodulation step [93],[2]. Great progress in image quality was possible thanks to the optimization of filtering windows [84] and the implementation of Convolutional Neural Networks to replace the Fourier's analysis, as proposed in [85].

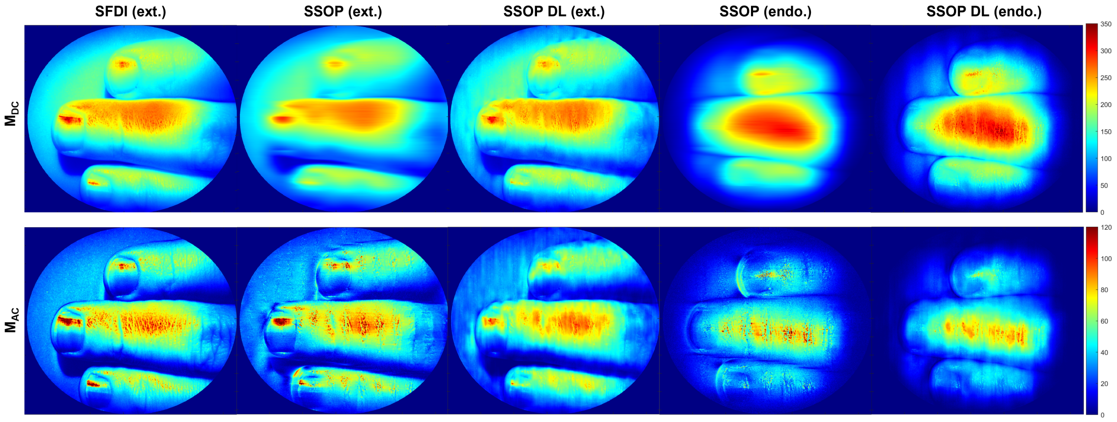

FIGURE 7.9: *Image quality evaluation of the Deep Learning-based SSOP endoscopic imaging system on in-vivo hand data. Demodulated M_{DC}, M_{AC} images as of: the first column refers to 7-phases SFDI acquired through the endoscope, by illuminating the sample with the external projection system; the second column refers to Fourier's transform SSOP obtained from the first AC frame of the SFDI sequence; the third column refers to Deep-Learning SSOP obtained from the same SSOP frame as shown in the second column; the fourth column refers to Fourier's transform SSOP obtained by projecting an AC pattern through the endoscope; the fifth column refers to Deep-Learning SSOP obtained from the frame projected through the endoscope.*

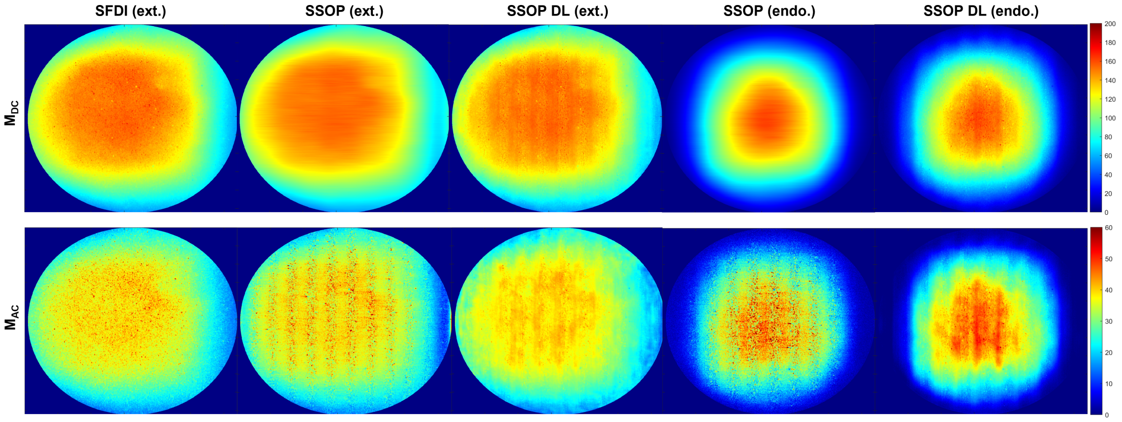

FIGURE 7.10: *Image quality evaluation of the Deep Learning-based SSOP endoscopic imaging system on a homogeneous phantom. Demodulated M_{DC}, M_{AC} images as of: the first column refers to 7-phases SFDI acquired through the endoscope, by illuminating the sample with the external projection system; the second column refers to Fourier's transform SSOP obtained from the first AC frame of the SFDI sequence; the third column refers to Deep-Learning SSOP obtained from the same SSOP frame as shown in the second column; the fourth column refers to Fourier's transform SSOP obtained by projecting an AC pattern through the endoscope; the fifth column refers to Deep-Learning SSOP obtained from the frame projected through the endoscope.*

In this work, we proposed the design of a dual channel rigid endoscope for oxygenation imaging of biological tissues with SSOP. The latest developments of Deep Learning processing, combined with a GPGPU computing power would allow us to significantly improve the overall image quality by maintaining the real-time capabilities of the system thanks to a small size neural architecture.

The instrument was validated on tissue mimicking phantoms for the quantification accuracy, showing promising agreement in optical properties reconstruction with respect to the ground truth given by SFDI and TDOS. A discrepancy below 20% was registered in reduced scattering, whereas the absorption maps showed higher errors ($> 20\%$) due to illumination heterogeneities. Indeed, due to the low coupling efficiency of the endoscope, the spatially modulated patterns projected through the first channel suffered from vignetting effects and low SNR at the boundaries of the field of view. In this sense, the isolation of the optical channels of the instrument was also addressed to reduce the effect of parasite light propagating inside the endoscope shaft, which are responsible for a degraded coupling efficiency and illumination artifacts on the acquired images.

The optimization of the image quality of the system was conducted by implementing the CNN architecture for the demodulation step. An external projection system was also employed to generate multi-phase SFDI pattern projection over the field of view of the endoscope. This data was used as training dataset for the neural network, following the validated algorithm described in [85]. The validation dataset acquired via the external projection system showed promising results for the application of the DL architecture to the endoscopic system. However, further investigation of the imaging capability of the instrument based on DL-SSOP through the endoscope provided unsuccessful outcomes in the extraction of the demodulated images. We believe that the low coupling efficiency of the instrument, in addition to the vignetting effects that characterize the imaging path, they both determine a true limitation of the system. As a consequence, demodulation artifacts and residual stripes were noticed in the resulting M_{DC} and M_{AC}, thus preventing a further analysis of the quantification of tissue optical properties. Evidently, the low SNR obtained with the projection and imaging through the endoscope shaft does not allows us to benefit from the DL architecture for the quality improvement at the same extent as shown in [85]. Additionally, the absence of cross polarization between the projection and imaging sides determines a strong detrimental effect due to specular reflections. This issue was not noticeable after the training of the network, thanks to the use of cross-polarization for the external projection. Clearly, for further improvements of the instrument, a solution for the implementation of a similar configuration needs to be designed to optimize the rejection of specular, non-diffused light propagating through the endoscope.

7.5 Conclusions

In this chapter we described the design and validation of an endoscopic imaging system based on 3-D profile corrected Single Snapshot Imaging of Optical Properties powered by the latest Deep Learning architectures. The instrument was built on a dual channel rigid endoscope that was adapted to SSOP imaging by designing an illumination path for the projection of the sinusoidal patterns through one channel, and by exploiting the second channel for the acquisition of the SSOP frames. A first benchtop system was validated on tissue mimicking phantoms to assess image quality and optical properties quantification accuracy. Furthermore, a successive development of the design would allow us to adapt the instrument to a surgical robot. Pre-clinical trials are the main goal for further validations of the design.

Chapter 8

SSOP FOR THE PERFUSION ASSESSMENT IN THE GASTRIC CONDUIT

Article Title : *"Single Snapshot Imaging of Optical Properties (SSOP) for Perfusion Assessment during Gastric Conduit Creation for Esophagectomy: An Experimental Study on Pigs"*

Authors : *L. Cinelli, E. Felli, L. Baratelli, S. Ségaud, A. Baiocchini, N. Okamoto, M.R. Rodríguez-Luna, U. Elmore , R. Rosati, S. Partelli, J. Marescaux, S. Gioux and M. Diana*

Journal : *Cancers*© 2021, 13, 6079. `https://doi.org/10.3390/cancers13236079`

On a worldwide scale, esophageal cancer is ranked eighth in terms of occurrence among all cancers, making it the sixth most common cause of cancer-related mortality [164]. Multimodal treatment includes surgery, radiotherapy, and chemotherapy. Surgery remains the best curative modality for patients with resectable esophageal cancer [165], although the 5-year survival rate ranges from 5 to 47%[1].

Two-stage Ivor Lewis esophagectomy was described for the first time in 1946 [166], becoming the most frequently performed surgical treatment for esophageal cancers located in the medial, distal, or esophagogastric junction of the esophagus [167].

Following this technique, esophagogastric continuity is restored through the anastomosis between the gastric conduit (GC) obtained from the tubulization of the stomach and the remaining esophagus. One of the most serious complications of this type of surgery is anastomotic leakage (AL), occurring in up to 53% of all cases [168],[169]. It is associated with a mortality rate of up to 35% [170] and with adverse effects on short-term and long-term outcomes [171],[172],[173], resulting in an increased recurrence of tumors [174]. Although the etiology of AL is multifactorial [175],[176], an insufficient perfusion of the anastomotic site is considered to be a significant and independent predicting factor to determine anastomotic failure [177],[178].

Currently, the adequate perfusion of GC is clinically assessed by surgeons using indicators such as serosal color or pulsatile flow of vessels. However, these parameters are subjective and inaccurate to rule out a marginally perfused anastomosis [179]. During the last two decades, several intraoperative optical imaging techniques have been developed and tested to monitor the perfusion of the gastric conduit [180], including laser Doppler flowmetry, near-infrared spectroscopy, laser speckle contrast imaging, infrared thermographic imaging, optical coherence tomography, and indocyanine green (ICG) fluorescence imaging. However, those methods lack reproducibility and/or provide operator-dependent results and/or lengthen the surgical workflow [180],[181]. New technologies based on optical properties including multispectral and hyperspectral imaging are progressively implemented in image-guided surgery. This increased interest can be partly explained by the enhanced ability of those endogenous imaging methods to quantify tissue optical properties in terms of physiology and morphology, allowing for improved and reproducible information during interventions, which can influence the surgical decision-making process [58].

Our group has recently assessed gastric tubulization via hyperspectral imaging (HSI) in a survival study on hybrid ischemic preconditioning of the stomach [182]. Additionally, the feasibility and potential interest of HSI during gastrointestinal surgeries, including esophageal resections, has been recently evaluated in preliminary clinical studies [182],[62],[183],[184]. HSI is a contrast-free technology which can provide a chemical quantification of tissue compounds, allowing to quantify tissue oxygen saturation ($StO_2\%$), among others. Although HSI showed encouraging and consistent results, its main downside remains the lack of video rate, which greatly limits its usability as a real-time surgical navigation tool.

Spatial Frequency Domain Imaging (SFDI) is an optical technique that can provide a 3D corrected profile and quantitative information of optical properties (i.e., absorption and reduced scattering coefficients) of biological tissues over a large field of view [45],[1]. The potential of SFDI to provide information related to tissue oxygenation has been demonstrated in the past at both preclinical and clinical levels [185],[186],[187],[80],[188]. However, the standard embodiment of SFDI requires several frames to be acquired and

---

[1] Cancer.Net Esophageal Cancer. *Cancer.Net. 2019.* Available online: `https://www.cancer.net/cancer-types/esophageal-cancer/`

it does not provide images in real-time. For this reason, Single Snapshot imaging of Optical Properties (SSOP) was developed to enable a video rate imaging capability in the SFDI, by limiting the number of required frames to only one [2],[189],[190],[85]. The natural drawbacks of this single snapshot technique include a loss of image resolution and the presence of edge artifacts. Nevertheless, with the implementation of the latest Convolution Neural Network (CNNs) architectures [85] and the use of state-of-the-art GPGPU computing, it was possible to achieve significant improvements in the overall image quality and profile correction, while maintaining real-time capabilities [85].

In the present study, our aim is to perform a preliminary validation of SSOP camera to intraoperative quantify serosal $StO_2\%$ in an experimental gastric conduit (GC) model.

8.1 Materials and Methods

8.1.1 Experimental Workflow

First of all, laparotomy was performed and the GC was prepared. After tubulization, the resected region of the stomach was maintained near the GC, still connected to the esophagus. Four ROIs were manually selected as follows: ROI-A (antrum), ROI-C (greater curvature/corpus), ROI-F (fundic region/future anastomotic site), and ROI-R (the resected upper part of the stomach). The post-procedural observational phase was held for 60 min, at 15 min time points (T0, T15, T30, T45, and T60). Following this timeline, for each ROI, the SSOP system was used to detect $StO_2\%$ values and LCLs were measured as biological "ground truth", together with systemic BGA. At the end of the 60 min observation period, histopathological evaluation and scoring were performed in the same four ROIs. Each animal served as its own control.

The study aimed to predict gastric conduit viability through the analysis of SSOP images in order: (i) to recognize perfused from non-perfused stomach, using ROI-R as ischemic control, (ii) to predict the level of gastric perfusion during the postoperative phase, and (iii) to predict biological data. The hypercube extracted from SSOP images was used to train two CNNs. Finally, the generated artificial intelligence (AI) score for the postoperative phase was generated and the quantitative analysis of SSOP images was correlated with biological and histopathological data (Fig.8.1 A–C).

8.1.2 Sample Size Calculation

Sample size calculation was performed using the correlation between optical and biological data. The calculation derived from previous publications on bowel ischemia, which showed a ρ correlation coefficient of -0.7 [183],[184]. The required sample size in terms of paired values was 4, considering $\alpha = 0.05$ with power $(1 - \alpha) = 0.9$. In the present study, 120 paired values of $StO_2\%$ and lactates values were obtained in a total of 6 pigs.

8.1.3 Animals

The present study, which was part of the QuantSURG COLORECTAL project (Imagerie optique quantitative pour le guidage du geste chirurgical dans le cancer colorectal), was approved by the local Ethical Committee on Animal Experimentation (ICOMETH 38.2019.01.121) on 3 September 2019, as well as by the French Ministry of Superior Education and Research (MESR) (APAFIS # 20819-2019052411591088v3). All animals used in the experiment were managed according to French laws for animal use and care, and according to the directives of the European Community Council (2010/63/EU) and ARRIVE guidelines [191]. Six adult pigs (*Sus scrofa ssp. domesticus*, mean weight: 36.5 ± 3.3

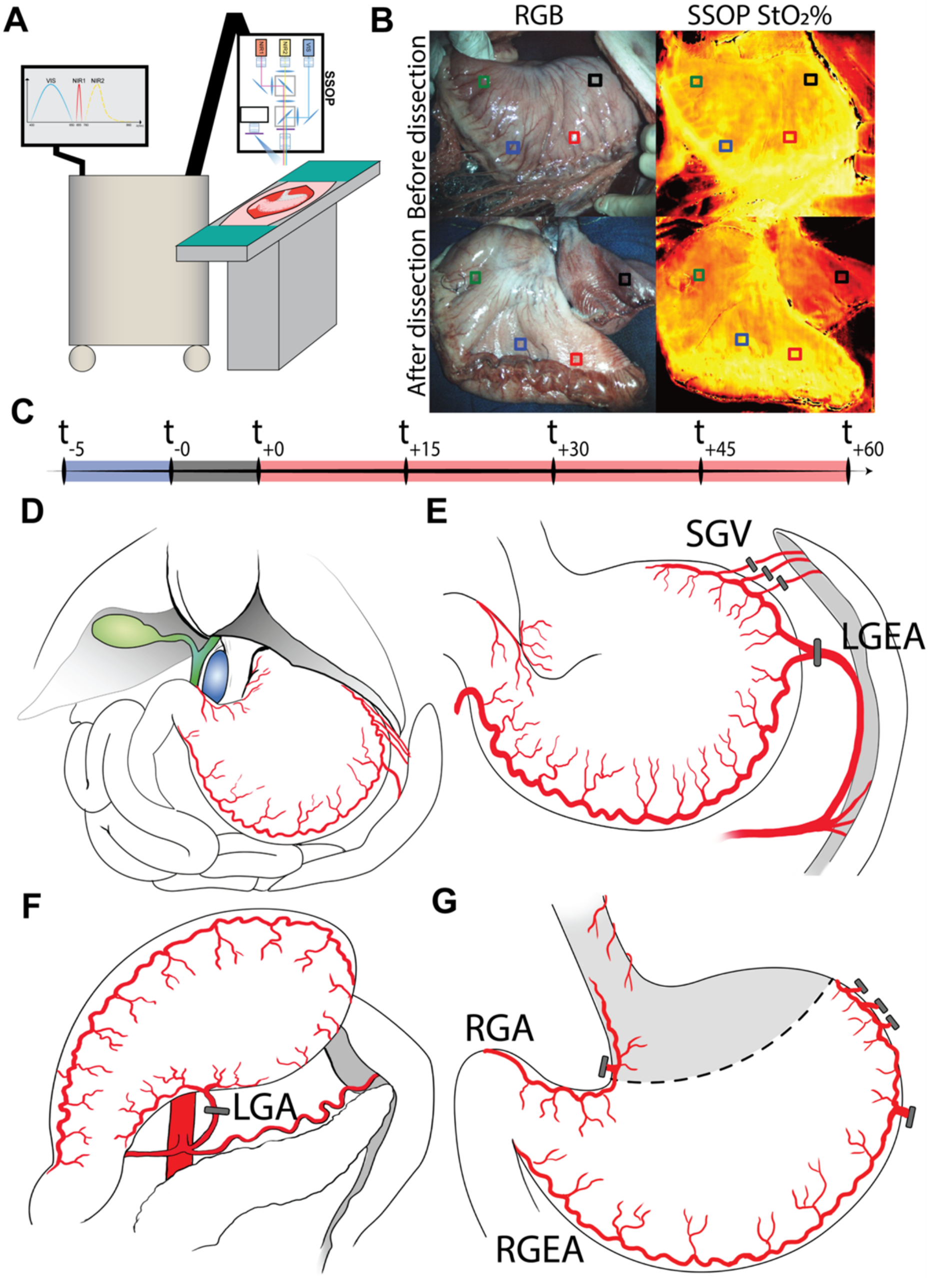

FIGURE 8.1: *SSOP experimental workflow. (A) First of all, the SSOP machine was prepared for data acquisition. (B) Regions of interest (ROIs) were marked with surgical stitches before any dissection in order to obtain* StO$_2$*% values and correspondent LCLs in the same ROIs along the entire timeline. Preselection of ROIs for antrum (ROI-A), corpus (ROI-C), fundus (ROI-F), and the future removed region (ROI-R) was essential to prevent any possible selection bias related to postoperative selection. (C) The acquisition of data started 5 min before the preparation of the gastric conduit (*t_{-5}*), with the baseline evaluation of the healthy stomach. After gastric conduit (GC) formation, the acquisition proceeded in 15 min time points, for a total of 60 min, which was the clinical estimated time between GC preparation and the packing of the esophagogastric anastomosis. During this period, the upper separated part of the stomach (ROI-R) was supposed to become increasingly ischemic after resection. (D) Normal porcine abdominal anatomy. Gastric vascularization is the same in humans, even if the stomach of the pig is two to three times larger and more bag-shaped. The vena cava (blue) and the biliary tree (green) are highlighted. (E) Ligation of the left gastroepiploic artery (LGEA) and short gastric vessels (SGV). (F) Ligation of the left gastric artery (LGA). (G) After transection, the perfusion of the gastric conduit was maintained via the right gastroepiploic arcade (RGEA); the antrum/duodenum was also perfused by the right gastric artery (RGA). ROI-R, even if partially perfused by distal esophageal vessels, received only a minimum amount of blood, enough to consider it ischemic, but not totally devascularized.*

kg) were housed and acclimatized for 48 h in an enriched environment, respecting circadian cycles of light–darkness, with constant humidity and temperature conditions. They were fasted 24 h before surgery, with ad libitum access to water, and finally sedated (zolazepam + tiletamine 10 mg/kg IM) 30 min before the procedure in order to decrease stress. Anesthesia was performed intravenously (18-gauge IV catheter in-ear vein) with Propofol 3 mg/kg and maintained with rocuronium 0.8 mg/kg along with inhaled isoflurane 2% via the automatic standard respiratory system. Vital parameters were monitored through a mechanical ventilator machine. Heartbeat was monitored with a pulse oximeter (Mindray PM-60). At the end of the protocol, pigs were euthanized with a lethal dose of Pentobarbital Sodium (40 mg/kg) (Exagon, Axience SAS, Pantin, France).

8.1.4 Surgical Procedure

Through a median laparotomy, the stomach was prepared leaving only the right gastroepiploic and pyloric vessels for its vascular supply. Gastric vessels were ligated using surgical clips (LIGACLIP Multi-Patient-Use Single Clip Appliers, Ethicon, Endosurgery Inc., Cincinnati, OH, USA). Successively, an approximately 4 cm wide GC was created, starting from the greater curvature, and using a surgical stapler (ENDO GIA^{TM} linear stapler equipped with 45 mm black reloads, Medtronic, Minneapolis, MN, USA) (Fig.8.1 D–G).

8.1.5 SSOP Imaging

SFDI is based on the projection of spatially modulated patterns of light on the sample (typically using a Digital Micromirror Device (DMD) system) and on the acquisition with a camera of the diffused backscattered light arising from it. In its simplest configuration, SFDI requires at least six frames: two different spatial frequency patterns (e.g., $f_x = 0\ mm^{-1}$, $f_x = 0.2\ mm^{-1}$) and three-phase shifts for each of them. The phase-shifted sequence is then used to demodulate the signal, hence obtaining the modulation amplitude maps of the given sample at each spatial frequency [45]. Using a calibration step involving the measurement of a calibration phantom with known optical properties, it is then possible to compute the diffuse reflectance maps, i.e., R_{DC} ($f_x = 0\ mm^{-1}$) and R_{AC} ($f_x = 0.2\ mm^{-1}$). Finally, solving the inverse problem using a light propagation model, here a Monte Carlo-based Look-Up Table (LUT) [83] algorithm, allows to retrieve the optical properties of the sample (i.e., absorption and reduced scattering coefficients) for each pixel of the image. Due to the need for at least six frames, SFDI cannot perform in real-time. Instead, SSOP allows to sensibly reduce acquisition time and to reach video rate performances, thanks to a single high spatial frequency frame required to extract the optical properties of the sample. The main difference in the workflow in comparison with SFDI consists of using a Fourier transform-based filtering technique for the demodulation step [189]. After the extraction of the modulation amplitude maps, the processing workflow is the same as for SFDI. It is worth noticing that degradation in image quality and the presence of edge artifacts are the main consequences of the use of a single frame. However, significant improvements have been achieved in recent years by first optimizing the filtering technique [84] and by adopting Deep Neural Network approaches for the demodulation [85]. Additionally, the latest developments on SSOP also account for a tridimensional profile correction of the sample in order to reduce the quantification error of SFDI associated with a variation of light intensity across non-flat sample surfaces [85].

8.1.6 Deep Learning Method for SSOP

In this study, the latest deep learning optimized SSOP workflow was adopted, as described by Aguénounon et al. [85]. In a nutshell, the standard Fourier domain filtering demodulation was replaced by two dedicated CNNs based on a U-Net architecture as follows: the former was dedicated to the extraction of the modulation amplitude of the signal for each spatial frequency, and the latter was used for the profilometry analysis. Both networks were trained using high quality images obtained with SFDI acquisition sequences (with 7 phase shifts instead of 3 to enhance quantification accuracy and image quality) and optimized for efficient and low-cost computation performances, by reducing the number of parameters and layers involved at a minimum, and subsequently allowing for a real-time high visual quality optical property quantification for up to 1 MP images. The training dataset consisted of a total of 200 high quality images divided into $n = 40$ images of tissue-mimicking silicone phantoms with different optical properties ranging from $\mu_a = 0.005$ to $0.05\ mm^{-1}$ for absorption and from $\mu_s' = 0.5$ to $3\ mm^{-1}$ for reduced scattering; $n = 52$ images of hands from different Caucasian men and women in various configurations; $n = 108$ images from ex vivo and in vivo swine organs in several orientations (stomach, small bowel, colon, kidney, pancreas, liver, and spleen).

8.1.7 Instrumentation

The imaging system (Fig.8.2 A,B) included a white light plasma lamp (Thorlabs Inc., Newton, NJ, USA) for the illumination of the surgical field, together with a fiber-coupled custom-made high-power two wavelengths laser source working at 665 and 860 nm. The projection of sinusoidal patterns on the sample was performed with a Digital Micromirror Device-based projector (Vialux GmbH, Chemnitz, Sachsen, Germany). The field-of-view (FOV) of the system was slightly greater than $15 \times 15\ cm$ at a working distance of 45 cm as shown in Fig.8.2 A. The imaging head was based on a 3-channel architecture: 2 near-infrared monochrome cameras (PCO.edge 5.5 and PCO.pixelfly USB, Excelitas PCO GmbH, Kelheim, Germany) were used for the acquisition of the SSOP frames with 1024×1280 pixel resolution at 665 and 860 nm, and an RGB camera (JAI GO-5000C-USB, JAI Ltd., Kanagawa, Japan) was also added to record the surgical field (Fig.8.2 C,D). The co-registration of the scene by the cameras was obtained thanks to a customized optomechanical system in which optical filters were included to separate the 3 channels at the collection side. In addition, a pair of linear polarizers (PPL05C, Moxtek, Orem, UT, USA) were used in crossed configurations at the projection and camera sides to reject the specular reflections originating from the sample surface. The working distance of the imaging system was $45 \pm 5\ cm$, hence offering a comfortable operating condition for the physicians during acquisition. Oxygenation computation was achieved applying Lambert–Beer's law for chromophore absorption inside the biological tissue [192].

8.1.8 Blood Analysis

LCLs were obtained through a full-thickness puncture of the gastric wall, in correspondence with the preselected ROIs. A blood drop was obtained and a portable strip-based lactate analyzer (EDGE, Apex Bio, Taipei, Taiwan) was used to quantify LCL levels, with a margin error of 0.35 mmol/L. The correlation analysis of data was performed between $StO_2\%$ parameters detected via the SSOP system and LCLs concentration. Systemic blood was sampled through a central catheter placed in the right external jugular vein (6 French IV catheter) and evaluated through a handheld wireless blood tester (Epoc® Blood Analysis System, Siemens Healthcare GmbH, Erlangen, Germany). These systemic BGA were used to monitor the surgical intervention to rule out any bias in

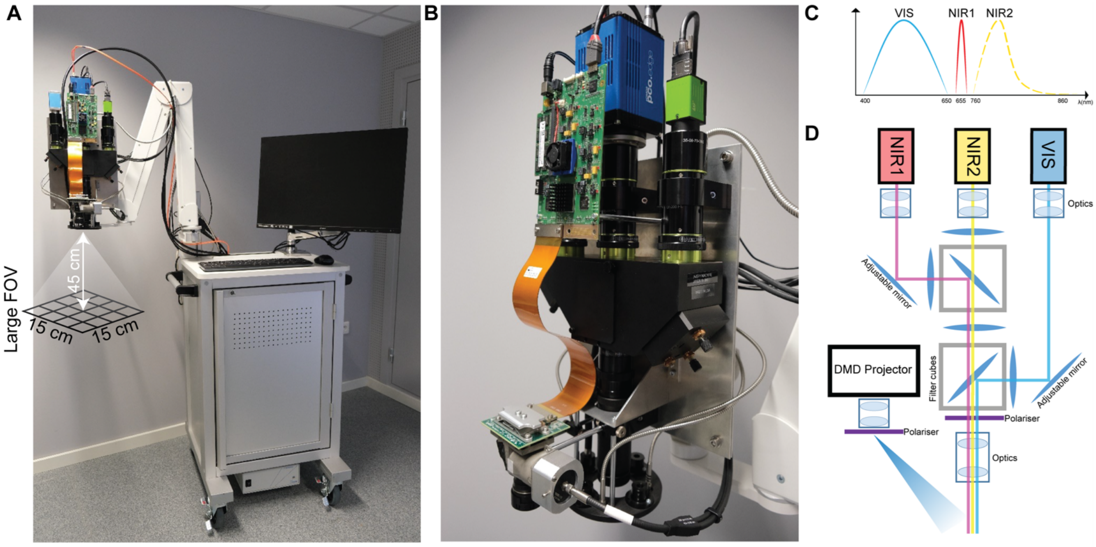

FIGURE 8.2: *SSOP descriptive figure. (A) Preclinical cart for fluorescence, SFDI, and SSOP imaging in the operating room. The imaging head is mounted onto an articulated arm for an easy positioning over the surgical table at the desired working distance. The main body of the cart contains the laser sources, the white light lamp, and the PC workstation. (B) Imaging head based on a trident architecture to enclose three separate channels for RGB, NIR1, and NIR2 imaging. A DMD-based projection system is also mounted onto the head for the generation of structured illumination over the FOV. The light source is delivered to the projector via a fiber-based coupling system. An illumination ring is used to homogeneously deliver white light illumination of the surgical field and fluorescence excitation wavelength. (C) Schematics of the imaging bands for the trident, namely: the RGB camera (JAI GO-5000C-USB, JAI Ltd., Kanagawa, Japan) covers the VIS bandwidth (400–650 nm); the NIR1 camera (pco.pixelfly USB, Excelitas PCO GmbH, Kelheim, Germany) covers the first near-infrared bandwidth (centered around 665 nm); and the NIR2 camera (pco.edge 5.5, PCO AG, Excelitas PCO GmbH, Kelheim, Germany) covers the second near-infrared bandwidth (700–900 nm). (D) Schematics of the optical path in the trident for the co-registration of the three imaging channels, together with the configuration of the DMD-based projector. A pair of filtering cubes are used to isolate the NIR1 and NIR2 channels, and a set of mirrors are used to align the FOV of the three cameras.*

the post-procedural observation of the GC. BGA measured pO_2, pCO_2, pH, base excess, bicarbonate, hemoglobin, hematocrit, glucose, creatinine, urea, BUN, electrolyte, and lactates.

8.1.9 Histology

A first gastric full-thickness biopsy was taken before the surgical procedure as healthy control. This control biopsy (CB) was removed from the posterior side of the future removed region of the stomach while the other four biopsies were collected in the selected ROIs 60 min after the GC formation. Sections of 5 μm were taken from formalin-fixed paraffin-embedded blocks and were dewaxed and rehydrated before staining at room temperature. A treatment with a hematoxylin Harris formula (Leica Biosystems, Nussloch GmbH, Heidelberg, Germany) for 10 min and then a wash with acid alcohol for 2 s and tap water for 2 min were performed. Eosin staining with Eosin 0.5% (Leica Biosystems) for 3 min was performed before washing with tap water for 30 s. Finally, the sections were dehydrated with ethanol 100% and placed in xylene until their mounting with coverslips. A semi-quantitative blinded analysis was performed by an expert pathologist using the following score and variables: necrosis, neutrophils infiltration, and congestion, with a score from 0 to 3 (none, mild, moderate, and severe, respectively).

8.1.10 Statistical Analysis

Statistics were performed using GraphPad 8.3 (GraphPad Software, San Diego, CA, USA). A Pearson's rho was analyzed to perform the correlation between optical and biological data. All data were expressed as means ± standard error (SEM). One-way and two-way ANOVA with Dunnett's multiple comparisons were performed for parametric tests to calculate differences in continuous paired variables. A two-tailed p-value < 0.05 was considered statistically significant. Principal component analysis (PCA) was used to cluster the population of data from 4 ROIs. StO_2% and LCL variables were used for the analysis. The PCA method was based on pre-standardization of the data with the largest eigenvalues. Finally, data were labeled as from the experimental design (ROI-A, ROI-C, ROI-F, and ROI-R).

8.2 Results

8.2.1 Blood Gas Analysis

The systemic blood gas analysis (BGA) supported the consistency of the experimental workflow and the healthy condition of pigs, showing only minimal changes over time when compared to T0. The full dataset and comparison are available in Table S1.

8.2.2 Histologic Analysis

Histological analysis of the biopsies of the selected regions of interest (ROIs) showed a progressive alteration of the cell morphology of the gastric wall layers. This aspect was more evident in the mucosa, characterized by superficial erosions and strong congestion, edema, and inflammatory components such as neutrophils and eosinophils, especially in ROI-R (removed region). Muscularis mucosae presented light and homogeneous alterations due to inflammation. Edema and congestion were present in the submucosae, while in ROI-R the muscularis externa presented a higher inflammatory infiltration which involved the serosa too. Nevertheless, the serosa showed no important alteration between ROIs (Fig.8.3 A,B). Control biopsies are available in Figure S1. Overall, histological alterations have grown gradually from ROI-A (antrum), ROI-C (corpus), and ROI-F (fundus) up to ROI-R. Statistical analysis was reported in Table S2. After 60 min of ischemia, the serosa showed non-statistically significant alterations in all ROIs (Fig.8.3 C). The muscularis externa presented a significantly higher damage in ROI-C and ROI-R when compared to ROI-A (p = 0.0004, p = 0.0373, respectively). The submucosa showed a statistically significantly higher histological alteration, mostly due to inflammation in ROI-F and ROI-R (p = 0.0013, p = 0.0073, respectively), while the mucosa showed an increased and significant damage in ROI-C and ROI-R (p = 0.0211, p = 0.0004, respectively). The average of the full-thickness biopsy damage presented a statistically significant increase going from ROI-A to ROI-C (p = 0.0010), ROI-F (p = 0.0187), and ROI-R (p = 0.0003), accordingly with the histopathological observation.

Additional analysis on neutrophils infiltration is reported in Figure S2.

8.2.3 Local Capillary Lactates Quantification

Mean local capillary lactate (LCL) values were not significantly different between the four ROIs at T0, upon the formation of the GC, as expected. ROI-A had similar LCLs for each time point, while ROI-C and ROI-F showed significant differences in terms of T0 vs. T15 (1.00 ± 0.28 mmol/L vs. 1.54 ± 0.18 mmol/L, p = 0.0307) and T0 vs. T60 (1.00 ± 0.24 mmol/L vs. 1.53 ± 0.22 mmol/L, p = 0.0451) respectively. Regarding ROI-R, LCL levels

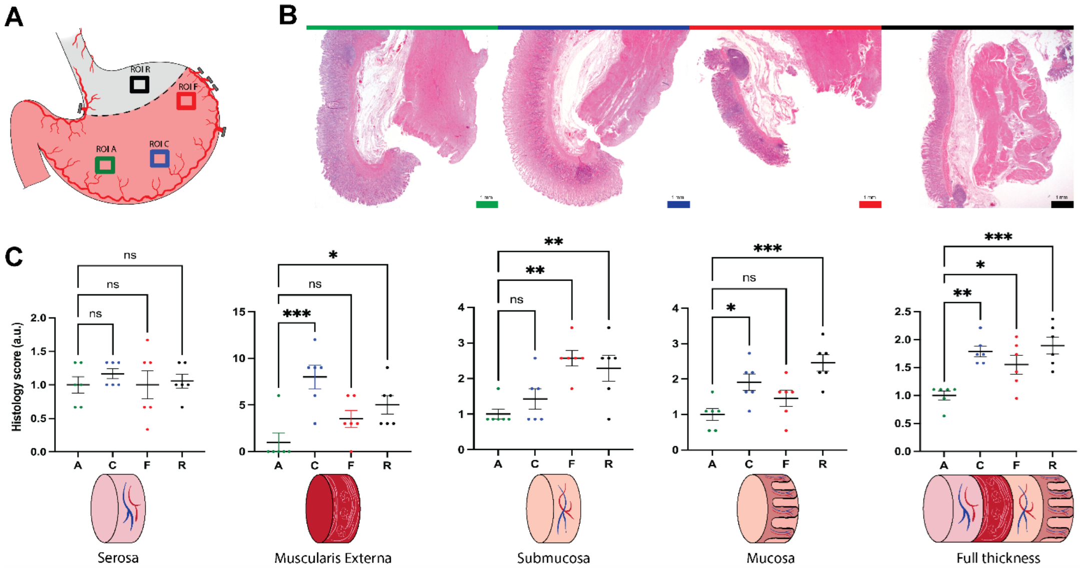

FIGURE 8.3: *Histopathological assessment. (A) ROIs localization map. (B) Hematoxylin and eosin staining of biopsies of all ROIs 60 min after tubulization, green (antrum, ROI-A), blue (corpus, ROI-C), red (fundus–future anastomotic site, ROI-F), black (resected region, ROI-R). Magnification 0.125×. Scale bar 1 mm. Pictures were sampled using microscope Zeiss AXIO scope A1. (C) Statistical analysis of the histology score, per single layer, and full-thickness. Data were expressed as mean and ± SEM and normalized with the antrum dataset. One-way ANOVA was used, ns $p > 0.05$, * $p \leq 0.05$, ** $p \leq 0.01$, *** $p \leq 0.001$ N = 6.*

obtained at T15, T30, T45, and T60 were statistically significantly higher than T0 ($p < 0.0001$) (Fig.8.4 A).

The comparison performed between different ROIs showed that mean lactate levels collected at ROI-A were significantly lower than those sampled at ROI-R at T15 (0.95 ± 0.24 mmol/L vs. 5.31 ± 0.89 mmol/L, p = 0.0091), T30 (1.06 ± 0.15 mmol/L vs. 6.44 ± 0.56 mmol/L, p = 0.0003), T45 (1.25 ± 0.17 mmol/L vs. 6.91 ± 0.69 mmol/L, p = 0.0007), and T60 (1.02 ± 0.20 mmol/L vs. 9.11 ± 0.76 mmol/L, p = 0.0002) (Fig.8.4 B). The same statistical relationship was shown by ROI-C and ROI-F when compared to ROI-R. Instead, lactate levels were not significantly different between ROI-A vs. ROI-C, ROI-A vs. ROI-F, and ROI-C vs. ROI-F (Fig.8.4 4B). LCLs were standardized for ROI-A lactate values at T0. Statistical analysis is reported in Table S3.

8.2.4 SSOP-Based StO$_2$% Quantification

SSOP images of StO_2% are shown in Fig.8.4 C. ROI-A had no differences in terms of StO_2% for each time point. Instead, ROI-C showed statistically significant lower T0 values than T45 (1.00 ± 0.03 vs. 1.08 ± 0.01, p = 0.0334) and T60 (1.00 ± 0.03 vs. 1.13 ± 0.01, p = 0.0010). Regarding ROI-F, StO_2% at T0 remained significantly lower when compared to T15, T30, T45, and T60 values (p = 0.0012, p = 0.0080, p = 0.0181, p = 0.0049, respectively). Regarding ROI-R, StO_2% was statistically higher at T0 when compared to T15, T30, T45, and T60 ($p < 0.0001$) (Fig.8.4 D). StO_2% curves of all pigs are available in Figure S3. The comparison between different ROIs showed no differences for T0. ROI-R had statistically significant lower StO_2% values when compared to all other ROIs at T15, T30, T45, and T60 ($p < 0.0001$). However, ROI-C and ROI-F showed higher values than ROI-A at T15 (ROI-C vs. ROI-A, p = 0.0007; ROI-F vs. ROI-A, $p < 0.0001$), T30 ($p < 0.0001$), T45 ($p < 0.0001$), and T60 ($p < 0.0001$) (Fig.8.4 E, Table S4).

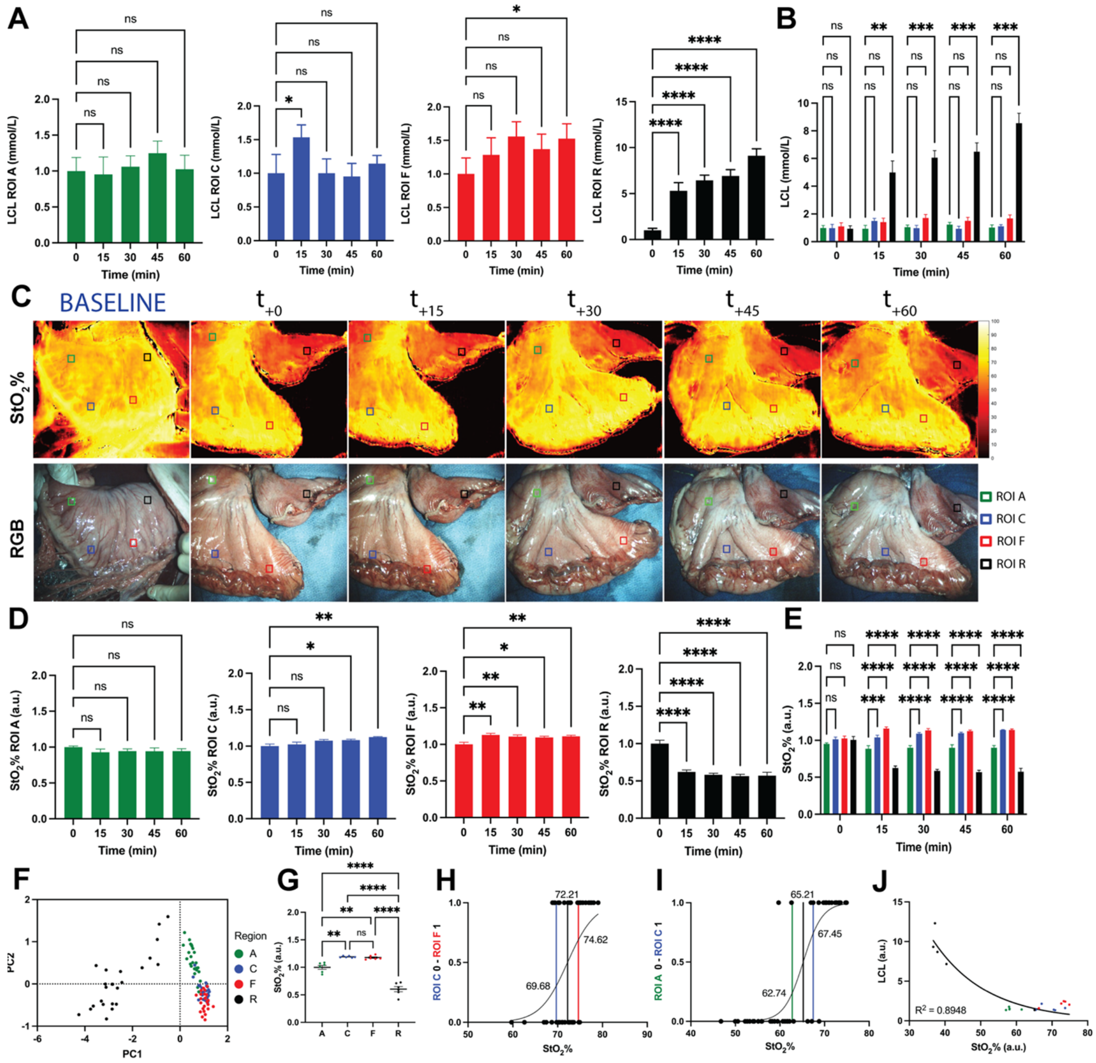

FIGURE 8.4: *LCLs and StO_2% quantification and analysis. Different colors indicate different ROIs: green (ROI-A), blue (ROI C), fundus (ROI-F), and black (ROI-R). (A) Evolution of LCLs for single ROIs. Only the removed region showed statistically significantly higher values of LCLs for each time point from T15 to T60 when compared to T0; the corpus showed this relationship for T0 vs. T15 and the fundus for T0 vs. T60. Data were normalized for T0 of ROI-A. (B) LCL comparison between ROIs. After gastric conduit formation, the removed region showed statistically significantly higher values of LCLs when compared to the other gastric regions. Data were normalized for T0 of ROI-A. (C) SSOP images showing StO_2% of the gastric conduit and the removed region from baseline to T60, and correspondent true color (RGB) images. (D) Oxygenation trends for each region of interest during the full ischemic period with a non-constant sampling rate. Between T0 (when the GC is complete) and T15, the sampling rate is around 10 s to monitor the dynamics of tissue perfusion, whereas for $t = -5$ min (baseline) and T30, T45, and T60, a single point was sampled. Data were normalized for T0 of ROI-A. (E) Evolution of StO_2% for single ROIs. StO_2% increased along time in the corpus (T45 and T60) and fundus (T15, T30, T45, and T60). Instead, as expected, StO_2% values at T15, T30, T45, and T60 were lower than T0. Data were normalized for T0 of ROI-A. (F) Principal component analysis of the ROIs. The variables selected are LCL and StO_2% and the label used is the ROI (A, C, F, R). ROI-R represents a separate cluster from the other ROIs. Principal Component (PC)1 and PC2 contribute to 94.83% of the variance. (G) StO_2% comparison between ROIs. After GC formation, the removed region showed lower StO_2% values than other gastric districts. Instead, StO_2% of the antrum appeared lower when compared to the corpus and fundus. Data were normalized for T0 of ROI-A. (H) Simple logistic regression analysis between ROI-A and ROI-F. (I) Simple logistic regression analysis between ROI-A and ROI-C. (J) Pearson's correlations between LCL and StO_2%. Higher LCL*

8.2.5 Correlation between StO_2% Values and LCLs

LCL values were normalized for LCL measurements of ROI-A at T0. Principal component analysis (PCA) of StO_2% and LCL values after resection showed ROI-R as a separated cluster from the other ROIs. ROI-A and ROI-F appeared as separate groups while ROI-C was overlapped between ROI-A and ROI-F (Fig.8.4 F). Similarly, data were normalized for ROI-A at T60 to investigate the power of the camera in discriminating between ROIs. As a result, measurements evaluated at ROI-A showed statistically significant differences when compared to ROI-C (p = 0.0013), ROI-F (p = 0.0028), and ROI-R (p < 0.0001). A significant difference was found for ROI-C vs. ROI-R (p < 0.0001) and ROI-F vs. ROI-R (p < 0.0001) while no difference was found regarding ROI-C vs. ROI-F (Fig.8.4 G). A simple logistic regression analysis was used to find the cut-off value to discriminate ROI-A from ROI-C and ROI-C from ROI-F. The threshold value to discriminate between ROI-C and ROI-F was 72.21%, with an AUC of 0.7274 (95% CI 0.5847 to 0.8702, p = 0.0069) (Fig.8.4 H) while the threshold value to distinguish between ROI-A and ROI-C was found to be 65.21%, with an AUC of 0.9688 (95% CI 0.9275 to 1.0000, p < 0.0001) (Fig.8.4 I). StO_2% and LCLs were found to be negatively correlated ($R = -0.8439$, 95% CI -0.9367 to -0.6407, p < 0.0001) (Fig.8.4 J).

8.3 Discussion

In the current experimental study, the SSOP imaging system was used to evaluate StO_2% values corresponding to selected ROIs, using the resected upper part of the stomach (ROI-R) as ischemic control.

ROI-R showed lower StO_2% values when compared to other ROIs. Interestingly, the corpus and fundus maintained StO_2% values higher than the antrum, probably due to the inflammatory process activated during the manipulation of the stomach. Gastric manipulation, the sequential ligation of vessels and the division of the stomach, are factors which can affect the physiology of healthy gastric tissue. Akiyama et al. [193] already described that the formation of the gastric conduit induces severe changes in microcirculation, particularly in the anastomotic region of the gastric fundus.

As a result of this manipulation, immune cells promote the acute inflammatory response by increasing the permeability of vessels and allowing the secretion of various cytokines and chemokines. Neutrophils are the first ones to be involved, by secreting vasoactive and pro-inflammatory mediators, including histamine, platelet-activating factors (PAFs), bradykinin, and thrombin. These mediators increase vascular permeability, promoting fluid accumulation (edema) and leukocyte extravasation (Figure S2). Polymorphonuclear neutrophils produce reactive oxygen species (ROS), responsible for endothelial dysfunction by oxidation of crucial cellular signaling proteins such as tyrosine phosphatases [194]. The presence of ROS together with the increased permeability of vessels could account for higher StO_2% values detected by the present experimental model, reflecting the growing trend of inflammation along time and from the antrum to the fundus. As described above, inflammation is part of the regular process of healing. However, persistent inflammation led to excessive quantities of pro-inflammatory macrophages, whereas the number of macrophages with anti-inflammatory phenotypes became lower. As a result, the establishment of a highly inflammatory environment with an overabundance of inflammatory mediators promotes the degradation of the extracellular matrix, preventing anastomotic healing [195].

The StO_2% values provided by means of SSOP negatively correlated with LCL values, confirming the biological validity of the method. Instead, no correlation was found between StO_2% and the histopathologic analysis. The limited period of ischemia (60 min), together with the residual perfusion of ROI-R from esophageal vessels, were probably accountable for non-significant histological changes in the gastric tissue. Nevertheless, this time frame is consistent since it is similar to the time between GC formation and the packing of the esophagogastric anastomosis in the Ivor Lewis procedure performed in humans.

Our group has previously used HSI and a system called HYPER (HYperspectral-based Enhanced Reality) to assess $StO_2\%$ and intraoperatively localize preselected ROIs during esophagectomy [196], small bowel ischemia [184], and hepatectomy [197]. HYPER allowed to compare HSI to LCLs and mucosal scan with confocal laser endomicroscopy (CLE) on the same ROI [196] with high accuracy. However, the time currently necessary for HSI acquisition is around 10 s and still not yet fully "real-time".

Instead, fluorescence angiography with indocyanine green (ICG) allows for the real-time visualization of tissue vascularization, showing promising results for the evaluation of perfusion in numerous surgical procedures, hence leading to modifications in the surgical strategy and consequently to a decrease in the rates of AL [198],[199]. However, the ICG interpretation is subjective while the quantitative evaluation of ICG is a widely unexplored field. In addition, serious adverse events after intravenous application of ICG are described, such as anaphylactic shock, up to sudden deaths in very rarely reported cases [200].

Several other methods for perfusion assessment are reported in the literature. However, they lack in terms of quantitative parameters, provide arbitrary perfusion units, and are influenced with vascular heterogeneity [180].

As a result, non-invasiveness, the absence of adverse events, quantification properties, and the video rate acquisition of the SSOP technology are advantages worthy of being highlighted. The real-time imaging capabilities of SSOP have already been demonstrated [39]. However, the configuration used for the present experiment did not allow to reach minimum requirements required for high frame rate acquisitions. It was due to the high integration times required on the imaging side (>100 ms). Further development of the laser sources has already been started to achieve better performance on the illumination side, hence allowing shorter exposure times during acquisitions in the next experimental steps.

Additionally, the potential SSOP system's ability to detect and quantify inflammation could make this new technology a useful tool to screen suffering tissues that are more likely to develop delayed anastomotic healing, moving beyond the concept of perfusion alone.

The main limitations of this study lie in the animal model, the very limited sample size, and the acute nature of the experiment. In addition, the absence of gold standard values of tissue oxygenation and inflammation makes it difficult to compare SSOP with other methods. Finally, SSOP has not yet been adapted to endoscopic systems, resulting in a lack of potential usefulness for an increasingly widespread minimally invasive surgery (MIS). Actually, a prototype based on a laparoscopic surgical instrument is being developed to bring SSOP to MIS, and it is soon going to be ready for validation via pre-clinical trials on other swine models.

8.4 Conclusions

The present study has demonstrated for the first time the safety and reliability of SSOP technology in determining the real-time adequate perfusion of GC when compared to a certain ischemic gastric tissue, providing a quantitative evaluation through $StO_2\%$ values, without exogenous fluorophores. SSOP is a suitable intraoperative tool which could potentially predict AL in the clinical setting. This preliminary validation provided a robust dataset useful to compare single snapshot images with the video rate as the next experimental step. Further studies are needed to validate the system and to develop a minimally invasive setup, to finally proceed to clinical application.

Supplementary Materials: The following data are available online at `https://www.mdpi.com/article/10.3390/cancers13236079/s1`, Figure S1: Control biopsy of the stomach (T0), Figure S2: Neutrophils distribution (A) and quantification (B), Figure S3: $StO_2\%$ curves of all pigs, Table S1: Blood gas analysis quantification, Table S2: Histological assessment and correlation, Table S3: LCL quantification and correlation, Table S4: $StO_2\%$ quantification and correlation.

Chapter 9

BOWEL PERFUSION ASSESSMENT VIA SSOP

Article Title : *"Quantification of bowel ischaemia using real-time Single Snapshot Imaging of Optical Properties (SSOP)"*

Authors : *M. R. Rodríguez-Luna, N. Okamoto, L. Cinelli, L. Baratelli, S. Ségaud, A. Rodriguez-Gomez, E. Bannone, E. Zonoobi, D. S Keller, J. Marescaux, M. Diana, S. Gioux*

Journal : *British Journal of Surgery*© *(in submission)*

Anastomotic leak (AL) is a major complication in digestive surgery accountable for considerable morbidity and mortality [201], [202]. The AL incidence is particularly high following esophageal (20-35%) and colorectal resections (4-19%)[184], and in cases which require extraperitoneal anastomosis [203]. The pathophysiology of AL is multifactorial and includes patient non-modifiable factors such as comorbidities, nutritional score, and oncological status including neoadjuvant treatment. Conversely, there are modifiable surgical factors that may influence the incidence of AL, such as the location of bowel transection, ensuring optimal perfusion. Adequate perfusion is a key component of the anastomotic healing process. However, an intraoperative evaluation of perfusion is mainly based on unreliable clinical criteria, including serosal discolouration, blood flow from the marginal artery, and pulsatile bleeding at the cut edge of the bowel [204]. As a result, there is a compelling clinical need to develop intraoperative technologies that enhance the surgeon's ability to quantify and identify transection and anastomotic sites.

Over recent years, near-infrared (NIR) fluorescence imaging (FI) based on indocyanine green (ICG) has been extensively studied as a tool to provide an enhanced evaluation of bowel perfusion in real time [205]. Promising results have been demonstrated in several prospective clinical trials in which ICG-FI improves surgical outcomes by decreasing the incidence of AL [206], [207]. The slow but consistent diffusion of the fluorophore from perfused to non-perfused areas and the lack of quantification of the fluorescence intensity signal may lead to errors in the identification of marginal zones. Additionally, the estimation of perfusion using fluorescence angiography (FA) is limited to perfusion-only metrics (as opposed to functional tissue status) and mandates the injection of an exogenous agent [204].

In parallel to exogenous fluorescence, non-invasive contrast-free (i.e. endogenous) real-time optical imaging technologies have been developed. They are promising tools since they allow for an adequate surgical workflow without the constraints of administering external chemical compounds to the human body. Consequently, the clinical translation of endogenous optical imaging devices is strongly accelerating and being disseminated. In order to obtain physiological local information, most devices used are based on NIR spectroscopy, such as hyperspectral (HSI) and multispectral (MSI) imaging technologies [183]. Spectroscopic imaging allows for contact-free reading of StO_2 with high spatial resolution and with a large field of view ($> 15x15\ cm^2$), thereby improving intraoperative decision-making by adding quantitative information.

Single Snapshot of Optical Properties (SSOP) has recently been developed [189]. It is a contrast-free real-time non-invasive optical imaging technique, which allows to evaluate physiological tissue properties. SSOP is based on the well-known diffuse optimal imaging method name spatial frequency domain imaging (SFDI) which uses light propagation models to quantify optical properties discriminating physiological contrast from tissue constituents [1]. Therefore, SSOP is able to determine tissue oxygenation (StO_2) by computing the fraction of oxygenated over total hemoglobin in real-time. It has proven to be an efficient method since it allows to reduce the number of image acquisitions to a single frame, which is very convenient in the surgical setting, hence enabling real-time video rate imaging of StO_2 and preventing workflow disruption [190]. The performance of SFDI and SSOP have previously been evaluated both *ex-vivo* and *in-vivo* and proven to achieve high accuracy (i.e. less than a 10% error) [85],[187],[86]. The aim of this experimental study was to preclinically evaluate the accuracy of SSOP in quantifying bowel perfusion using robust and validated biomarkers such as capillary lactates.

9.1 Methods

9.1.1 Animal models

A total of six adult swines (*Sus scrofa domesticus*, ssp. Large white, mean weight in kg) were involved in this non-survival study. The present experimental study is part of the QuantSURG (Quantitative Surgical Guidance for Colorectal Surgery) project, which received full approval from the local Ethical Committee on Animal Experimentation (ICOMETH No. 038.2019.01.121) and by the French Ministry of Superior Education and Research (MESR) under the following reference: APAFIS # 20819-2019052411591088 v3. All animals used in the experimental laboratory were managed according to French laws for animal use and care and according to the directives of the European Community Council (2010/63/EU) and ARRIVE guidelines [191]. The animals were fasted for 24 hours with free access to water before surgery. Animals were premedicated, 10 minutes before surgery with an intramuscular injection of ketamine (20 mg/kg) and azaperone (2 mg/kg) (Stresnil; Janssen-Cilag, Belgium). Intravenous propofol (3 mg/kg) combined with rocuronium (0.8 mg/kg) were used for induction. Anesthesia was maintained with 2% isoflurane. At the end of the procedures, pigs were sacrificed with an intravenous injection of a lethal dose of potassium chloride.

9.1.2 SSOP imaging

Single Snapshot imaging of Optical Properties (SSOP) is based on the projection of spatially modulated patterns of light on the sample and on the acquisition with a camera of the diffused back reflected light. SSOP was developed as a real-time implementation of more time-consuming Spatial Frequency Domain Imaging (SFDI) methods that requires several frames to extract the optical properties of tissues. Indeed, in a standard SFDI workflow, two different spatial frequency profiles (e.g., $f_x = 0\ mm^{-1}$, $f_x = 0.2\ mm^{-1}$) with three-phase shifts for each of them are projected on the sample surface, allowing for the demodulation of the signal into its DC and AC components [45]. Differently, SSOP requires only a single high frequency pattern to be projected on the tissue, thanks to a Fourier's domain filtering approach for the demodulation step [86],[189], [85], thus reducing from six to one the number of frames needed for the acquisition and enabling for a real-time capability of the imaging system. Following the demodulation, both SFDI and SSOP share the same workflow starting from a calibration step involving the measurement of a calibration phantom with known optical properties. The measurements of this tissue mimicking phantom allows us to to compute the diffuse reflectance maps for the sample, i.e., R_{DC} ($f_x = 0\ mm^{-1}$) and R_{AC} ($f_x = 0.2\ mm^{-1}$). A Monte Carlo-based Look-Up Table (LUT) algorithm, was applied to retrieve the optical properties of the sample (i.e., absorption and reduced scattering coefficients) for each pixel of the image [83]. The natural consequences of the single frame approach are a degradation in image quality and the presence of edge artifacts. Significant improvements have been achieved in recent years by first optimising the filtering technique [84] and by adopting Deep Neural Network approaches for the demodulation [86],[85]. The latest developments on SSOP also account for a tridimensional profile correction of the sample in order to reduce the quantification error of SSOP associated with a variation of light intensity across non-flat sample surfaces [85].

FIGURE 9.1: *(A) The ischaemic bowel loop is placed in a standard position in order to facilitate image acquisition by means of the Trident imagining system. The withe arrow point at the camera head which mounted onto an articulated arm. A standardized picture orientation and distance is use preventing from any bias. Please note that light interference is avoided during image acquisition. (B) Pre-clinical patient cart of the Trident imaging system for fluorescence, SFDI, and SSOP imaging. Imaging head enclose three separate channels for RGB, NIR1, and NIR2 imaging. A DMD-based projection system is also mounted onto the head for the generation of structured illumination over the field of view. The light source is delivered to the projector via a fiber-based coupling system. An illumination ring is used to homogeneously deliver white light illumination of the surgical field and fluorescence excitation wavelength. The main body of the cart contains the laser sources, the white light lamp, and the PC workstation. (C) Schematics of the optical path in the trident imaging system for the co-registration of the three imaging channels, together with the configuration of the DMD-based projector. A pair of filtering cubes are used to isolate the NIR1 and NIR2 channels, and a set of mirrors are used to align the field of view of the three cameras.*

9.1.3 Deep learning method for SSOP

For this study, the latest SSOP deep learning approach replaced the standard Fourier's domain filtering technique to improve the overall image quality, as described by Aguénounon et al.[85]. Briefly, two dedicated CNNs based on a U-Net architecture were used to extract the modulation amplitude of the signal for each spatial frequency, and for the profilometry analysis of the surface profile of the sample. Both networks were trained using high quality images obtained with SFDI acquisition sequences (with 7 phase shifts instead of 3 to enhance quantification accuracy and image quality) and optimised for efficient and low-cost computation performances, enabling a real-time capability and achieving high visual quality optical property quantification for up to 1 MP images. The training dataset consisted of a total of 200 high quality images divided into n = 40 images of tissue-mimicking silicone phantoms with different optical properties ranging from $\mu_a = 0.005$ to $0.05\ mm^{-1}$ for absorption and from $\mu_s' = 0.5$ to $3\ mm^{-1}$ for reduced scattering; n = 52 images of hands from different Caucasian men and women in various configurations; n = 108 images from ex vivo and in vivo swine organs in several orientations (stomach, small bowel, colon, kidney, pancreas, liver, and spleen).

9.1.4 Trident imaging system

The Trident imaging system (Fig.9.1 (B-C)) is based on a digital-micro-mirror device (DMD, Vialux GmbH, Chemnitz, Sachsen, Germany) to project structured light in the form of sinusoidal patterns at 45 ± 5 cm working distance. The projection system is fibre-coupled to a dedicated, custom-made, class 3R high-power laser source composed of laser diodes (LDX Optronics, Maryville, TN) and used here to project patterns at 665 nm and 860 nm for oxygen saturation measurements [192]. A white high power LED lamp (FTIII24017-12, Fiberoptics Technology, CT) is also used to illuminate the surgical field to provide anatomical visualisation specifically filtered to avoid impeding oxygen saturation measurements. The imaging head is built with three CMOS cameras (JAI GO-5000M-USB, JAI Ltd., Kanagawa, Japan, PCO.edge 4.2, Excelitas PCO GmbH, Kelheim, Germany, JAI GO-5000C-USB, JAI Ltd., Kanagawa, Japan) sharing the same field of view of 15×15 cm^2 for the collection of the NIR1 (665 nm), NIR2 (860 nm) and the RGB channels with a resolution of 1024×1280 pixels. In addition, low-pass and high-pass filters are used in the optical path to isolate the different wavelengths (Chroma,VT). A pair of linear polarisers (PPL05C, Moxtek, Orem, UT, USA) in crossed configuration are also employed at the projection and imaging sides to reject the contribution from specular reflections at the surface of the sample. A silicone-based optical phantom (21 $cm \times 21$ $cm \times 2$ cm) with known optical properties ($\mu_a = 0.01$ mm^{-1} and $\mu_s' = 1.1$ mm^{-1}) at 665 nm, and $\mu_a = 0.02$ mm^{-1} and $\mu_s' = 0.8$ mm^{-1} at 860 nm) is used to calibrate the Trident imaging system. The imaging workflow consists of the simultaneous projection of a high frequency sinusoidal pattern (i.e. $f_x = 0.2$ mm^{-1}) at the two wavelengths (665 nm and 860 nm) followed by the three channels acquisition of the images for the extraction of the oxygen saturation level of the tissue.

9.1.5 Surgical set-up pure ischemia model

A central venous line was placed through internal jugular vein venodissection. A midline laparotomy was performed using electrocautery. A self-retaining retractor was then placed and a 10 cm small bowel loop was exposed to create bowel ischaemia by diving arcade branches. Five regions of interest (ROIs) were marked with an interrupted suture in the antimesenteric border (ROI 1: central ischaemic; ROI 2: left marginal; ROI 3: left vascularised (2.5 cm from ROI 2); ROI 4: right marginal; ROI 5: right vascularised (2.5 cm from ROI 4)). The small bowel was imaged with the multispectral camera through SSOP before and after the ischaemia at different time points (T0, T15, T30, T45, T60 min). The SSOP image acquisitions were performed in the dark (i.e., with the light turned off in the operating room), to reduce the risk of bias. The system can be also operated in standard ambient light conditions via an adapted calibration routine (Fig.9.1 (A)).

9.1.6 Surgical set-up ischemia/reperfusion model

To assess the accuracy of the Trident system in detecting oxygenation changes we create a short ischemia/reperfusion model. The same surgical technique was applied for laparotomy. Six small bowel loops measuring 10 cm each were exposed to create short bowel ischaemia by diving the peritoneal layers of the mesentery with enough length to apply a bulldog clamp. Similarly to the pure ischaemia model, five regions of interest (ROIs) were marked with an interrupted suture in the antimesenteric border (ROI 1: central ischaemic; ROI 2: left marginal; ROI 3: left vascularised (2.5 cm from ROI 2); ROI 4: right marginal; ROI 5: right vascularised (2.5 cm from ROI 4) in each loop. Each small bowel loop was imaged with the Trident system through SSOP before, during clamping and after declamping at the reperfusion phase (T0, and T10 and T14 min respectively) (Fig.9.1 (B)).

9.1.7 Analysis of capillary and systemic lactates

At each time points, capillary lactates ($mmol/L$) were measured using a portable analyser (EDGE® lactate analyser, ApexBio, Taipei, Taiwan, People's Republic of China). Lactate is the product of glycolysis and its accumulation reflects a lowered mitochondrial activity in the presence of reduced O2 concentration. This method has been described earlier in studies on the metabolic effect of bowel resection [208], [209]. Systemic lactates were also measured in venous blood retrieved from the central line and using the EPOC® Blood Analysis System (Siemens Healthcare, Germany), a portable blood analyser.

9.1.8 Pathological examination

Pathological examination was assessed for the pure ischaemia model only. Full thickness biopsies were retrieved at the end of the procedure, specimens were fixed in a 4% formalin solution for at least 24 hours. Four μm thick sections were cut from paraffin-embedded tissues and stained with haematoxylin and eosin. Biopsies were taken from each ROI after 60 minutes of ischaemia and one from a distal part before creating the ischaemic loop, which served as a control. A microscopic assessment was made (Leica 2000 LED, Leica Biosystems GmbH, Wetzlar, Germany) using Park/Chiu's scoring system of intestinal ischaemic damage [210], [211].

9.1.9 Statistical analysis

All statistical analyses were performed using the GraphPad Prism software for macOS (GraphPad Software, Inc. USA), version 9.1.1. Data are shown as mean and standard deviation (SD) unless otherwise indicated. Capillary lactates were normalised according to systemic lactates to reduce variability. In order to assess a possible correlation between normalised lactates and SSOP-StO_2, a Pearson's rank correlation coefficient was calculated. A Student's t-test was used to compare continuous variables after confirming a parametric distribution using the Kolmogorov-Smirnov normality test. A p value < 0.05 was considered statistically significant.

9.2 Results

In the pure ischaemia model the mean value of normalised lactates in ROI 1 was found to be 4.804 $mmol/L \pm 2.591$ and was significantly higher when compared to marginal ROIs (ROI 2 + ROI 4: 1.026 $mmol/L \pm 0.472$, $p < 0.0001$), and to vascularised ROIs (ROI 3 + ROI 5: 0.749 ± 0.246 $mmol/L$, $p < 0.0001$). The difference between marginal and vascularised ROIs also showed a statistically significant difference ($p < 0.0001$) (Fig.9.2 (A) and (B)). The mean value of SSOP-StO_2 in ROI 1 was 30.08% $\pm$ 6.963 and was significantly lower when compared to marginal ROIs (ROI 2 + ROI 4: 45.67% $\pm$ 10.02, $p =< 0.0001$), and to vascularised ROIs (ROI 3 + ROI 5: 48.08% $\pm$ 7.083, $p =< 0.0001$). Although the SSOP-StO_2 was higher in vascularised ROIs, this difference was not statistically significant ($p = 0.1298$) (Fig.9.2 (C) and (D)). The cumulative Pearson's correlation analysis between normalised lactates and SSOP-StO_2 was -0.5892, $p < 0.0001$ (Fig.9.2 (E)).

As for the histopathological confirmation, the mean Park/Chiu's score at ROI 1 was 4.500 ± 0.8367 and was significantly higher than marginal zones (ROI 2+ROI 4: 1.583 ± 1.097) $p < 0.0001$ and vascularised (ROI 3 + ROI 5: 0.667 ± 0.650), $p < 0.0001$ (Fig.9.2 (F)).

At T65, the Park/Chiu's score correlation between SSOP-StO_2 was $r = -0.6251$, $p = 0.0002$ and between normalised lactates was $r = 0.7102$, $p < 0.0001$. In the short

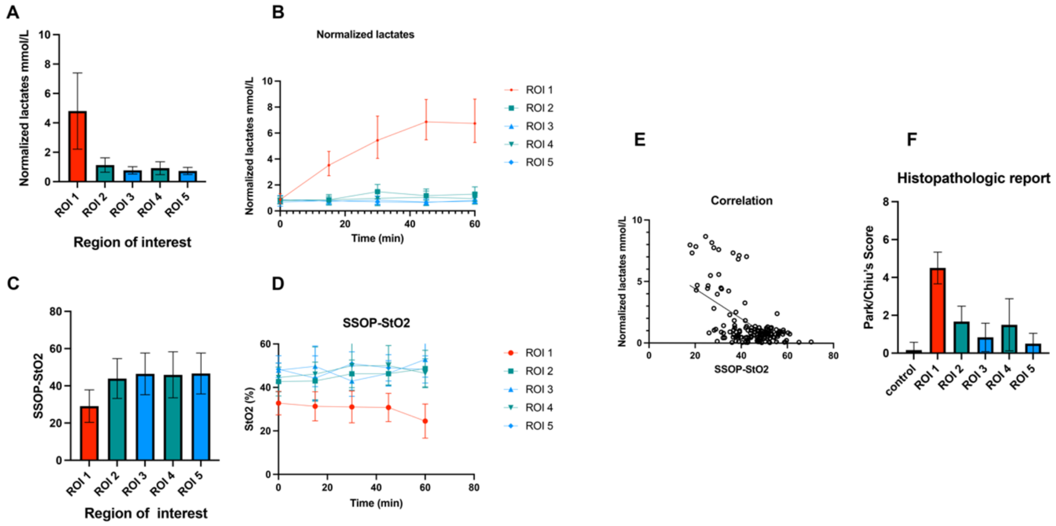

FIGURE 9.2: ***A***. *Normalised lactates values (mmol / L) acquired during 1 hour of ischaemia: the mean value of normalised lactates in ROI 1 was* 4.8 ± 2.5 *and was significantly higher compared to marginal ROIs (ROI2+ROI 4:* 1.0 ± 0.4, $p < 0,0001$*), and to vascularised ROIs (ROI 3+ROI 5:* 0.7 ± 0.2, $p < 0.0001$*). The difference between marginal and vascularised ROIs showed a statistically significant difference* $p < 0.0001$. ***B***. *Kinetics of normalised lactates values (mmol/L).* ***C***. *SSOP-*StO_2 *values acquired during 1 hour of ischaemia: the mean value of SSOP-*StO_2 *in ROI 1 was* 30.08 ± 6.9 *and was significantly lower compared to marginal ROIs (ROI 2+ROI 4:* 45.6 ± 10.0, $p =< 0.0001$*), and to vascularised ROIs (ROI 3+ROI 5:* 48.0 ± 7.0, $p =< 0.0001$*). Although SSOP-*StO_2 *was higher in vascularised ROIs, it did not show any statistically significant difference (*$p = 0.1298$*).* ***D***. *Kinetics of* StO_2 *cartography in each ROI.* ***E***. *Pearson's correlation analysis between normalised lactates and SSOP-*StO_2 *in all identified ROIs.* ***G***. *Histopathological report: the mean Park/Chiu's score at ROI 1 was* 4.500 ± 0.8367 *and was significantly higher than marginal zones (ROI 2 and ROI 4:* 1.583 ± 1.097, $p < 0,0001$*) and vascularised (ROI 3 and ROI 5:* 0.667 ± 0.650, $p < 0.0001$*).*

ischaemia/reperfusion model we found that ROI 1 has a mean $57,54 \pm 5,35$, $37,6 \pm 4{,}12$ and $62,40 \pm 7,28$ StO_2 at T0, T10 and T15 respectively. The difference in term of StO_2 value from occlusion to reperfusion was statistically significant ($p = 0,00017$) (Fig.9.4 and Fig.9.5) Marginal ROIs (ROI 2 + ROI 4) had a mean $57,22 \pm 5,61$, $56,89 \pm 5,49$ and $60,93 \pm 6,91$ StO_2 at T0, T10 and T15. While for the vascularized ROIs (ROI 3 + ROI 5) $62,53 \pm 5,43$, $59,71 \pm 6,37$ and $64,406,80$ StO_2 at T0, T10 and T15 was found. In marginal ROIs (ROI 2 + ROI 4) the differences in terms of StO_2 from occlusion to reperfusion was not statistically significant different ($p = 0,1511$), similarly to vascularised ones ($p = 0,1167$).

9.3 Discussion

In the present experimental pure bowel ischaemia model, the Trident imaging system could accurately quantify tissue StO_2, which is a useful biomarker of tissue viability. Additionally, StO_2 images from the Trident imaging system were correlated with a validated marker of tissue perfusion such as strip-based capillary lactates [209]. Local bowel capillary lactates were normalised via systemic lactates to reduce the variability between animals. The high number of paired normalised capillary lactates and StO_2 datasets (175) at different time points allowed to compute a statistically significant negative correlation between those two parameters. StO_2 images from the Trident imaging system were also correlated with the histopathological ischaemic score. The Park/Chiu's score used in

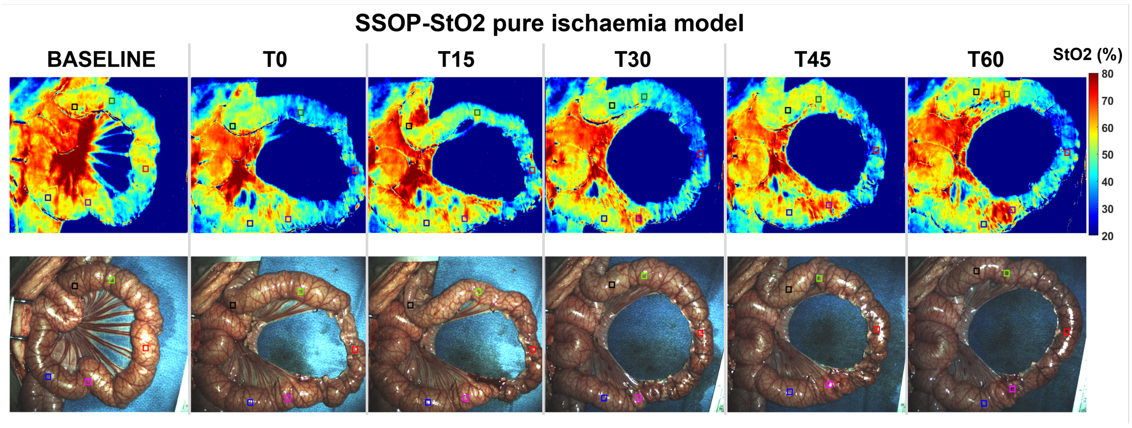

FIGURE 9.3: *SSOP images showing StO_2% during the full ischemic period in the small bowel loop from baseline to T60, and correspondent true colour (RGB) images*

this experiment was based on all intestinal layers. Although it is well-known that the intestinal mucosa and submucosa are the first ones affected by impaired perfusion since they receive most of the mesenteric blood flow (70%), the muscularis and the serosal layer can also be damaged during ischaemic periods [212]. Ischaemic ROIs mostly presented with denuded villi and dilated capillaries but the evaluation of the StO_2 images was performed on the serosal side turning histopathological repercussions in external layers into elements of interest. One must stress that this was a short-term ischaemia model (1 hour), and transmural necrosis is mostly developed after longer ischaemic periods (6 hours)[212]. In fact, the higher Park/Chiu's score of 6, which represents crypt layer injury was found in one case only. To verify the accuracy of the Trident system we create the short ischaemia/reperfusion model in which the Trident system was able to detect the decrease of StO_2 as soon as the clamping occurred. As for the reperfusion, once the bulldog clamp was released the Trident system was able to detect an StO_2 improvement in the ischemic area. Intraoperative perfusion assessment constitutes a critical issue during digestive surgery. In NIR-FA, ICG has been the most commonly used fluorophore to evaluate local microperfusion [213]. ICG-FA has been rapidly expanded by the increasing availability of optical imaging systems [214],[215],[216]. However, ICG-FA has limitations, and most ICG-FA optical systems are based on relative fluorescence intensity without considering diffusion, since perfusion is a dynamic process in which the fluorophore tends to distribute into ischemic areas overtime, the static evaluation can lead to an overestimation on non-perfused areas. Secondly, the fluorescence intensity is inversely correlated to the source-to-target distance, this fact makes those structures closer to the source brighter than areas faraway. To prevent from distance bias, distance standardisation between the NIR-endoscope and the surgical field and/or the use of a reference calibration tool must be performed during image acquisiton [217]. In order to overcome ICG-FA drawbacks, quantification methods which are independent of distance have been developed to obtain a perfusion cartogram based on the dynamic uptake of the fluorophore over time such as FLER [213] or Q-ICG [218],[219]. Although the use of quantitative methods offers significant improvement as a reproductible and robust solution, at present they have not been extensively adopted. Despite exogenous fluorescence is a well-established intraoperative technology to assess gastrointestinal perfusion, there is still no standardised approach regarding its use as reported in the IHU-IRCAD-EAES EURO-FIGS registry recently [220]. The highest level of evidence holds promising result regarding the impact of ICG-FA in decreasing AL, but the quality of non-randomised retrospective clinical studies included in the latest meta-analyses should be considered

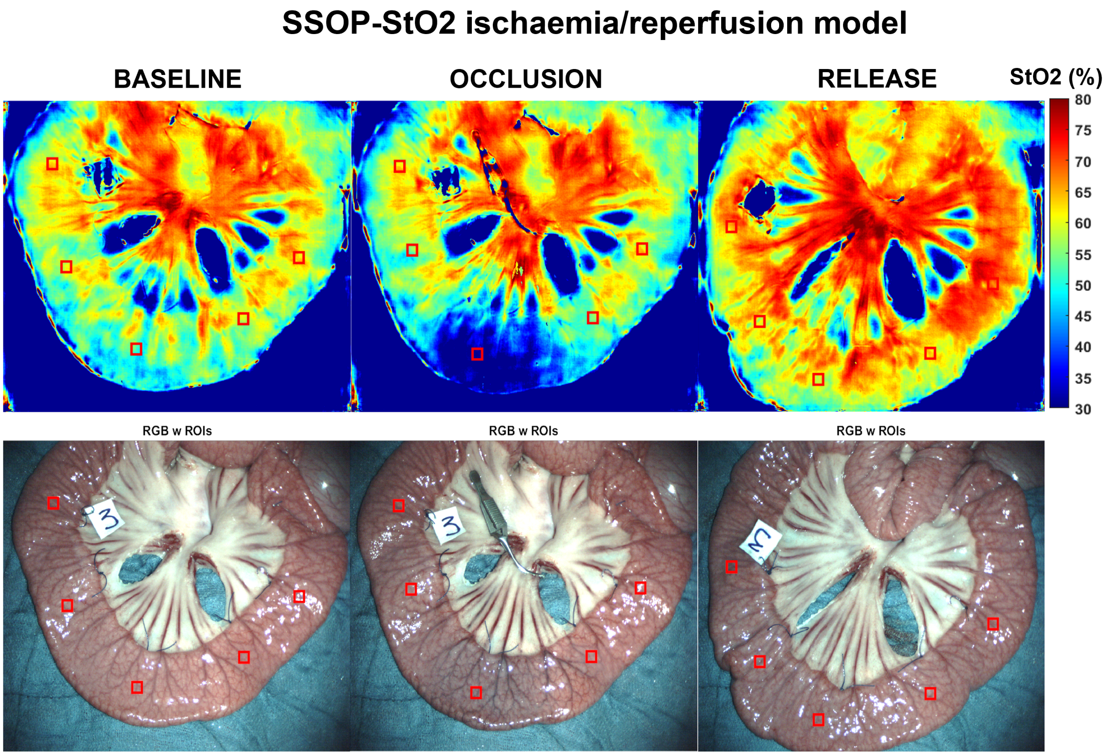

FIGURE 9.4: *Ischemia/reperfusion model. SSOP-StO_2 (upper row) and RGB small bowel images (lower row) at baseline, during vascular (arteries and veins) occlusion and after clamp release (corresponding to the reperfusion phase). Red squares represent ROIs.*

[199],[221], as well as non-quantitative methods used to estimate perfusion in the RCT [20],[222].

As compared to FA, endogenous imaging methods including SSOP can provide a greater amount of quantitatively significant data by characterising several tissue components including StO_2 which reflects intracellular metabolic changes induced by ischaemia. HSI is an eminent example of endogenous imaging technology, as previously discussed data extraction by means of HSI is based on NIR spectroscopy. The accuracy of HSI to evaluate perfusion has been studied during esophagectomy, in 22 patients HSI was able to discriminate between gastric conduits with and without laparoscopic ischaemic preconditioning (StO_2 66% vs 78%, p = 0.03)[63]. Additionally, perfusion assessment in colorectal surgery has been compared between HSI and FA showing comparable results in detecting the optimal demarcation line [62]. Although HSI is a promising technology, it does not allow for a video rate acquisition and the large datasets require post-processing algorithms to discriminate features according to spectral curves. To overcome this limitation, our group created the concept of HYPerspectral Enhanced Reality (HYPER). HYPER has shown in a preclinical trial superior results in detecting tissue oxygenation as compared to quantitative fluorescence angiography [183]. However, HYPER requires images superimposition using augmented reality onto real-time videos to achieve real-time intraoperative guidance making its use currently limited [184]. At present, SSOP is a more adapted surgical navigation system method since it allows for a video rate (> 25 frames per second) non-invasive, wide-field ($> 100\ cm^2$), quantitative multispectral characterisation of metabolic properties through a single frame acquisition [2]. As previously stressed, SSOP is based on SFDI, a non-contact multispectral optical imaging method that allows for accurate measurement of tissue optical properties over large fields of view [45],

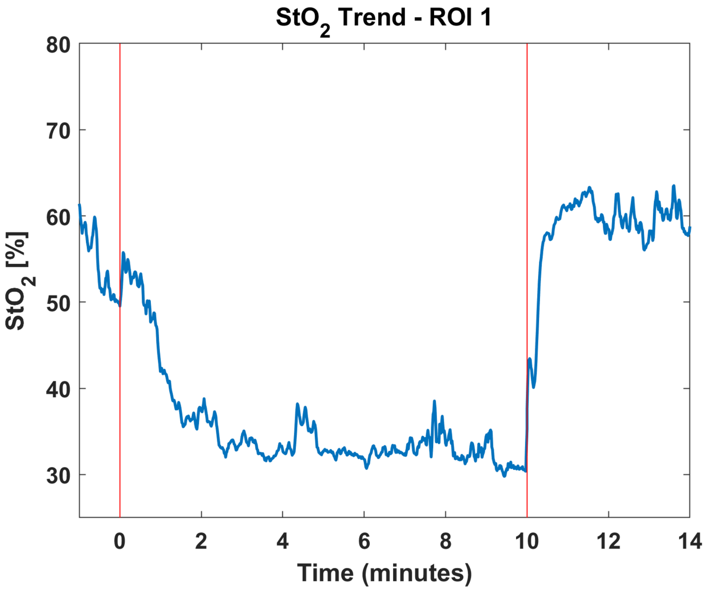

FIGURE 9.5: *The graph shows the overtime evolution of SSOP-StO2 parameter at baseline, occlusion and reperfusion phases on ROI 1. Red bars represent the clamping (T0) and declampling (T10) respectively. The SSOP-StO2 could precisely discriminate when the ischemia started with a more evident decrease in 50% appreciated after 2 minutes of occlusion. Once the surgical clamp was released (second red bar) an improvement on saturation occurred.*

[223]. The importance of SFDI-based imaging methods lies on the independent measurement of light absorption and scattering.

In the first in-human pilot trial which evaluated three patients, SFDI proved to be accurate in assessing oxygenation of microsurgical deep inferior epigastric perforator flaps during reconstructive breast surgery [81]. Nevertheless, SFDI is time consuming since it requires the acquisition of several images (i.e., at least 6) being inconvenient for the surgical workflow. To address these constraints SSOP was developed as an enhanced fast optical intraoperative navigation tool. However, with the conventional process with images reduction SSOP initially suffered from degraded visual quality as compared to the 7-phase SFDI. Artificial intelligence has been used to overcome these issues, a Graphics Processing Units (GPU) GPU-accelerated deep learning (DL) as a processing technology has been previously described. SSOP GPU-accelerated DL evaluation of in vivo human hands and ex vivo animal organs showed superior image resolution and degradation compared to the classical SSOP-filtering approach. Errors as low as $7.5 \pm 2.7\%$ were presented with this DL processing methodology [85].

The Trident imaging system uses SSOP GPU-accelerated-DL using Convolutional Neural Networks (CCNs) and allows for a non-contrast physiological real-time assessment in an in vivo one-hour ischaemic model (Fig.9.3). Additionally, the use of artificial intelligence helped to maintain high image quality comparable to the 7-phase SDFI. The promising results presented in this article of SSOP-StO_2 can be potentially expanded into other fields for surgical guidance. Despite this study relies on a robust methodology, the limited number of animals may represent a limitation since six pigs were only studied, which could account for the inter-animal variation in terms of capillary lactates and StO_2 values. Another downside of the present study lies in its non-survival design, which does not make it possible to evaluate the impact of SSOP on anastomotic healing. As a result, the next sensible step will be to evaluate SSOP performance in a survival anastomotic model. Since the current SSOP-based optical imaging system is designed for open settings, a potential improvement making way for clinical translation relies on hardware refinement. Presently, our group is strongly considering this parameter to enhance such an optical imaging technology [1]. In conclusion, based on standardised metabolic biomarkers, SSOP-StO_2 allows for a contrast-free accurate assessment of small bowel perfusion identifying physiological tissue properties.

9.4 Conclusions

In this study we proposed the validation of SSOP as a constrast-free, real-time optical imaging technology for the assessment of tissue perfusion in the small bowel. A complete ischemia protocol of a total duration of 1 hour was performed to address the capability of SSOP to correctly quantify StO_2, in correlation to the measurements of capillary lactates in the regions of interest identified on the investigated section of the loop. In addition, an ischemia/reperfusion model over 15 minutes was also conducted to determine the ability of the instrument to record a dynamic change in oxygen saturation in real-time. Once again, capillary lactates were exploited as a comparative measure of the physiological damage in the tissue, with statistically significant correlation. In conclusion, the system was demonstrated to accurately monitor the tissue perfusion in the small bowel with high image quality and in real-time.

Chapter 10

CONCLUSIONS & PERSPECTIVES

10.1 Conclusions

In this manuscript we presented the results of a three years work dedicated to the development of advanced optical imaging technologies for surgical guidance. The main goal that inspired this project was to contribute to the implementation of novel multi-modal instruments for the real-time quantification of tissue optical properties in a clinical setting. To achieve this challenging objective, we focused on the exploitation of Spatial Frequency Domain Imaging as a powerful tool for the non-invasive, contactless and real-time imaging of turbid media in the therapeutic window. Despite the capability of this technique to provide quantitative information on biological tissues, the need for real-time acquisition and visualization pushed our work in the direction of Single Snapshot imaging of Optical Properties. This relatively novel technique was recently demonstrated to guarantee high image quality comparable to SFDI, with the advantage of being based on a single frame acquisition workflow. In this sense, the adoption of efficient Deep Learning architectures based on Convolutional Neural Networks resulted to boost the image rendering quality with respect to the standard Fourier's domain filtering, and the custom implementation of GPGPU accelerated computation allowed for ultrafast optical properties extraction and visualization.

Despite the great potentiality of these spatial frequency domain techniques, a first scientific challenge had to be addressed concerning the accuracy assessment of the quantification of tissue optical properties. More specifically, the lack of a ground truth for absorption and reduced scattering extraction in biological tissues was the starting point for a first pipeline of our work, that was presented in Chapter 5. In this sense, we designed and implemented a multi-modal referencing platform for diffuse optical instruments aiming at setting the way towards a cross-validation approach for the retrieval of tissue optical properties from different domain-based techniques. In the platform we combined a Time-resolved Diffuse Optical Spectroscopic system with a Spatial Frequency Domain Imaging set-up for the spectroscopic characterization of turbid media in the therapeutic window. Indeed, as shown in the literature, time domain approaches are usually considered an accurate standard for the quantification of absorption and reduced scattering. For this reason, we proposed to investigate the performance of the two approaches with a particular focus on the accuracy in the retrieval of μ_a and $\mu_s^{'}$. The platform was therefore validated on homogeneous tissue mimicking phantoms owing to a collaboration with other research institutions under the European action conducted within the BITMAP exercise (Chapter 6). Standardized protocols (i.e. MEDPHOT and BIP) were performed to assess linearity, accuracy, stability and reproducibility, together with the characterization of the instrumental properties of the system, such as sensitivity and noise. The results of this validation are reported in Chapter 5 and Chapter 6. In the former, we cover the design of the platform, the results of the BITMAP exercise and the outcomes of a further validation on custom made silicon-based phantoms. Overall, we noticed a fundamental discrepancy between TDOS and SFDI in the retrieval of tissue optical properties for different types of phantoms, with a more significant error for silicon matrices. However, the platform showed robust stability and reproducibility despite the mentioned discrepancy in the quantification. In Chapter 6, we described the first publication stemming from the European action in which we took part with the platform.

The second pipeline of our work focused on the development of an endoscopic imaging system based on SSOP. The Chapter 7 is hence dedicated to illustrate the design, implementation and validation of the instrument. The purpose of this project was to bring SSOP to minimally invasive surgery for real-time tissue perfusion monitoring, by deploying the latest achievements in image quality improvements of SSOP by the use of CNN architectures. In this sense, we proposed an imaging system based on a dual channel rigid endoscope capable of performing 3D profile corrected SSOP, by exploiting one channel of the instrument for the projection on the surgical field of high frequency spatially modulated patterns of light. The second channel was instead dedicated to the acquisition path of the SSOP snapshots through the use of a multi-sensors (RGB and two NIR bands), high frame rate sCMOS camera. A first validation of the instrument was performed to address the quantification accuracy of tissue optical properties. In this sense, a set of tissue mimicking phantoms (silicon-based) were measured with three techniques (i.e. SFDI, TDOS and SSOP) for a comparative analysis of the outcomes. On average, $< 20\%$ error in absorption and $\sim 20\%$ error in reduced scattering was obtained with respect to SFDI, in large part as a result of inhomogeneities in the projected pattern. Secondly, we assessed the image quality behavior of the instrument by comparing the results of standard SSOP and SFDI (obtained by external projection of multi-phase modulated light) measurements conducted on *in-vivo* hands from different subjects. In agreement to the literature, standard Fourier's-based SSOP suffered from edge artifacts and lower resolution with respect to SFDI. As a consequence, we proposed the implementation of Deep Learning architectures for the extraction of the modulation amplitudes of the acquired signal, as well as for the retrieval of profilometry information from the phase analysis of the same. A small improvement was noticed thanks to the neural network approach, but the expected artifacts-free demodulation and higher image quality rendering has not yet been achieved.

The aforementioned results on both the multi-modal platform and the SSOP endoscopic imaging system allowed us to take part in national and international conference (i.e. SPIE Photonics WEST 2021 - BIOS) with presentation sessions, posters and proceeding papers, as reported in Chapter 11.

In parallel to the mentioned work, we achieved successful contributions on real-time tissue perfusion monitoring *in-vivo* during pre-clinical trials on swine models. For the studies conducted in the pre-clinical setting, a novel imaging platform (i.e. *Trident imaging system*) was developed with a specific design to allow for SFDI, SSOP and fluorescence imaging in an open surgery framework.

In Chapter 8 we presented the study conducted on oxygenation monitoring via SSOP during the creation of a gastric conduit in esophageal surgery. In particular, we demonstrated for the first time the reliability of Single Snapshot Imaging of Optical Properties to assess the accurate real-time perfusion of the gastric conduit in a completely non-invasive way. We provided quantitative evaluation through $StO_2\%$ values, without exogenous fluorophores, showing the suitability of SSOP as an intraoperative tool for the potential prediciton of anastomotic leak in the clinical setting.

In Chapter 9 we also reported the results of a pre-clinical trial aiming at assessing the blood perfusion with SSOP in swine small bowels. More specifically, we performed a full ischemic protocol, as well as an ischemia/reperfusion model to evaluate the accuracy and sensitivity of SSOP in quantifying tissue oxygenation, by correlating the output values of StO_2 with capillary lactates measured on the investigated section of the small bowel.

10.2 Limitations

Clearly, the work conducted still presents some limitations that need to be addressed for the future development of the imaging technologies employed. To summarize:

1. The multi-modal referencing platform provided promising results for the validation of the cross-referencing approach based on the combination of TDOS and SFDI. However, a discrepancy in the accurate quantification of tissue optical properties

represents the main limitation of the instrument which requires further investigation from either a more fundamental point of view related to the physics of the problem, or from an instrumentation standpoint.

2. The SSOP endoscopic imaging system showed an error in the retrieval of μ_a and $\mu_s^{'}$ that was similar to the case of the multi-modal platform. Nevertheless, we believe that the main limitation of instrument is associated to the low coupling efficiency of the spatially modulated patterns of light that had a significant impact on the sample illumination and on the presence of image artifacts. These effects also impact the demodulation outcome of the Deep Learning powered SSOP algorithm, that showed poorer image quality compared with the already validated open (non-endoscopic) implementation. In addition, the absence of cross-polarization in the SSOP configuration resulted into a disruptive effect of the acquired signal, thus preventing for a robust, high quality extraction of the information embedded in the modulation amplitude and phase content of the sinusoidal patterns projected on the field.

3. The pre-clinical trials conducted on swine models with the trident imaging system suffered from a limited sample size. Statistical significance in the retrieved correlation factors was achieved in the vast majorities of the performed analyses, but a more numerous population would guarantee a more solid basis for the correct evaluation of the quantification properties of SSOP for StO_2 monitoring in several surgical applications. In addition, the measurements of capillary lactates during the ischemic models were proven to be a challenge in terms of speed, reliability and consistency.

10.3 Perspectives

A solution to the limitations highlighted in Section 10.2 ought to be the substantial work of further developments. In this sense, we foresee the following perspectives.

For the multi-modal referencing platform a transition to a Monte Carlo modeling framework for both the time-domain instrument and the spatial frequency domain approach could represent a robust solution for discrepancy in the quantification of tissue optical properties. In particular, this reasoning stems from the discussion proposed in Chapter 5 (Section 5.4) where we analyzed the potential contribution to the measured error associated to the different depth sensitivity of the two techniques and to the difference in mathematical modeling between the Diffusion Approximation approach and the stochastic analysis based on Monte Carlo.

In addition, we believe that it could be worth investigating the effect of the different materials adopted for the tissue mimicking phantoms on the characterization of absorption and reduced scattering. Indeed, we can notice that in the literature all the protocols proposed for the standardization of instrument performance assessment in diffuse optics are based on the measurement of epoxy resin-based substrates. In this sense, we also foresee a more robust calibration approach for spatial frequency domain systems, based on the exploitation of multiple calibration points covering a larger area of the optical properties spectrum with additional benefits from the introduction of multi-material phantoms.

Concerning the endoscopic imaging system, the main effort should be directed towards a further optimization of the illumination path to guarantee high SNR and artifacts-free raw acquisitions. This is undoubtedly a challenge considering the optical design of the endoscope which prevents an efficient light coupling which results fundamental for homogeneous projection of the spatially modulated patterns. However, the instrument would certainly benefit from this improvement, not only in terms of image quality (with better extraction of the demodulated data) but also from an imaging speed point of view (lower exposure times would be required to obtain the same SNR).

Different spatial modulation techniques can also be implemented for the system to obtain real-time imaging of optical properties. In particular, one possible candidate for this application could be spatio-temporal modulation of light, in a similar configuration to the one validated by Schmidt et al. [190]. This approach enables real-time functional (and structural) imaging capabilities through the simultaneous modulation in time of a multispectral illumination and of a spatial modulation following an SSOP workflow. A second candidate could be represented by speckle imaging as proposed by Chen et al. [224]. In this case, the technique is based on the computation of the power spectrum acquired from illuminating the sample with a random speckle pattern, which guarantees a projector-free configuration. Another benefit from this approach is related to the higher depth of field compared to projector-based SFDI implementations.

Clearly, a final *in-vivo* validation on animal models should also be conducted to assess the feasibility of the instrument as a minimally invasive tool for the surgical guidance. This means that a full characterization of the system design and its adaptation to surgical robots such as a *"Da Vinci Surgical System"* need to be addressed. Furthermore, these experiments will also be an opportunity to obtain relevant feedback from surgeons in order to improve the ergonomics and visual interface of the system. This step would be crucial for further developments of the instrument towards the validation during in-human clinical trials.

The additional value associated to this imaging technology is demonstrated in the literature and in the studies conducted during this thesis, therefore we believe that the instrument can potentially find its role in the medical setting for functional imaging in real-time over a large field of view.

Chapter 11

SCIENTIFIC CONTRIBUTIONS

11.1 Articles publication on Scientific Journals

- "***Single Snapshot Imaging of Optical Properties (SSOP) for Perfusion Assessment during Gastric Conduit Creation for Esophagectomy: An Experimental Study on Pigs***"
  L. Cinelli, E. Felli, **L. Baratelli**, S. Ségaud, A. Baiocchini, N. Okamoto, M. R. Rodríguez-Luna, U. Elmore, R. Rosati, S. Partelli, J. Marescaux, S. Gioux and M. Diana.
  Cancers, 2021, 13, 6079. `https://doi.org/10.3390/cancers13236079`

- "***Multi-laboratory Performance Assessment of Diffuse Optics Instruments: the BitMap Exercise***"
  P. Lanka, L. Yang, D. Orive-Miguel, J. Deepak Veesa, S. Tagliabue, A. Sudakou, S. Samaei, M. Forcione, Z. Kovacsova, A. Behera, T. Gladytz, D. Grosenick, L. Hervé, T. Durduran, K. Bejm, M. Morawiec, M. Kacprzak, P. Sawosz, A. Gerega, A. Liebert, A. Belli, I.Tachtsidis, F. Lange, G. Bale, **L. Baratelli**, S. Gioux, K. Alexander, M. Wolf, S. Konugolu Venkata Sekar, M. Zanoletti, I. Pirovano, M. Lacerenza, L. Qiu, E. Ferocino, G. Maffeisa, C. Amendola, L. Colombo, M. Buttafava, M. Renna, L. Di Sieno, R. Re, A. Farina, L. Spinelli, A. Dalla Mora, D. Contini, P. Taroni, A. Tosi, A. Torricelli, H. Dehghani, H. Wabnitz, and A. Pifferi.
  Journal of Biomedical Optics (submitted Nov. 2021).

- "***Quantification of bowel ischaemia using real-time Single Snapshot Imaging of Optical Properties (SSOP)***"
  M. Rita Rodríguez-Luna, N. Okamoto, L. Cinelli, L.Baratelli, S. Ségaud, A. Rodriguez-Gomez, E. Bannone, E. Zonoobi, D. S. Keller, J. Marescaux, M. Diana, S. Gioux.
  British Journal Of Surgery (in submission).

11.2 Proceedings

- "***A multi-laboratory comparison of photon migration instruments and their performances: the BitMap exercise***"
  P. Lanka, L. Yang, D. Orive-Miguel, J. Deepak Veesa, S. Tagliabue, A. Sudakou, S. Samaei, M. Forcione, Z. Kovacsova, A. Behera, T. Gladytz, D. Grosenick, L. Hervé, T. Durduran, K. Bejm, M. Morawiec, M. Kacprzak, P. Sawosz, A. Gerega, A. Liebert, A. Belli, I.Tachtsidis, F. Lange, G. Bale, **L. Baratelli**, S. Gioux, K. Alexander, M. Wolf, S. Konugolu Venkata Sekar, M. Zanoletti, I. Pirovano, M. Lacerenza, L. Qiu, E. Ferocino, G. Maffeisa, C. Amendola, L. Colombo, M. Buttafava, M. Renna, L. Di Sieno, R. Re, A. Farina, L. Spinelli, A. Dalla Mora, D. Contini, P. Taroni, A. Tosi, A. Torricelli, H. Dehghani, H. Wabnitz, and A. Pifferi.
  Proc. SPIE 11639, Optical Tomography and Spectroscopy of Tissue XIV, 116390F (5 March 2021); `doi:10.1117/12.2578521`.

11.3 International Conferences

SPIE Photonics West BIOS 2021:

- "***Real-time, wide-field endoscopic quantitative imaging based on 3D profile corrected Deep Learning SSOP***", L. Baratelli, E. Aguénounon, M. Flury, S. Gioux. `doi:10.1117/12.2577498`

- "***Multi-modal referencing platform for diffuse optical spectroscopic instruments***", L. Baratelli, M. Flury, S. Gioux. `doi:10.1117/12.2577506`

European Conference on Biomedical Optics (ECBO) 2021:

- "*Real-time, wide-field endoscopic quantitative imaging based on 3D profile corrected Deep-Learning SSOP*", L. Baratelli, E. Aguénounon, M. Flury, S. Gioux.

SPIE Photonics Europe 2022:

- "*Wide field, deep-learning endoscopic oxygenation imaging of biological tissues in real-time with 3D profile corrected SSOP*", L. Baratelli, M. Flury, S. Gioux.

11.4 National Conferences

16émes Journées Imagerie Optique Non Conventionnelle, 31 March – 1 April 2021:

- "*Real-Time, wide-field endoscopic quantitative imaging based on 3D profile corrected deep-learning SSOP*", L. Baratelli, E. Aguénounon, M. Flury, S. Gioux.

8émes Journées Scientifiques de la Fédération de Médecine Translationnelle de Strasbourg (FMTS), 22-23 April 2021:

- "*Real-time, wide-field endoscopic quantitative imaging based on 3D profile corrected SSOP with deep learning*", L. Baratelli, E. Aguénounon, M. Flury, S. Gioux. (POSTER SESSION)

Chapter 12

EXTENDED ABSTRACT (FRENCH)

12.1 Introduction

L'application de l'optique biomédicale au guidage chirurgical est caractérisée par un intérêt accru de la part de nombreux domaines au cours des dernières décennies. Les informations quantitatives, la non-invasivité et le temps réel sont les principaux avantages des derniers développements technologiques en matière d'imagerie optique diffuse pour la chirurgie. La Spatial Frequency Domain Imaging (SFDI) et Single Snapshot imaging of Optical Properties (SSOP) sont les techniques choisies pour remédier au manque d'outils de quantification dont disposent les médecins pour surveiller des cibles physiologiques spécifiques pendant les procédures chirurgicales, que ce soit par une approche à ciel ouvert ou par une approche mini-invasive avec des sondes endoscopiques. En outre, la spectroscopie optique diffuse dans le domaine temporel (Time Domain Diffuse Optical Spectroscopy – TDOS) est utilisée de manière plus fondamentale pour évaluer la précision des instruments développés pour l'utilisation clinique.

12.2 Medical Imaging and Surgical Guidance

Plusieurs technologies d'imagerie sont aujourd'hui disponibles dans un environnement clinique. Les rayons X, l'imagerie par résonance magnétique (IRM) et l'ultrasonographie (US) sont typiquement la norme en matière de soins et sont largement utilisés pour le dépistage, le diagnostic et la surveillance, que ce soit en préopératoire ou en peropératoire. Les rayons X sont la plus ancienne technologie d'imagerie médicale qui repose sur la mesure du signal produit par un rayonnement électromagnétique de haute énergie à travers le corps humain. Facilement applicable à des tissus de conformation et de nature différentes, elle offre une haute résolution mais une faible spécificité, avec l'inconvénient supplémentaire de l'effet perturbateur du rayonnement sur le patient. L'IRM, au contraire, exploite les modes de résonance des protons à des champs magnétiques de haute intensité, ce qui permet d'obtenir des capacités d'imagerie à haute résolution des tissus mous et une grande profondeur de pénétration. Les principaux avantages étant l'applicabilité aux scans du corps entier, ainsi que les approches tomographiques par l'acquisition de plusieurs couches. Bien qu'ils soient totalement non invasifs pour le corps, ils nécessitent des procédures strictes pour être utilisés dans un contexte chirurgical, et les capacités en temps réel sont encore difficiles à atteindre. Les ultrasons couvrent une des plus grandes parts des applications de l'imagerie médicale grâce à leur capacité à fournir des informations en profondeur et en temps réel. Les US exploite l'écho des ondes sonores émises par une sonde spécifique, pour coder le temps de propagation dans les tissus en distances par rapport à l'émetteur. La gynécologie et la médecine cardiovasculaire sont deux des domaines d'application les plus courants, et la résolution spatiale est certainement l'une des principales limites. Enfin, la chirurgie guidée par fluorescence est un domaine en pleine expansion qui se concentre sur les biomarqueurs luminescents endogènes et exogènes utilisés pour cibler des composés spécifiques et fournir des capacités d'imagerie améliorées pendant les procédures chirurgicales. Une mention spéciale est également accordée à l'introduction de l'intelligence artificielle et de la réalité virtuelle dans l'environnement chirurgical.

12.3 Advanced Optical Imaging

L'optique diffuse est l'étude de la migration des photons à travers des milieux hautement diffusants. La propagation de la lumière à travers les tissus biologiques dans la fenêtre thérapeutique (600 nm - 1100 nm), peut être expliquée par deux phénomènes principaux :

l'absorption et la diffusion. Dans ce régime de longueur d'onde spécifique, les absorbeurs les plus courants sont entre autres: l'hémoglobine (oxygénée et désoxygénée), l'eau, les lipides, le collagène et la mélanine. La physique de la diffusion dépend plutôt de la micro-structure du tissu, qui détermine la déviation de la trajectoire d'un photon dans des directions préférentielles. La description mathématique de l'interaction lumière-matière dans les milieux hautement diffusifs peut être dérivée selon deux approches : 1) l'approximation de diffusion (DE) de l'équation de transfert radiatif (RTE) ; 2) un modèle de Monte Carlo basé sur la marche aléatoire pour une description stochastique des propriétés d'absorption et de diffusion des tissus biologiques. Dans les tissus biologiques, l'absorption de la lumière dans une certaine gamme spectrale peut également déterminer des phénomènes de luminescence et, en particulier, l'émission de fluorescence. Un fluorophore est une molécule caractérisée par une empreinte de fluorescence particulière qui peut être identifiée dans ses spectres d'absorption et d'émission.

L'imagerie quantitative des propriétés optiques des tissus est l'objectif principal de l'optique biomédicale appliquée au guidage chirurgical en raison des énormes avantages que peut offrir une technologie d'imagerie quantitative en temps réel. En général, il est utile de distinguer le domaine physique dans lequel chaque technique est appliquée : onde continue (réponse à un éclairage constant) ; domaine temporel (le résultat d'une mesure est la fonction d'étalement du point temporel (t-PSF)) ; domaine fréquentiel (le résultat d'une mesure est la fonction de transfert de modulation temporelle (t-MTF)) ; domaine spatial (le résultat d'une mesure est la fonction d'étalement du point spatial (s-PSF)) ; domaine fréquentiel spatial (le résultat d'une mesure est la fonction de transfert de modulation spatiale (s-MTF)).

La chirurgie guidée par l'image de fluorescence (FIGS) représente une vaste portion des technologies d'imagerie pour le support du guidage chirurgical à la fois comme outil de diagnostic et comme outil de surveillance intra-opératoire sur le terrain. Dans l'ensemble, ce domaine a connu un développement important au cours des dernières décennies grâce à la mise au point de nombreux outils d'imagerie pour le guidage chirurgical non seulement en chirurgie ouverte mais aussi en chirurgie laparoscopique mini-invasive. En général, ces dispositifs sont caractérisés par des composants fondamentaux communs tels que : une source de lumière pour la génération du champ d'excitation pour le colorant spécifique, des filtres optiques pour la sélection de la bande d'imagerie appropriée, des optiques de détection pour une imagerie de haute sensibilité. Quelques exemples de dispositifs FIGS de l'état de l'art sont pour la chirurgie ouverte : SolarisTM Open-Air Fluorescence Imaging System, NOVADAQ Spy-EliteTM, Fluobeam(R). Pour la chirurgie mini-invasive: IMAGE1 S NIR/ICG fluorescence imaging system (Karl Storz), PINPOINTTM Endoscopic Fluorescence Imaging System (NOVADAQ), FireflyTM (da Vinci).

L'imagerie hyperspectrale (HSI) (ou imagerie hyperspectrale médicale (MHSI)) appartient aux techniques CW ainsi qu'aux systèmes basés sur la fluorescence CW et repose sur la combinaison de l'imagerie pure et de la spectroscopie en acquérant en plus des informations spectrales pour chaque pixel d'un réseau de capteurs 2-D, produisant ainsi un ensemble de données 3-D appelé hypercube. L'imagerie hyperspectrale est aujourd'hui utilisée dans plusieurs applications médicales, soit à des fins de diagnostic, soit comme outil pour la chirurgie guidée par l'image, grâce à la capacité de fournir des taux d'imagerie presque en temps réel et des informations quantitatives sur des paramètres utiles tels que la perfusion sanguine et la consommation métabolique des tissus. Le TIVITA® Tissue et le TIVITA® Mini Endoscopy Edition, de Diaspective Vision© sont deux exemples de dispositifs médicaux qui ont été récemment approuvés. L'analyse spectroscopique à résolution temporelle des propriétés optiques des tissus biologiques dans la région des longueurs d'onde du proche infrarouge peut être réalisée à l'aide de plusieurs implémentations de trois composants principaux : une source de lumière pulsée picoseconde à large bande pour couvrir la gamme spectrale de 600 à 1000 nm; des éléments optiques pour fournir la lumière d'illumination à l'échantillon et pour récolter le signal diffusé; une chaîne de détection pour le comptage de photons uniques corrélés dans le temps (TCSPC) pour récupérer la forme d'onde du signal optique extrêmement faible provenant de l'échantillon (en géométrie de réflectance ou de transmittance). Un exemple notable d'instrument d'optique diffuse de pointe basé sur la spectroscopie optique diffuse dans le domaine temporel est produit par PIONIRS© (Italie) : la "NIRSbox" a été lancée en 2020 dans le but de fournir une solution portable, "plug-and-play" pour l'étude de l'oxygénation des tissus.

La Spatial Frequency Domain Imaging (SFDI) permet de visualiser les propriétés optiques d'un tissu (c'est-à-dire les coefficients d'absorption et de diffusion réduite) sur un grand champ de vision. En projetant des motifs lumineux modulés spatialement sur l'échantillon, il est possible de mesurer directement les coefficients d'absorption et de diffusion réduite sur l'ensemble du champ de vision, grâce à l'utilisation de modèles de propagation de la lumière tels que Monte-Carlo dans le domaine des fréquences spatiales. MODULIM© est le leader mondial des systèmes d'imagerie dans le domaine des fréquences spatiales qui trouvent des applications dans les soins de santé, l'agriculture et l'industrie.

12.4 Motivations and Objectives

La précision de la quantification des propriétés optiques des tissus doit être validée à plusieurs niveaux et l'un des plus importants est la validation croisée entre des techniques basées sur des domaines différents. L'accord entre des technologies ayant des principes de fonctionnement différents a toujours représenté un grand défi pour la communauté, et un effort important est nécessaire dans cette direction pour parvenir à une sorte de normalisation des instruments afin de garantir la précision (et pas seulement) des mesures effectuées. La combinaison de SFDI et TDOS dans une seule plateforme de caractérisation est donc l'un des objectifs de ce travail.

Un deuxième grand défi concerne l'adaptation des approches d'imagerie dans le domaine des fréquences spatiales aux outils chirurgicaux mini-invasifs. En effet, malgré l'essor de la SFDI et de la SSOP au cours des dernières années, il n'existe encore pratiquement aucun projet de traduction clinique complet impliquant un dispositif d'imagerie basé sur la SSOP pour les soins mini-invasifs avec la compatibilité supplémentaire à la chirurgie assistée par robot.

12.5 Multi-modal Referencing Platform for DOS Instruments

Une plateforme de mesure multimodale pour la caractérisation optique des tissus biologiques a été conçue et validée. Le but de ce travail était de combiner deux techniques d'imagerie spectroscopique en optique diffuse afin d'obtenir une capacité de recoupement pour la validation de l'instrumentation développée par l'équipe pour l'imagerie des tissus biologiques. La plateforme multimodale est basée sur la SFDI et la spectroscopie optique diffuse à résolution temporelle (Time-resolved Diffuse Optical Spectroscopy - TDOS). Grâce à son approche grand champ, la première technique joue un rôle central dans le développement de systèmes d'imagerie optique diffuse pour la chirurgie guidée par l'image. La seconde technologie, en revanche, exploite une configuration d'illumination ponctuelle et est généralement considérée comme la norme de référence pour la quantification des propriétés optiques.

Dans notre plateforme multimodale, la SFDI et la TDOS partagent la même conception du côté de la source. Un laser supercontinuum à impulsions courtes nous permet de fournir une illumination laser sur un large spectre de longueurs d'onde. Un étage de filtrage optique est ensuite utilisé pour sélectionner la longueur d'onde et la largeur de bande à fournir au tissu. Le signal optique correspondant est couplé dans une fibre après avoir traversé un atténuateur variable. À ce stade, le chemin optique du côté TDOS se termine par la transmission en fibre du signal optique à l'échantillon, tandis que pour la SFDI, un système de projection basé sur un dispositif numérique à micromiroirs est utilisé pour générer la modulation spatiale de la lumière sur un grand champ de vision. La chaîne d'acquisition pour la technique résolue en temps est mise en œuvre pour une récupération ponctuelle de lumière, et analysée grâce à une fibre et une diode à avalanche à photon unique (Single Photon Avalanche Diode - SPAD), qui est ensuite connectée à un convertisseur temps-numérique (Time-to-Digital Converter - TDC) afin de récupérer la forme d'onde de l'impulsion lumineuse propagée dans l'échantillon. En ce qui concerne le côté SFDI de la plate-forme, l'acquisition des images est obtenue à l'aide d'une caméra sCMOS 16 bits rapide. En outre, une paire de polariseurs en configuration croisée est utilisée pour rejeter la composante spéculaire de la lumière réfléchie provenant de l'échantillon. Les deux sous-systèmes, c'est-à-dire la partie SFDI et la partie TDOS, sont contrôlés par des logiciels personnalisés.

Enfin, la validation de la plateforme multimodale a été réalisée grâce à une collaboration avec le Politecnico di Milano (Italie). Plus particulièrement, une évaluation des performances des deux sous-systèmes a été réalisée en conduisant un protocole européen référencé pour les instruments de spectroscopie optique diffuse (MEDPHOT) sous le parrainage (BitMAP) d'une collaboration multi-laboratoire entre plusieurs équipes de recherche européennes. La validation de la plateforme a montré des résultats prometteurs pour l'approche de référencement croisé pour les instruments d'optique diffuse. Néanmoins, une partie du travail a été déterminée par la mise à niveau de la plate-forme pour atteindre une gamme de longueur d'onde plus large, c'est-à-dire de 500 à 1000 nm, contre la gamme limitée auparavant entre 600 et 800 nm.

Afin d'atteindre cet objectif, une nouvelle architecture de monochromateur basée sur un dispositif de filtrage acousto-optique a été installée et testée, permettant une meilleure sélection des longueurs d'onde sur une gamme spectrale beaucoup plus large de 500 à 1100 nm. De plus, cette technologie nous permet d'obtenir une largeur de bande spectrale plus étroite à partir de la source supercontinuum pulsée, réduisant ainsi les effets de bande qui sont préjudiciables, notamment du point de vue de la résolution temporelle. En outre, afin de tirer parti de la région spectrale étendue, un nouveau détecteur a été utilisé pour remplacer la diode à avalanche à photon unique (SPAD), précédemment présente dans le montage. Ce nouveau dispositif est un photomultiplicateur au silicium (Silicon Photomultiplier - SiPM) présentant des caractéristiques intéressantes telles que : une large surface active (100 fois plus grande que la surface active de la SPAD), une résolution temporelle similaire à celle de la SPAD, un faible taux de comptage de l'obscurité et une probabilité de post-pulsation extrêmement faible. Du point de vue des performances, ces caractéristiques nous permettent d'exploiter l'intégralité du spectre disponible après filtrage ainsi qu'une gamme étendue de propriétés optiques grâce à un meilleur rapport signal/bruit associé à des tissus très absorbants et peu diffusants, qui constituaient un facteur limitant pour la version précédente de la plateforme. La conception et la validation de la plateforme multimodale a été la contribution la plus importante de la première année de thèse, mais j'ai également travaillé sur la fabrication d'échantillons imitant des tissus solides. Il s'agit de structures artificielles à base de silicone qui reproduisent les propriétés optiques des tissus biologiques, devenant ainsi un composant essentiel pour la validation des instruments d'optique diffuse. Plus précisément, une validation du protocole de fabrication a été effectuée, afin d'obtenir une routine reproductible et fiable pour la réalisation des structures à base de silicone et pour le réglage des propriétés optiques requises pour les différentes applications.

12.6 SSOP Endoscopic Imaging

Un autre aspect du projet de thèse était consacré à la conception et à la validation d'un système d'imagerie endoscopique pour l'imagerie quantitative en temps réel de tissus biologiques pendant les procédures chirurgicales minimalement invasives. Plus précisément, l'instrument est basé sur un endoscope à double canal disponible dans le commerce qui est généralement intégré à un dispositif chirurgical robotisé pour fournir un guidage chirurgical pendant les interventions laparoscopiques. Dans cette application, une intégration optique de la tête de l'endoscope a été conçue afin d'effectuer une imagerie en temps réel par le biais de la SSOP. En effet, les ouvertures normalement dédiées à l'illumination en lumière blanche du champ chirurgical ont été momentanément désactivées, tandis que les deux canaux utilisés pour la vue stéréoscopique du champ ont été convertis en canal d'injection pour l'illumination laser modulée pour le premier, et pour l'acquisition des images SSOP pour le second.

Un ensemble d'échantillons à base de silicon a été caractérisé optiquement par la SSOP comme premier schéma de validation. De plus, afin d'évaluer la précision de l'instrument, un ensemble de mesures comparatives sur les mêmes échantillons a été réalisé avec des SFDI et TDOS standard. Les résultats sur la diffusion réduite montrent un accord solide entre les trois techniques, tandis que la quantification de l'absorption a montré une différence légèrement plus élevée en raison de certains problèmes d'illumination. Dans ce sens, une optimisation robuste du chemin optique d'illumination a été réalisé pour l'injection des motifs SSOP afin de réduire les effets des artefacts d'illumination sur les capacités de quantification du système. En outre, j'ai effectué des mesures plus qualitatives sur un sujet "in-vivo", afin de comparer la qualité d'image du système SSOP, par rapport à une approche SFDI standard et toujours mise en œuvre via l'endoscope avec projection externe des motifs. Comme prévu, les images SFDI sont de meilleure qualité avec un rendu sans artefacts, alors que pour la version SSOP, on observe une qualité moindre et des artefacts de bord sur les cartes d'absorption et de diffusion réduite. Pour cette raison, j'ai travaillé sur l'adaptation du système avec une approche Deep Learning pour l'amélioration de la qualité globale de l'image en exploitant la méthode d'acquisition SFDI comme configuration d'entraînement pour le network. Le système est toujours capable de réaliser l'extraction des propriétés optiques en temps réel (et surtout l'imagerie des paramètres physiologiques) grâce à l'implémentation du « pipeline » complet d'acquisition et de traitement sur des architectures GPGPU. Enfin, en vue de la validation de l'instrument sur le terrain, un boîtier compact et compatible avec les robots a été conçu pour le système de projection et d'acquisition développé sur mesure.

12.7 BITMAP Exercise

Les initiatives multi-laboratoires sont essentielles pour l'évaluation et la normalisation des performances - cruciales pour amener la biophotonique à une utilisation clinique mature - afin d'établir des protocoles et de développer des fantômes de tissus de référence qui permettront une comparaison universelle des instruments. L'étude présente la plus grande comparaison multi-laboratoire d'évaluation des performances en optique diffuse dans le proche infrarouge, impliquant 28 instruments et 12 institutions sur un total de 8 expériences basées sur 3 protocoles consolidés (BIP, MEDPHOT, NEUROPT) mis en œuvre sur 3 kits de fantômes de tissus. Un total de 20 indicateurs synthétiques a été extrait de l'ensemble des données, certains d'entre eux étant définis ici de manière nouvelle. L'exercice est issu du réseau de formation innovant BITMAP financé par la Commission européenne et étendu à d'autres laboratoires européens. Une grande variété d'instruments d'optique diffuse a été examiné, basés sur différentes approches (domaine temporel/domaine fréquentiel/ondes continues), à différents stades de maturité et conçus pour différentes applications comme par exemple, l'oxymétrie, la spectroscopie, l'imagerie. Cette étude met en évidence une différence substantielle dans les performances du matériel (par exemple, 9 ordre de grandeur en termes de réactivité, 4 décennies en termes de taux de comptage sombre, 1 décennie en termes de résolution temporelle). La concordance des estimations des propriétés optiques homogènes était de 12% de la valeur médiane pour la moitié des systèmes, avec une stabilité temporelle de $< 5\%$ sur 1 heure, et une reproductibilité journalière de $< 3\%$. D'autres tests ont porté sur la linéarité, la diaphonie, l'incertitude et la détection des inhomogénéités optiques. Ce vaste exercice multi-laboratoire fournit une évaluation détaillée des instruments optiques diffus dans le proche infrarouge et peut être utilisé pour le classement de référence. L'ensemble de données - bientôt disponible dans un dépôt de données ouvert - peut être évalué de multiples façons, par exemple pour comparer différents outils d'analyse ou étudier l'impact des implémentations matérielles.

Ces travaux ont donné lieu à une publication scientifique sur le *Journal of Biomedical Optics* (JBO) intitulée:
"Multi-laboratory Performance Assessment of Diffuse Optics Instruments: the BITMAP Exercise", P. Lanka, L. Yang, D. Orive-Miguel, J. Deepak Veesa, S. Tagliabue, A. Sudakou, S. Samaei, M. Forcione, Z. Kovacsova, A. Behera, T. Gladytz, D. Grosenick, L. Hervé, T. Durduran, K. Bejm, M. Morawiec, M. Kacprzak, P. Sawosz, A. Gerega, A. Liebert, A. Belli, I. Tachtsidis, F. Lange, G. Bale, L. Baratelli, S. Gioux, K. Alexander, M. Wolf, S. Konugolu Venkata Sekar, M. Zanoletti, I. Pirovano, M. Lacerenza, L. Qiu, E. Ferocino, G. Maffeis, C. Amendola, L. Colombo, M. Buttafava, M. Renna, L.Di Sieno, R. Re, A. Farina, L. Spinelli, A. Dalla Mora, D. Contini, P. Taroni, A. Tosi, A. Torricelli, H. Dehghani, H. Wabnitz, and A. Pifferi.

12.8 SSOP for the Perfusion Assessment in the Gastric Conduit

L'Anastomotic leak (AL) est la complication la plus dangereuse survenant après une œsophagectomie et sa relation avec une perfusion viscérale inadéquate est largement reconnue. Actuellement, la perfusion adéquate du conduit gastrique est évaluée en peropératoire par les chirurgiens à l'aide d'indicateurs subjectifs (par exemple, la couleur de la séreuse ou le flux pulsatile des vaisseaux), ce qui entraîne une faible précision. Une nouvelle technologie est nécessaire pour améliorer l'évaluation peropératoire de l'oxygénation des tissus. Au cours des dernières décennies, plusieurs techniques optiques innovantes, basées sur l'interaction de la lumière avec les tissus, ont été développées pour surveiller la perfusion en chirurgie œsophagogastrique. Cependant, ces approches innovantes sont caractérisées par un manque de fréquence vidéo et de reproductibilité. Elles fournissent également des résultats dépendants de l'opérateur et allongent le flux de travail chirurgical. L'imagerie des propriétés optiques par cliché unique (SSOP) est une technique d'optique diffuse relativement nouvelle, qui peut surmonter ces limitations, en fournissant des informations quantitatives sur les propriétés optiques des tissus biologiques sur un large champ de vision. Il s'agit de la première étude à démontrer la précision de la SSOP dans la quantification de la $StO_2\%$ séreuse dans un modèle de conduit gastrique (GC) porcin. Après la création d'un conduit gastrique, la StO_2% locale a été mesurée avec un système SSOP préclinique pendant 60 minutes dans l'antrus (ROI-A), le corpus (ROI-C) et le fundus (ROI-F). La région enlevée (ROI-R) a servi de contrôle ischémique. La ROI-R présentait une StO_2% statistiquement inférieure par rapport à toutes les autres ROI à T15, T30, T45 et T60 ($p < 0,0001$). La corrélation entre les lactates capillaires locaux (LCL) et la StO_2% était statistiquement significative ($R = -0,8439$, IC 95% -0,9367 à -0,6407, $p < 0,0001$). Enfin, la SSOP pouvait distinguer les régions réséquées des régions perfusées et le ROI-A du ROI-F (le futur site anastomotique). En conclusion, la SSOP pourrait bien être une technologie appropriée pour évaluer la perfusion peropératoire de la CG, en fournissant une quantification cohérente du StO_2% et une discrimination des ROIs.

Ces travaux ont donné lieu à une publication scientifique sur le journal *Cancers* (2021, 13, 6079. `https://doi.org/10.3390/cancers13236079`) intitulée:
"Single Snapshot Imaging of Optical Properties (SSOP) for Perfusion Assessment during Gastric Conduit Creation for Esophagectomy: An Experimental Study on Pigs", L. Cinelli, E. Felli, L. Baratelli, S. Ségaud, A. Baiocchini, N. Okamoto, M.R. Rodríguez-Luna, U. Elmore , R. Rosati, S. Partelli, J. Marescaux, S. Gioux and M. Diana.

12.9 Bowel Perfusion Assessment via SSOP

Le Single Snapshot Imaging of Optical Properties (SSOP) est une technologie relativement nouvelle d'imagerie optique non invasive en temps réel et sans contraste, qui permet l'évaluation quantitative en temps réel des propriétés physiologiques, notamment l'oxygénation des tissus (StO_2). Cette étude évalue la précision de la SSOP pour quantifier l'ischémie intestinale dans un modèle expérimental préclinique. Chez six porcs, un segment d'intestin ischémique a été créé en divisant les branches de l'arcade. Cinq régions d'intérêt (ROI) ont été identifiées sur la boucle intestinale, comme suit : ROI 1 ischémique centrale, ROI 2 marginale gauche, ROI 3 vascularisée gauche, ROI 4 marginale droite, et ROI 5 vascularisée droite. Le système d'imagerie Trident, développé pour l'imagerie de l'oxygénation des tissus en temps réel à l'aide du SSOP, a été utilisé pour réaliser des images avant (T0) et après l'induction de l'ischémie. Les lactates capillaires et systémiques ont été mesurés à chaque point de temps (T0, T15, T30, T45, T60) et les valeurs de StO_2 ont été acquises en utilisant SSOP. La valeur moyenne de la SSOP-StO_2 dans la ROI 1 était de $30,08 \pm 6,963$ et était significativement plus faible par rapport aux ROIs marginales (ROI 2 + ROI 4 : $45,67 \pm 10,02$, $p =< 0,0001$), et aux ROIs vascularisées (ROI 3 + ROI 5 : $48,08 \pm 7,083$, $p \leq 0,0001$). La SSOP-StO_2 était significativement corrélée aux lactates normalisés $R = -0.5892$, $p < 0.0001$ et à l'histologie $R = -0.6251$, $p = 0.0002$. La SSOP permet une évaluation précise et sans contraste de la perfusion de l'intestin grêle en identifiant l'oxygénation physiologique des tissus, confirmée par les biomarqueurs de perfusion.

Ces travaux ont donné lieu à une publication scientifique sur le *British Journal of Surgery* (BJS) intitulée:
"Quantification of bowel ischaemia using real-time Single Snapshot Imaging of Optical Properties (SSOP)", M. R. Rodríguez-Luna, N. Okamoto, L. Cinelli, L. Baratelli, S. Ségaud, A. Rodriguez-Gomez, E. Bannone, E. Zonoobi, D. S Keller, J. Marescaux, M. Diana, S. Gioux.

12.10 Conclusions & Perspectives

L'objectif principal de ce projet était de contribuer à la mise en œuvre de nouvelles technologies d'imagerie optique multimodale pour la quantification en temps réel des propriétés optiques des tissus dans un contexte clinique. Dans ce sens, nous nous sommes concentrés sur l'imagerie du domaine de fréquence spatiale et l'imagerie des propriétés optiques par instantané unique, qui sont les meilleurs candidats pour le guidage chirurgical optique sans contact et en temps réel.

La précision de la quantification des propriétés optiques des tissus a déterminé le premier défi scientifique abordé dans ce travail. À cette fin, une plateforme de référencement multimodale pour les instruments optiques diffus a été développée en combinant TDOS et SSOP pour étudier une approche de validation croisée. Des performances prometteuses en matière de stabilité ont été obtenues, mais l'instrument a également montré une divergence dans la récupération de l'absorption et de la diffusion réduite, ce qui représente la principale limite du système qui nécessite une étude plus approfondie. Dans ce sens, des approches de multi-calibration pour SFDI et une transition vers la modélisation Monte Carlo pour TDOS sont prévues pour le développement futur du système comme une solution potentielle au problème de précision.

Une autre partie de notre travail s'est concentré sur la conception, la mise en œuvre et la validation d'un système d'imagerie endoscopique basé sur le SSOP pour l'imagerie d'oxygénation en temps réel dans les traitements mini-invasifs. Les dernières réalisations en matière d'amélioration de la qualité d'image de la SSOP par l'utilisation d'architectures CNN ont été mises en œuvre sur le système endoscopique. L'instrument était basé sur un endoscope rigide à double canal compatible avec les outils chirurgicaux robotisés. Une première validation de l'instrument a été effectuée sur des fantômes imitant des tissus, avec pour résultat une erreur moyenne de $< 20\%$ en absorption et de $\sim 10\%$ en diffusion réduite par rapport à la SFDI. La qualité de l'image a également été évaluée en comparant les résultats de la SSOP standard, de la SSOP améliorée par le Deep Learning et de l'IDFS sur des mains *in-vivo* de différents sujets. Une amélioration constante a été remarquée grâce à l'approche par réseau de neurones, avec une démodulation presque sans artefacts et un rendu de qualité d'image supérieure. La principale limite de l'instrument est associée à la faible efficacité de couplage des modèles de lumière modulés dans l'espace qui détermine un éclairage hétérogène de l'échantillon et des artefacts d'image, ce qui nécessite une optimisation supplémentaire pour une imagerie de meilleure qualité.

Parallèlement à ces travaux, nous avons réussi à contrôler la perfusion tissulaire en temps réel dans l'intestin grêle et dans le conduit gastrique sur des modèles porcins in vivo en déployant une nouvelle plateforme d'imagerie (le système d'imagerie Trident) conçue pour permettre l'imagerie par SFDI, SSOP et fluorescence dans un contexte de chirurgie ouverte.

Bibliography

[1] Sylvain Gioux, Amaan Mazhar, and David J. Cuccia. “Spatial frequency domain imaging in 2019: principles, applications, and perspectives”. In: *Journal of Biomedical Optics* 24.7 (June 20, 2019), p. 1. ISSN: 1083-3668. DOI: 10.1117/1.JBO.24.7.071613.

[2] Jean Vervandier and Sylvain Gioux. “Single snapshot imaging of optical properties”. In: *Biomedical Optics Express* 4.12 (Dec. 1, 2013), p. 2938. ISSN: 2156-7085, 2156-7085. DOI: 10.1364/BOE.4.002938.

[3] Antonio Pifferi et al. “New frontiers in time-domain diffuse optics, a review”. In: *Journal of Biomedical Optics* 21.9 (June 17, 2016), p. 091310. ISSN: 1083-3668. DOI: 10.1117/1.JBO.21.9.091310.

[4] Xiaofeng Zhang, Nadine Smith, and Andrew Webb. “Medical imaging”. In: *Biomedical Information Technology*. Elsevier, 2020, pp. 3–49. ISBN: 978-0-12-816034-3. DOI: 10.1016/B978-0-12-816034-3.00001-8.

[5] *Philips® BV Pulsera Mobile C-Arm*. URL: https://www.usa.philips.com/healthcare/product/HC718095/bv-pulsera-mobile-c-arm.

[6] Mahesh V. Jayaraman et al. “Detection of Intracranial Aneurysms: Multi–Detector Row CT Angiography Compared with DSA”. In: *Radiology* 230.2 (2004), pp. 510–518. DOI: 10.1148/radiol.2302021465.

[7] E H Dillon et al. “CT angiography: application to the evaluation of carotid artery stenosis.” In: *Radiology* 189.1 (1993), pp. 211–219. DOI: 10.1148/radiology.189.1.8372196.

[8] Gotz Benndorf et al. “Angiographic CT in Cerebrovascular Stenting”. In: (2005), p. 6.

[9] Vijay P.B. Grover et al. “Magnetic Resonance Imaging: Principles and Techniques: Lessons for Clinicians”. In: *Journal of Clinical and Experimental Hepatology* 5.3 (Sept. 2015), pp. 246–255. ISSN: 09736883. DOI: `10.1016/j.jceh.2015.08.001`.

[10] Edward A. Ashton and Tong Du. “Semi-automated measurement of anatomical structures using statistical and morphological priors”. In: Medical Imaging 2004. Ed. by Dev P. Chakraborty and Miguel P. Eckstein. San Diego, CA, May 4, 2004, p. 476. DOI: `10.1117/12.533047`.

[11] Jasmin M. Kizilirmak et al. “Neural Correlates of Learning from Induced Insight: A Case for Reward-Based Episodic Encoding”. In: *Frontiers in Psychology* 7 (Nov. 1, 2016). ISSN: 1664-1078. DOI: `10.3389/fpsyg.2016.01693`.

[12] Daniela Kuhnt, Miriam H. A. Bauer, and Christopher Nimsky. “Brain shift compensation and neurosurgical image fusion using intraoperative MRI: current status and future challenges.” In: *Critical reviews in biomedical engineering* 40.3 (2012). Place: United States, pp. 175–185. ISSN: 0278-940X. DOI: `10.1615/critrevbiomedeng.v40.i3.20`.

[13] Yi Lu et al. “Comparative Effectiveness of Frame-Based, Frameless, and Intraoperative Magnetic Resonance Imaging–Guided Brain Biopsy Techniques”. In: *World Neurosurgery* 83.3 (Mar. 2015), pp. 261–268. ISSN: 18788750. DOI: `10.1016/j.wneu.2014.07.043`.

[14] Karl Theo Dussik. “Uber die Moeglichkeit, hochfrequente mechanische Sehwingungen als diagnostisehes Hilfsmittel zu verwerten”. In: (Sept. 12, 1941).

[15] William R. Hendee and E. Russell Ritenour. *Medical Imaging Physics*. New York, USA: John Wiley & Sons, Inc., Oct. 1, 2002. ISBN: 978-0-471-38226-3 978-0-471-22115-9. DOI: `10.1002/0471221155`.

[16] Peter N. T. Wells, Hai-Dong Liang, and Terry P. Young. “Ultrasonic imaging technologies in perspective”. In: *Journal of Medical Engineering & Technology* 35.6 (Oct. 2011), pp. 289–299. ISSN: 0309-1902, 1464-522X. DOI: `10.3109/03091902.2011.595531`.

[17] Mary Jacob et al. “An Echocardiography Training Program for Improving the Left Ventricular Function Interpretation in Emergency Department; a Brief Report”. In: (), p. 5.

[18] Hakan Orbay et al. “Intraoperative Targeted Optical Imaging: A Guide towards Tumor-Free Margins in Cancer Surgery”. In: *Current Pharmaceutical Biotechnology* 14.8 (Jan. 31, 2014), pp. 733–742. ISSN: 13892010. DOI: `10.2174/1389201014666131226113300`.

[19] Chensu Wang et al. “Optical molecular imaging for tumor detection and image-guided surgery”. In: *Biomaterials* 157 (2018), pp. 62–75. ISSN: 0142-9612. DOI: `https://doi.org/10.1016/j.biomaterials.2017.12.002`.

[20] Paola De Nardi et al. “Intraoperative angiography with indocyanine green to assess anastomosis perfusion in patients undergoing laparoscopic colorectal resection: results of a multicenter randomized controlled trial”. In: *Surgical Endoscopy* 34.1 (Jan. 1, 2020), pp. 53–60. ISSN: 1432-2218. DOI: `10.1007/s00464-019-06730-0`.

[21] Baowei Fei. “Chapter 3.6 - Hyperspectral imaging in medical applications”. In: *Hyperspectral Imaging*. Ed. by José Manuel Amigo. Vol. 32. Data Handling in Science and Technology. ISSN: 0922-3487. Elsevier, 2020, pp. 523–565. DOI: `https://doi.org/10.1016/B978-0-444-63977-6.00021-3`.

[22] Alberto Espino et al. "Advanced Imaging Technologies for the Detection of Dysplasia and Early Cancer in Barrett Esophagus". In: *Clinical Endoscopy* 47.1 (2014), p. 47. ISSN: 2234-2400, 2234-2443. DOI: `10.5946/ce.2014.47.1.47`.

[23] Hanna Zimmermann et al. "Optical coherence tomography for retinal imaging in multiple sclerosis". In: *Degenerative Neurological and Neuromuscular Disease* (Dec. 2014), p. 153. ISSN: 1179-9900. DOI: `10.2147/DNND.S73506`.

[24] David Huang et al. "Optical Coherence Tomography". In: (2015), p. 12.

[25] Sweta Narayanan Iyer and Guoqiang Chen. "riboflavin and its derivative Flavin". In: (), p. 17.

[26] Kim S. de Valk et al. "A zwitterionic near-infrared fluorophore for real-time ureter identification during laparoscopic abdominopelvic surgery". In: *Nature Communications* 10.1 (Dec. 2019), p. 3118. ISSN: 2041-1723. DOI: `10.1038/s41467-019-11014-1`.

[27] Michele Diana. "Fluorescence-guided Surgery Applied to the Digestive System: The Cybernetic Eye to See the Invisible". In: *Cirugía Española (English Edition)* 96.2 (Feb. 2018), pp. 65–68. ISSN: 21735077. DOI: `10.1016/j.cireng.2017.10.002`.

[28] Omri Bar et al. "Impact of data on generalization of AI for surgical intelligence applications". In: *Scientific Reports* 10.1 (Dec. 2020), p. 22208. ISSN: 2045-2322. DOI: `10.1038/s41598-020-79173-6`.

[29] Daniel Hashimoto. *Artificial intelligence in surgery: an AI primer for surgical practice*. OCLC: on1158159217. New York: McGraw-Hill Medical, 2021. 409 pp. ISBN: 978-1-260-45273-0.

[30] Sheng Bin, Saleha Masood, and Younhyun Jung. "Virtual and augmented reality in medicine". In: *Biomedical Information Technology*. Elsevier, 2020, pp. 673–686. ISBN: 978-0-12-816034-3. DOI: `10.1016/B978-0-12-816034-3.00020-1`.

[31] Miguel J Palet, Marcela Antúnez-Riveros, and Maximiliano Barahona. "Construct Validity of a Virtual Reality Simulator for Surgical Training in Knee Arthroscopy". In: *Cureus* (May 25, 2021). ISSN: 2168-8184. DOI: `10.7759/cureus.15237`.

[32] *Echopixel® True 3D glasses*. URL: `https://echopixeltech.com/`.

[33] Laura Di Sieno et al. "SOLUS Project: Bringing Innovation into Breast Cancer Diagnosis and in the Time-Domain Diffuse Optical Field". In: *Biophotonics Congress: Biomedical Optics 2020 (Translational, Microscopy, OCT, OTS, BRAIN)*. Journal Abbreviation: Biophotonics Congress: Biomedical Optics 2020 (Translational, Microscopy, OCT, OTS, BRAIN). Optical Society of America, 2020, STu1D.5. DOI: `10.1364/OTS.2020.STu1D.5`.

[34] Rebecca Richards-Kortum and Eva Sevick-Muraca. "QUANTITATIVE OPTICAL SPECTROSCOPY FOR TISSUE DIAGNOSIS". In: *Annual Review of Physical Chemistry* 47.1 (Oct. 1996), pp. 555–606. ISSN: 0066-426X, 1545-1593. DOI: `10.1146/annurev.physchem.47.1.555`.

[35] Felix Scholkmann et al. "A review on continuous wave functional near-infrared spectroscopy and imaging instrumentation and methodology". In: *NeuroImage* 85 (Jan. 2014), pp. 6–27. ISSN: 10538119. DOI: `10.1016/j.neuroimage.2013.05.004`.

[36] Steven L. Jacques and Brian W. Pogue. "Tutorial on diffuse light transport". In: *Journal of Biomedical Optics* 13.4 (2008), p. 041302. ISSN: 10833668. DOI: `10.1117/1.2967535`.

[37] S. A. Prahl. "A Monte Carlo model of light propagation in tissue". In: Institutes for Advanced Optical Technologies. Ed. by Gerhard J. Mueller, David H. Sliney, and Roy F. Potter. Berlin, Germany, Jan. 10, 1989, p. 1030509. DOI: `10.1117/12.2283590`.

[38] Toru Katsumata et al. "Quantitative analysis of fat and protein concentrations of milk based on fibre-optic evaluation of back scattering intensity". In: *International Dairy Journal* 109 (Oct. 2020), p. 104743. ISSN: 09586946. DOI: `10.1016/j.idairyj.2020.104743`.

[39] B. C. Wilson and G. Adam. "A Monte Carlo model for the absorption and flux distributions of light in tissue". In: *Medical Physics* 10.6 (1983), pp. 824–830. DOI: `https://doi.org/10.1118/1.595361`.

[40] Iyad S. Saidi, Steven L. Jacques, and Frank K. Tittel. "Mie and Rayleigh modeling of visible-light scattering in neonatal skin". In: *Applied Optics* 34.31 (Nov. 1, 1995), p. 7410. ISSN: 0003-6935, 1539-4522. DOI: `10.1364/AO.34.007410`.

[41] Xiaogang Lin et al. "Light scattering from normal and cervical cancer cells." In: *Applied optics* 56.12 (Apr. 20, 2017). Place: United States, pp. 3608–3614. ISSN: 1539-4522 1559-128X. DOI: `10.1364/AO.56.003608`.

[42] J. W. McLaren and R. F. Brubaker. "Measurement of fluorescein and fluorescein monoglucuronide in the living human eye." In: *Investigative ophthalmology & visual science* 27.6 (June 1986). Place: United States, pp. 966–974. ISSN: 0146-0404.

[43] Joseph R. Lakowicz and Barry R. Masters. "Principles of Fluorescence Spectroscopy, Third Edition". In: *Journal of Biomedical Optics* 13.2 (2008), p. 029901. ISSN: 10833668. DOI: `10.1117/1.2904580`.

[44] Tadanobu Nagaya et al. "Fluorescence-Guided Surgery". In: *Frontiers in Oncology* 7 (Dec. 22, 2017), p. 314. ISSN: 2234-943X. DOI: `10.3389/fonc.2017.00314`.

[45] David J. Cuccia et al. "Quantitation and mapping of tissue optical properties using modulated imaging". In: *Journal of Biomedical Optics* 14.2 (2009), p. 024012. ISSN: 10833668. DOI: `10.1117/1.3088140`.

[46] Fabrizio Martelli, ed. *Light propagation through biological tissue and other diffusive media: theory, solutions, and software*. OCLC: ocn457155087. Bellingham, Wash: SPIE Press, 2010. 274 pp. ISBN: 978-0-8194-7658-6.

[47] Brian Pogue et al. "Instrumentation and design of a frequency-domain diffuse optical tomography imager for breast cancer detection". In: *Optics Express* 1.13 (Dec. 22, 1997), p. 391. ISSN: 1094-4087. DOI: `10.1364/OE.1.000391`.

[48] Michael S. Patterson et al. "Frequency-domain reflectance for the determination of the scattering and absorption properties of tissue". In: *Appl. Opt.* 30.31 (Nov. 1991). Publisher: OSA, pp. 4474–4476. DOI: `10.1364/AO.30.004474`.

[49] Zuzana Kovacsova et al. "Absolute quantification of cerebral tissue oxygen saturation with multidistance broadband NIRS in newborn brain". In: *Biomedical Optics Express* 12.2 (Feb. 1, 2021), p. 907. ISSN: 2156-7085, 2156-7085. DOI: `10.1364/BOE.412088`.

[50] Andrea Bassi et al. "Temporal propagation of spatial information in turbid media". In: *Optics Letters* 33.23 (Dec. 1, 2008), p. 2836. ISSN: 0146-9592, 1539-4794. DOI: `10.1364/OL.33.002836`.

[51] Lars O. Svaasand et al. "Reflectance measurements of layered media with diffuse photon-density waves: a potential tool for evaluating deep burns and subcutaneous lesions". In: *Physics in Medicine and Biology* 44.3 (Jan. 1999). Publisher: IOP Publishing, pp. 801–813. DOI: `10.1088/0031-9155/44/3/020`.

[52] Richard C. Haskell et al. "Boundary conditions for the diffusion equation in radiative transfer". In: *Journal of the Optical Society of America A* 11.10 (Oct. 1, 1994), p. 2727. ISSN: 1084-7529, 1520-8532. DOI: `10.1364/JOSAA.11.002727`.

[53] Zahid Yaqoob, Jigang Wu, and Changhuei Yang. "Spectral domain optical coherence tomography: a better OCT imaging strategy". In: *BioTechniques* 39.6 (Dec. 2005), S6–S13. ISSN: 0736-6205, 1940-9818. DOI: `10.2144/000112090`.

[54] Jeff Meganck et al. "Open air fluorescence imaging using the Solaris imaging system". In: (), p. 1.

[55] *IMAGE1 S NIR/ICG fluorescence imaging system from KARL STORZ (KARL STORZ Endoscopy- America, Inc.)* URL: `https://www.karlstorz.com/de/en/nir-icg-near-infrared-fluorescence.htm`.

[56] Pieterjan Debie and Sophie Hernot. "Emerging Fluorescent Molecular Tracers to Guide Intra-Operative Surgical Decision-Making". In: *Frontiers in Pharmacology* 10 (May 14, 2019), p. 510. ISSN: 1663-9812. DOI: `10.3389/fphar.2019.00510`.

[57] Alisha V. DSouza et al. "Review of fluorescence guided surgery systems: identification of key performance capabilities beyond indocyanine green imaging". In: *Journal of Biomedical Optics* 21.8 (Aug. 16, 2016), p. 080901. ISSN: 1083-3668. DOI: `10.1117/1.JBO.21.8.080901`.

[58] Neil T. Clancy et al. "Surgical spectral imaging". In: *Medical Image Analysis* 63 (July 2020), p. 101699. ISSN: 13618415. DOI: `10.1016/j.media.2020.101699`.

[59] Guolan Lu and Baowei Fei. "Medical hyperspectral imaging: a review". In: *Journal of Biomedical Optics* 19.1 (Jan. 20, 2014), p. 010901. ISSN: 1083-3668. DOI: `10.1117/1.JBO.19.1.010901`.

[60] D. Landgrebe. "Hyperspectral image data analysis". In: *IEEE Signal Processing Magazine* 19.1 (Jan. 2002), pp. 17–28. ISSN: 1558-0792. DOI: `10.1109/79.974718`.

[61] Himar Fabelo et al. "Deep Learning-Based Framework for In Vivo Identification of Glioblastoma Tumor using Hyperspectral Images of Human Brain". In: *Sensors* 19.4 (Feb. 22, 2019), p. 920. ISSN: 1424-8220. DOI: `10.3390/s19040920`.

[62] Boris Jansen-Winkeln et al. "Comparison of hyperspectral imaging and fluorescence angiography for the determination of the transection margin in colorectal resections—a comparative study". In: *International Journal of Colorectal Disease* 36.2 (Feb. 2021), pp. 283–291. ISSN: 0179-1958, 1432-1262. DOI: `10.1007/s00384-020-03755-z`.

[63] Lukas H. Kohler et al. "Hyperspectral Imaging (HSI) as a new diagnostic tool in free flap monitoring for soft tissue reconstruction: a proof of concept study". In: *BMC Surgery* 21.1 (Dec. 2021), p. 222. ISSN: 1471-2482. DOI: `10.1186/s12893-021-01232-0`.

[64] Chad R. Tracy et al. "First Prize: Characterization of Renal Ischemia Using DLP® Hyperspectral Imaging: A Pilot Study Comparing Artery-Only Occlusion Versus Artery and Vein Occlusion". In: *Journal of Endourology* 24.3 (2010), pp. 321–325. DOI: `10.1089/end.2009.0184`.

[65] Megumu Mori et al. “Intraoperative visualization of cerebral oxygenation using hyperspectral image data: a two-dimensional mapping method”. In: *International Journal of Computer Assisted Radiology and Surgery* 9.6 (Nov. 2014), pp. 1059–1072. ISSN: 1861-6410, 1861-6429. DOI: `10.1007/s11548-014-0989-9`.

[66] Manuel Barberio et al. “Intraoperative Guidance Using Hyperspectral Imaging: A Review for Surgeons”. In: *Diagnostics* 11.11 (Nov. 8, 2021), p. 2066. ISSN: 2075-4418. DOI: `10.3390/diagnostics11112066`.

[67] *TIVITA® Tissue and TIVITA® Mini Endoscopy Edition*. URL: `https://diaspective-vision.com/en/produkte/`.

[68] Sebastian Hennig et al. “Novel Intraoperative Imaging of Gastric Tube Perfusion during Oncologic Esophagectomy—A Pilot Study Comparing Hyperspectral Imaging (HSI) and Fluorescence Imaging (FI) with Indocyanine Green (ICG)”. In: *Cancers* 14.1 (Dec. 25, 2021), p. 97. ISSN: 2072-6694. DOI: `10.3390/cancers14010097`.

[69] *"Time-correlated single photon counting", guide by Becker and Hickl GmbH, July, 2002*. URL: `https://www.becker-hickl.com/literature/documents/flim/the-bh-tcspc-handbook/`.

[70] Desmond V. O’Connor and D. Phillips. *Time-correlated single photon counting*. London ; Orlando: Academic Press, 1984. 288 pp. ISBN: 978-0-12-524140-3.

[71] *NIRSbox from PIONIRS® s.r.l.* URL: `https://www.pionirs.com/wp/nirsbox/`.

[72] Michele Lacerenza et al. “Wearable and wireless time-domain near-infrared spectroscopy system for brain and muscle hemodynamic monitoring”. In: *Biomedical Optics Express* 11.10 (Oct. 1, 2020), p. 5934. ISSN: 2156-7085, 2156-7085. DOI: `10.1364/BOE.403327`.

[73] David J. Cuccia et al. “Modulated imaging: quantitative analysis and tomography of turbid media in the spatial-frequency domain”. In: *Optics Letters* 30.11 (June 1, 2005), p. 1354. ISSN: 0146-9592, 1539-4794. DOI: `10.1364/OL.30.001354`.

[74] Jiří Novák, Pavel Novák, and Antonín Mikš. “Multi-step phase-shifting algorithms insensitive to linear phase shift errors”. In: *Optics Communications* 281.21 (Nov. 2008), pp. 5302–5309. ISSN: 00304018. DOI: `10.1016/j.optcom.2008.07.060`.

[75] Sylvain Gioux et al. “Three-dimensional surface profile intensity correction for spatially modulated imaging”. In: *Journal of Biomedical Optics* 14.3 (2009), p. 034045. ISSN: 10833668. DOI: `10.1117/1.3156840`.

[76] *Clairfy® by MODULIM® Inc.* URL: `https://modulim.com/clarifi/`.

[77] Craig Weinkauf et al. “Near-instant noninvasive optical imaging of tissue perfusion for vascular assessment”. In: *Journal of Vascular Surgery* 69.2 (Feb. 2019), pp. 555–562. ISSN: 07415214. DOI: `10.1016/j.jvs.2018.06.202`.

[78] Grant A Murphy et al. “Quantifying dermal microcirculatory changes of neuropathic and neuroischemic diabetic foot ulcers using spatial frequency domain imaging: a shade of things to come?” In: *BMJ Open Diabetes Research & Care* 8.2 (Nov. 2020), e001815. ISSN: 2052-4897. DOI: `10.1136/bmjdrc-2020-001815`.

[79] Samuel Jett et al. “Stratification of Microvascular Disease Severity in the Foot Using Spatial Frequency Domain Imaging.” In: *Journal of diabetes science and technology* (July 5, 2021). Place: United States, p. 19322968211024666. ISSN: 1932-2968. DOI: `10.1177/19322968211024666`.

[80] Amr Yafi et al. "Quantitative skin assessment using spatial frequency domain imaging (SFDI) in patients with or at high risk for pressure ulcers". In: *Lasers in Surgery and Medicine* 49.9 (2017), pp. 827–834. DOI: `https://doi.org/10.1002/lsm.22692`.

[81] John T. Nguyen et al. "A Novel Pilot Study Using Spatial Frequency Domain Imaging to Assess Oxygenation of Perforator Flaps During Reconstructive Breast Surgery". In: *Annals of Plastic Surgery* 71.3 (Sept. 2013), pp. 308–315. ISSN: 0148-7043. DOI: `10.1097/SAP.0b013e31828b02fb`.

[82] Adrien Ponticorvo et al. "Spatial Frequency Domain Imaging (SFDI) of clinical burns: A case report". In: *Burns Open* 4.2 (Apr. 2020), pp. 67–71. ISSN: 24689122. DOI: `10.1016/j.burnso.2020.02.004`.

[83] Joseph Angelo et al. "Ultrafast optical property map generation using lookup tables". In: *Journal of Biomedical Optics* 21.11 (Nov. 30, 2016), p. 110501. ISSN: 1083-3668. DOI: `10.1117/1.JBO.21.11.110501`.

[84] Enagnon Aguénounon et al. "Single snapshot of optical properties image quality improvement using anisotropic two-dimensional windows filtering". In: *Journal of Biomedical Optics* 24.7 (Mar. 29, 2019), p. 1. ISSN: 1083-3668. DOI: `10.1117/1.JBO.24.7.071611`.

[85] Enagnon Aguénounon et al. "Real-time, wide-field and high-quality single snapshot imaging of optical properties with profile correction using deep learning". In: *Biomedical Optics Express* 11.10 (Oct. 1, 2020), p. 5701. ISSN: 2156-7085, 2156-7085. DOI: `10.1364/BOE.397681`.

[86] Swapnesh Panigrahi and Sylvain Gioux. "Machine learning approach for rapid and accurate estimation of optical properties using spatial frequency domain imaging". In: *Journal of Biomedical Optics* 24.7 (Dec. 12, 2018), p. 1. ISSN: 1083-3668. DOI: `10.1117/1.JBO.24.7.071606`.

[87] Yanyu Zhao et al. "Deep learning model for ultrafast multifrequency optical property extractions for spatial frequency domain imaging". In: *Optics Letters* 43.22 (Nov. 15, 2018), p. 5669. ISSN: 0146-9592, 1539-4794. DOI: `10.1364/OL.43.005669`.

[88] Yann LeCun, Koray Kavukcuoglu, and Clement Farabet. "Convolutional networks and applications in vision". In: *Proceedings of 2010 IEEE International Symposium on Circuits and Systems*. 2010 IEEE International Symposium on Circuits and Systems - ISCAS 2010. Paris, France: IEEE, May 2010, pp. 253–256. ISBN: 978-1-4244-5308-5. DOI: `10.1109/ISCAS.2010.5537907`.

[89] Mason T. Chen et al. "GANPOP: Generative Adversarial Network Prediction of Optical Properties from Single Snapshot Wide-field Images". In: *arXiv:1906.05360 [cs, eess, stat]* (June 20, 2019). arXiv: `1906.05360`.

[90] Stijn Keereweer et al. "Optical Image-guided Surgery—Where Do We Stand?" In: *Molecular Imaging and Biology* 13.2 (Apr. 2011), pp. 199–207. ISSN: 1536-1632, 1860-2002. DOI: `10.1007/s11307-010-0373-2`.

[91] Antonio Pifferi et al. "Performance assessment of photon migration instruments: the MEDPHOT protocol". In: (Jan. 1, 2005), p. 11.

[92] Heidrun Wabnitz et al. "Performance assessment of time-domain optical brain imagers, part 2: nEUROPt protocol". In: *Journal of Biomedical Optics* 19.8 (Aug. 14, 2014), p. 086012. ISSN: 1083-3668. DOI: `10.1117/1.JBO.19.8.086012`.

[93] Joseph P. Angelo, Martijn van de Giessen, and Sylvain Gioux. "Real-time endoscopic optical properties imaging". In: *Biomedical Optics Express* 8.11 (Nov. 1, 2017), p. 5113. ISSN: 2156-7085, 2156-7085. DOI: `10.1364/BOE.8.005113`.

[94] Heidrun Wabnitz et al. "Performance assessment of time-domain optical brain imagers, part 1: basic instrumental performance protocol". In: *Journal of Biomedical Optics* 19.8 (Aug. 14, 2014), p. 086010. ISSN: 1083-3668. DOI: `10.1117/1.JBO.19.8.086010`.

[95] Nico Bodenschatz et al. "Sources of errors in spatial frequency domain imaging of scattering media". In: *Journal of Biomedical Optics* 19.7 (Jan. 27, 2014), p. 071405. ISSN: 1083-3668. DOI: `10.1117/1.JBO.19.7.071405`.

[96] Jean-Pierre Bouchard et al. "Reference optical phantoms for diffuse optical spectroscopy Part 1 – Error analysis of a time resolved transmittance characterization method". In: *Optics Express* 18.11 (May 24, 2010), p. 11495. ISSN: 1094-4087. DOI: `10.1364/OE.18.011495`.

[97] Michael S. Patterson, B. Chance, and B. C. Wilson. "Time resolved reflectance and transmittance for the noninvasive measurement of tissue optical properties". In: *Applied Optics* 28.12 (June 15, 1989), p. 2331. ISSN: 0003-6935, 1539-4522. DOI: `10.1364/AO.28.002331`.

[98] Sri Rama Pranav Kumar Lanka et al. "A multi-laboratory comparison of photon migration instruments and their performances: the BitMap exercise". In: *Optical Tomography and Spectroscopy of Tissue XIV*. Optical Tomography and Spectroscopy of Tissue XIV. Ed. by Sergio Fantini and Paola Taroni. Online Only, United States: SPIE, Mar. 5, 2021, p. 11. ISBN: 978-1-5106-4113-6 978-1-5106-4114-3. DOI: `10.1117/12.2578521`.

[99] T Durduran et al. "Diffuse optics for tissue monitoring and tomography". In: *Reports on Progress in Physics* 73.7 (July 1, 2010), p. 076701. ISSN: 0034-4885, 1361-6633. DOI: `10.1088/0034-4885/73/7/076701`.

[100] Samuel S. Streeter, Steven L. Jacques, and Brian W. Pogue. "Perspective on diffuse light in tissue: subsampling photon populations". In: *Journal of Biomedical Optics* 26.7 (July 2, 2021). ISSN: 1083-3668. DOI: `10.1117/1.JBO.26.7.070601`.

[101] Gemma Bale, Clare E. Elwell, and Ilias Tachtsidis. "From Jöbsis to the present day: a review of clinical near-infrared spectroscopy measurements of cerebral cytochrome-c-oxidase". In: *Journal of Biomedical Optics* 21.9 (May 11, 2016), p. 091307. ISSN: 1083-3668. DOI: `10.1117/1.JBO.21.9.091307`.

[102] Marco Ferrari and Valentina Quaresima. "A brief review on the history of human functional near-infrared spectroscopy (fNIRS) development and fields of application". In: *NeuroImage* 63.2 (Nov. 2012), pp. 921–935. ISSN: 10538119. DOI: `10.1016/j.neuroimage.2012.03.049`.

[103] M. Mazurenka et al. "Non-contact in vivo diffuse optical imaging using a time-gated scanning system". In: *Biomedical Optics Express* 4.10 (Oct. 1, 2013), p. 2257. ISSN: 2156-7085, 2156-7085. DOI: `10.1364/BOE.4.002257`.

[104] D. W. Green and G. Kunst. "Cerebral oximetry and its role in adult cardiac, non-cardiac surgery and resuscitation from cardiac arrest". In: *Anaesthesia* 72 (Jan. 2017), pp. 48–57. ISSN: 00032409. DOI: `10.1111/anae.13740`.

[105] Dirk Grosenick et al. "Review of optical breast imaging and spectroscopy". In: *Journal of Biomedical Optics* 21.9 (July 11, 2016), p. 091311. ISSN: 1083-3668. DOI: `10.1117/1.JBO.21.9.091311`.

[106] Takafumi Hamaoka et al. "Near-Infrared Time-Resolved Spectroscopy for Assessing Brown Adipose Tissue Density in Humans: A Review". In: *Frontiers in Endocrinology* 11 (May 19, 2020), p. 261. ISSN: 1664-2392. DOI: `10.3389/fendo.2020.00261`.

[107] Valentina Quaresima and Marco Ferrari. "Functional Near-Infrared Spectroscopy (fNIRS) for Assessing Cerebral Cortex Function During Human Behavior in Natural/Social Situations: A Concise Review". In: *Organizational Research Methods* 22.1 (Jan. 2019), pp. 46–68. ISSN: 1094-4281, 1552-7425. DOI: `10.1177/1094428116658959`.

[108] Stephane Perrey and Marco Ferrari. "Muscle Oximetry in Sports Science: A Systematic Review." In: *Sports medicine (Auckland, N.Z.)* 48.3 (Mar. 2018). Place: New Zealand, pp. 597–616. ISSN: 1179-2035 0112-1642. DOI: `10.1007/s40279-017-0820-1`.

[109] Paul C DeRose. *Recommendations and guidelines for standardization of fluorescence spectroscopy*. NIST IR 7457. Edition: 0. Gaithersburg, MD: National Institute of Standards and Technology, 2007, NIST IR 7457. DOI: `10.6028/NIST.IR.7457`.

[110] Hiroyuki Hori et al. "The Thickness of Human Scalp: Normal and Bald". In: *Journal of Investigative Dermatology* 58.6 (June 1972), pp. 396–399. ISSN: 0022202X. DOI: `10.1111/1523-1747.ep12540633`.

[111] Jeeseong Hwang, Jessica C. Ramella-Roman, and Robert Nordstrom. "Introduction: Feature Issue on Phantoms for the Performance Evaluation and Validation of Optical Medical Imaging Devices". In: *Biomedical Optics Express* 3.6 (June 1, 2012), p. 1399. ISSN: 2156-7085, 2156-7085. DOI: `10.1364/BOE.3.001399`.

[112] "Keeping up standards". In: *Nature Photonics* 12.3 (Mar. 2018), pp. 117–117. ISSN: 1749-4885, 1749-4893. DOI: `10.1038/s41566-018-0131-6`.

[113] "Scrutinizing lasers". In: *Nature Photonics* 11.3 (Mar. 2017), pp. 139–139. ISSN: 1749-4885, 1749-4893. DOI: `10.1038/nphoton.2017.28`.

[114] *"Performance Assessement and Standardization in Biophotonics Workshop, Digital Single Market"*. URL: `https://ec.europa.eu/digital-single-market/en/news/performanceassessement-and-standardization-biophotonics-workshop`.

[115] L. Spinelli et al. "Determination of reference values for optical properties of liquid phantoms based on Intralipid and India ink". In: *Biomedical Optics Express* 5.7 (July 1, 2014), p. 2037. ISSN: 2156-7085, 2156-7085. DOI: `10.1364/BOE.5.002037`.

[116] Bruce J. Tromberg et al. "Predicting Responses to Neoadjuvant Chemotherapy in Breast Cancer: ACRIN 6691 Trial of Diffuse Optical Spectroscopic Imaging". In: *Cancer Research* 76.20 (Oct. 15, 2016), pp. 5933–5944. ISSN: 0008-5472, 1538-7445. DOI: `10.1158/0008-5472.CAN-16-0346`.

[117] Mathias Lühr Hansen et al. "Cerebral near-infrared spectroscopy monitoring versus treatment as usual for extremely preterm infants: a protocol for the SafeBoosC randomised clinical phase III trial". In: *Trials* 20.1 (Dec. 2019), p. 811. ISSN: 1745-6215. DOI: `10.1186/s13063-019-3955-6`.

[118] Anne M. Plomgaard et al. "The SafeBoosC II randomized trial: treatment guided by near-infrared spectroscopy reduces cerebral hypoxia without changing early biomarkers of brain injury". In: *Pediatric Research* 79.4 (Apr. 2016), pp. 528–535. ISSN: 0031-3998, 1530-0447. DOI: `10.1038/pr.2015.266`.

[119] S. Kleiser et al. "Comparison of Near-Infrared Oximeters in a Liquid Optical Phantom with Varying Intralipid and Blood Content." In: *Advances in experimental medicine and biology* 876 (2016). Place: United States, pp. 413–418. ISSN: 0065-2598. DOI: `10.1007/978-1-4939-3023-4_52`.

[120] S. Kleiser et al. "Comparison of tissue oximeters on a liquid phantom with adjustable optical properties: an extension". In: *Biomedical Optics Express* 9.1 (Jan. 1, 2018), p. 86. ISSN: 2156-7085, 2156-7085. DOI: `10.1364/BOE.9.000086`.

[121] *"SNIRF, The Society for functional Near Infrared Spectroscopy"*. URL: `https://fnirs.org/resources/software/snirf/`.

[122] Antonio Pifferi et al. "Mechanically switchable solid inhomogeneous phantom for performance tests in diffuse imaging and spectroscopy". In: *Journal of Biomedical Optics* 20.12 (July 28, 2015), p. 121304. ISSN: 1083-3668. DOI: `10.1117/1.JBO.20.12.121304`.

[123] Fabrizio Martelli et al. "Phantoms for diffuse optical imaging based on totally absorbing objects, part 1: basic concepts". In: *Journal of Biomedical Optics* 18.6 (June 18, 2013), p. 066014. ISSN: 1083-3668. DOI: `10.1117/1.JBO.18.6.066014`.

[124] *"Technology readiness levels (TRL)"*. URL: `https://ec.europa.eu/research/participants/data/ref/h2020/wp/2014_2015/annexes/h2020-824wp1415-annex-g-trl_en.pdf`.

[125] Pranav Lanka et al. "Non-invasive investigation of adipose tissue by time domain diffuse optical spectroscopy". In: *Biomedical Optics Express* 11.5 (May 1, 2020), p. 2779. ISSN: 2156-7085, 2156-7085. DOI: `10.1364/BOE.391028`.

[126] L. Di Sieno et al. "Probe-hosted large area silicon photomultiplier and high-throughput timing electronics for enhanced performance time-domain functional near-infrared spectroscopy". In: *Biomedical Optics Express* 11.11 (Nov. 1, 2020), p. 6389. ISSN: 2156-7085, 2156-7085. DOI: `10.1364/BOE.400868`.

[127] Lin Yang et al. "Space-enhanced time-domain diffuse optics for determination of tissue optical properties in two-layered structures". In: *Biomedical Optics Express* 11.11 (Nov. 1, 2020), p. 6570. ISSN: 2156-7085, 2156-7085. DOI: `10.1364/BOE.402181`.

[128] *"NIRO-200NX Near infrared oxygenation monitor C10448, Hamamatsu Photonics"*. URL: `https://www.hamamatsu.com/jp/en/product/type/C10448/index.html`.

[129] *"ISS_OxiplexTS200_DataSheet"*. URL: `http://iss.com/resources/pdf/datasheets/ISS_OxiplexTS200_DataSheet.pdf`.

[130] Anna Gerega et al. "Multiwavelength time-resolved near-infrared spectroscopy of the adult head: assessment of intracerebral and extracerebral absorption changes". In: *Biomedical Optics Express* 9.7 (July 1, 2018), p. 2974. ISSN: 2156-7085, 2156-7085. DOI: `10.1364/BOE.9.002974`.

[131] Aleh Sudakou et al. "Time-domain NIRS system based on supercontinuum light source and multi-wavelength detection: validation for tissue oxygenation studies". In: *Biomedical Optics Express* 12.10 (Oct. 1, 2021), p. 6629. ISSN: 2156-7085, 2156-7085. DOI: `10.1364/BOE.431301`.

[132] Saeed Samaei et al. "Time-domain diffuse correlation spectroscopy (TD-DCS) for noninvasive, depth-dependent blood flow quantification in human tissue in vivo". In: *Scientific Reports* 11.1 (Dec. 2021), p. 1817. ISSN: 2045-2322. DOI: `10.1038/s41598-021-81448-5`.

[133] Ramona Rothfischer, Dirk Grosenick, and Rainer Macdonald. "Time-resolved transmittance: a comparison of the diffusion model approach with Monte Carlo simulations". In: *Diffuse Optical Imaging V*. Ed. by Hamid Dehghani and Paola Taroni. Vol. 9538. Backup Publisher: International Society for Optics and Photonics. SPIE, 2015, pp. 165 –170. DOI: 10.1117/12.2183762.

[134] Michal Kacprzak et al. "Frequency analysis of oscillations in cerebral hemodynamics measured by time domain near infrared spectroscopy". In: *Biomedical Optics Express* 10.2 (Feb. 1, 2019), p. 761. ISSN: 2156-7085, 2156-7085. DOI: 10.1364/BOE.10.000761.

[135] Piotr Sawosz et al. "Influence of intra-abdominal pressure on the amplitude of fluctuations of cerebral hemoglobin concentration in the respiratory band". In: *Biomedical Optics Express* 10.7 (July 1, 2019), p. 3434. ISSN: 2156-7085, 2156-7085. DOI: 10.1364/BOE.10.003434.

[136] Wojciech Weigl et al. "Confirmation of brain death using optical methods based on tracking of an optical contrast agent: assessment of diagnostic feasibility". In: *Scientific Reports* 8.1 (Dec. 2018), p. 7332. ISSN: 2045-2322. DOI: 10.1038/s41598-018-25351-6.

[137] Michal Kacprzak et al. "Application of a time-resolved optical brain imager for monitoring cerebral oxygenation during carotid surgery". In: *Journal of Biomedical Optics* 17.1 (2012), p. 016002. ISSN: 10833668. DOI: 10.1117/1.JBO.17.1.016002.

[138] Frederic Lange et al. "MAESTROS: A Multiwavelength Time-Domain NIRS System to Monitor Changes in Oxygenation and Oxidation State of Cytochrome-C-Oxidase". In: *IEEE Journal of Selected Topics in Quantum Electronics* 25.1 (Jan. 2019), pp. 1–12. ISSN: 1077-260X, 1558-4542. DOI: 10.1109/JSTQE.2018.2833205.

[139] Lorenzo Cortese et al. "The LUCA device: a multi-modal platform combining diffuse optics and ultrasound imaging for thyroid cancer screening". In: *Biomedical Optics Express* 12.6 (June 1, 2021), p. 3392. ISSN: 2156-7085, 2156-7085. DOI: 10.1364/BOE.416561.

[140] Rebecca Re et al. "A compact time-resolved system for NIR spectroscopy". In: *Clinical and Biomedical Spectroscopy*. Ed. by Irene Georgakoudi, Jürgen Popp, and Katarina Svanberg M.D. Vol. 7368. Backup Publisher: International Society for Optics and Photonics. SPIE, 2009, pp. 146 –152. DOI: 10.1117/12.831610.

[141] Rebecca Re et al. "Multi-channel medical device for time domain functional near infrared spectroscopy based on wavelength space multiplexing". In: *Biomedical Optics Express* 4.10 (Oct. 1, 2013), p. 2231. ISSN: 2156-7085, 2156-7085. DOI: 10.1364/BOE.4.002231.

[142] Mauro Buttafava et al. "A Compact Two-Wavelength Time-Domain NIRS System Based on SiPM and Pulsed Diode Lasers". In: *IEEE Photonics Journal* 9.1 (Feb. 2017), pp. 1–14. ISSN: 1943-0655. DOI: 10.1109/JPHOT.2016.2632061.

[143] *"Artinis Medical Systems , fNIRS and NIRS devices-Near Infrared Spectroscopy Introduction Theory," Artinis Medical*. URL: https://www.artinis.com/octamon.

[144] Edoardo Ferocino et al. "High throughput detection chain for time domain optical mammography". In: *Biomedical Optics Express* 9.2 (Feb. 1, 2018), p. 755. ISSN: 2156-7085, 2156-7085. DOI: 10.1364/BOE.9.000755.

[145] Paola Taroni et al. "Seven-wavelength time-resolved optical mammography extending beyond 1000 nm for breast collagen quantification". In: *Optics Express* 17.18 (Aug. 31, 2009), p. 15932. ISSN: 1094-4087. DOI: 10.1364/OE.17.015932.

[146] P. Zerbini et al. "Optical properties, ethylene production and softening in mango fruit". In: *Postharvest Biology and Technology* 101 (Nov. 2014). DOI: 10.1016/j.postharvbio.2014.11.008.

[147] David Orive-Miguel et al. "Real-Time Dual-Wavelength Time-Resolved Diffuse Optical Tomography System for Functional Brain Imaging Based on Probe-Hosted Silicon Photomultipliers". In: *Sensors* 20.10 (May 15, 2020), p. 2815. ISSN: 1424-8220. DOI: 10.3390/s20102815.

[148] Andrea Farina et al. "Time-Domain Functional Diffuse Optical Tomography System Based on Fiber-Free Silicon Photomultipliers". In: *Applied Sciences* 7.12 (Nov. 29, 2017), p. 1235. ISSN: 2076-3417. DOI: 10.3390/app7121235.

[149] Martina Giovannella. "BabyLux device: a diffuse optical system integrating diffuse correlation spectroscopy and time-resolved near-infrared spectroscopy for the neuromonitoring of the premature newborn brain". In: *Neurophotonics* 6.2 (May 10, 2019), p. 1. ISSN: 2329-423X. DOI: 10.1117/1.NPh.6.2.025007.

[150] Pranav Lanka et al. "Optical signatures of radiofrequency ablation in biological tissues". In: *Scientific Reports* 11.1 (Dec. 2021), p. 6579. ISSN: 2045-2322. DOI: 10.1038/s41598-021-85653-0.

[151] M. Pagliazzi et al. "Time domain diffuse correlation spectroscopy with a high coherence pulsed source: in vivo and phantom results". In: *Biomedical Optics Express* 8.11 (Nov. 1, 2017), p. 5311. ISSN: 2156-7085, 2156-7085. DOI: 10.1364/BOE.8.005311.

[152] Giulia Maffeis et al. "In vivo test-driven upgrade of a time domain multi-wavelength optical mammograph". In: *Biomedical Optics Express* 12.2 (Feb. 1, 2021), p. 1105. ISSN: 2156-7085, 2156-7085. DOI: 10.1364/BOE.412210.

[153] A. Di Costanzo-Mata et al. "Time-Resolved NIROT 'Pioneer' System for Imaging Oxygenation of the Preterm Brain: Preliminary Results." In: *Advances in experimental medicine and biology* 1232 (2020). Place: United States, pp. 347–354. ISSN: 0065-2598. DOI: 10.1007/978-3-030-34461-0_44.

[154] Fabrizio Martelli et al. "There's plenty of light at the bottom: statistics of photon penetration depth in random media". In: *Scientific Reports* 6.1 (July 2016), p. 27057. ISSN: 2045-2322. DOI: 10.1038/srep27057.

[155] Theodore J. Huppert et al. "HomER: a review of time-series analysis methods for near-infrared spectroscopy of the brain". In: *Applied Optics* 48.10 (Apr. 1, 2009), p. D280. ISSN: 0003-6935, 1539-4522. DOI: 10.1364/AO.48.00D280.

[156] Hamid Dehghani et al. "Near infrared optical tomography using NIRFAST: Algorithm for numerical model and image reconstruction". In: *Communications in Numerical Methods in Engineering* 25.6 (2009), pp. 711–732. DOI: https://doi.org/10.1002/cnm.1162.

[157] *"SNIRF, The Society for functional Near Infrared Spectroscopy, Serving the fNIRS community"*. URL: https://fnirs.org/.

[158] *"International Photoacustic Standardisation Consortium (IPASC)"*. URL: https://www.ipasc.science/ipasc.science/.

[159] Sarah Bohndiek. "Addressing photoacoustics standards". In: *Nature Photonics* 13.5 (May 2019), pp. 298–298. ISSN: 1749-4885, 1749-4893. DOI: 10.1038/s41566-019-0417-3.

[160] Charlotte Tsui, Rachel Klein, and Matthew Garabrant. “Minimally invasive surgery: national trends in adoption and future directions for hospital strategy.” In: *Surgical endoscopy* 27.7 (July 2013). Place: Germany, pp. 2253–2257. ISSN: 1432-2218 0930-2794. DOI: `10.1007/s00464-013-2973-9`.

[161] Enagnon Aguénounon et al. “Real-time optical properties and oxygenation imaging using custom parallel processing in the spatial frequency domain”. In: *Biomedical Optics Express* 10.8 (Aug. 1, 2019), p. 3916. ISSN: 2156-7085, 2156-7085. DOI: `10.1364/BOE.10.003916`.

[162] Kyle P. Nadeau, Anthony J. Durkin, and Bruce J. Tromberg. “Advanced demodulation technique for the extraction of tissue optical properties and structural orientation contrast in the spatial frequency domain”. In: *Journal of Biomedical Optics* 19.5 (May 23, 2014), p. 056013. ISSN: 1083-3668. DOI: `10.1117/1.JBO.19.5.056013`.

[163] Lorenzo Cinelli et al. “Single Snapshot Imaging of Optical Properties (SSOP) for Perfusion Assessment during Gastric Conduit Creation for Esophagectomy: An Experimental Study on Pigs”. In: *Cancers* 13.23 (Dec. 2, 2021), p. 6079. ISSN: 2072-6694. DOI: `10.3390/cancers13236079`.

[164] Hyuna Sung et al. “Global Cancer Statistics 2020: GLOBOCAN Estimates of Incidence and Mortality Worldwide for 36 Cancers in 185 Countries”. In: *CA: A Cancer Journal for Clinicians* 71.3 (May 2021), pp. 209–249. ISSN: 0007-9235, 1542-4863. DOI: `10.3322/caac.21660`.

[165] P. van Hagen et al. “Preoperative Chemoradiotherapy for Esophageal or Junctional Cancer”. In: *New England Journal of Medicine* 366.22 (May 31, 2012), pp. 2074–2084. ISSN: 0028-4793, 1533-4406. DOI: `10.1056/NEJMoa1112088`.

[166] I. LEWIS. “The surgical treatment of carcinoma of the oesophagus; with special reference to a new operation for growths of the middle third.” In: *The British journal of surgery* 34 (July 1946). Place: England, pp. 18–31. ISSN: 0007-1323. DOI: `10.1002/bjs.18003413304`.

[167] Lingling Huang and Mark Onaitis. “Minimally invasive and robotic Ivor Lewis esophagectomy”. In: *Journal of Thoracic Disease* 6 (2014), p. 8.

[168] Lukas F. Liesenfeld et al. “Prognostic value of inflammatory markers for detecting anastomotic leakage after esophageal resection”. In: *BMC Surgery* 20.1 (Dec. 2020), p. 324. ISSN: 1471-2482. DOI: `10.1186/s12893-020-00995-2`.

[169] Anja Schaible et al. “Significant decrease of mortality due to anastomotic leaks following esophageal resection: management makes the difference”. In: *Langenbeck's Archives of Surgery* 402.8 (Dec. 1, 2017), pp. 1167–1173. ISSN: 1435-2451. DOI: `10.1007/s00423-017-1626-1`.

[170] Donald E. Low. “Diagnosis and Management of Anastomotic Leaks after Esophagectomy”. In: *Journal of Gastrointestinal Surgery* 15.8 (Aug. 1, 2011), pp. 1319–1322. ISSN: 1873-4626. DOI: `10.1007/s11605-011-1511-0`.

[171] Mikkel Jessen et al. “Risk factors for clinical anastomotic leakage after right hemicolectomy”. In: *International Journal of Colorectal Disease* 31.9 (Sept. 1, 2016), pp. 1619–1624. ISSN: 1432-1262. DOI: `10.1007/s00384-016-2623-5`.

[172] Steen Christian Kofoed et al. “Intrathoracic anastomotic leakage after gastroesophageal cancer resection is associated with reduced long-term survival.” In: *World journal of surgery* 38.1 (Jan. 2014). Place: United States, pp. 114–119. ISSN: 1432-2323 0364-2313. DOI: `10.1007/s00268-013-2245-9`.

[173] Sami A. Chadi et al. “Emerging Trends in the Etiology, Prevention, and Treatment of Gastrointestinal Anastomotic Leakage”. In: *Journal of Gastrointestinal Surgery* 20.12 (Dec. 1, 2016), pp. 2035–2051. ISSN: 1873-4626. DOI: `10.1007/s11605-016-3255-3`.

[174] E. Booka et al. “Meta-analysis of the impact of postoperative complications on survival after oesophagectomy for cancer: Effect of postoperative complications on survival after oesophagectomy”. In: *BJS Open* 2.5 (Sept. 2018), pp. 276–284. ISSN: 24749842. DOI: `10.1002/bjs5.64`.

[175] Koianka Trencheva et al. “Identifying Important Predictors for Anastomotic Leak After Colon and Rectal Resection: Prospective Study on 616 Patients”. In: *Annals of Surgery* 257.1 (2013). ISSN: 0003-4932.

[176] Catherine Chioreso et al. “Association Between Hospital and Surgeon Volume and Rectal Cancer Surgery Outcomes in Patients With Rectal Cancer Treated Since 2000: Systematic Literature Review and Meta-analysis”. In: *Diseases of the Colon & Rectum* 61.11 (Nov. 2018), pp. 1320–1332. ISSN: 0012-3706. DOI: `10.1097/DCR.0000000000001198`.

[177] John D. Mitchell. “Anastomotic leak after esophagectomy.” In: *Thoracic surgery clinics* 16.1 (Feb. 2006). Place: United States, pp. 1–9. ISSN: 1547-4127. DOI: `10.1016/j.thorsurg.2006.01.011`.

[178] Carrie E. Ryan et al. “Transthoracic Anastomotic Leak After Esophagectomy: Current Trends”. In: *Annals of Surgical Oncology* 24.1 (Jan. 1, 2017), pp. 281–290. ISSN: 1534-4681. DOI: `10.1245/s10434-016-5417-7`.

[179] A. Karliczek et al. “Surgeons lack predictive accuracy for anastomotic leakage in gastrointestinal surgery”. In: *International Journal of Colorectal Disease* 24.5 (May 2009), pp. 569–576. ISSN: 0179-1958, 1432-1262. DOI: `10.1007/s00384-009-0658-6`.

[180] S. M. Jansen et al. “Optical techniques for perfusion monitoring of the gastric tube after esophagectomy: a review of technologies and thresholds.” In: *Diseases of the esophagus : official journal of the International Society for Diseases of the Esophagus* 31.6 (June 1, 2018). Place: United States. ISSN: 1442-2050 1120-8694. DOI: `10.1093/dote/dox161`.

[181] Linas Urbanavičius. “How to assess intestinal viability during surgery: A review of techniques”. In: *World Journal of Gastrointestinal Surgery* 3.5 (2011), p. 59. ISSN: 1948-9366. DOI: `10.4240/wjgs.v3.i5.59`.

[182] Manuel Barberio et al. “A Novel Technique to Improve Anastomotic Perfusion Prior to Esophageal Surgery: Hybrid Ischemic Preconditioning of the Stomach. Preclinical Efficacy Proof in a Porcine Survival Model”. In: *Cancers* 12.10 (Oct. 14, 2020), p. 2977. ISSN: 2072-6694. DOI: `10.3390/cancers12102977`.

[183] Manuel Barberio et al. “Quantitative fluorescence angiography versus hyperspectral imaging to assess bowel ischemia: A comparative study in enhanced reality.” In: *Surgery* 168.1 (July 2020). Place: United States, pp. 178–184. ISSN: 1532-7361 0039-6060. DOI: `10.1016/j.surg.2020.02.008`.

[184] Manuel Barberio et al. “HYPerspectral Enhanced Reality (HYPER): a physiology-based surgical guidance tool”. In: *Surgical Endoscopy* 34.4 (Apr. 1, 2020), pp. 1736–1744. ISSN: 1432-2218. DOI: `10.1007/s00464-019-06959-9`.

[185] Adrien Ponticorvo et al. “Quantitative assessment of graded burn wounds in a porcine model using spatial frequency domain imaging (SFDI) and laser speckle imaging (LSI)”. In: *Biomedical Optics Express* 5.10 (Oct. 1, 2014), p. 3467. ISSN: 2156-7085, 2156-7085. DOI: `10.1364/BOE.5.003467`.

[186] Michael R. Pharaon et al. “Early Detection of Complete Vascular Occlusion in a Pedicle Flap Model Using Quantitation Spectral Imaging:” in: *Plastic and Reconstructive Surgery* 126.6 (Dec. 2010), pp. 1924–1935. ISSN: 0032-1052. DOI: `10.1097/PRS.0b013e3181f447ac`.

[187] Sylvain Gioux et al. “First-in-human pilot study of a spatial frequency domain oxygenation imaging system”. In: *Journal of Biomedical Optics* 16.8 (2011), p. 086015. ISSN: 10833668. DOI: `10.1117/1.3614566`.

[188] Daniel J. Rohrbach et al. “Preoperative Mapping of Nonmelanoma Skin Cancer Using Spatial Frequency Domain and Ultrasound Imaging”. In: *Academic Radiology* 21.2 (Feb. 2014), pp. 263–270. ISSN: 10766332. DOI: `10.1016/j.acra.2013.11.013`.

[189] Martijn van de Giessen, Joseph P. Angelo, and Sylvain Gioux. “Real-time, profile-corrected single snapshot imaging of optical properties”. In: *Biomedical Optics Express* 6.10 (Oct. 1, 2015), p. 4051. ISSN: 2156-7085, 2156-7085. DOI: `10.1364/BOE.6.004051`.

[190] Manon Schmidt et al. “Real-time, wide-field, and quantitative oxygenation imaging using spatiotemporal modulation of light”. In: *Journal of Biomedical Optics* 24.7 (Mar. 13, 2019), p. 1. ISSN: 1083-3668. DOI: `10.1117/1.JBO.24.7.071610`.

[191] Carol Kilkenny et al. “Animal research: Reporting in vivo experiments: The ARRIVE guidelines: Animal research: reporting in vivo experiments the ARRIVE guidelines”. In: *British Journal of Pharmacology* 160.7 (Aug. 2010), pp. 1577–1579. ISSN: 00071188. DOI: `10.1111/j.1476-5381.2010.00872.x`.

[192] Amaan Mazhar et al. “Wavelength optimization for rapid chromophore mapping using spatial frequency domain imaging”. In: *Journal of Biomedical Optics* 15.6 (2010), p. 061716. ISSN: 10833668. DOI: `10.1117/1.3523373`.

[193] Hiroshi Akiyama, Mamoru Hiyama, and Chiaki Hashimoto. “Resection and reconstruction for carcinoma of the thoracic oesophagus”. In: *British Journal of Surgery* 63.3 (Dec. 2005), pp. 206–209. ISSN: 0007-1323. DOI: `10.1002/bjs.1800630310`.

[194] Manish Mittal et al. “Reactive Oxygen Species in Inflammation and Tissue Injury”. In: *Antioxidants & Redox Signaling* 20.7 (Mar. 2014), pp. 1126–1167. ISSN: 1523-0864, 1557-7716. DOI: `10.1089/ars.2012.5149`.

[195] Kamila Raziyeva et al. “Immunology of Acute and Chronic Wound Healing”. In: *Biomolecules* 11.5 (May 8, 2021), p. 700. ISSN: 2218-273X. DOI: `10.3390/biom11050700`.

[196] Manuel Barberio et al. “Quantitative serosal and mucosal optical imaging perfusion assessment in gastric conduits for esophageal surgery: an experimental study in enhanced reality”. In: *Surgical Endoscopy* 35.10 (Oct. 2021), pp. 5827–5835. ISSN: 0930-2794, 1432-2218. DOI: `10.1007/s00464-020-08077-3`.

[197] Takeshi Urade et al. “Hyperspectral enhanced reality (HYPER) for anatomical liver resection”. In: *Surgical Endoscopy* 35.4 (Apr. 1, 2021), pp. 1844–1850. ISSN: 1432-2218. DOI: `10.1007/s00464-020-07586-5`.

[198] Kenji Kawada et al. “Evaluation of intestinal perfusion by ICG fluorescence imaging in laparoscopic colorectal surgery with DST anastomosis.” In: *Surgical endoscopy* 31.3 (Mar. 2017). Place: Germany, pp. 1061–1069. ISSN: 1432-2218 0930-2794. DOI: 10.1007/s00464-016-5064-x.

[199] R. Blanco-Colino and E. Espin-Basany. “Intraoperative use of ICG fluorescence imaging to reduce the risk of anastomotic leakage in colorectal surgery: a systematic review and meta-analysis.” In: *Techniques in coloproctology* 22.1 (Jan. 2018). Place: Italy, pp. 15–23. ISSN: 1128-045X 1123-6337. DOI: 10.1007/s10151-017-1731-8.

[200] Monique Hope-Ross et al. “Adverse Reactions due to Indocyanine Green”. In: *Ophthalmology* 101.3 (Mar. 1, 1994). Publisher: Elsevier, pp. 529–533. ISSN: 0161-6420. DOI: 10.1016/S0161-6420(94)31303-0.

[201] Daniel Dindo, Nicolas Demartines, and Pierre-Alain Clavien. “Classification of Surgical Complications: A New Proposal With Evaluation in a Cohort of 6336 Patients and Results of a Survey”. In: *Annals of Surgery* 240.2 (Aug. 2004), pp. 205–213. ISSN: 0003-4932. DOI: 10.1097/01.sla.0000133083.54934.ae.

[202] Matteo Frasson et al. “Risk Factors for Anastomotic Leak After Colon Resection for Cancer: Multivariate Analysis and Nomogram From a Multicentric, Prospective, National Study With 3193 Patients.” In: *Annals of surgery* 262.2 (Aug. 2015). Place: United States, pp. 321–330. ISSN: 1528-1140 0003-4932. DOI: 10.1097/SLA.0000000000000973.

[203] F. D. McDermott et al. “Systematic review of preoperative, intraoperative and postoperative risk factors for colorectal anastomotic leaks.” In: *The British journal of surgery* 102.5 (Apr. 2015). Place: England, pp. 462–479. ISSN: 1365-2168 0007-1323. DOI: 10.1002/bjs.9697.

[204] T. Pampiglione and M. Chand. “Enhancing colorectal anastomotic safety with indocyanine green fluorescence angiography: An update”. In: *Surgical Oncology* (2021), p. 101545. ISSN: 0960-7404. DOI: https://doi.org/10.1016/j.suronc.2021.101545.

[205] Pietro Mascagni et al. “New intraoperative imaging technologies: Innovating the surgeon’s eye toward surgical precision.” In: *Journal of surgical oncology* 118.2 (Aug. 2018). Place: United States, pp. 265–282. ISSN: 1096-9098 0022-4790. DOI: 10.1002/jso.25148.

[206] Mehraneh D. Jafari et al. *Perfusion assessment in laparoscopic left-sided/anterior resection (PILLAR II): a multi-institutional study.* ISSN: 1879-1190 1072-7515 Issue: 1 Journal Abbreviation: J Am Coll Surg Pages: 82-92.e1 Publication Title: Journal of the American College of Surgeons. United States, Jan. 2015. DOI: 10.1016/j.jamcollsurg.2014.09.015.

[207] F Ris et al. “Multicentre phase II trial of near-infrared imaging in elective colorectal surgery”. In: *British Journal of Surgery* 105.10 (Aug. 7, 2018), pp. 1359–1367. ISSN: 0007-1323, 1365-2168. DOI: 10.1002/bjs.10844.

[208] Giuseppe Quero et al. “Discrimination between arterial and venous bowel ischemia by computer-assisted analysis of the fluorescent signal”. In: *Surgical Endoscopy* 33.6 (June 1, 2019), pp. 1988–1997. ISSN: 1432-2218. DOI: 10.1007/s00464-018-6512-6.

[209] Michele Diana et al. "Metabolism-Guided Bowel Resection: Potential Role and Accuracy of Instant Capillary Lactates to Identify the Optimal Resection Site." In: *Surgical innovation* 22.5 (Oct. 2015). Place: United States, pp. 453–461. ISSN: 1553-3514 1553-3506. DOI: 10.1177/1553350615598620.

[210] J. S. Quaedackers et al. "An evaluation of methods for grading histologic injury following ischemia/reperfusion of the small bowel." In: *Transplantation proceedings* 32.6 (Sept. 2000). Place: United States, pp. 1307–1310. ISSN: 0041-1345. DOI: 10.1016/s0041-1345(00)01238-0.

[211] C. J. Chiu et al. "Intestinal mucosal lesion in low-flow states. I. A morphological, hemodynamic, and metabolic reappraisal." In: *Archives of surgery (Chicago, Ill. : 1960)* 101.4 (Oct. 1970). Place: United States, pp. 478–483. ISSN: 0004-0010. DOI: 10.1001/archsurg.1970.01340280030009.

[212] Barbara Seeliger et al. "Simultaneous computer-assisted assessment of mucosal and serosal perfusion in a model of segmental colonic ischemia." In: *Surgical endoscopy* 34.11 (Nov. 2020). Place: Germany, pp. 4818–4827. ISSN: 1432-2218 0930-2794. DOI: 10.1007/s00464-019-07258-z.

[213] M. Diana et al. "Intraoperative fluorescence-based enhanced reality laparoscopic real-time imaging to assess bowel perfusion at the anastomotic site in an experimental model." In: *The British journal of surgery* 102.2 (Jan. 2015). Place: England, e169–176. ISSN: 1365-2168 0007-1323. DOI: 10.1002/bjs.9725.

[214] Christoph Hirche et al. "An experimental study to evaluate the Fluobeam 800 imaging system for fluorescence-guided lymphatic imaging and sentinel node biopsy." In: *Surgical innovation* 20.5 (Oct. 2013). Place: United States, pp. 516–523. ISSN: 1553-3514 1553-3506. DOI: 10.1177/1553350612468962.

[215] Shin-ichi Yamashita et al. "Video-assisted thoracoscopic indocyanine green fluorescence imaging system shows sentinel lymph nodes in non-small-cell lung cancer." In: *The Journal of thoracic and cardiovascular surgery* 141.1 (Jan. 2011). Place: United States, pp. 141–144. ISSN: 1097-685X 0022-5223. DOI: 10.1016/j.jtcvs.2010.01.028.

[216] Philippa Meershoek et al. "Multi-wavelength fluorescence imaging with a da Vinci Firefly—a technical look behind the scenes". In: *Journal of Robotic Surgery* 15.5 (Oct. 2021), pp. 751–760. ISSN: 1863-2483, 1863-2491. DOI: 10.1007/s11701-020-01170-8.

[217] Antonio D'Urso et al. "Computer-assisted quantification and visualization of bowel perfusion using fluorescence-based enhanced reality in left-sided colonic resections." In: *Surgical endoscopy* 35.8 (Aug. 2021). Place: Germany, pp. 4321–4331. ISSN: 1432-2218 0930-2794. DOI: 10.1007/s00464-020-07922-9.

[218] Nikolaj Nerup et al. "Quantification of fluorescence angiography in a porcine model". In: *Langenbeck's Archives of Surgery* 402.4 (June 1, 2017), pp. 655–662. ISSN: 1435-2451. DOI: 10.1007/s00423-016-1531-z.

[219] Kristina Gosvig et al. "Quantification of ICG fluorescence for the evaluation of intestinal perfusion: comparison between two software-based algorithms for quantification". In: *Surgical Endoscopy* 35.9 (Sept. 1, 2021), pp. 5043–5050. ISSN: 1432-2218. DOI: 10.1007/s00464-020-07986-7.

[220] Andrea Spota et al. "Fluorescence-based bowel anastomosis perfusion evaluation: results from the IHU-IRCAD-EAES EURO-FIGS registry". In: *Surgical Endoscopy* 35.12 (Dec. 1, 2021), pp. 7142–7153. ISSN: 1432-2218. DOI: 10.1007/s00464-020-08234-8.

[221] Dedrick Kok Hong Chan, Sean Kien Fatt Lee, and Jia Jun Ang. "Indocyanine green fluorescence angiography decreases the risk of colorectal anastomotic leakage: Systematic review and meta-analysis". In: *Surgery* 168.6 (Dec. 2020), pp. 1128–1137. ISSN: 00396060. DOI: `10.1016/j.surg.2020.08.024`.

[222] M. Alekseev et al. "A study investigating the perfusion of colorectal anastomoses using fluorescence angiography: results of the FLAG randomized trial." In: *Colorectal disease : the official journal of the Association of Coloproctology of Great Britain and Ireland* 22.9 (Sept. 2020). Place: England, pp. 1147–1153. ISSN: 1463-1318 1462-8910. DOI: `10.1111/codi.15037`.

[223] N. Dögnitz and G. Wagniéres. "Determination of tissue optical properties by steady-state spatial frequency-domain reflectometry". In: *Lasers in Medical Science* 13.1 (1998), pp. 55–65. ISSN: 0268-8921, 1435-604X. DOI: `10.1007/BF00592960`.

[224] Mason T. Chen, Taylor L. Bobrow, and Nicholas J. Durr. "Towards SFDI endoscopy with structured illumination from randomized speckle patterns". In: *Advanced Biomedical and Clinical Diagnostic and Surgical Guidance Systems XIX*. Ed. by Caroline Boudoux and James W. Tunnell. Vol. 11631. Backup Publisher: International Society for Optics and Photonics. SPIE, 2021, pp. 43 –48. DOI: `10.1117/12.2578940`.

[225] Hiroshi Kubota and Hitoshi Ohzu. "Method of Measurement of Response Function by Means of Random Chart". In: *Journal of the Optical Society of America* 47.7 (July 1, 1957), p. 666. ISSN: 0030-3941. DOI: `10.1364/JOSA.47.000666`.

[226] Mitsuo Takeda and Kazuhiro Mutoh. "Fourier transform profilometry for the automatic measurement of 3-D object shapes". In: *Applied Optics* 22.24 (Dec. 15, 1983), p. 3977. ISSN: 0003-6935, 1539-4522. DOI: `10.1364/AO.22.003977`.

[227] V. Srinivasan, H. C. Liu, and M. Halioua. "Automated phase-measuring profilometry of 3-D diffuse objects". In: *Applied Optics* 23.18 (Sept. 15, 1984), p. 3105. ISSN: 0003-6935, 1539-4522. DOI: `10.1364/AO.23.003105`.

[228] T.R. Judge and P.J. Bryanston-Cross. "A review of phase unwrapping techniques in fringe analysis". In: *Optics and Lasers in Engineering* 21.4 (Jan. 1994), pp. 199–239. ISSN: 01438166. DOI: `10.1016/0143-8166(94)90073-6`.

[229] W.-S. Zhou and X.-Y. Su. "A Direct Mapping Algorithm for Phase-measuring Profilometry". In: *Journal of Modern Optics* 41.1 (Jan. 1994), pp. 89–94. ISSN: 0950-0340, 1362-3044. DOI: `10.1080/09500349414550101`.

[230] Shao-Pow Lin et al. "Measurement of tissue optical properties by the use of oblique-incidence optical fiber reflectometry". In: *Applied Optics* 36.1 (Jan. 1, 1997), p. 136. ISSN: 0003-6935, 1539-4522. DOI: `10.1364/AO.36.000136`.

[231] Johannes Swartling, Jan S. Dam, and Stefan Andersson-Engels. "Comparison of spatially and temporally resolved diffuse-reflectance measurement systems for determination of biomedical optical properties". In: *Applied Optics* 42.22 (Aug. 1, 2003), p. 4612. ISSN: 0003-6935, 1539-4522. DOI: `10.1364/AO.42.004612`.

[232] Magali Estribeau and Pierre Magnan. "Fast MTF measurement of CMOS imagers using ISO 12333 slanted-edge methodology". In: Optical Systems Design. Ed. by Jean-Pierre Chatard and Peter N. J. Dennis. St. Etienne, France, Feb. 19, 2004, p. 243. DOI: `10.1117/12.513320`.

[233] Nola Hylton. "Magnetic Resonance Imaging of the Breast: Opportunities to Improve Breast Cancer Management". In: *Journal of Clinical Oncology* 23.8 (Mar. 10, 2005), pp. 1678–1684. ISSN: 0732-183X, 1527-7755. DOI: `10.1200/JCO.2005.12.002`.

[234] Etta D Pisano, Janet K Baum, and Lawrence Bassett. "Diagnostic Performance of Digital versus Film Mammography for Breast-Cancer Screening". In: *The New England Journal of Medicine* (2005), p. 11.

[235] C. D'Andrea et al. "Time-resolved spectrally constrained method for the quantification of chromophore concentrations and scattering parameters in diffusing media". In: *Optics Express* 14.5 (2006), p. 1888. ISSN: 1094-4087. DOI: `10.1364/OE.14.001888`.

[236] Mei-Li Hsieh. "Modulation transfer function for a digital micromirror device". In: *Optical Engineering* 45.3 (Mar. 1, 2006), p. 034001. ISSN: 0091-3286. DOI: `10.1117/1.2179809`.

[237] J.A. Noble and D. Boukerroui. "Ultrasound image segmentation: a survey". In: *IEEE Transactions on Medical Imaging* 25.8 (Aug. 2006), pp. 987–1010. ISSN: 0278-0062. DOI: `10.1109/TMI.2006.877092`.

[238] Brian W. Pogue and Michael S. Patterson. "Review of tissue simulating phantoms for optical spectroscopy, imaging and dosimetry". In: *Journal of Biomedical Optics* 11.4 (2006), p. 041102. ISSN: 10833668. DOI: `10.1117/1.2335429`.

[239] S. J. Buckley et al. "Fully integrated sub 100ps photon counting platform". In: Integrated Optoelectronic Devices 2007. Ed. by Kong-Thon Tsen et al. San Jose, CA, Feb. 8, 2007, p. 647116. DOI: `10.1117/12.700843`.

[240] Paulo J. Tavares and Mário A. Vaz. "Linear calibration procedure for the phase-to-height relationship in phase measurement profilometry". In: *Optics Communications* 274.2 (June 2007), pp. 307–314. ISSN: 00304018. DOI: `10.1016/j.optcom.2007.02.038`.

[241] S. N. Friedman and I. A. Cunningham. "Normalization of the modulation transfer function: The open-field approach: Open-field normalization of the modulation transfer function". In: *Medical Physics* 35.10 (Sept. 12, 2008), pp. 4443–4449. ISSN: 00942405. DOI: `10.1118/1.2977536`.

[242] Andrea Bassi et al. "Detection of inhomogeneities in diffusive media using spatially modulated light". In: *Optics Letters* 34.14 (July 15, 2009), p. 2156. ISSN: 0146-9592, 1539-4794. DOI: `10.1364/OL.34.002156`.

[243] A. Farina et al. "Bandpass Effects in Time-Resolved Diffuse Spectroscopy". In: *Applied Spectroscopy* 63.1 (Jan. 2009), pp. 48–56. ISSN: 0003-7028, 1943-3530. DOI: `10.1366/000370209787169795`.

[244] Andrea Farina et al. "Effects of a finite spectral bandwidth light source in time-resolved diffuse spectroscopy". In: European Conferences on Biomedical Optics. Ed. by Rinaldo Cubeddu and Andreas H. Hielscher. Munich, Germany, July 2, 2009, p. 73690V. DOI: `10.1117/12.831695`.

[245] John H. G. M. Klaessens et al. "Non-invasive skin oxygenation imaging using a multi-spectral camera system: effectiveness of various concentration algorithms applied on human skin". In: SPIE BiOS: Biomedical Optics. Ed. by Bruce J. Tromberg et al. San Jose, CA, Feb. 12, 2009, p. 717408. DOI: `10.1117/12.808707`.

[246] Sylvain Gioux, Hak Soo Choi, and John V. Frangioni. "Image-Guided Surgery Using Invisible Near-Infrared Light: Fundamentals of Clinical Translation". In: *Molecular Imaging* 9.5 (Sept. 2010), p. 7290.2010.00034. ISSN: 1536-0121, 1536-0121. DOI: `10.2310/7290.2010.00034`.

[247] Amaan Mazhar et al. “Structured illumination enhances resolution and contrast in thick tissue fluorescence imaging”. In: *Journal of Biomedical Optics* 15.1 (2010), p. 010506. ISSN: 10833668. DOI: `10.1117/1.3299321`.

[248] P D Sasieni et al. “What is the lifetime risk of developing cancer?: the effect of adjusting for multiple primaries”. In: *British Journal of Cancer* 105.3 (July 2011), pp. 460–465. ISSN: 0007-0920, 1532-1827. DOI: `10.1038/bjc.2011.250`.

[249] Wendie A. Berg et al. “Shear-wave Elastography Improves the Specificity of Breast US: The BE1 Multinational Study of 939 Masses”. In: *Radiology* 262.2 (Feb. 2012), pp. 435–449. ISSN: 0033-8419, 1527-1315. DOI: `10.1148/radiol.11110640`.

[250] the BE1 Study Group et al. “Shear wave elastography for breast masses is highly reproducible”. In: *European Radiology* 22.5 (May 2012), pp. 1023–1032. ISSN: 0938-7994, 1432-1084. DOI: `10.1007/s00330-011-2340-y`.

[251] Thomas D. O’Sullivan et al. “Diffuse optical imaging using spatially and temporally modulated light”. In: *Journal of Biomedical Optics* 17.7 (July 18, 2012), p. 0713111. ISSN: 1083-3668. DOI: `10.1117/1.JBO.17.7.071311`.

[252] Claudio Luparello. “Aspects of Collagen Changes in Breast Cancer”. In: *Journal of Carcinogenesis & Mutagenesis* S13 (2013). ISSN: 21572518. DOI: `10.4172/2157-2518.S13-007`.

[253] Thomas D. Vreugdenburg et al. “A systematic review of elastography, electrical impedance scanning, and digital infrared thermography for breast cancer screening and diagnosis”. In: *Breast Cancer Research and Treatment* 137.3 (Feb. 2013), pp. 665–676. ISSN: 0167-6806, 1573-7217. DOI: `10.1007/s10549-012-2393-x`.

[254] Alberto Dalla Mora and Ing Edoardo Martinenghi. “Caratterizzazione di fotomoltiplicatori in silicio come rivelatori di singolo fotone”. In: (), p. 82.

[255] Qi Pian et al. “Multimodal Biomedical Optical Imaging Review: Towards Comprehensive Investigation of Biological Tissues”. In: *Current Molecular Imaging* 3.2 (Feb. 4, 2015), pp. 72–87. ISSN: 22115552. DOI: `10.2174/2211555203666141117231651`.

[256] Alberto Dalla Mora et al. “Fast silicon photomultiplier improves signal harvesting and reduces complexity in time-domain diffuse optics”. In: *Optics Express* 23.11 (June 1, 2015), p. 13937. ISSN: 1094-4087. DOI: `10.1364/OE.23.013937`.

[257] Alberto Dalla Mora et al. “Towards next-generation time-domain diffuse optics for extreme depth penetration and sensitivity”. In: *Biomedical Optics Express* 6.5 (May 1, 2015), p. 1749. ISSN: 2156-7085, 2156-7085. DOI: `10.1364/BOE.6.001749`.

[258] Kyle P. Nadeau et al. “Multifrequency synthesis and extraction using square wave projection patterns for quantitative tissue imaging”. In: *Journal of Biomedical Optics* 20.11 (Nov. 2, 2015), p. 116005. ISSN: 1083-3668. DOI: `10.1117/1.JBO.20.11.116005`.

[259] Paola Taroni et al. “Breast Tissue Composition and Its Dependence on Demographic Risk Factors for Breast Cancer: Non-Invasive Assessment by Time Domain Diffuse Optical Spectroscopy”. In: *PLOS ONE* 10.6 (June 1, 2015). Ed. by Surinder K. Batra, e0128941. ISSN: 1932-6203. DOI: `10.1371/journal.pone.0128941`.

[260] Michael Ghijsen et al. “Real-time simultaneous single snapshot of optical properties and blood flow using coherent spatial frequency domain imaging (cSFDI)”. In: *Biomedical Optics Express* 7.3 (Mar. 1, 2016), p. 870. ISSN: 2156-7085, 2156-7085. DOI: `10.1364/BOE.7.000870`.

[261] Sanathana Konugolu Venkata Sekar et al. "In Vivo, Non-Invasive Characterization of Human Bone by Hybrid Broadband (600-1200 nm) Diffuse Optical and Correlation Spectroscopies". In: *PLOS ONE* 11.12 (Dec. 20, 2016). Ed. by Yoko Hoshi, e0168426. ISSN: 1932-6203. DOI: `10.1371/journal.pone.0168426`.

[262] Sanathana Konugolu Venkata Sekar et al. "Broadband (600–1350 nm) Time-Resolved Diffuse Optical Spectrometer for Clinical Use". In: *IEEE Journal of Selected Topics in Quantum Electronics* 22.3 (May 2016), pp. 406–414. ISSN: 1077-260X, 1558-4542. DOI: `10.1109/JSTQE.2015.2506613`.

[263] Syeda Tabassum et al. "Feasibility of spatial frequency domain imaging (SFDI) for optically characterizing a preclinical oncology model". In: *Biomedical Optics Express* 7.10 (Oct. 1, 2016), p. 4154. ISSN: 2156-7085, 2156-7085. DOI: `10.1364/BOE.7.004154`.

[264] "Edge detection and mathematic fitting for corneal surface with Matlab software". In: *International Journal of Ophthalmology* (Mar. 18, 2017). ISSN: 22223959, 22274898. DOI: `10.18240/ijo.2017.03.02`.

[265] Pablo A. Valdes et al. "qF-SSOP: real-time optical property corrected fluorescence imaging". In: *Biomedical Optics Express* 8.8 (Aug. 1, 2017), p. 3597. ISSN: 2156-7085, 2156-7085. DOI: `10.1364/BOE.8.003597`.

[266] Joseph P. Angelo et al. "Review of structured light in diffuse optical imaging". In: *Journal of Biomedical Optics* 24.7 (Sept. 14, 2018), p. 1. ISSN: 1083-3668. DOI: `10.1117/1.JBO.24.7.071602`.

[267] Simon R Arridge. "Optical Tomographic Reconstruction from MultiSpectral data using a Spectral Model". In: (), p. 3.

[268] Michael T. Ghijsen et al. "Quantitative real-time optical imaging of the tissue metabolic rate of oxygen consumption". In: *Journal of Biomedical Optics* 23.3 (Mar. 24, 2018), p. 1. ISSN: 1083-3668. DOI: `10.1117/1.JBO.23.3.036013`.

[269] Vivian Pera et al. "Optical property uncertainty estimates for spatial frequency domain imaging". In: *Biomedical Optics Express* 9.2 (Feb. 1, 2018), p. 661. ISSN: 2156-7085, 2156-7085. DOI: `10.1364/BOE.9.000661`.

[270] Stephane Perrin and Paul Montgomery. "Fourier optics: basic concepts". In: (June 4, 2018). arXiv: `1802.07161`.

[271] Anton Travinsky and Zoran Ninkov. "Measurement of Modulation Transfer Function using Digital Micromirror Devices". In: *Imaging and Applied Optics 2018 (3D, AO, AIO, COSI, DH, IS, LACSEA, LS&C, MATH, pcAOP)*. Imaging Systems and Applications. Orlando, Florida: OSA, 2018, IW2B.2. ISBN: 978-1-943580-44-6. DOI: `10.1364/ISA.2018.IW2B.2`.

[272] Sanathana Konugolu Venkata Sekar et al. "Solid phantom recipe for diffuse optics in biophotonics applications: a step towards anatomically correct 3D tissue phantoms". In: *Biomedical Optics Express* 10.4 (Apr. 1, 2019), p. 2090. ISSN: 2156-7085, 2156-7085. DOI: `10.1364/BOE.10.002090`.

[273] Yi Sun et al. "K-means clustering of coherent Raman spectra from extracellular vesicles visualized by label-free multiphoton imaging". In: *Optics Letters* 45.13 (July 1, 2020), p. 3613. ISSN: 0146-9592, 1539-4794. DOI: `10.1364/OL.395838`.

[274] Michele Lacerenza et al. "Monitoring the motor cortex hemodynamic response function in freely moving walking subjects: a time-domain fNIRS pilot study". In: *Neurophotonics* 8.1 (Feb. 22, 2021). ISSN: 2329-423X. DOI: `10.1117/1.NPh.8.1.015006`.

[275] Syeda Tabassum et al. “Optical scattering as an early marker of apoptosis during chemotherapy and antiangiogenic therapy in murine models of prostate and breast cancer”. In: *Neoplasia* 23.3 (Mar. 2021), pp. 294–303. ISSN: 14765586. DOI: `10.1016/j.neo.2021.01.005`.

[276] Yu-Jin Lee et al. “A narrative review of fluorescence imaging in robotic-assisted surgery”. In: *Laparoscopic Surgery* 5 (July 2021), pp. 31–31. ISSN: 26164221. DOI: `10.21037/ls-20-98`.

[277] Joab R Winkler. “Numerical recipes in C: The art of scientific computing, second edition”. In: *Endeavour* 17.4 (Jan. 1993), p. 201. ISSN: 01609327. DOI: `10.1016/0160-9327(93)90069-F`.

[278] Junichi Nakamura, ed. *Image sensors and signal processing for digital still cameras*. Boca Raton, FL: Taylor & Francis, 2006. 336 pp. ISBN: 978-0-8493-3545-7.

[279] S. M. Sze and Kwok Kwok Ng. *Physics of semiconductor devices*. 3rd ed. Hoboken, N.J: Wiley-Interscience, 2007. 815 pp. ISBN: 978-0-471-14323-9.

[280] Orazio Svelto. *Principles of Lasers*. Boston, MA: Springer US, 2010. ISBN: 978-1-4419-1301-2 978-1-4419-1302-9. DOI: `10.1007/978-1-4419-1302-9`.

[281] John Cheng. *Professional Cuda C programming*. Wrox programmer to programmer. Indianapolis, IN: John Wiley and Sons, Inc, 2014. 497 pp. ISBN: 978-1-118-73932-7.

[282] Virendra N. Mahajan. *Fundamentals of Geometrical Optics*. SPIE, June 3, 2014. ISBN: 978-0-8194-9999-8. DOI: `10.1117/3.1002529`.

[283] P. N. T. Wells. “Ultrasonics in medicine and biology”. In: *Physics in Medicine and Biology* 22.4 (July 1977). Publisher: IOP Publishing, pp. 629–669. DOI: `10.1088/0031-9155/22/4/001`.

[284] Krzysztof Jakubczak. “High-order Harmonic Generation”. In: *Laser Pulse Phenomena and Applications*. Ed. by F. J. Duarte. InTech, Nov. 30, 2010. ISBN: 978-953-307-405-4. DOI: `10.5772/13048`.

[285] Runar J Strand-Amundsen et al. “Ischemia/reperfusion injury in porcine intestine - Viability assessment”. In: *World Journal of Gastroenterology* 24.18 (May 14, 2018), pp. 2009–2023. ISSN: 1007-9327. DOI: `10.3748/wjg.v24.i18.2009`.

[286] Nikolaj Nerup et al. “Quantification of fluorescence angiography in a porcine model”. In: *Langenbeck's Archives of Surgery* 402.4 (June 1, 2017), pp. 655–662. ISSN: 1435-2451. DOI: `10.1007/s00423-016-1531-z`.

[287] F. B. Achterberg et al. “Clinical translation and implementation of optical imaging agents for precision image-guided cancer surgery”. In: *European Journal of Nuclear Medicine and Molecular Imaging* 48.2 (Feb. 2021), pp. 332–339. ISSN: 1619-7070, 1619-7089. DOI: `10.1007/s00259-020-04970-0`.

[288] R. F. Bonner et al. “Model for photon migration in turbid biological media.” In: *Journal of the Optical Society of America. A, Optics and image science* 4.3 (Mar. 1987). Place: United States, pp. 423–432. ISSN: 0740-3232. DOI: `10.1364/josaa.4.000423`.

[289] Brian S. Peters et al. “Review of emerging surgical robotic technology.” In: *Surgical endoscopy* 32.4 (Apr. 2018). Place: Germany, pp. 1636–1655. ISSN: 1432-2218 0930-2794. DOI: `10.1007/s00464-018-6079-2`.

[290] Alessandro Torricelli et al. “*In vivo* optical characterization of human tissues from 610 to 1010 nm by time-resolved reflectance spectroscopy”. In: *Physics in Medicine and Biology* 46.8 (Aug. 1, 2001), pp. 2227–2237. ISSN: 0031-9155, 1361-6560. DOI: `10.1088/0031-9155/46/8/313`.

[291] Dizem Arifler et al. "Light Scattering from Collagen Fiber Networks: Micro-Optical Properties of Normal and Neoplastic Stroma". In: *Biophysical Journal* 92.9 (May 2007), pp. 3260–3274. ISSN: 00063495. DOI: 10.1529/biophysj.106.089839.

[292] Valentina Bellini et al. "Machine learning in perioperative medicine: a systematic review". In: *Journal of Anesthesia, Analgesia and Critical Care* 2.1 (Dec. 2022), p. 2. ISSN: 2731-3786. DOI: 10.1186/s44158-022-00033-y.

[293] Alexander L. Vahrmeijer et al. "Image-guided cancer surgery using near-infrared fluorescence". In: *Nature Reviews Clinical Oncology* 10.9 (Sept. 2013), pp. 507–518. ISSN: 1759-4774, 1759-4782. DOI: 10.1038/nrclinonc.2013.123.

[294] N.L. Everdell et al. "A portable wireless near-infrared spatially resolved spectroscopy system for use on brain and muscle". In: *Medical Engineering & Physics* 35.11 (Nov. 2013), pp. 1692–1697. ISSN: 13504533. DOI: 10.1016/j.medengphy.2013.04.011.

[295] Z. Kovacsova et al. "Investigation of Confounding Factors in Measuring Tissue Saturation with NIRS Spatially Resolved Spectroscopy". In: *Oxygen Transport to Tissue XL*. Ed. by Oliver Thews, Joseph C. LaManna, and David K. Harrison. Vol. 1072. Series Title: Advances in Experimental Medicine and Biology. Cham: Springer International Publishing, 2018, pp. 307–312. ISBN: 978-3-319-91285-1 978-3-319-91287-5. DOI: 10.1007/978-3-319-91287-5_49.

[296] Samuel Ortega et al. "Use of Hyperspectral/Multispectral Imaging in Gastroenterology. Shedding Some–Different–Light into the Dark". In: *Journal of Clinical Medicine* 8.1 (Jan. 1, 2019), p. 36. ISSN: 2077-0383. DOI: 10.3390/jcm8010036.

Author: **Luca Baratelli**

QUANTITATIVE MULTI-MODAL OPTICAL IMAGING FOR SURGERY

Résumé

L'obtention d'informations quantitatives lors du guidage chirurgical est encore aujourd'hui un besoin majeur non satisfait. L'objectif de ce projet de thèse est de développer des techniques innovantes d'imagerie optique multimodale en temps réel pour le guidage chirurgical et peu invasif, en fournissant des informations quantitatives sur les paramètres physiologiques fondamentaux d'un certain tissu, comme la saturation en oxygène. Ce travail s'appuie surtout sur la Spatial Frequency Domain Imaging (SFDI) et sur la Single Snapshot Imaging of Optical Properties (SSOP). Un système d'imagerie endoscopique basé sur la SSOP a été conçu et validé sur des étalons imitant des tissus, puis développé en une version portable adaptée aux essais précliniques. Une plateforme de référencement multimodal a également été développée pour la caractérisation spectroscopique des milieux diffusifs. L'instrument combine la SFDI et la Time-resolved Diffuse Optical Spectroscopy (TDOS) pour la mise en œuvre d'une approche de référence croisée dans la quantification des propriétés optiques des tissus.

Mots-clés: Imagerie optique diffuse, spatial frequency domain imaging, time domain spectroscopy, endoscopie, chirurgie guidée par l'image, deep learning.

Abstract

The lack of quantitative information during surgical guidance is still nowadays a major unmet need. The aim of this thesis project is to develop innovative, real-time multi-modal optical imaging techniques for open and minimally invasive surgical guidance, by providing quantitative information on fundamental physiological parameters of a certain tissue, such as oxygen saturation. This work is largely built on Spatial Frequency Domain Imaging (SFDI) and Single Snapshot Imaging of Optical Properties (SSOP). An endoscopic imaging system based on SSOP was implemented and validated on tissue mimicking phantoms and then further developed into an handheld version adapted for pre-clinical trials. A multi-modal referencing platform was also developed for the spectroscopic characterization of diffusive media. The instrument combines SFDI and Time-resolved Diffuse Optical Spectroscopy (TDOS) for the implementation of a cross-reference approach in the quantification of tissue optical properties.

Keywords: Diffuse optical imaging, spatial frequency domain imaging, time domain spectroscopy, endoscopic imaging, image-guided surgery, deep learning.